Directing macromolecular assemblies by tailored surface functionalizations of nanoporous alumina

Doctoral thesis

A thesis submitted to the Georg-August-Universität Göttingen
in partial fulfillment of the requirements of the degree of
Doctor of Philosophy
Ph.D.
Division of Mathematics and Natural Sciences
of the Georg-August-Universität Göttingen

Thomas Dominic Lazzara
Montréal (Québec), Canada

Göttingen 2011

Members of the thesis committee:

Prof. Dr. Claudia Steinem (research supervisor)
Georg August University Göttingen
Institute for Organic and Biomolecular Chemistry

Prof. Dr. Ulf Diederichsen
Georg August University Göttingen
Institute for Organic and Biomolecular Chemistry

Prof. Dr. Christoph Schmidt
Georg-August-Universität Göttingen
III. Physics Institute

Date of oral defense: *16 May 2011*

Three things come not back -
the sped arrow,
the spoken word,
and the spent moment ...

Pontiac (1720-1769)
Ottawa Native American Chief

To my father, mother and sister

good times – bad times – they're the only ones always there…

– Table of Contents –

Thesis Section **Page**

I. Research Independence and Intellectual Property I
II. Acknowledgements II
III. Abstract / Zusammenfassung IV
IV. List of Symbols VI
V. List of Abbreviations VII
VI. List of Figures IX
VII. List of Tables XI

1. Introduction 1
1.1. Nano- and Micro-Structured Materials 1
1.1.1. Top-down and Bottom-up 1
1.1.2. Porous Materials 3
1.2. Metal & Inorganic Surface Functionalization and Modification Strategies 5
1.2.1. SAMs on Gold Surfaces 6
1.2.2. Silanization of surfaces with Organofunctional Silanes 7
1.2.3. Plasma Surface Modification 11
1.3. Artificial Lipid Membranes to Study Biological Systems 12
1.3.1. Phospholipid Liposome Self-Assembly 14
1.3.2. Investigation of Artificial Membrane Systems 18
1.3.3. Pore-Spanning Lipid Membranes 21
1.4. Scope of Thesis 22
1.5. Contributions of Co-Authors 24
1.6. References 25

2. Methods, Materials, Instruments: Extended Experimental 33
2.1. Anodic Aluminum Oxide (AAO) Membranes 33
2.1.1. Structure and Physical Properties of AAO 33
2.1.2. AAO Preparation 37
2.1.3. Mounting AAO Thin-Films on Solid Supports 40
2.1.4. Preparation of AAO from Sputtered Al Thin-Tilms 41
2.2. The Dielectric Constant of AAO: an Effective Medium Theory Approach 42
2.3. Total Internal Reflection Techniques 49
2.3.1. Surface Plasmon Resonance Spectroscopy (SPR) 51
2.3.2. Optical Waveguide Spectroscopy (OWS) 54
2.4. Fluorescence Microscopy 58

2.4.1. Upright Fluorescence Microscopy 60
2.4.2. Confocal Laser Scanning Microscopy (CLSM) 61
2.4.3. Fluorescence Recovery after Photobleaching (FRAP) 63
2.5. Scanning Electron Microscopy (SEM) 64
2.6. References 66

3. Mounted Nanoporous Anodic Alumina thin Films as Planar Optical Waveguides 69
3.1. Introduction 70
3.2. Experimental Details 71
3.3. Results and Discussion 73
3.4. Conclusion 79
3.4. References 80

4. Polyelectrolyte Layer-by-Layer deposition in Cylindrical Nanopores 83
4.1. Introduction 84
4.2. Results and Discussion 87
4.2.1. LbL Deposition Within and Atop Nanoporous AAO Membranes 87
4.2.2. Ionic Strength & Charge Effects on LbL within Nanopores 94
4.2.3. Selective Formation of Polyelectrolyte Membranes Atop AAO 100
4.3. Conclusion 101
4.5. Experimental Section 102
4.4. References 105
4.6. Supporting Information 110

5. The Importance of Macromolecular Shape and Interactions in Layer-by-Layer assemblies within Cylindrical Nanopores 113
5.1. Introduction 114
5.2. Results and Discussion 117
5.2.1. Layer-by-Layer Growth within AAO 119
5.2.2. Effective Volume of LbL Deposition Steps 122
5.3. Concluding Remarks 128
5.4. Experimental Section 129
5.5. References 133

6. Benefits and Limitations of Porous Substrates as Biosensors for Protein Adsorption 137
6.1. Introduction 138
6.2. Theory 140
6.2.1. Mass Balance on a Flat Surface 140
6.2.2. Porous Surfaces 141
6.2.3. Simplified Adsorption Kinetics in Porous Media 142
6.3. Results and Discussion 143
6.3.1. Simulating Protein Adsorption Kinetics on Flat Surfaces 143
6.3.2. Simulating Protein Adsorption Kinetics in Porous Media 145
6.3.3. Adsorption Kinetics of Avidin Binding to Porous AAO 147
6.3.3. Desorption of Proteins from Porous Walls 150
6.4. Concluding Remarks 152
6.5. Experimental Section 153
6.6. References 154
6.7. Supporting Information 156

7. Orthogonal Functionalization of Nanoporous Substrates: Control of 3D Surface Functionality 159
7.1. Introduction 160
7.2. Results and Discussion 163
7.2.1. Functionalization Strategies 164
7.2.2. Selective Deposition of Hybrid Solid-Supported Membranes 165
7.2.3. Patterned Substrates 169
7.2.4. Pore-Spanning Lipid Membranes 170
7.3. Concluding Remarks 173
7.4. Experimental Section 174
7.5. References 178
7.6. Supporting Information 180

8. Phospholipids as an Alternative to Direct Covalent Coupling: Surface Functionalization of Nanoporous Alumina for Protein Recognition 185
8.1. Introduction 187
8.2. Results and Discussion 189
8.2.1. Lipid Monolayer Formation on AAO, Streptavidin Adsorption 190
8.2.2. Investigation of Biomacromolecular Assemblies in Nanopores 194
8.2.3. Direct Protein Extraction from a Cell Lysate 197
8.3. Concluding Remarks 198
8.4. Experimental Section 199
8.5. References 204
8.6. Supporting Information 205

9. Separating Attoliter-Sized Compartments using Fluid Pore-Spanning Lipid Bilayers 207
9.2. Introduction 208
9.2. Results and Discussion 210
9.2.1. Pore-Spanning Lipid Membranes on Functionalized AAO 210
9.2.2. Macromolecular Exclusion and Molecular Encapsulation by Pore-Spanning Membranes 214
9.2.3. Impact of Surface Functionalization on Pore-Spanning Membrane Formation 217
9.3. Concluding Remarks 219
9.4. Materials and Methods 220
9.5. References 224
9.6. Supporting Information 227

10. Discussion 231
10.1. 10.1. AAO studied by optical waveguide spectroscopy 231
10.2. 10.2. What limits macromolecular deposition in nanopores 232
10.3. 10.3. The Importance of Controlling Surface Chemistry in 3D 233
10.4. References 237

I. Research Independence and Intellectual Property

I hereby certify that that the work presented in this thesis has been carried out by myself and originates from my own intellectual labor. Wherever collaborators have assisted in data acquisition, data interpretation, data analysis and data simulations, their contributions have been acknowledged: both in the form of co-authorship on published or prepared manuscripts. These contributions have been made explicit in section 1.5.

I further certify that no part of this thesis has been presented for any other degree or diploma or earlier title.

I declare that, to the best of my knowledge, my thesis does not infringe upon anyone's copyright, nor does it violate any proprietary rights and that any ideas, techniques, quotations, or any other material from the work of other people included in my thesis, published or otherwise, are fully acknowledged in accordance with the standard academic referencing practices.

The original ideas and concepts, presented in this thesis, were developed by myself during the course of my doctoral studies. Obviously, where collaborators have assisted in the development of ideas, credit for has been shared with the concerned persons, see section 1.5. The results presented in this thesis are considered my intellectual property, with the underlying understanding that this research is a product of collaborative work. Credit was and should be given, where credit was/is due. Any use and/or reproduction of the methods and results presented in this work should be accordingly rightfully recognized.

_____

Thomas Dominic Lazzara
Wednesday, the 6th of April 2011

II. Acknowledgements

I gratefully acknowledge financial assistance from the province of Québec's *Le Fonds Québécois de la Recherche sur la Nature et les Technologies* for a 3-year doctoral scholarship. Furthermore, I am also thankful to the Göttingen Graduate School of Neuroscience and Molecular Biology for providing supplemental financial assistance during the last two years of my thesis and for helping with additional bridging funds to help finalize my projects.

I would like to firstly thank Prof. Dr. Claudia Steinem for her guidance and support during the second part of my PhD thesis. I really appreciated her open mind and scientific curiosity. I am particularly grateful that she always found time to listen to my ideas, discuss and motivate me. Thanks for the freedom and the confidence you gave me to pursue my projects and bring my ideas to life.

I also thank Prof. Dr. Andreas Janshoff (aka problem-solver) for co-supervision and our frequent short stimulating discussions.

I must especially thank Dr. Aaron K.H. Lau for all his help and mentoring at the beginning of my PhD at the Max Planck Institute for Polymer Research (MPIP) in Mainz. He took the time to teach me all he knew about alumina preparation and optical waveguide spectroscopy. He guided my research, helped me develop my ideas about transport within nanopores and helped shape how I take on scientific problems.

I am grateful to Prof. Dr. Wolfgang Knoll for inviting and convincing me to come and study in Germany for my PhD. I am grateful to have had the opportunity to experience research in the motivated and dynamic environment of the MPIP.

I thank Torben-Tobias Kliesch, my bachelor student, who skillfully performed the experiments I prepared for him. I thank Christian Carnarius for his collaboration with giant vesicle spreading experiments during the development of chapter 9 experiments with pore-spanning membranes. Ingo Mey for running simulations on the COMSOL program. Daniela Behn for helping with protein expression and OWS experiments with cell lysates.

Jutta Gerber-Nolte for keeping the lab in order and making sure things ran smoothly. Although he might not realize it, Alexander Orth, with whom I had the most useful and frequent scientific/nerdy discussions about lipids at interfaces! I thank the Werkstatt, especially Mr. Tao, for fabricating my measurement cells so that all this data could be collected. I would also like to thank Alex, Christian, Marta and Bärbel for a good time in Gomadingen 2010. Thank you to the Steinem and Janshoff group members for support and a good time during the last 2 years.

Finally, I would like to thank the people behind the research scene.

My parents, for always staying in touch with those lunch phone calls, and encouraging me. I got to where I am today because they always expected that I aim to be the best at anything I did, that I never settle for being average. I thank you for teaching me the value of dedication and hard work; to always strive for perfection, the only way to excel at anything.

Laura Lazzara, Charlie Ciliberto, Rami Hourani, Geneviève Giroux, prof. M.A. Whitehead, prof. Theo van de Ven, Matthew Hassler, Katerina Krumova, Renata Vyhnalkova, Gilles Bourret, Olivier Basle, Nuria Queralto, Andrea Pomozzi for encouragement from across the ocean during the last 3 years.

I would like to finish by thanking Marta, who took on this eventful journey with me. She was always there to comfort and love me in the worst of time and to enjoy life and share the happiness in the best of times. She's my motivation, the reason I continue pushing myself to go beyond what I think I am capable. I could not, and would not have done it without you.

III. Abstract

Anodic aluminum oxide (AAO) is a nanoporous material with parallel, hexagonally-ordered, cylindrical pores running straight through the material's thickness. A method to deposit highly ordered AAO thin-films, with adjustable 1-10 μm thicknesses, on various surfaces was developed to allow the *in-situ* study of its dielectric response by optical waveguide spectroscopy (OWS). The Layer-by-Layer deposition within AAO of different types of macromolecules was studied: dendrimer polyelectrolytes, linear polyelectrolytes and proteins. Working at low ionic strength was found to inhibit macromolecular transport within the cylindrical nanopores due to electrostatic repulsion between macromolecules in solution and those adsorbed atop the AAO. Under optimal charge screening conditions, LbL proceeded in a similar fashion as on a planar surface, until multilayer growth became inhibited due to the confined cylindrical geometry that imposes a physical limit to macromolecular deposition and the pore diameter was reduced to 20-35 nm. The LbL growth was dependent on the physical structure of the LbL film, dictated by the size, shape and nature of the interaction between macromolecules. A method for the orthogonal functionalization of AAO was developed to selectively protect the silanized pore-rim AAO surface with a thin gold layer. Subsequent plasma treatments remove the unprotected silanization, such that AAO with different pore-rim and pore-interior surface chemistries were produced. This method was used to direct the formation of both hybrid and fluid pore-spanning membranes on the AAO surface by giant liposome rupture. These lipid membranes effectively encapsulate the AAO pore-interior liquid environment and act as real physical barriers. We demonstrated that these membranes could exclude proteins from entering the nanopores, or alternatively, that they can prevent encapsulated fluorescent dyes from escaping the nanopores. Finally, the homogeneous modification of AAO with a laterally mobile lipid monolayer in three-dimensions was achieved in order to control the amount of protein deposition within the AAO pores.

III. Zusammenfassung

Poröse Aluminate (*Anodic aluminium oxide* (AAO)) bilden Strukturen hoher Ordnung mit parallel angeordneten, hexagonal zylindrischen Poren, welche die Schichtdicke des Materials bestimmen. In dieser Arbeit wurde eine Methode zur Herstellung von hochgeordneten, dünnen Aluminiumoxidfilmen mit variablen Schichtdicken von 1 bis 10 µm auf verschiedenen Oberflächen entwickelt. Die dielektrischen Eigenschaften des AAO ermöglichte *in-situ* Studien mithilfe von Optischer Wellenleiter Spektroskopie (*Optical Waveguide Spectroscopy* (OWS)). So konnte die Schicht-für-Schicht (*Layer-by-Layer* (LbL)) Anlagerung innerhalb der porösen Aluminate von verschiedenen Makromolekülen wie Dendrimer Polyelektrolyte, lineare Polyelektrolyte und Proteine analysiert werden. Experimente bei niedriger Ionenstärke zeigten, dass der molekulare Transport in die zylindrischen Poren inhibiert wird. Grund hierfür ist die elektrostatische Abstoßung der Makromoleküle, welche auf den Porenstegen des AAO adsorbiert sind und den Makromolekülen in Lösung. Unter optimalen Ladungsbedingungen findet die LbL-Ablagerung in gleicher Weise wie auf planaren Oberflächen statt. Das Wachstum der Schichten war demnach lediglich durch die gegebene zylindrische Geometrie begrenzt und konnte bis zur physikalischen Grenze (Reduktion des Porendurchmessers auf 20 bis 35 nm) ungehindert stattfinden. Das Schichtwachstum ist dabei abhängig vom strukturellen Aufbau der Schicht, und wird durch deren Größe, Form und Art der Wechselwirkung zwischen den Makromolekülen bestimmt. Desweiteren wurde in dieser Arbeit eine Methode zur orthogonalen Funktionalisierung der porösen Aluminate entwickelt, mit welcher die silanisierten Porenstege des AAO durch eine dünne Goldschicht geschützt werden können. Die darauffolgende Behandlung des AAO mit Plasma entfernt die ungeschützte Silanisierung innerhalb der zylindrischen Poren, so dass schließlich poröse Aluminate mit unterschiedlicher Oberflächenchemie auf den Porenstegen und im Poreninneren erhalten werden. Diese Methode wurde für die Bildung von hybriden sowie fluiden porenüberspannenden Membranen auf Aluminiumoxid durch das Spreiten von Riesenvesikeln (*Giant Unilamellar Vesicles* (GUVs)) verwendet. Mithilfe dieser Lipidmembranen konnte effektiv das Volumen physikalische des Poreninneren von dem umgebenden Medium abgegrenzt werden, so dass eine physische Barriere entsteht. Dies konnte zum Einen durch den Ausschluss von Protein vom Poreninneren durch die Lipidmembran und zum Anderen durch den Einschluss eines fluoreszierenden Farbstoffs im Poreninneren durch die Lipidmembran gezeigt werden. Schließlich gelang es durch homogene Modifizierung des AAO mit einer lateral beweglichen Lipidmonoschicht, die Menge der Proteinanlagerung innerhalb der dreidimensionalen Strukturen zu verfolgen und zu kontrollieren.

IV. List of Symbols

Symbol	Description
°	Degree
α	decay constants in the *y*-direction
$A_{hexagon}$	Area of a hexagon (AAO unit cell)
Al	Aluminum
A_{pore}	Area of a pore (cross-section)
Au	Gold
β	Correction factor for anisotropy
b	Evanescent field decay length
C	Carbon
c	Speed of ligth in vacuum
c_b	Protein concentration
Cl	Chlorine
Cr	Chromium
Cu	Copper
Δ	Variation
D	Diffusion coefficient
δ	Diffusion layer thickness
D_0, d_0	Initial AAO pore diameter
d_{local}, D_{local}	Local AAO pore diameter
d_{native}	AAO native pore diameter
d_{pore}	AAO pore diameter
ε	Dielectric constant
E	Electric field
ε_0	Dielectric constant of vacuum
E_0	Electric field amplitude
ε_{AAO}	Dielectric constant of anodized AAO
ε_{air}	Dielectric constant of air (1.000)
ε_{buffer}	Dielectric constant of buffer (1.775)
ε_{domain}	Dielectric constant of the domains
$\varepsilon_{effective}$	Effective dielectric constant
ε_L , ε_Z , $\varepsilon_\perp$	Perpendicular component of ε_{AAO}
ε_{matrix}	Dielectric constant of the matrix
ε_{pore}	ε of pore before deposition
ε'_{pore}	Dielectric constant of pore after deposition
ε_{water}	Dielectric constant of water (1.774)
$\varepsilon_{//}$	Parallel component of AAO ε
$f_{deposited\ material}$	Volume fraction of deposited material
f_{domain}	Porous fraction domains
f_{pore}	Porous fraction of AAO
$f_{unfilled\ pore}$	Volume fraction occupied of unfilled pore
Γ	Protein surface concentration
G_f	Gauss radius
h	AAO membrane thickness
H	Hydrogen
H	Magnetic field
h, l	AAO membrane thickness
H_0	Magnetic field amplitude
i	$\sqrt{-1}$
I	Iodine
J	Flux within the AAO pores
κ	Propagation constants in the y-direction
K	Potassium
k	Wavevector
k_{ad}	Adsorption constant
k_{des}	Desorption constant
k_x	Momentum to excite a surface plasmon
λ	Wavelength of light
L	Adsorption area length
L_{apex}	AAO unit cell apex line
$\lambda_{C\text{-}C}$	AAO lattice constant
μ	relative magnetic susceptibility
m	Waveguide mode order
μ_0	Magnetic susceptibility in vacuum
n	Refractive index
N	Nitrogen
ν	Absorption coefficient of a material

n	Refractive index	R_{pore}	Pore radius
∇	Laplace operator	S	Sulfur
O	Oxygen	S_i	Initial linear response of kinetics
π	Pi = 3.1416…	τ	
P_i	Depolarization factor (i = x, y, z)	t	Time, or thickness (consult text)
θ	Incidence angle	$t_{optical}$	Optical thickness
Θ	Surface coverage	$t_{organic}$	Thicknesss of the material
θ_{max}	Max. angle to record waveguide modes	t_{total}	Total deposited thickness
R	Reflectivity	t_{volume}	Thickness: volume of the material
r_{ij}	Amplitude reflection coefficient	u_{max}	maximum velocity
ρ_{pore}	Pore density of AAO substrate	ω	Angular frequency

V. List of Abbreviations

Abbreviation	Description
EZ-LC-LC-biotin	(sulfosuccinimidyl-6-[biotinamido]-6-hexanamidohexanoate)
DOGS-NTA(Ni)	1,2-dioleoyl-sn-glycero-3-{(N-(5-amino-1-carboxypentyl)iminodiacetic acid)succinyl} nickel salt
DOPC	1,2-dioleoyl-sn-glycero-3-phosphocholine
DPPC	1,2-dipalmitoyl-*sn*-glycero-3-phosphocholine
DPhPC	1,2-diphytanoyl-sn-glycero-3-phosphocholine
POPC	1-palmitoyl-2-oleoyl-sn-glycero-3-phosphocholine
APMES	Aminopropyl-dimethylethoxysilane
APDMES	Aminopropyl-dimethyl-ethoxysilane
APTES	Aminopropyl-triethoxysilane
AAO	Anodic Aluminum Oxide
AFM	Atomic Force Microscopy
ATIR	Attenuated total-internal reflection
Av	Avidin
b-BSA	Biotinylated Bovine Serum Albumen (13 biotins / protein)
BLM	Black Lipid Membrane
BSA	Bovine Serum Albumen
C	Celcius
CLSM	Confocal Laser Scanning Microscopy
Dendrimer-Pes	Dendrimer polyelectrolytes
LaSFN9	Dense Lanthanum flint (borosilicate or silico-borate glasses with RE oxides)
DHPE	Dihexanoyl phosphatidylethanolamine
C_{12}-TCS	Dodecyl-trichlorosilane
EMT	Effective Medium Theory
Eq.	Equation
EtOH	Ethanol
EDTA	Ethylenediaminetetraacetic acid

FRAP	Fluorescence Recovery After Photobleaching
FTIR	Fourier Transform Infrared
FWHM	Full Width Half Minimum
GUV	Giant Unilamellar Vesicle
GO	Göttingen
g	Gram
h	Hour
IC	Internal conversion
ISC	Intersystem crossing
kJ	Kilojoule
LUV	Large Unilamellar Vesicle
Linear-PEs	Linear polyelectrolytes
L	Liter
MPIP	Max Planck Institute for Polymer Research
MG	Maxwell-Garnett
SHTES	Mercaptopropyl-triethoxysilane
m	Meter
µm	micrometer
ml	Milliliter
mm	millimeter
min	Minute
M	mol/l
mol	mole
nm	Nanometer
NOA	Norland Optical Adhesives
OWS	Optical Waveguide Spectroscopy
OWSF	Optical Waveguide Spectroscopy Fluorescence
G4-	Phosphorous based dendrimers of the 4^{th} generation, 96 peripheral negative charges
G4+	Phosphorous based dendrimers of the 4^{th} generation, 96 peripheral positive charges
PEO	Poly(ethylene oxide)
R	Reflectivity
SEM	Scanning Electron Microscopy
s	Second
SAM	Self-Assembled Monolayer
SUV	Small Unilamellar Vesicle
SSM	Solid-Supported Membrane
StAv	Streptavidin
SP	Surface Plasmon
SPR	Surface Plasmon Resonance
TEOS	Tetraethoxysilane
TIR	Total-internal reflection
TE_x	Transverse Electric, mode of order x
TM_x	Transverse Magnetic, mode of order x
VR	Vibrational relaxation
V	Volt
vol.	Volume
wt.	Weight
XPS	X-ray Photoelectron Spectroscopy

VI. List of Figures

Lengthy figure captions have been shortened, consult text for full versions.

Figure Descriptions

Chapter 1:

Figure 1.1. *Top-down* approach to microfabrication.
Figure 1.2. Classification of porous materials based on pore size according.
Figure 1.3. General schematic view of the concept of surface functionalization.
Figure 1.4. Chemical structure of functional organosilanes and reactivity on surfaces.
Figure 1.5. Structure and reactivity of tri-functional and mono-functional silanes.
Figure 1.6. Fluid mosaic model and more complex view of the lipid membrane.
Figure 1.7. Chemical structure of a commonly used lipid.
Figure 1.8. Probability density curves illustrating the average positions of the different functional groups with respect to the center of a DOPC bilayer, Wiener *et al.*
Figure 1.9. Schematic of a phospholipid vesicle and preparation methods.
Figure 1.10. In the lipid bilayer, rotational and lateral lipid diffusion occurs at $T > T_m$.
Figure 1.11. Schematics of different model membranes.

Chapter 2:

Figure 2.1. 3D schematic and SEM of self-ordered anodic aluminum oxide (AAO).
Figure 2.2. Initial steps leading to steady-state AAO growth.
Figure 2.3. Optical waveguide spectrum and SEM of AAO from Al annealed at 500°C.
Figure 2.4. Anodization of Al metal on glass slides.
Figure 2.6. AAO unit-cell and pertinent dimensions used to estimate porosity
Figure 2.7. Pore fraction as a function of AAO pore diameter (d_0) for $\lambda_{C\text{-}C}$ = 100 nm.
Figure 2.8. Dielectric constant ($\varepsilon_{x,y}$) of AAO when a material ($\varepsilon = 2.1$) deposits uniformly within the entire depth of the cylindrical nanopores.
Figure 2.9. OWS spectra and ε of AAO pore-widened for different times.
Figure 2.10. Reflection and transmission of p-polarized light at the interface between two optically transparent media, $n_2 > n_1$.
Figure 2.11. Surface plasmon at metal-dielectric interface, Kretschmann configuration.
Figure 2.12. Dispersion relation of free photons in air and and in a coupling prism.
Figure 2.13. SPR angular reflectivity spectra, molecular adsorption.
Figure 2.14. Slab waveguide schematic and optical waveguide spectroscopy.
Figure 2.15. OWS TM-spectra simulations for substrates with different parameters.
Figure 2.16. The chemical structures of the 4 molecular fluorophores used.
Figure 2.17. The Perrin-Jablonski diagram.
Figure 2.18. Schematic of an upright epifluorescent microscope.
Figure 2.19. Schematic of a confocal laser scanning microscope (CLSM).
Figure 2.20. Z-stack principle behind 3-dimensional image reconstitution.
Figure 2.21. Overview of fluorescence recovery after photobleaching.

Chapter 3:

Figure 3.1. Preparation scheme for AAO thin film preparation on different surfaces.
Figure 3.2. SEM cross-section of an AAO film mounted as a slab waveguide.
Figure 3.3. Optical waveguide R vs. θ spectra in air for a mounted alumina film.
Figure 3.4. R vs. θ spectra of a mounted AAO and Fresnel calculations.
Figure 3.5. Characterization of a 1.4 μm thick AAO membrane mounted on the curved metallic surface of a steel syringe needle, 1 mm in diameter.

Chapter 4:

Figure 4.1: Chemical structure of the phosphorus-containing dendrimers

Figure 4.2. Schematic of the OWS set-up used to measure waveguide modes.

Figure 4.3. Optical waveguide measurements with Fresnel calculations for an APDMES-functionalized AAO waveguide with D_0 = 65 nm in water and after 3, 6 and 9 depositions.

Figure 4.4. Thicknesses of the G4-polyelectrolyte layers deposited from 100 mM NaCl aqueous solutions, within (t_{in}, (**A**)) and atop (t_{atop}, (**B**)) nanoporous AAO membranes with various pore diameters.

Figure 4.5. SEM images of the interior and atop the AAO membrane (D_0 = 65 nm) after 10 deposition steps from 100 mM and 0 NaCl.

Figure 4.6. Thicknesses of the G4-polyelectrolyte layers deposited from ultrapure water solutions, within (t_{in}, (**A**)) and atop (t_{atop}, (**B**)) nanoporous AAO membranes with various pore diameters.

Figure 4.7. Initial G4-polyelectrolyte layer thickness deposited within AAO pores at increasing NaCl concentrations, flat and porous surface.

Figure 4.8. Dendrimer deposition regimes and local pore-diameter.

Figure 4.9. t_{atop} (circles) and t_{in} (squares) obtained by a 2-step protocol for selectively depositing a polyelectrolyte membrane atop empty pores.

Figure 4.S1: Layer model used for Fresnel calculations to obtain an interior and atop.

Figure 4.S2: SPR of polyelectrolyte dendrimer LbL on flat surface.

Figure 4.S3: LbL deposition process within the pores on the top surface (50 mM NaCl).

Figure 4.S4: Pore diameter reduction as the number of polyelectrolyte dendrimer layers increases at different NaCl concentrations.

Figure 4.S5: Transverse magnetic waveguide modes for deposition on a 55 nm pore AAO membrane from 500 mM NaCl solutions of dendrimers (1 mg/mL).

Chapter 5:

Scheme 1. Schematic of LbL for different types of macromolecules in AAO.

Figure 1. Flat vs porous behavior for linear-PEs, proteins and dendrimer-PEs.

Figure 2. Optical thickness of the growing LbL multilayer film on the inner-surface of the AAO cylindrical nanopores for proteins and linear-PEs.

Figure 3. Maximum number of macromolecular LbL steps (n_{max}) for proteins, linear-PEs and dendrimer-PEs.

Scheme 2. The total volume occupied by a macromolecular layer, schematic.

Figure 4. Estimated d_{local} as a function of d_0, for the studied macromolecules.

Figure 5. SEM image of AAO with d_0 = 69 nm pores before and after linear-PEs LbL.

Chapter 6:

Figure 6.1. Flow cell geometry used for FES and OWS studies of protein adsorption.

Figure 6.2. FES of the adsorption process on a flat surface.

Figure 6.3. Surface coverage *vs* time for different pore lengths, simulations. Initial response *vs* concentration and pore depth, simulations.

Figure 6.4. Experimental adsorption kinetics of avidin on a flat and porous surfaces.

Figure 6.5. Adsorption kinetics of avidin as a function of different parameters.

Figure 6.6. Desorption kinetics of proteins, simulations and experiment.

Figure 6.S1. Finite element simulations, flat surfaces.

Figure 6.S2. Kinetics of single pore-filling as a function of pore length h.

Figure 6.S3. Schematic of the system used to simulate the kinetics using COMSOL.

Figure 6.S4. Kinetics simulated for 1 (black), 100 (gray) and 1200 pores (dotted).

Figure 6.S5. Concentration profiles (1200 pores) at different times, low k_{ad} and high k_{ad}.

Figure 6.S6. Initial linear response (S_i) from simulations (1200 pores), various k_{ad} values.

Figure 6.S7. Experimental avidin adsorption regeneration curves.

Figure 6.S8. Experimental OWS spectra before and after avidin adsorption.

Chapter 7:

Figure 7.1. AAO membranes in applications requiring dual-functionality.
Scheme 7.1. Two experimental protocols to prepare AAO with dual-functionality.
Figure 7.2. AAO substrates differing in their orthogonal surface functionalities. Small unilamellar POPC vesicles interact differently with these surfaces.
Figure 7.3. Kinetics of SUV interaction with different orthogonal AAO substrates.
Figure 7.4. Confocal fluorescence of orthogonally functionalized AAO with SUVs.
Figure 7.5. Illustration of the steps leading to the formation of hybrid pore-spanning lipid membranes on orthogonally functionalized AAO with hydrophobic pore rims obtained from silanization with C_{12}-TCS following Scheme 1.
Figure 7.6. FRAP recovery curve obtained on a pore-spanning lipid membrane patch.
Figure 7.S1. Glass modified with cyanine-3-maleimide dye, orthogonally functionalized.
Figure 7.S2. Fresnel simulations of the OWS spectrum for the case for a 25 nm film forming only atop and for a 2.5 nm film on the entire AAO film.
Figure 7.S3. OWS spectrum before and after vesicle adsorption onto substrate **1.**
Figure 7.S4. 50 nm of Au were evaporated onto AAO to observe Au contamination.
Figure 7.S5. Photographs showing the transparency of free-standing AAO films.

Chapter 8:

Scheme 8.1. Sheme to cover hydrophobic AAO substrates with a lipid monolayer.
Figure 8.1. Kinetics of SUV spreading and streptavidin adsorption to lipid monolayer.
Figure 8.2. Lipid monolayer and streptavidin thicknesses, different biotin-DOPE mol %.
Figure 8.3. FRAP showing fluorescence inside bleached area recovers after minutes.
Figure 8.4. *Z*-direction CLSM fluorescence profiles taken at progressive times showing the evolution of streptavidin adsorption using 10 mol % biotin-DOPE.
Figure 8.5. Kinetic measurements of lipid POPC monolayer formation containing 20 mol % biotin-DOPE followed by three protein deposition steps.
Figure 8.5. His-tag labeled PIGEA14 protein adsorption on 10 mol % DGS-NTA(Ni).
Figure S1. SUV spreading kinetics on hydrophobic AAO, different vesicle sizes.

Chapter 9:

Figure 9.1. Schematic of solvent-free fluid pore-spanning membrane on AAO nanopore.
Figure 9.2. Pore-spanning lipid bilayer patches obtained by the rupture of giant unilamellar POPC vesicles doped with 1 mol % Texas Red DHPE on AAO.
Figure 9.3. GUV before and after rupture and FRAP experiment.
Figure 9.4. POPC pore-spanning membrane that exclude Alexa-488 avidin.
Figure 9.5. Pyranine encapsulation in attoliter pores by lipid bilayers on AAO.
Figure 9.6. Pore spanning membranes prepared from mercaptoethanol on gold.
Figure 9.7. AAO functionalization protocol and schematic of surface functionalization.
Figure 9.S1. POPC GUVs interact differently, depending on AAO functionalization.
Figure 9.S2. Wetting behavior of water on freshly silanized glass: TEOS, SHTES, APTES.
Figure 9.S3. Labeled Alexa488-avidin adsorbed on alumina.
Figure 9.S4. Pyranine encapsulation experiments: high POPC membrane coverage.
Figure 9.S5. Pyranine entrapped in AAO nanopores by POPC membrane, bleaching.
Figure 9.S6. FRAP on a lipid membrane patch lying on the flat adhesive (next to AAO).
Movie 9.S1. Videomicroscopy frames of GUVs rupturing on hydrophilic AAO.

VII. List of Tables

Table 1.1. Gases used in plasma cleaner and surface modification.
Table 1.2. Chemical structure of some phospholipids, names, abbreviations, M_w and T_m.
Table 2.1. Depolarization factors (P) along principle axes of a transparent nanostructured thin-film.
Table 2.2. Dielectric constant of AAO grown from annealed and non-annealed Al.
Table 5.1. Details of the macromolecular species used and their deposition properties.

Chapter 1 Introduction

1.1. Micro- and Nano-Structured Materials

1.1.1. *Top-down* and *Bottom-up*

As the structural features of materials are reduced to the nanoscale (10-100 nm), various properties become size dependent.[1-8] Nano-structured materials provide new possibilities to exploit and manipulate the physical and chemical properties on a 3D scale, going beyond the limitations of planar 2D surfaces. Nanoscience has been pushed by both the development of *top-down* and *bottom-up* approaches to designing novel micro- and nano-materials. In *top-down* approaches, materials are designed by precision engineering using lithographic tools for generating nanostructures.[9] *Top-down* lithographic approaches to 2D and 3D substrate patterning have been used to produce features ranging from 200 nm, up to several tens of μm. Microfabrication techniques, in general, involve various surface protection and surface etching steps that ultimately produced micro-structures. For example, atomic force microscopy (AFM) tips on cantilevers (SEM, figure 1.1B) are produced by controlled etching of Si and Si_3N_4 wafers. In microfabrication, a material is typically protected by a UV-curable photoresist and illuminated with a patterned-mask where only UV-exposed areas are cured. The substrate is then treated with an etching agent that essentially dissolves part of the material from the non-protected areas, forming grooves and producing 3-dimensional structures. Macroporous silicon is another example, which develops when an n-type Si wafer is anodically biased and electrochemically etched in HF; back-irradiation of a pattern establishes pore-ordering. Microcontact printing and embossing are often used to pattern the surface with chemically distinct, and spatially localized domains.[10]

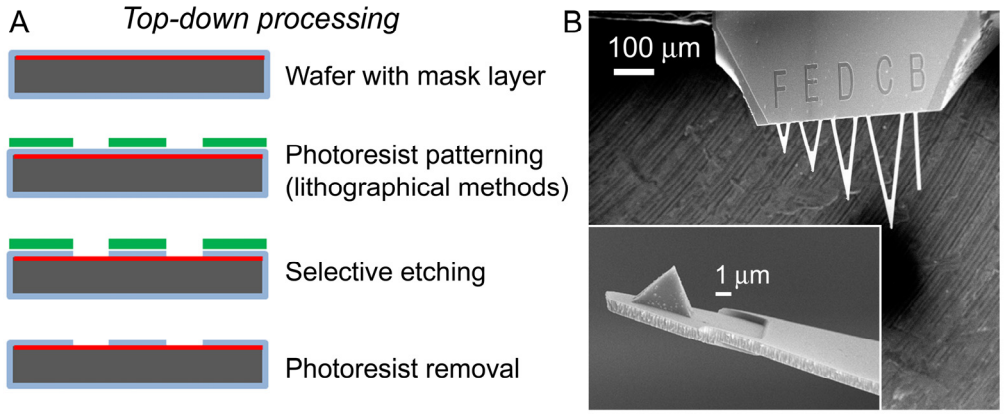

Figure 1.1. (**A**) *Top-down* approach to microfabrication. Overview of the process-flow used to pattern a Si wafer though the selective use of a photoresist. (**B**) Example of a functional micro-structured material that can be produced by a *top-down* approach: AFM tips on cantilevers.

However, when the geometrical features start decreasing below the diffraction limit of UV-radiation, fabrication costs increase exponentially and resolution limits are challenging to overcome; Intel Inc. is currently achieving 32 nm features with high-*n* immersion lithography. Although nanometer surface structures are thus possible (< 200 nm), the equipment required for such lithography is out of reach for most laboratories. Significant research efforts over the past decades have therefore been motivated at using the self-organization of various materials, often inspired from natural systems,[11-13] to create nano-structured materials and achieve < 200 nm resolution; referred to *bottom-up* approach.[14-17] *Bottom-up* techniques rely on functional materials or molecules that spontaneously produce long-range ordered nanostructures. This includes the well-established self-assembly of block-copolymers into lamellas, gyroid phase and cylindrical domains on surfaces.[14-15, 18-22] Alternatively, dip-pen lithography[23-24] can also be used to design complex nanometer patterns, consisting in modifying the surface through interactions with an AFM tip, 10-50 nm wide at the apex.

Recently, merging *top-down* with *bottom-up*, [25-27] consisting in the formation of self-assembled nanostructures within or atop micrometer features produced by lithographic means has been used to produce hybrid materials. Development of *top-down* and *bottom-up* approaches has provided us with numerous useful materials and techniques that can be implemented to overcome challenges in industrial chemical purification processes,[28] sustainable energy development[29] and as characterization tools for the elucidation of biologically relevant systems, to name a few.[30-31]

1.1.2. Porous Materials

Flat surfaces have the inherent advantage of geometrical simplicity. However, studies are restricted to 2D systems. Porous materials that take advantage of a 3rd structural dimension can be used for a variety of novel studies that aim at exploiting a 3D geometry. Studying solution gradients across porous sieves for biomolecular[32] or bio-macromolecular[28] separation, pore-compartmentalization[33] for high-throughput sensing and high-sensitivity biosensors[34-35] are a few examples of novel applications that can be improved using porous materials instead of planar interfaces.

Porous materials can be defined as solids containing multiple pores, which provide a porosity (f_{pore}) being defined as the fraction of pore volume (V_{pore}) to total volume ($V_{material}$):

$$f_{pore} = \frac{V_{pore}}{V_{material}} \qquad \text{equation (1.1)}$$

Porous materials are ubiquitously present in multiple applications, specifically those that require size exclusion, such as filters. Size exclusion is a unique property associated with pore channels lying within these materials, which can be exploited for either size-selectively allowing analytes within/through the porous matrix, or alternatively to selective exclude undesired material. These channels have also been used as templates for the growth or deposition of a second material inside the pores in order to create novel 3D template replicas or novel 2-component hybrid materials. Porous materials with large pores, $d_0 > 200$ nm, are easily prepared by *top-down* approaches, while materials with $d_0 < 200$ nm require *bottom-up* approaches for fabrication. The international pure and applied chemistry (IUPAC) has established a specific nomenclature for porous materials based on average pore diameter (d_0): microporous ($d_0 < 2$ nm), mesoporous materials (2 nm < d_0 < 50 nm) and macroporous materials (d_0 > 50 nm). Figure 1.2 shows different types of 3D porous materials. For example, the interior of microcroporous channels ($d_0 \sim$ a few Å) in naturally occurring inorganic aluminosilicate crystals, known as zeolites, are highly acidic and are commonly used in the petrochemical industry to catalyze hydrocarbon cracking. Other materials, such as self-assembled block-copolymer films, with sub-nanometer pores can be used for potential gas-separation or carbon-capture devices.[36] Mesoporous materials can be used for applications that require size-selective molecular and macromolecular separation such porous Al_2O_3 or porous TiO_2. Macroporous materials can be used for sieving bacteria or dust particles (fluxxion pores, figure 1.2, used for beer filtering). Recently, many *bottom-up* approaches have been used to develop materials that lie at the interface between mesoporous and macroporous, commonly referred to as nanoporous to describe their pore

dimensions: $0.2 < d_0 < 100$ nm. Two examples of nanoporous materials are shown in figure 1.2: anodic aluminum oxide and a polycyanurate nanorod array.

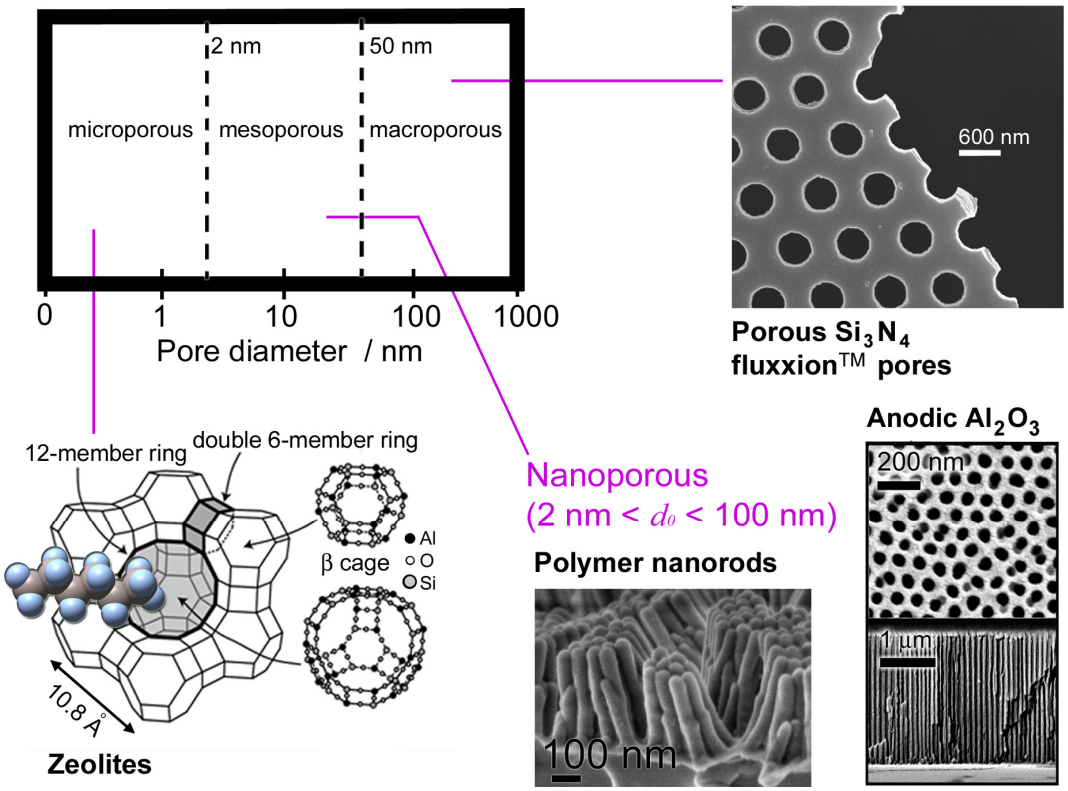

Figure 1.2. Classification of porous materials based on pore size according to the IUPAC recommendations. Examples of different porous material classes are shown (schematic and electron microscopy).

A number of different nanoporous materials have been studied as potential platforms for high-sensitivity sensors devices,[34] or to enhance physical properties such as photosensitivity[37-38] or catalytic efficiency.[39] Anodic Aluminum Oxide (AAO) is of significant interest because of its mechanical stability, the predictability of its 3-D structure and for its simple and reliable method of fabrication. Nanoporous AAO is a self-ordered material having non-intersecting, hexagonally ordered cylindrical pores that run straight through the film thickness and whose monodisperse pore diameter can be conveniently adjusted between 10 to 420 nm.[40-43] AAO has been a preferred candidate for novel sensing platforms owing to the achievable 1-3 orders in magnitude increased surface area. For AAO with d_0 = 60 nm, the surface area of a 25 µm deep AAO is about 800 × larger than a flat surface. The main advantage of AAO over isotropic porous networks comes from its well-ordered structure that can be used to more easily and reliably predict the amount of deposited materials and the expected adsorption-desorption properties that ensue. In many practical industrial applications, the use of nanopores has been towards more efficient size-selective molecular and macromolecular filtering.[44-47] AAO has been used for size-

dependent filtration applications that have proven effective to separate proteins[28], DNA,[32] and large macromolecules.[48] Sensing applications rely on the increased instrumental response associated with probing a porous material, as opposed to a flat surface.[49-53] Novel 1D and 3D materials have also been produced by the negative replication of the structure of a first sacrificial nanoporous material; a technique referred to as template-replication. AAO has been extensively used to produce a variety of metal, inorganic and polymer nanorods[54-56] and nanotubes[57] of various axis ratios, by controlling both pore depth and pore diameter of the cylindrical nanopores. Furthermore, because the size of nano-structured features are below the scattering limit of visible light, optical characterization of nanoporous material properties becomes possible by direct confocal and epi-fluorescence microscopy to investigate phenomena occurring within the substrate, or by optical thin-film analysis techniques such ellipsometry, optical waveguide spectroscopy and thin-film reflectometry.

1.2. Metal & Inorganic Surface Functionalization/Modification Strategies

A range of chemical strategies is available to chemically modify solid and porous substrates, effectively producing a new surface that has a different chemistry and therefore different interfacial properties than the original surface. For example, a hydrophobic modification of a glass surface with a single molecular layer of alkyl-molecules changes the wetting properties of the surface, which becomes water-repellant. For other applications, one may require charged moieties, reactive monomers, protein covered or polymer coated surfaces. All require surface tailored surface modification strategies. Coinage metals,[58-64] polymers,[65-67] and inorganic or metal oxide[1, 68-73] substrates can be functionalized by the formation of functional monolayers through surface reactions such as silanizations,[68-70, 74] reactive plasma treatments,[75-76] thiols[58-59, 61-63, 77-80] and phosphonate chemistry.[81-83] All strategies, other than those involving reactive plasma, generally rely on the adsorption of amphifunctional molecules on the solid surface, as illustrated in figure 1.3. These amphifunctional molecules can be represented as having two parts. The first is a reactive part that has a strong affinity to the surface, and is in general capable of making a covalent bond or strong physisorption. The remainder of the amphifunctional molecule has no affinity, or very weak, to the surface and carries the desired interfacial surface functionality.

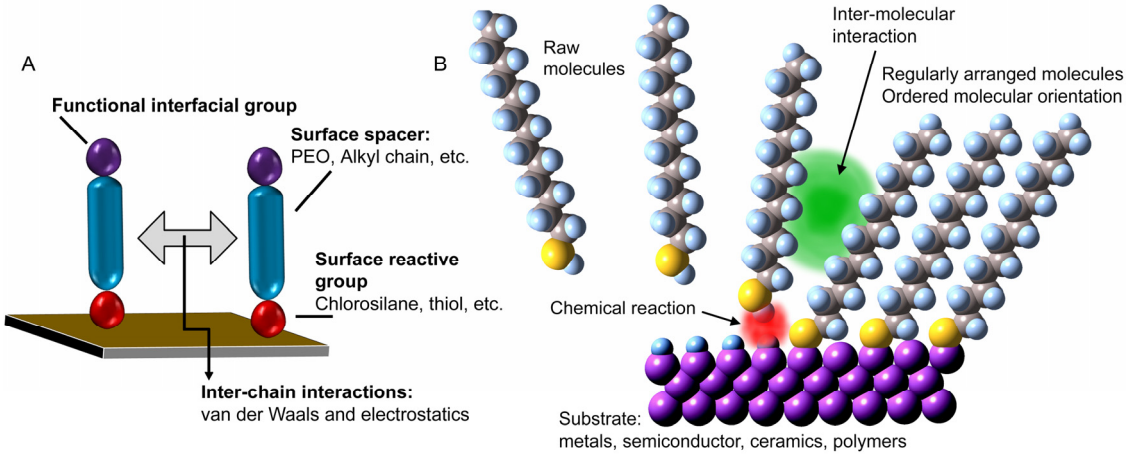

Figure 1.3. (**A**) General schematic view of the concept of surface functionalization. (**B**) Illustration of the self-assembly process; balance between inter-molecular and surface interactions of functional molecules.[84]

1.2.1. SAMs on Gold Surfaces

Self-assembled monolayers (SAMs) of thiol and disulfide molecules are prepared from solution or gas-phase deposition on gold surfaces, silver and copper, as well as onto other transition metals deemed "soft" due to their large atomic size and favorable electronic interactions toward sulfur (Ru, Pt, Pd).[85-87] X-ray photoelectron spectroscopy,[88] electrochemical,[89] as well as FTIR techniques have shown that the thiol and disulfide[77] chemisorption onto gold occurs through the formation of thiolate species,[85, 90] eq. (1.2, 1.3).

$$RS\text{–}H + Au^0_n \rightarrow RS^-Au^+ \cdot Au^0_{n-1} + \tfrac{1}{2} H_2 \qquad \text{equation (1.2)}$$

$$RS\text{–}SR + Au^0_n \rightarrow 2\, RS^-Au^+ \cdot Au^0_{n-2} \qquad \text{equation (1.3)}$$

Au surfaces are also known to reduce disulfide bonds and form two surface-bound thiolates, which typically leads to less ordered SAMs. The surface functionalization procedure is typically carried by immersion, of the *a priori* cleaned metal surface, into a self-assembly solution in a few mM solution of the thiol in ethanol. While the physisorption reaction is very rapid (< 15 min),[91-92] over a few hours (2-4),[92] surface coverage and order usually improves.

Mixed SAMs, obtained by mixing thiols in various ratios, have also been shown useful in creating multi-functional surfaces, although the thiol composition in solution is seldom reproduced onto the surface[93] and without any guaranteed homogeneity (*i.e.* domains may form), although asymmetric disulfide reduction at the surface can ensure better surface

mixing. This simple method of functionalizing gold surfaces has been demonstrated to be robust and reliable and has therefore gained significant importance in tailoring planar surfaces for directed chemistry in adsorption studies, protein binding kinetics, multilayer studies and artificial membrane systems. Often, Au is evaporated over a range of different substrates for the sole and simple reason to take advantage of the simplicity and predictability associated with Au-thiol chemistry.

1.2.2. Silanization of Surfaces with Organofunctional Silanes

Many other surfaces are unreactive towards thiols and cannot be coated with Au metal for either economical reasons or for practical considerations that would adversely modify material properties: transparency and conductivity for example. Low atomic number semiconductors and metals (Al, Mg, Si, Ge), organic and oxide materials (SiO_2, GeO_2) are inert towards thiols. For such surfaces, silanization reactions are useful surface functionalization and modification tools. Silanes are a particular class of tetrahedral molecules with a similar chemical versatility to that of carbon, but whose Si-X covalent bonds are prone to nucleophilic substitution through SN_2 mechanism, and therefore the labile –X moieties are more easily displaced than for similar carbon-based molecules. The general chemical structure of silanes is illustrated, and contrasted to a carbon counterpart, in figure 1.4A. CCl_4 does not react easily with OH^- anions, but $SiCl_4$ react vigorously with water. The Si-Cl covalent bond enthalpy (391 kJ mol^{-1}) is larger than for the C-Cl bond (327 kJ mol^{-1}),[94] and the Si-Cl bond (222 pm) is longer than the C-Cl bond (177 pm).[95] Furthermore, the covalent radius of Cl (99 pm) is slightly larger than that of carbon (77 pm) and slightly smaller than the Si radius (119 pm).[96] Structurally, these compounds are similar, but electronically they are very distinct. Silicon atoms have accessible empty *d*-orbitals, whereas carbon does not. The larger size of the Si atom also reduces steric hindrance to incoming lone electron pair of nucleophiles, *e.g.* OH^-. The combined electronic and steric factors allow the formation of the required 5-coordinate transition state (sp^3d hybrid).[97] The availability of the *d*-orbitals facilitates the formation of the transition state and implies that the Si-Cl bond does not have to be broken first, to accommodate nucleophile addition. The overall result is a kinetically faster hydrolysis of silicon halides, and by analogy also silicon alkoxydes.

$Si(X)_3R$ silane involves 3 labile -X functional groups and an organofunctional -R group such as mercaptopropyl, aminopropyl, alkyls, perfluoroalkyls, phenyl, vinyl, and other derivatives, which are stable in the presence of the Si-X groups. Certain combination are not possible, such as X = Cl and R = $CH_2CH_2CH_2NH_2$, since they would lead to self-polymerization. The most prevalent industrial application of organofunctional silanes is found as coupling agents to bind two materials with distinctly different surface properties such as polymers and glass fibers. Reactive organosilanes react at the Si-X moiety with water, present as surface moisture or in solution, to form silanol –Si-OH group by displacement of the labile -X group. Siloxanes are generated under hydrolysis conditions from chloro- or alkoxysilanes, thereby involving silanols –Si-OH as labile intermediates. Typical -X groups are in order of reactivity: Cl > OCH_3 > OCH_2CH_3 > $OCH_2CH_2CH_3$. This displacement reaction is shown in figure 1.4C with a tri-functional silane. The general silanization mechanism for all such silane coupling agents is illustrated in figure 1.4C and involves: (i) partial to complete hydrolysis with some uncontrolled oligomerisation prior to interaction with the surface, (ii) surface adsorption through hydrogen bonding between surface hydroxyl and silanol groups and (iii) condensation reaction by heating leading to siloxane bond formation at the surface. Functional organosilanes are therefore covalently coupled to the surface via strong resilient siloxane (Si-O-Surface) bonds, while providing a remaining organofunctional group that can be used for reaction between the silanized surface and a second material interface.

Silanes can react with most pre-treated surfaces because hydroxyl bonds are easily formed on various materials, either by chemical oxidation in solution or by plasma treatment. Silanizations can be carried out in solution or in gas-phase, as long as a source of moisture, and in some instances even an acid or heat (especially for alkoxysilanes), are present to drive the hydrolysis reaction. Depending on the experimental conditions (*humidity %, reaction time, silane concentration*) multiple silanol groups are generated by hydrolysis of the Si-OX group. Irrespective of how the film is formed, di- and tri-functional ($Si(X)_2R_1R_2$ and $Si(X)_3R$) silanes generally form multiple siloxane layers on the surface by a series of cross-linking reactions.

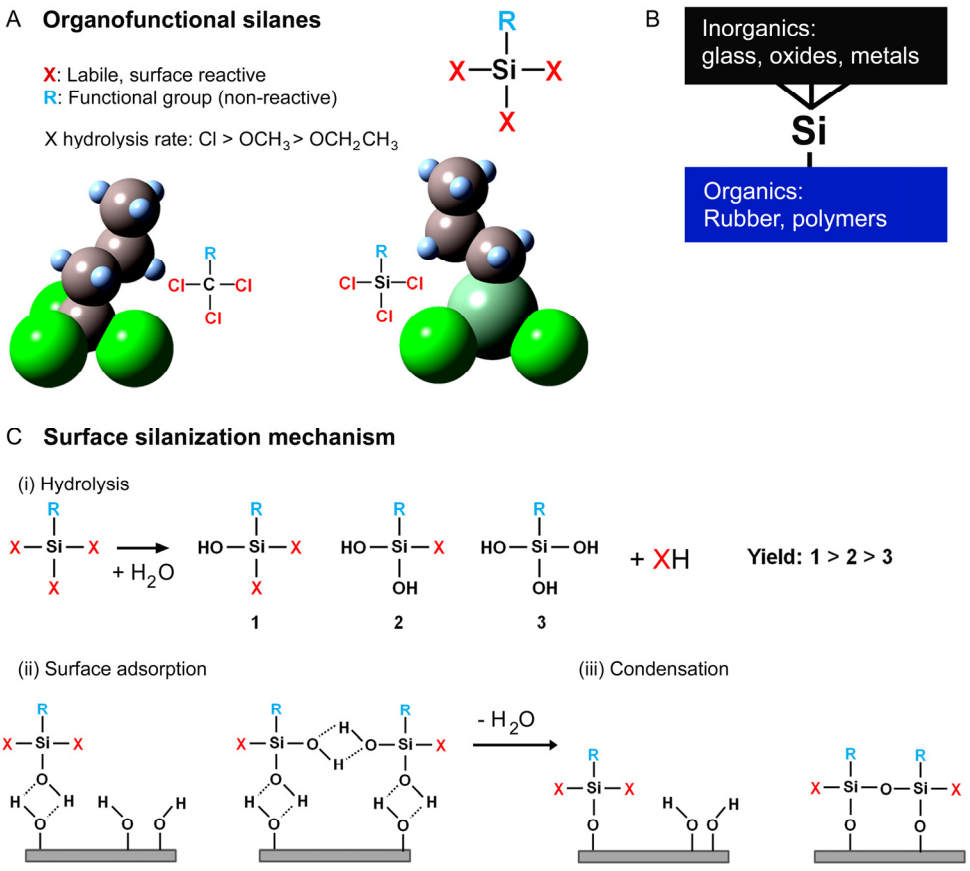

Figure 1.4. (**A**) General chemical structure of functional organosilanes.[84] (**B**) Silanes are typically used as adhesion promoters: covalently binding of two distinctly different materials, SiO_2 and rubber for example. (**C**) Surface silanization with organofunctional silanes: (i) hydrolysis, (ii) surface adsorption, (iii) condensation.

As was mentioned above, the crucial steps in the activation of organosilanes is the reaction with water adsorbed on the surface, present in solution or in vapor phase. However, it is precisely this requirement of having water present for activation of the coupling agent that poses a challenge in terms of the method's reproducibility and surface deposition behavior. These aspects are particularly important in nanoscience, where sub-nanometer to nanometer variations often impact experimental outcomes. Ideally, a self-assembled monolayer of organosilanes should assemble into a uniform monolayer, horizontally polymerized, as shown in figure 1.5B. Unfortunately, this is rarely the case when working with silanes, especially for di- and tri-functional silanes, where non-optimal experimental conditions lead to cross-linking and uncontrolled vertical polymerization. While this may be irrelevant for industrial applications, the nanometer control of the surface properties becomes problematic. Obtaining uniform monolayers is always a challenge with silanes, and requires a careful adjustment of experimental conditions to limit excessive vertical polymerization and surface aggregation, especially for di- and tri-reactive silanes (figure

1.5C). Using a mono-reactive silane can reduce the formation of overlayers, but comes at the cost of lower surface coverages. Such SAMs are not densely packed and for this reason more reactive di- and tri-functional organosilanes are typically used to achieve higher surface densities of organofunctional groups, similar as those obtained for SAMs on Au.

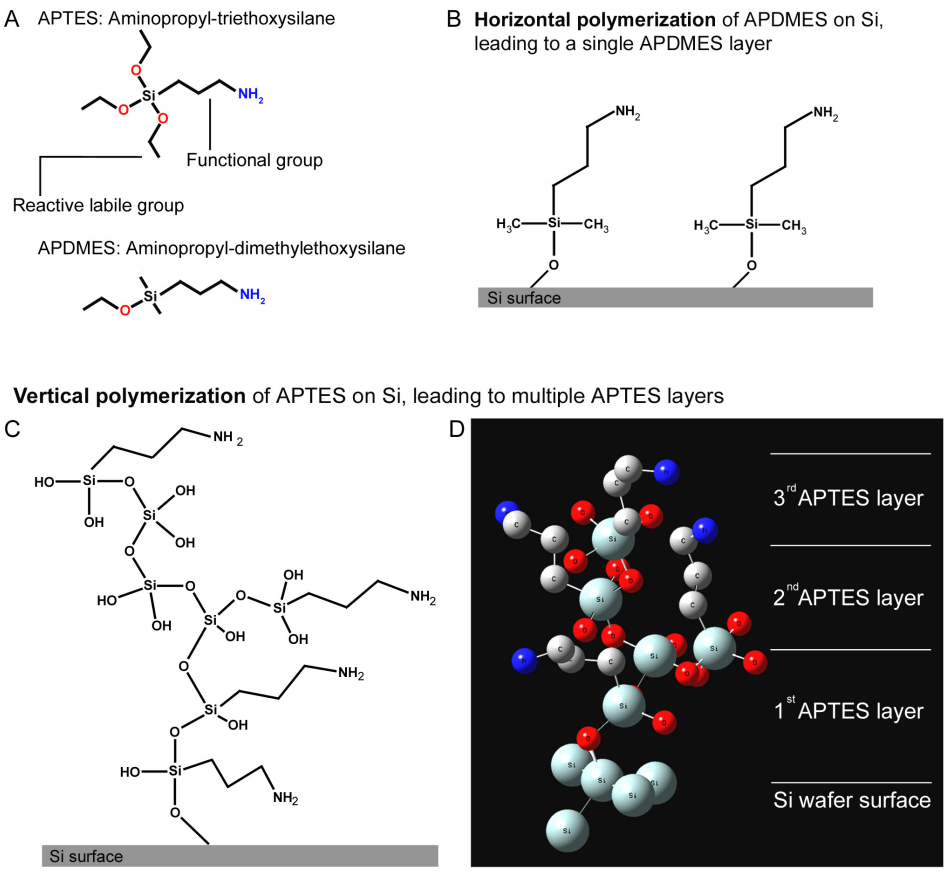

Figure 1.5. (**A**) Structure of tri-functional and mono-functional silanes: aminopropyl-triethoxysilane (APTES) and aminopropyl-dimethylethoxysilane (APDMES). (**B**) Horizontal polymerization leads to uniform and homogeneous monolayers. (**C**) More reactive di- and tri-functional silanes often lead to vertical polymerized film, a few to many molecular layers thick. (**D**) Molecular 3D model[84] of a vertical polymerized APTES illustrating the disordered arrangement of the desired amine groups (Hydrogens omitted for clarity).

Although silane chemistry is not as straightforward as using thiols on Au, the ease of industrial production, combined with its versatile reactivity towards a range of different pre-treated surfaces has kept silanes as an important surface functionalization tool. Often, this type of chemistry is the only viable option to functionalize materials, hence precise control of reaction conditions is a painstaking operation, but nevertheless essential for establishing functionalization procedures that are reproducible. Parameters to adjust involve: silane reactivity, silane degree of functionalization (mono-, di- or tri-functional), reaction temperature, water content, relative humidity, silane concentration, pH adjustment and also

pressure for gas-phase procedures. An in-depth study has been performed by Howarter *et al.*, who have measured the surface properties by AFM and ellipsometry of APTES (the most widely used organofunctional triethoxysilane).[98]

1.2.3. Plasma Surface Modification

Plasmas are partially ionized gases that consist of electrons, ions, neutral atoms and neutral molecules. For low pressure and low temperature plasmas, the gases are at near-ambient temperature, while the electrons are around 10^4 K. Low temperature plasmas are formed by generating a Radio-Frequency (RF) oscillating electric field in the gas region using either capacitor plates or a magnetic induction coil. When the pressure is sufficiently low, the combined effect of the electric field acceleration of the electrons provides them with high kinetic energies. Plasma energies are sufficient to ionize neutral atoms and break molecules apart for reactive radical species formation. Surface interactions with reactive plasma species depends on 3 important parameters: pressure, applied voltage and the nature of the gas. Detailed studies have shown that controlling these 3 parameters can lead to controlled surface modifications.[99] More elaborate operating systems can control gas pressure over 10^{-7}–10^{-3} bar range and have powerful capacitors to ignite the plasma: these systems are typically referred to as plasma etchers. Systems that only offer a looser control of the plasma parameters are typically referred as plasma cleaners and operate under pressures of ~10^{-3} bar and offer only moderate control over the generated RF-field. Depending on the process gases and parameters, plasmas can perform both mechanical work and chemical work, through either the ablative effect of kinetic transfer of electrons and ions with the surface or through the interaction of reactive radical species with the surface. Plasmas can interact with a surface and modify it through several mechanisms: ablation, activation, cross-linking and deposition. Loose control over reaction parameters typically leads to varying degrees of modification efficiencies, as well as different mechanism occurring simultaneously within the reaction chamber due to gas mixtures.

Plasma ablation mechanically removes surface material by energetic electron and ion bombardment. Ablation easily breaks weak covalent bonds in polymers, which undergo repetitive chain scission until their M_w is sufficiently low that they transfer into the vacuum phase. Argon is inert towards surfaces and therefore the surface chemistry is only affected at the outermost molecular layers. Plasma surface activation creates surface chemical functional groups through the use of plasma gases such as O_2 , H_2, N_2 or NH_3 that dissociate and react with the surface forming new functional groups and thus strongly modifying the

surface chemistry. The plasma environment breaks down weak surface bonds, such as C-C and C-H. Using O_2 can create reactive carbonyl, carboxyl and hydroxyl groups. This activation alters the chemical functionality of the surface, which changes wetting and adhesion properties. For example, polydimethylsiloxane (PDMS) is hydrophobic when prepared, but after O_2 plasma cleaning, becomes hydrophilic. Cross-linking reactions, with inert Ar, typically establish new chemical links between polymer chains. Plasma deposition is the process through which a thin polymer coating is applied to a substrate through the introduction of monomer species within the reaction chamber. These coatings are usually highly cross-linked and much denser than those obtained from solution polymerization. Some surface modifications are summarized in table 1.1 for different processing plasma gases.[100]

Table 1.1. Gases used in plasma cleaner and surface modification.

Type of gas	Surface modification
Air	Surface cleaning (general) Oxidation Contamination removal
Ar	Physical ablation of contaminants Surface monolayer etching
O_2	Surface cleaning (general) Surface hydroxylation Surface etching (polymers) Oxidation
N_2	N-groups incorporation in polymers Surface cleaning (general)
H_2O vapor	Surface hydroxylation
H_2	Surface cleaning (general) Surface hydrogenation
NH_3	Amine formation (NH_2)

1.3. Artificial Lipid Membranes to Study Biological Systems

The cellular plasma membrane envelops the entirety of cells and different cellular components such as the mitochondria, the Golgi apparatus and the nucleus. The purpose of the membrane is primarily to compartmentalize different chemical environments, but has an additional crucial function of controlling the transport of chemical species in and out of cells: nutrients, proteins, ions, and water. Transport functions are primarily carried out by proteins, which are functional macromolecular polymers with specific amino acid sequences. Protein functionality and their membrane insertion are attributed to higher order secondary and tertiary structures, which determine their 3-dimensional shape and the localization of selective functional domains that carry hydrophobic, charged, or bio-

recognition moieties. Proteins are involved in a variety of cellular processes such as cell adhesion, ion channel conductance and cell signaling. The plasma membrane also serves as attachment point for the intracellular cytoskeleton.

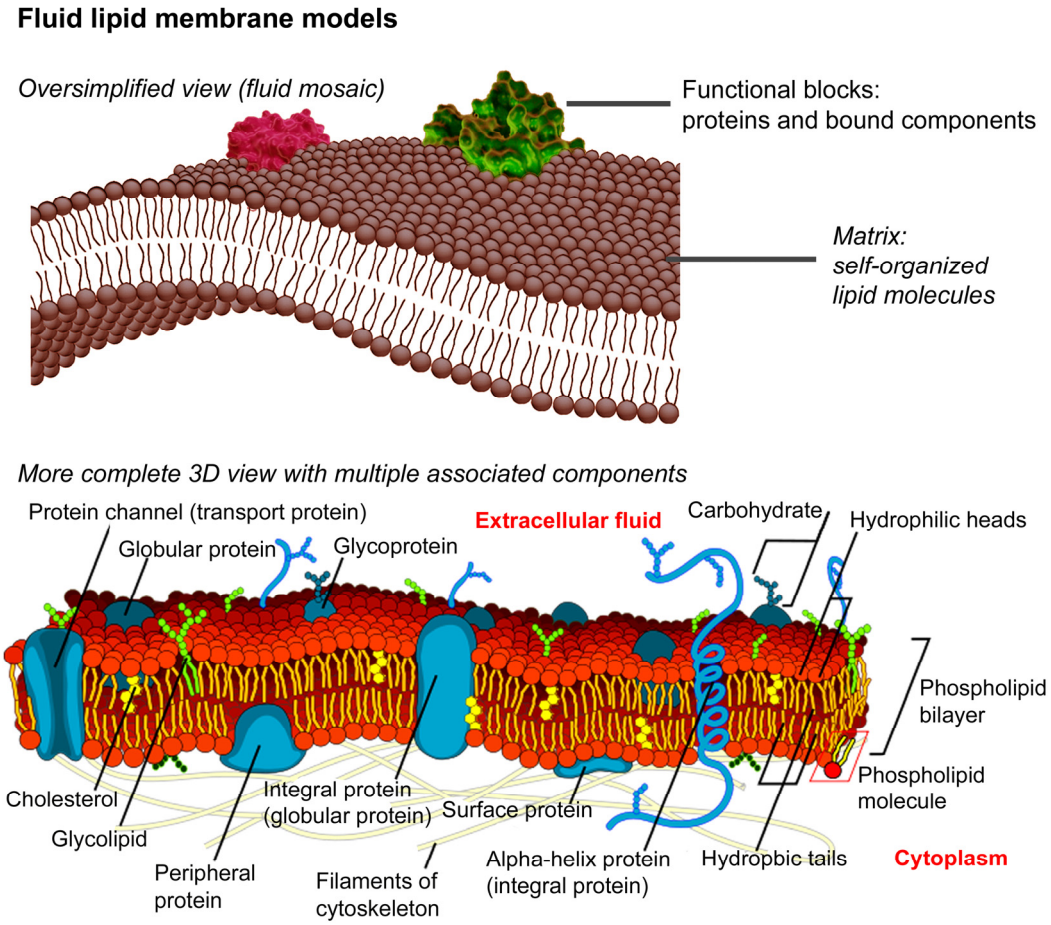

Figure 1.6. (**A**) Schematic of the simplified fluid mosaic model put forward by Singer et al. in 1972: Proteins in a self-organized phopholipid matrix. (**B**) More complete and complex 3-dimensional schematic of a biological lipid membrane with embedded proteins, cytoskeleton, glycolipids, to name a few that are identified.[101]

The fluid mosaic model[102-103] brought forward by S. J. Singer and G. Nicolson in 1972, describes the biological membrane as a two-dimensional liquid composed of a matrix of phospholipid molecules where protein molecules are embedded, as shown in figure 1.6A. Although these components are of different sizes, they can move with similar diffusion coefficients,[104] which is a consequence of the 2-dimensional fluid nature of lipid membranes. However, in reality this picture may only be valid for a spatial length scale of about 10 nm and for proteins that are not coupled to any other membrane component. The plasma membrane contains more complex hierarchical structures that cannot be described by the oversimplified fluid mosaic model (figure 1.6B), such as protein-protein complexes, and possible lipid rafts,[105-107] pickets and fences[108-112] from the actin-based cytoskeleton.

Nevertheless, the fluid mosaic model remains useful in many circumstances where the behavior of studied protein can be simplified to this 2D conceptualization. This is often the case when considering the artificial lipid membrane systems commonly investigated in biophysical studies which often incorporate different membrane components in a matrix of lipids in a step-wise fashion.

1.3.1. Phospholipid Liposome Self-Assembly

Studying the physics and chemistry of the plasma membrane and its components by directly investigating the cellular membrane is quite unproductive, mostly because one cannot easily decouple the behavior of particular membrane components from the others. This impossibility is mainly due to the small size of most membrane components, no larger than 5 nm at most, which approaches the resolution limit of typical electron microscopy techniques and is well below the resolution of optical microscopy. Secondly, the inherent structural complexity of lipid membranes, both from the complex lipid matrix composition and from the thousands of membrane components that are either attached or embedded within the matrix, does not permit an adequate control over the number of variables. For most investigations, studying the behavior of isolated membrane components is therefore almost impossible. To tackle this complexity problem, the development of artificial membrane systems has been ongoing since the early 1970's. The production of synthetic phospholipids, the development of adequate characterization techniques, lipid membrane preparation protocols and membrane component incorporation methodologies are aimed at simplifying the biological membrane to a tangible, experimentally reproducible, system.

Before the 1960's, lipid extraction methods were the only source of phospholipids. Synthetic pathways were reliably established to allow the large scale production of different phospholipids with control over the structure and purity.[113-114] Phospholipids are amphilic molecules with a hydrophilic phosphate head group and a hydrophobic tail, consisting of a glycerol and 2 fatty acids, see figure 1.7. The fatty acid chains typically have an even number of carbon atoms varying between 14-24; with 16-18 being most prevalent. Typically, they are unbranched and either are saturated or contain a non-conjugated double bond in the cis-configuration. The head group always carries charged groups, which one is a negatively charged phosphate while remaining terminus is either an amine, a quaternary amine, an hydroxy group or a sugar, to name a few. Typical native head-groups are serine (negative charge), glycerol (negative charge), choline (neutral), or ethanolamine (neutral,

pH < 8). The chemical structure of a commonly used phospholipid, POPC, and its 3-D space-filling structure, are shown in figure 1.7.

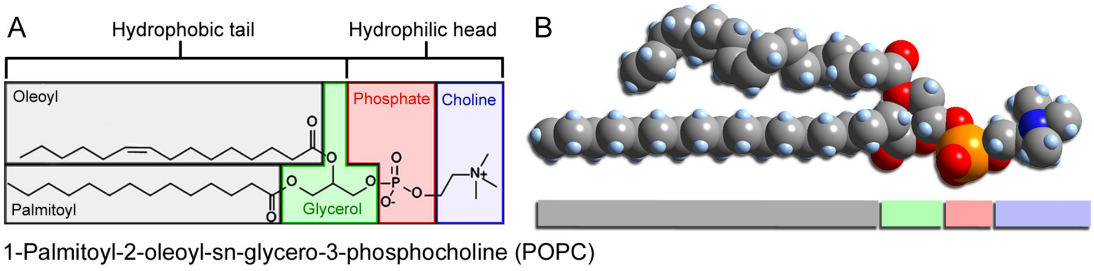

Figure 1.7. (**A**) Chemical structure of a commonly used lipid: 1-palmitoyl-2-oleoyl-*sn*-glycero-3-phosphocholine (POPC). (**B**) A 3D space-filling structure of POPC.[84]

The lipid bilayer membrane structure is composed of two leaflets of phospholipid molecules self-assembled parallel to each other into 2D sheets, with headgroups oriented towards the aqueous solution and the hydrophobic tails that interact with each other in the hydrocarbon-center (HC) of the bilayer,[115-116] which is 3-5 nm in thickness. The density probability of functional phospholipid chemical groups and charge density distribution in an artificial lipid membrane of DOPC, as a function of the distance from the HC center, was calculated by Wiener et al. in the early 1990's from x-ray and neutron diffraction experiment; their results are reproduced in figure 1.8. The vesicle self-assembly mechanism relies on an intricate balance between hydrophobic and hydrophilic hydration interactions in an aqueous medium, commonly summarized as the hydrophobic effect.[117-118] Similarly to living cells, a giant liposome can be composed of millions of lipids, which form a stable, impermeable, high aspect-ratio membrane. The self-assembly relies both on van der Waals forces between phospholipid tails and on the hydrophilic aqueous environment that promotes hydrophobic phase segregation of the HC.[118] The hydrophilic head-groups facilitate this process by interacting with water through hydration forces and hydrogen bonding, which further stabilizes the bilayer architecture. As long as the overall phospholipid structure (figure 1.7A) is preserved, with a hydrophobic-tail and a charged hydrophilic-head, different chemical variations in the tail and head groups can be introduced without perturbing the vesicle structure. In biological systems, hundreds of lipid variations are present with different associated functions. In artificial systems, the controlled incorporation of different lipids is commonly used to elucidate the role of lipid composition in biological processes. From a material's chemistry perspective, this platform is viewed as a versatile tool for surface modifications, since the vesicle surface composition can be finely controlled with multiple functionalities and then reliably reproduced onto

surfaces. At the head-group location, covalent modification is usually achieved by coupling of heterobifunctional cross-linkers to reactive lipids (phosphoethanolamines). These phospholipids can be used to insert a variety of functional groups (biotin, maleimide, etc) into liposomes and provide added functionality on the surface of lipid bilayers, for coupling reactions.

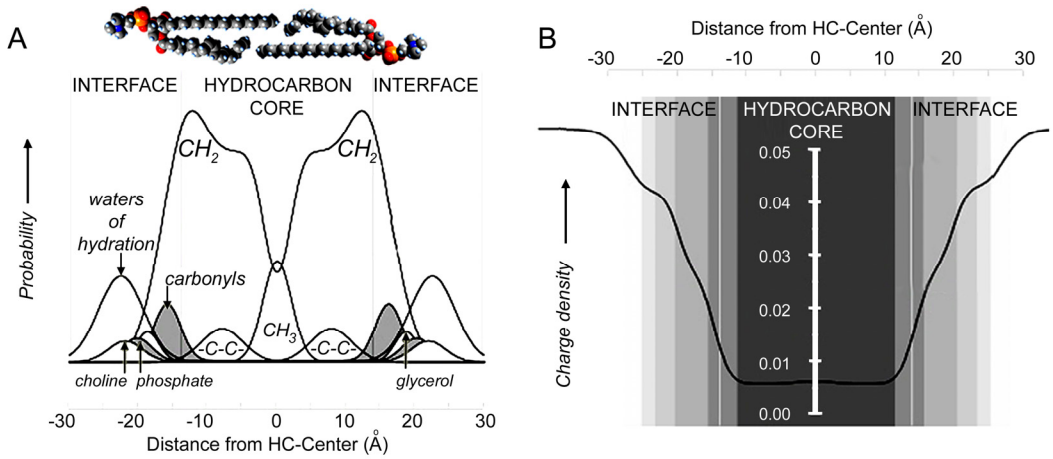

Figure 1.8. (**A**) Probability density curves illustrating the average positions of the different functional groups with respect to the center of a DOPC phospholipid bilayer (hydrocarbon center: HC), obtained from a combination of x-ray and neutron diffraction studies, data reproduced from Wiener *et al.*[119-120] (**B**) Charge density as a function of distance from the HC center; increases approaching head-groups.

In solution, phospholipids form spherical vesicle structures, as shown in figure 1.9. A polydisperse mixture of multilamellar and unilamellar lipid vesicles, ranging in diameter from 20 nm to over 25 μm, is easily formed through rehydration of a dried lipid film by immersion into a near zero ionic strength; referred to as gentle hydration.[121] However, generating monodisperse unilamellar vesicles in an electrolytic solution is an important pre-requisite for various studies. Therefore, different techniques are employed to control a unilammelar vesicle size distribution. To obtain small unilamellar vesicles (SUVs) in saline aqueous solution, with diameters between 20-50 nm, the hydrated lipid films are ultra-sonicated using a metal tip-sonicator for several minutes.[122-123] These are typically unstable over time and grow into large unilamellar vesicles (LUVs), > 50 nm diameter. LUVs, with diameters ranging from 50-5000 nm, can be prepared by extrusion of a hydrated lipid film solution through a polycarbonate membrane having an average pore diameter distribution;[124-127] 50-5000 nm are available. This method typically yields a skewed vesicle population with vesicle diameters typically well below the average pore size of the polycarbonate membrane, particularly for larger diameters than 100-200 nm; *e.g.* for 1000 nm pores, the average diameter is about 400 nm. Finally, to obtain a large amount of giant vesicles, with diameters > 5 μm and up to 100 μm, electroformation[128-130] is required.

Electroformed giant unilamellar vesicles (GUVs) are prepared using conductive Indium Tin Oxide (ITO) slides, onto which lipid films are dried and then mounted in a liquid cell configuration such that a specific alternating voltage program is applied. Figure 1.9 shows the range of different vesicle sizes, drawn to scale, that can be prepared.

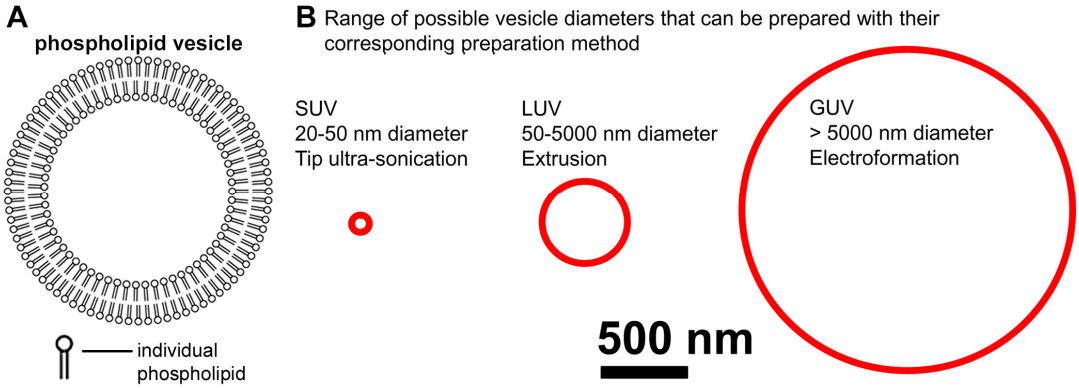

Figure 1.9. (**A**) Schematic of the structure of a phospholipid vesicle, *i.e.* liposomes. (**B**) Different preparation methods are used to control the size of the phospholipid vesicles that are formed, which is crucial in many studies that require a relatively monodisperse size distribution. The vesicles are drawn to scale.

Phospholipid bilayers have distinctive polymorphic phases that occur at different pressures and temperatures; determined by the chemical structure of the hydrophobic-tail, *i.e.*, by the degree of chain saturation, chain-length and acyl chain symmetry.[131] The main phases are L_d = liquid disordered (*fluid*-phase) and S_o = solid ordered (*gel*-phase).[132] For the acyl chains having all *trans* conformations in the gel phase, strong van der Waals interaction between the chains results in a reduction of rotational motion and lateral diffusion of the lipid molecules. At the main phase transition temperature (T_m), transition from *gel*- into *fluid*-phase occurs,[133] as shown in figure 1.10. The name of commonly used lipids, their chemical structure and main transition temperature are shown in table 1.2.

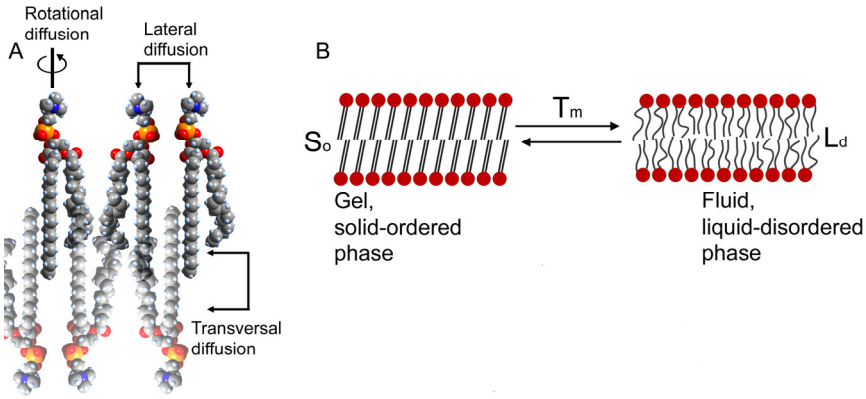

Figure 1.10. (**A**) In the lipid bilayer, rotational and lateral diffusion of lipid occurs at $T > T_m$, while transversal

diffusion rarely ever occurs. (**B**) Above the main phase transition temperature, $S_o \rightarrow L_d$.

Table 1.2. Chemical structure of some phospholipids, names, abbreviations, M_w and T_m.

Lipid structure	Lipid name	Transition temperature / °C
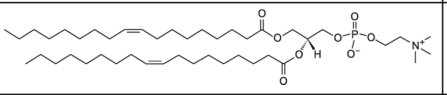	1,2-dioleoyl-*sn*-glycero-3-phosphocholine (DOPC) 785.6 g/mol	- 20
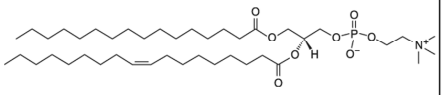	1-palmitoyl-2-oleoyl-*sn*-glycero-3-phosphocholine (POPC) 759.6 g/mol	- 2
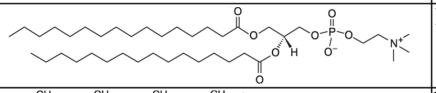	1,2-dipalmitoyl-*sn*-glycero-3-phosphocholine (DPPC) 733.6 g/mol	+ 41
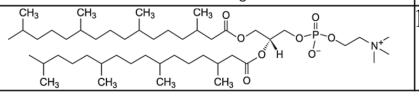	1,2-diphytanoyl-*sn*-glycero-3-phosphocholine (DPhPC) 845.7 g/mol	–

1.3.2. Investigation of Artificial Membrane Systems

Black lipids membranes (BLM) were the first form of an artificial phospholipid membrane. BLMs derived their name from the disappearance of colorful interference bands after single bilayer membrane formation, when observed by optical microscopy. These were first obtained by Müller from extracted brain lipids.[134-135] The method consists in dissolving the phospholipids (1-2 %) in an organic solvent such as *n*-decane or squalene, and painting this solution across a circular aperture that typically varies from 0.5-1000 μm in diameter. The hole is formed through a hydrophobic material used to separate two aqueous compartments (teflon or polyethylene). The solvent thins-out across the periphery of the hole and the lipids slowly organize into a single lipid bilayer that spans the opening. This method has been used to reliably produce phospholipid membranes, into which functional components can be inserted and studied by electrochemistry, such as peptides,[136-137] proteins[138-140] and antibiotics.[141] Typical detection of the channel activity is carried by electrical conduction experiments to reveal the membrane-component conductance properties such as gate potential and number of conductance states for proteins. Unfortunately, membranes formed with this method have low mechanical stability, due to the large aspect-ratio of the lipid membrane with respect to the aperture size. Furthermore, organic solvent is permanently present, and can potentially interfere with the biological functions of certain proteins.

A more robust method of studying artificial lipid membranes involves the formation of a lipid membrane onto a planar support, figure 1.11. Such membranes are generally referred to as solid-supported membranes (SSM).[104] They are significantly more stable than BLMs

and do not rupture since the motion of the lipid membrane is restricted to a 2-dimensional plane. Solid supported lipid membranes are typically obtained by vesicle spreading, seldom from solvent thinning. Depending on the hydrophobicity of the surface, as well as the functional groups present at the surface, different types of SSMs are possible. In the simplest case, a lipid membrane is formed on a planar hydrophilic surface, consisting of two fluid leaflets forming a fluid bilayer, as illustrated in figure 1.11. Typical phospholipid diffusion coefficients in these SSMs range from 1-4 $\mu m^2/s$.[142] The hydrophilicity plays a crucial role in determining if and how the vesicles will rupture to form this fluid bilayer. One of the most common surfaces used is SiO_2, onto which vesicles first adsorb, then undergo a flattening deformation, until too large of a stress creates a rupture point and the vesicle's membrane unrolls and covers the planar surface.[143] Clean and smooth surfaces are additional pre-requisites for SSM formation. Freshly cleaned glass slides, borosilicate glass,[144] mica,[145] freshly oxidized Si wafers,[146] O_2-plasma cleaned Si and SiO_2 substrates,[146-147] or some alcohol terminated self-assembled monolayers will induce vesicle spreading. The membrane fluidity is maintained by a 10-20 Å layer of water trapped between the substrate and the membrane, referred to as a water-cushion.[146-147] Peripheral membrane proteins, can be studied, but integral membrane proteins cannot due their protrusion from the bottom lipid leaflet.

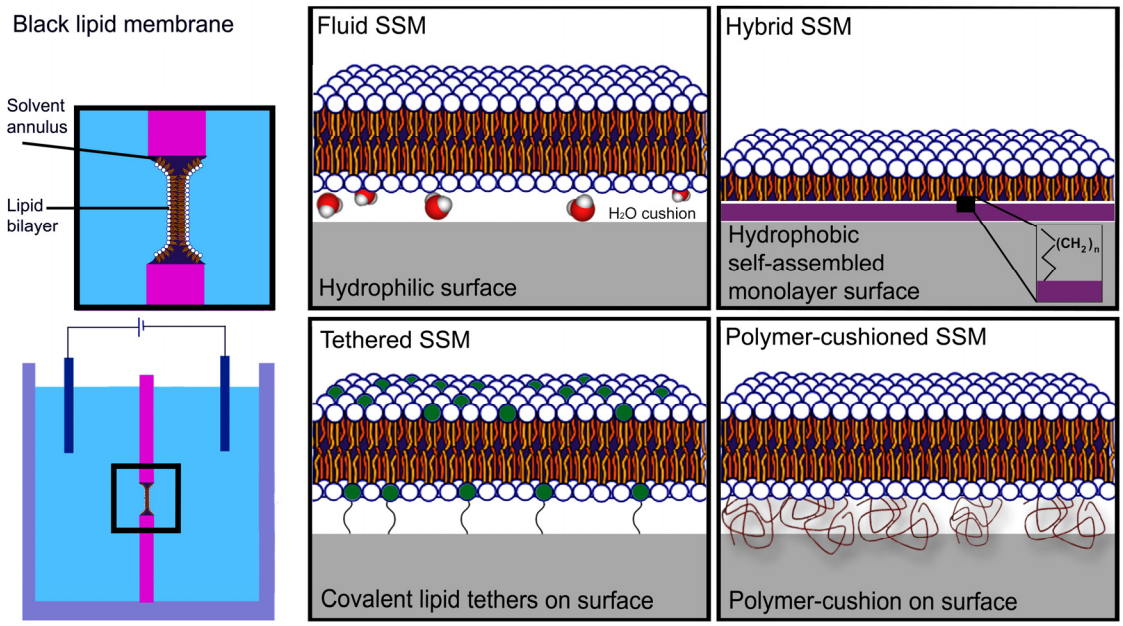

Figure 1.11. Schematics of different model membranes: black lipid membrane (left) and 4 types of solid supported lipid membranes.

Hybrid SSMs are obtained by covalently modifying a planar substrate with a hydrophobic self-assembled monolayer. Au surfaces can be modified by alkylthiols and glass surfaces

with alkylchlorosilanes. When vesicles interact with these surfaces, the hydrophobic lipid tails align towards the hydrophobic SAM and form a single lipid leaflet monolayer.[78, 148] The bilayer formed is hybrid, in the sense that the top leaflet consists of mobile phospholipids, while the bottom leaflet is the immobile SAM. Two routes are typically used: 1) Langmuir-Blodgett transfer from an air-water interface[149] and 2) vesicle fusion.[79, 150] Hybrid SSMs have proven useful for sensor applications since the exact lipid composition of vesicles can be efficiently transferred onto the hydrophobic surface. Also, because they allow to couple lipids directly to metal surfaces, surface interactions with the SSMs can be investigated with direct electrical measurements,[151] surface plasmon resonance spectroscopy[152] and quartz crystal microbalance detection.[153] Hybrid SSMs are typically more robust than fluid SSMs because of the strong interactions of the lipids with the underlying SAM. Lipid composition of ghost cells can been transferred to a planar surface and used as a sensor platform.[154-155]

As an alternative to hybrid SSMs, tethered-SSMs can be used, where the planar surface is modified by reactive groups that can covalently bind to modified head-group lipids, *a priori* incorporated in the lipid vesicles.[156-158] For example, a 5 mol % thiol-terminated surface interacting with vesicles having 5 mol % maleimide head-groups. Covalent interactions are sufficient to induce vesicle rupture and form tethered bilayers on the surface where the top leaflet remains fluid, but the bottom leaflet looses mobility due to multiple pinning-points. A similar strategy involves the modification of planar surfaces with a low surface coverage self-assembled monolayer of molecules that reproduces the hydrophobic-tail structure of phospholipids; this induces vesicle rupture by insertion of the artificial moieties in between the vesicle's lipids.

The most difficult component to study in SSMs are trans-membrane proteins because they tend to protrude from the distal side and need to be accommodated between the surface and the membrane. These proteins often interact strongly with the underlying surface, which may immobilize them or even denature them, especially for hybrid SSMs.[159] For this purpose, more elaborate surface modifications have been developed involving polymer-modified surfaces that effectively decouple the membrane from the surface, while leaving sufficient available volume beneath the bilayer to accommodate proteins.[159-160] The SSMs formed are referred to as polymer-cushioned SSMs. Surface analysis techniques can still be used on these SSMs. In the first instance, the planar surface is modified with a soft polymer brush, such as polyethyleneoxide[161], dextran,[162] cellulose,[163] chitosan[164], maleic acid[165] or polyelectrolytes.[164] These polymers must have the proper hydrophilicity, polarity and

structure to induce vesicle spreading. Reactive groups can be inserted into the polymer for covalent lipid coupling: tethered polymer-cushioned SSMs. Another alternative involves lipopolymers: polymers with lipid-like groups emulating the phospholipid structure. These groups insert into liposomes and induce vesicle spreading resulting in a more mobile tethered polymer-cushioned SSM.[166-167]

1.3.3. Pore-Spanning Lipid Membranes

Micro- and nano- black lipid membranes have been developed as a hybrid system between BLMs and SSMs, combining the pore-spanning advantages of the former, together with longer-term stability of the latter SSMs.[31, 168-172] These micro- and nano-BLMs are obtained on porous support, with pore diameters ranging from 60-2000 nm, by first modifying the porous surface with Au and then forming a hydrophobic SAM with either an alkanethiol,[169] or a less hydrophobic cholesterol tether.[31] Alternatively, a hydrophobic fluorinated silane[168] can be use to modify a porous oxide surface. A pore-spanning membrane is then formed by painting the lipids across the pores and waiting for the solvent to thin-out until a lipid bilayer is obtained. Pore-spanning lipid membranes from GUVs are significantly more challenging to obtain[173-174] because the porous surface chemistry must be controlled such that vesicles can: 1) deform on the surface and rupture without loss of membrane integrity, 2) remain preferentially pore-spanning rather than line the interior of the pores and 3) this pore-spanning lipid bilayer must remain stable on the substrate over sufficiently long periods to allow handling, imaging and time-dependent experiments. Fluid pore-spanning lipid membranes have not been frequently reported in literature mainly due to the difficulty in finding a functionalization strategy that offers a proper balance between the aforementioned points. Different silicon dioxide porous surfaces[175-178] have however recently been shown to be capable of acting as fluid lipid bilayer supports.

1.4. Scope of Thesis

Each chapter should be read as individual manuscript. Each chapter has a dedicated introduction that reviews relevant concept ideas and challenges related to the field. Results, discussion and conclusions are presented for each chapter. The format of each chapter slightly differs given that the figures and style were produced for a specific journal. An in-depth discussion can be found within each chapter. An general discussion is provided in Chapter 10.

The goal of this PhD project was to demonstrate that anodic aluminum oxide (AAO) can be used as a versatile platform whose surface chemistry can be conveniently tailored to carry-out high sensitivity assays using the method of optical waveguide spectroscopy (OWS). During the course of these studies, we developed tools to direct the assembly of functional components exclusively at the pore-rim surface or homogeneously on the AAO surface. These methodologies open new possibilities to differentiate the pore-interior medium of the cylindrical attoliter compartments of AAO in order to study molecular transport phenomena.

The first challenge in this research was obtaining a reliable source of AAO substrates to carry out OWS studies. Previous methods of producing AAO by anodization of micrometer thick sputtered Al films could not provide an adequate number of substrates to carry out in depth studies, which required multiple measurements, for two main reasons. Firstly, these vacuum deposited samples were expensive to produce. Secondly, the anodization of vacuum deposited Al films was itself very time consuming, but also could only produce at most 1–1.5 μm thick AAO and yielded AAO with larger pore-size distributions and lower order than were desired. A technique was developed to produce high quality AAO slab waveguides from the direct anodization of bulk Al metal. By carefully controlling the Al metal removal procedure, free-standing highly ordered AAO films, with controllable thicknesses and lattice spacing, were achieved and could then be mounted as a thin film slab waveguides. The details of this procedure are described in **Chapter 3**.

In **chapters 4** and **5**, the factors that influence the growth of Layer-by-Layer (LbL) multilayers within the cylindrical nanopores of AAO were studied using polyelectrolyte dendrimers, proteins, linear polyelectrolytes, all of approximately the same size in solution. The results of all three multilayer systems were compared. Pore-filling limitations are directly related to the shape of the macromolecule (globular rigid or flexible random coil)

and its interaction type (electrostatic or by molecular recognition). The limitations to pore-filing are discussed in terms of electrostatic and steric hindrance.

In **chapter 6**, the potential use of AAO as a biosensor for protein detection was investigated experimentally using avidin adsorption and varying different experimental parameters. The experimental data showed that mass transport within the AAO is the limiting step to sensor performance. Finite element simulations corroborated the conclusion.

In **Chapter 7**, the first steps towards the orthogonal functionalization of AAO are presented in details. Orthogonal functionalization is a pre-requisite for the formation of pore-spanning membranes. The resulting AAO substrates have a different pore-rim *vs* pore-interior surface chemistry that allows the directed self-assembly of different functional macromolecular building blocks.

In **Chapter 8**, the concept of homogeneous surface functionalization using vesicle spreading on hydrophobically modified AAO, presented in **Chapter 6**, was extended as a method to create functional surfaces for biosensors and protein capture applications. Specifically, we show that the amount of streptavidin deposited within AAO nanopores is directly proportional to the amount of biotinylated lipids in the lipid monolayer. Furthermore, we show that the method can be used in practical settings to extract a protein directly from a cell lysate.

Finally in **Chapter 9**, the orthogonal silane-based functionalization scheme presented in chapter 7 was used to form fluid pore-spanning membranes from GUV rupture on hydrophilic AAO substrates. These pore-spanning membranes act as real physical barriers that either prevent the entry of material into the nanopores or prevent the escape of entrapped molecules within the nanopores. Hence, this system effectively isolates the pore-interior chemical environment from the bulk solution. Finally these membranes are overall a better mimic for biological systems since they are solvent-free and are not pre-tensed by pore-rim tethering.

1.5. Contributions of Co-Authors

Enumerated by chapter

1. **Thomas D. Lazzara, K.H. Aaron Lau, Wolfgang Knoll, (2010) *J. Nanosci. nanotechnol.* 10, 4293-4299.**

   Experiment designed, conceived and performed by T. D. Lazzara. Data analyzed by T. D. Lazzara and K.H.A. Lau. Manuscript written by T. D. Lazzara. Manuscript edited by T.D.L., K.H.A. Lau and W. Knoll. Scientific Material provided by W. Knoll.

2. **Thomas D. Lazzara, K.H. Aaron Lau, Ahmed I Abou-Kandil, Jean-Pierre Majoral, Wolfgang Knoll (2010) *ACS nano* 4, 3909–3920.**

   Experiment designed and conceived by T. D. Lazzara and K.H.A. Lau. Experiments performed by T. D. Lazzara. Data analyzed by T. D. Lazzara and K.H.A. Lau. Manuscript written by T. D. Lazzara. Manuscript edited by T. D. Lazzara, K.H.A. Lau and W. Knoll. Dendrimers provided by A. M. Caminade and J. P. Majoral. Scientific Material provided by W. Knoll.

3. **Lazzara, T. D.; Lau, K. H. A.;Wolfgang Knoll; Andreas Janshoff, Claudia Steinem, *Manuscript prepared for publication 2011*.**

   Experiments designed and conceived by T. D. Lazzara. Experiments performed by T. D. Lazzara. Data analyzed by T. D. Lazzara and K.H.A. Lau. Manuscript written by T. D. Lazzara. Manuscript edited by T.D.L., K.H.A. Lau and C. Steinem. Scientific Material provided by C. Steinem and A. Janshoff.

4. **Thomas D. Lazzara, Ingo Mey, Andreas Janshoff, Claudia Steinem (2011) *Manuscript submitted to Analytical Chemistry, 2011.***

   Experiments designed and conceived by T. D. Lazzara, C. Steinem and A. Janshoff. Experiments performed by T. D. Lazzara. Simulations performed by I. Mey. Data analyzed by T. D. Lazzara and I. Mey. Manuscript written by T. D. Lazzara and A. Janshoff. Manuscript edited by T. D. Lazzara, I. Mey, A. Janshoff and C. Steinem. Scientific Material provided by C. Steinem and A. Janshoff.

5. **Thomas D. Lazzara, Torben-Tobias Kliesch, Andreas Janshoff, Claudia Steinem (2011) *ACS appl. mater. interfaces*, in press**

   Experiments designed and conceived by T. D. Lazzara, C. Steinem. Experiments performed by T. D. Lazzara and T. Tobias-Kliesch. Data analyzed by T. D. Lazzara. Manuscript written by T. D. Lazzara and C. Steinem. Manuscript edited by T.D.Lazzara, A. Janshoff and C. Steinem. Scientific Material provided by C. Steinem and A. Janshoff.

6. **Thomas D. Lazzara, Daniela Behn, Torben-Tobias Kliesch, Andreas Janshoff, Claudia Steinem, *Manuscript prepared for publication 2011.***

   Experiments designed and conceived by T. D. Lazzara, C. Steinem. Experiments performed by T. D. Lazzara Daniela Behn and T. Tobias-Kliesch. Protein expression and purification performed by Daniela Behn. Data analyzed by T. D. Lazzara. Manuscript written by T. D. Lazzara and C. Steinem. Manuscript edited by T.D.Lazzara, A. Janshoff and C. Steinem. Scientific Material provided by C. Steinem and A. Janshoff.

7. **Thomas D. Lazzara, Christian Carnarius, Marta Kocun, Andreas Janshoff, Claudia Steinem (2011) *Manuscript submitted to ACS nano, 2011.***

   Experiments designed and conceived by T. D. Lazzara, C. Carnarius and C. Steinem. Experiments performed by T. D. Lazzara, C. Carnarius and M. Kocun. Data analyzed by T. D. Lazzara. Manuscript written by T. D. Lazzara and C. Steinem. Manuscript edited by T.D. Lazzara and C. Steinem. Scientific Material provided by C. Steinem and A. Janshoff.

1.6. References

1. Ozin, G. A.; Nanochemistry - Synthesis in Diminishing Dimensions. *Adv. Mater.* **1992,** *4*, 612-649.

2. Pitcher, M. W.; Nanochemistry - a Chemical Approach to Nanomaterials. *Science* **2006,** *313*, 300-300.

3. Brust, M.; Walker, M.; Bethell, D.; Schiffrin, D. J.; Whyman, R.; Synthesis of Thiol-Derivatized Gold Nanoparticles in a 2-Phase Liquid-Liquid System. *J. Am. Chem. Soc.* **1994**, 801-802.

4. Daniel, M. C.; Astruc, D.; Gold Nanoparticles: Assembly, Supramolecular Chemistry, Quantum-Size-Related Properties, and Applications toward Biology, Catalysis, and Nanotechnology. *Chem. Rev.* **2004,** *104*, 293-346.

5. Sun, Y. G.; Xia, Y. N.; Shape-Controlled Synthesis of Gold and Silver Nanoparticles. *Science* **2002,** *298*, 2176-2179.

6. Alivisatos, A. P.; Semiconductor Clusters, Nanocrystals, and Quantum Dots. *Science* **1996,** *271*, 933-937.

7. Dabbousi, B. O.; RodriguezViejo, J.; Mikulec, F. V.; Heine, J. R.; Mattoussi, H.; Ober, R.; Jensen, K. F.; Bawendi, M. G.; (Cdse)Zns Core-Shell Quantum Dots: Synthesis and Characterization of a Size Series of Highly Luminescent Nanocrystallites. *j. PHys. Chem. B* **1997,** *101*, 9463-9475.

8. Klimov, V. I.; Mikhailovsky, A. A.; Xu, S.; Malko, A.; Hollingsworth, J. A.; Leatherdale, C. A.; Eisler, H. J.; Bawendi, M. G.; Optical Gain and Stimulated Emission in Nanocrystal Quantum Dots. *Science* **2000,** *290*, 314-317.

9. Xia, Y. N.; Whitesides, G. M.; Soft Lithography. *Ann. Rev. Mat. Sc.* **1998,** *28*, 153-184.

10. Gates, B. D.; Xu, Q. B.; Stewart, M.; Ryan, D.; Willson, C. G.; Whitesides, G. M.; New Approaches to Nanofabrication: Molding, Printing, and Other Techniques. *Chem. Rev.* **2005,** *105*, 1171-1196.

11. Zhang, S. G.; Fabrication of Novel Biomaterials through Molecular Self-Assembly. *Nat. Biotechnol.* **2003,** *21*, 1171-1178.

12. Whitesides, G. M.; Boncheva, M.; Beyond Molecules: Self-Sssembly of Mesoscopic and Macroscopic Components. *PNAS* **2002,** *99*, 4769-4774.

13. Lehn, J. M.; Toward Complex Matter: Supramolecular Chemistry and Self-Organization. *PNAS* **2002,** *99*, 4763-4768.

14. Park, M.; Harrison, C.; Chaikin, P. M.; Register, R. A.; Adamson, D. H.; Block Copolymer Lithography: Periodic Arrays of Similar to 10(11) Holes in 1 Square Centimeter. *Science* **1997,** *276*, 1401-1404.

15. Park, C.; Yoon, J.; Thomas, E. L.; Enabling Nanotechnology with Self Assembled Block Copolymer Patterns. *Polymer* **2003,** *44*, 6725-6760.

16. Balzani, V.; Venturi, M.; Credi, A., *Molecular Devices and Machines: A Journey into the Nano World*. Wiley-VCH: 2003.

17. Klabunde, K. J.; Richards, R., *Nanoscale Materials in Chemistry*. John Wiley and Sons: 2009.

18. Bates, F. S.; Fredrickson, G. H.; Block Copolymer Thermodynamics - Theory and Experiment. *Ann. Rev. Phys. Chem.* **1990,** *41*, 525-557.

19. Fredrickson, G. H.; Bates, F. S.; Dynamics of Block Copolymers: Theory and Experiment. *Ann. Rev. Mater. Sc.* **1996,** *26*, 501-550.

20. Green, P. F.; Limary, R.; Block Copolymer Thin Films: Pattern Formation and Phase Behavior. *Adv. Colloid Interface Sci.* **2001,** *94*, 53-81.

21. Guarini, K. W.; Black, C. T.; Yeuing, S. H. I.; Optimization of Diblock Copolymer Thin Film Self Assembly. *Adv. Mater.* **2002,** *14*, 1290.

22. Kim, D. H.; Lau, K. H. A.; Robertson, J. W. F.; Lee, O. J.; Jeong, U.; Lee, J. I.; Hawker, C. J.; Russell, T. P.; Kim, J. K.; Knoll, W.; Thin Films of Block Copolymers as Planar Optical Waveguides. *Adv. Mater.* **2005,** *17*, 2442.

23. Piner, R. D.; Zhu, J.; Xu, F.; Hong, S. H.; Mirkin, C. A.; "Dip-Pen" Nanolithography. *Science* **1999,** *283*, 661-663.

24. Smith, R. K.; Lewis, P. A.; Weiss, P. S.; Patterning Self-Assembled Monolayers. *Prog. Surf. Sc.* **2004,** *75*, 1-68.

25. Cheng, J. Y.; Ross, C. A.; Smith, H. I.; Thomas, E. L.; Templated Self-Assembly of Block Copolymers: Top-Down Helps Bottom-Up. *Adv. Mater.* **2006,** *18*, 2505-2521.

26. Hawker, C. J.; Russell, T. P.; Block Copolymer Lithography: Merging "Bottom-Up"

With "Top-Down" Processes. *Mrs Bulletin* **2005,** *30*, 952-966.

27. Shimomura, M.; Sawadaishi, T.; Bottom-up Strategy of Materials Fabrication: A New Trend in Nanotechnology of Soft Materials. *Curr. Opin. Colloid Interface Sci.* **2001,** *6*, 11-16.

28. Roy, P.; Dey, T.; Lee, K.; Kim, D.; Fabry, B.; Schmuki, P.; Size-Selective Separation of Macromolecules by Nanochannel Titania Membrane with Self-Cleaning (Declogging) Ability. *J. Am. Chem. Soc.* **2010,** *132*, 7893-5.

29. Kwon, C.-W.; Son, J.-W.; Lee, J.-H.; Kim, H.-M.; Lee, H.-W.; Kim, K.-B.; High-Performance Micro-Solid Oxide Fuel Cells Fabricated on Nanoporous Anodic Aluminum Oxide Templates. *Adv. Funct. Mater.* **2011,** *21*, 1154-1159.

30. Kresak, S.; Hianik, T.; Naumann, R. L. C.; Giga-Seal Solvent-Free Bilayer Lipid Membranes: From Single Nanopores to Nanopore Arrays. *Soft Matter* **2009,** *5*, 4021-4032.

31. Schmitt, E. K.; Weichbrodt, C.; Steinem, C.; Impedance Analysis of Gramicidin D in Pore-Suspending Membranes. *Soft Matter* **2009,** *5*, 3347-3353.

32. Vlassiouk, I.; Krasnoslobodtsev, A.; Smirnov, S.; Germann, M.; "Direct" Detection and Separation of DNA Using Nanoporous Alumina Filters. *Langmuir* **2004,** *20*, 9913-9915.

33. Hennesthal, C.; Drexler, J.; Steinem, C.; Membrane-Suspended Nanocompartments Based on Ordered Pores in Alumina. *Chemphyschem* **2002,** *3*, 885-889.

34. Alvarez, S. D.; Li, C. P.; Chiang, C. E.; Schuller, I. K.; Sailor, M. J.; A Label-Free Porous Alumina Interferometric Immunosensor. *Acs Nano* **2009,** *3*, 3301-3307.

35. Trivinho-Strixino, F.; Guerreiro, H. A.; Gomes, C. S.; Pereira, E. C.; Guimaraes, F. E. G.; Active Waveguide Effects from Porous Anodic Alumina: An Optical Sensor Proposition. *Appl. Phys. Lett.* **2010,** *97*.

36. Ting Xu; Nana Zhao; Feng Ren; Rami Hourani; Ming Tsang Lee; Jessica Y. Shu; Samuel Mao; Helms, B. A.; Subnanometer Porous Thin Films by the Co-Assembly of Nanotube Subunits and Block Copolymers. *ACS nano* **2011,** *5*, 1376–1384.

37. Haberkorn, N.; Gutmann, J. S.; Theato, P.; Template-Assisted Fabrication of Free-Standing Nanorod Arrays of a Hole-Conducting Cross-Linked Triphenylamine Derivative: Toward Ordered Bulk-Heterojunction Solar Cells. *Acs Nano* **2009,** *3*, 1415-1422.

38. Haberkorn, N.; Lechmann, M. C.; Sohn, B. H.; Char, K.; Gutmann, J. S.; Theato, P.; Templated Organic and Hybrid Materials for Optoelectronic Applications. *Macromol. Rapid Commun.* **2009,** *30*, 1146-1166.

39. Lee, J.; Orilall, M. C.; Warren, S. C.; Kamperman, M.; Disalvo, F. J.; Wiesner, U.; Direct Access to Thermally Stable and Highly Crystalline Mesoporous Transition-Metal Oxides with Uniform Pores. *Nat. Mat.* **2008,** *7*, 222-228.

40. O'Sullivan, J. P.; Wood, G. C.; The Morphology and Mechanism of Formation of Porous Anodic Films on Aluminium. *Proc. R. Soc. Lond. A* **1970,** *317*, 511-543.

41. Mikulskas, I.; Juodkazis, S.; Tomasiunas, R.; Dumas, J. G.; Aluminum Oxide Photonic Crystals Grown by a New Hybrid Method. *Adv. Mater.* **2001,** *13*, 1574.

42. Martin, C. R.; Nanomaterials - a Membrane-Based Synthetic Approach. *Science* **1994,** *266*, 1961-1966.

43. Nielsch, K.; Choi, J.; Schwirn, K.; Wehrspohn, R. B.; Gosele, U.; Self-Ordering Regimes of Porous Alumina: The 10% Porosity Rule. *Nano Lett.* **2002,** *2*, 677-680.

44. Bowen, W. R.; Sharif, A. O.; The Hydrodynamic and Electrostatic Interactions on the Approach and Entry of a Charged Spherical Particle to a Charged Cylindrical Pore in a Charged Planar Surface with Implications for Membrane Separation Processes. *Proc. R. Soc. Lond. A* **1996,** *452*, 2121-2140.

45. Chen, W.; Yuan, J. H.; Xia, X. H.; Characterization and Manipulation of the Electroosmotic Flow in Porous Anodic Alumina Membranes. *Anal. Chem.* **2005,** *77*, 8102-8108.

46. Han, J. Y.; Fu, J. P.; Schoch, R. B.; Molecular Sieving Using Nanofilters: Past, Present and Future. *Lab on a Chip* **2008,** *8*, 23-33.

47. Jiang, X. Q.; Mishra, N.; Turner, J. N.; Spencer, M. G.; Diffusivity of Sub-1,000 Da Molecules in 40 Nm Silicon-Based Alumina Pores. *Microfluid. Nanofluid.* **2008,** *5*, 695-701.

48. Wang, Y.; Angelatos, A. S.; Dunstan, D. E.; Caruso, F.; Infiltration of Macromolecules into Nanoporous Silica Particles. *Macromolecules* **2007,** *40*, 7594-7600.

49. Bonanno, L. M.; Kwong, T. C.; DeLouise, L. A.; Label-Free Porous Silicon Immunosensor for Broad Detection of Opiates in a

Blind Clinical Study and Results Comparison to Commercial Analytical Chemistry Techniques. *Anal. Chem.* **2010,** *82*, 9711-9718.

50. Hotta, K.; Yamaguchi, A.; Teramae, N.; Properties of a Metal Clad Waveguide Sensor Based on a Nanoporous-Metal-Oxide/Metal Multilayer Film. *Anal. Chem.* **2010,** *82*, 6066-6073.

51. Schwartz, M. P.; Alvarez, S. D.; Sailor, M. J.; Porous Sio2 Interferometric Biosensor for Quantitative Determination of Protein Interactions: Binding of Protein a to Immunoglobulins Derived from Different Species. *Anal. Chem.* **2007,** *79*, 327-334.

52. Wang, M. L.; Meng, G. W.; Huang, Q.; Li, M. T.; Li, Z. B.; Tang, C. L.; Fluorescence Detection of Trace Pcb101 Based on Pitc Immobilized on Porous Aao Membrane. *Analyst* **2011,** *136*, 278-281.

53. Yamaguchi, A.; Hotta, K.; Teramae, N.; Optical Waveguide Sensor Based on a Porous Anodic Alumina/Aluminum Multilayer Film. *Anal. Chem.* **2009,** *81*, 105-111.

54. Schmid, G.; Materials in Nanoporous Alumina. *J. Mater. Chem.* **2002,** *12*, 1231-1238.

55. Metzger, R. M.; Konovalov, V. V.; Sun, M.; Xu, T.; Zangari, G.; Xu, B.; Benakli, M.; Doyle, W. D.; Magnetic Nanowires in Hexagonally Ordered Pores of Alumina. *IEEE Trans. Magn.* **2000,** *36*, 30-35.

56. Zhang, Z. B.; Ying, J. Y.; Dresselhaus, M. S.; Bismuth Quantum-Wire Arrays Fabricated by a Vacuum Melting and Pressure Injection Process. *J. Mat. Res.* **1998,** *13*, 1745-1748.

57. Hou, S. F.; Wang, J. H.; Martin, C. R.; Template-Synthesized Protein Nanotubes. *Nano Lett.* **2005,** *5*, 231-234.

58. Bain, C. D.; Biebuyck, H. A.; Whitesides, G. M.; Comparison of Self-Assembled Monolayers on Gold - Coadsorption of Thiols and Disulfides. *Langmuir* **1989,** *5*, 723-727.

59. Bain, C. D.; Troughton, E. B.; Tao, Y. T.; Evall, J.; Whitesides, G. M.; Nuzzo, R. G.; Formation of Monolayer Films by the Spontaneous Assembly of Organic Thiols from Solution onto Gold. *J. Am. Chem. Soc.* **1989,** *111*, 321-335.

60. Dubois, L. H.; Nuzzo, R. G.; Synthesis, Structure, and Properties of Model Organic-Surfaces. *Ann. Rev. Phys. Chem.* **1992,** *43*, 437-463.

61. Dubois, L. H.; Zegarski, B. R.; Nuzzo, R. G.; Molecular Ordering of Organosulfur Compounds on Au(111) and Au(100) - Adsorption from Solution and in Ultrahigh-Vacuum. *J. Chem. Phys.* **1993,** *98*, 678-688.

62. Laibinis, P. E.; Whitesides, G. M.; Allara, D. L.; Tao, Y. T.; Parikh, A. N.; Nuzzo, R. G.; Comparison of the Structures and Wetting Properties of Self-Assembled Monolayers of Normal-Alkanethiols on the Coinage Metal-Surfaces, Cu, Ag, Au. *J. Am. Chem. Soc.* **1991,** *113*, 7152-7167.

63. Schreiber, F.; Structure and Growth of Self-Assembling Monolayers. *Prog. Surf. Sc.* **2000,** *65*, 151-256.

64. Sellers, H.; Ulman, A.; Shnidman, Y.; Eilers, J. E.; Structure and Binding of Alkanethiolates on Gold and Silver Surfaces - Implications for Self-Assembled Monolayers. *J. Am. Chem. Soc.* **1993,** *115*, 9389-9401.

65. Gombotz, W. R.; Guanghui, W.; Horbett, T. A.; Hoffman, A. S.; Protein Adsorption to Poly(Ethylene Oxide) Surfaces. *J. Biomed. Mater. Res.* **1991,** *25*, 1547-1562.

66. Liston, E. M.; Martinu, L.; Wertheimer, M. R.; Plasma Surface Modification of Polymers for Improved Adhesion - a Critical-Review. *J. Adhes. Sci. Technol.* **1993,** *7*, 1091-1127.

67. Tran, Y.; Auroy, P.; Synthesis of Poly(Styrene Sulfonate) Brushes. *J. Am. Chem. Soc.* **2001,** *123*, 3644-3654.

68. Brzoska, J. B.; Benazouz, I.; Rondelez, F.; Silanization of Solid Substrates - a Step toward Reproducibility. *Langmuir* **1994,** *10*, 4367-4373.

69. Brzoska, J. B.; Shahidzadeh, N.; Rondelez, F.; Evidence of a Transition Temperature for the Optimum Deposition of Grafted Monolayer Coatings. *Nature* **1992,** *360*, 719-721.

70. Fadeev, A. Y.; McCarthy, T. J.; Self-Assembly Is Not the Only Reaction Possible between Alkyltrichlorosilanes and Surfaces: Monomolecular and Oligomeric Covalently Attached Layers of Dichloro- and Trichloroalkylsilanes on Silicon. *Langmuir* **2000,** *16*, 7268-7274.

71. Nanci, A.; Wuest, J. D.; Peru, L.; Brunet, P.; Sharma, V.; Zalzal, S.; McKee, M. D.; Chemical Modification of Titanium Surfaces for Covalent Attachment of Biological Molecules. *J. Biomed. Mater. Res.* **1998,** *40*, 324-335.

72. Oner, D.; McCarthy, T. J.; Ultrahydrophobic Surfaces. Effects of Topography

Length Scales on Wettability. *Langmuir* **2000,** *16*, 7777-7782.

73. Weetall, H. H.; Preparation of Immobilized Proteins Covalently Coupled through Silane Coupling Agents to Inorganic Supports. *Appl. Biochem. Biotechnol.* **1993,** *41*, 157-188.

74. Fadeev, A. Y.; McCarthy, T. J.; Trialkylsilane Monolayers Covalently Attached to Silicon Surfaces: Wettability Studies Indicating That Molecular Topography Contributes to Contact Angle Hysteresis. *Langmuir* **1999,** *15*, 3759-3766.

75. Kobayash.H; Bell, A. T.; Shen, M.; Plasma Polymerization of Saturated and Unsaturated-Hydrocarbons. *Macromolecules* **1974,** *7*, 277-283.

76. Medard, N.; Soutif, J. C.; Poncin-Epaillard, F.; Characterization of Co2 Plasma-Treated Polyethylene Surface Bearing Carboxylic Groups. *Surf. Coat. Technol.* **2002,** *160*, 197-205.

77. Biebuyck, H. A.; Whitesides, G. M.; Interchange between Monolayers on Gold Formed from Unsymmetrical Difulfides and Solutions of Thiols - Evidence for Sulfur-Sulfur Bond Cleavage by Gold Metal. *Langmuir* **1993,** *9*, 1766-1770.

78. Hubbard, J. B.; Silin, V.; Plant, A. L.; Self-Assembly Driven by Hydrophobic Interactions at Alkanethiol Monolayers: Mechanism of Formation of Hybrid Bilayer Membranes. *Biophys. Chem.* **1998,** *75*, 163-176.

79. Plant, A. L.; Self-Assembled Phospholipid Alkanethiol Biometic Bilayers on Gold. *Langmuir* **1993,** *9*, 2764-2767.

80. Ron, H.; Matlis, S.; Rubinstein, I.; Self-Assembled Monolayers on Oxidized Metals. 2. Gold Surface Oxidative Pretreatment, Monolayer Properties, and Depression Formation. *Langmuir* **1998,** *14*, 1116-1121.

81. Kelley, T. W.; Boardman, L. D.; Dunbar, T. D.; Muyres, D. V.; Pellerite, M. J.; Smith, T. Y. P.; High-Performance Otfts Using Surface-Modified Alumina Dielectrics. *J. Phys. Chem. B* **2003,** *107*, 5877-5881.

82. Templeton, M. K.; Weinberg, W. H.; Adsorption and Decomposition of Dimethyl Methylphosphonate on an Aluminum-Oxide Surface. *J. Am. Chem. Soc.* **1985,** *107*, 97-108.

83. Templeton, M. K.; Weinberg, W. H.; Decomposition of Phosphonate Esters Adsorbed on Aluminum-Oxide. *J. Am. Chem. Soc.* **1985,** *107*, 774-779.

84. 3-D Composite Generated Using Gaussview 03w Software. In.

85. Love, J. C.; Estroff, L. A.; Kriebel, J. K.; Nuzzo, R. G.; Whitesides, G. M.; Self-Assembled Monolayers of Thiolates on Metals as a Form of Nanotechnology. *Chem. Rev.* **2005,** *105*, 1103-1169.

86. Bertilsson, L.; Liedberg, B.; Infrared Study of Thiol Monolayer Assemblies on Gold - Preparation, Characterization, and Functionalization of Mixed Monolayers. *Langmuir* **1993,** *9*, 141-149.

87. Tao, Y. T.; Wu, C. C.; Eu, J. Y.; Lin, W. L.; Wu, K. C.; Chen, C. H.; Structure Evolution of Aromatic-Derivatized Thiol Monolayers on Evaporated Gold. *Langmuir* **1997,** *13*, 4018-4023.

88. Castner, D. G.; Hinds, K.; Grainger, D. W.; X-Ray Photoelectron Spectroscopy Sulfur 2p Study of Organic Thiol and Disulfide Binding Interactions with Gold Surfaces. *Langmuir* **1996,** *12*, 5083-5086.

89. Porter, M. D.; Bright, T. B.; Allara, D. L.; Chidsey, C. E. D.; Spontaneously Organized Molecular Assemblies.4. Structural Characterization of Normal-Alkyl Thiol Monolayers on Gold by Optical Ellipsometry, Infrared-Spectroscopy, and Electrochemistry. *J. Am. Chem. Soc.* **1987,** *109*, 3559-3568.

90. Steed, J. W.; Atwood, J. L., *Supramolecular Chemistry*. John Wiley and Sons: 2009.

91. Schwartz, D. K.; Mechanisms and Kinetics of Self-Assembled Monolayer Formation. *Ann. Rev. Phys. Chem.* **2001,** *52*, 107-137.

92. Karpovich, D. S.; Blanchard, G. J.; Direct Measurement of the Adsorption-Kinetics of Alkanethiolate Self-Assembled Monolayers on a Microcrystalline Gold Surface. *Langmuir* **1994,** *10*, 3315-3322.

93. Schmidt, A.; Spinke, J.; Bayerl, T.; Sackmann, E.; Knoll, W.; Streptavidin Binding to Biotinylated Lipid Layers on Solid Supports - a Neutron Reflection and Surface-Plasmon Optical Study. *Biophys. J.* **1992,** *63*, 1385-1392.

94. Housecroft, C. E.; Sharpe, A. G., *Inorganic Chemistry*. Pearson Education: 2005.

95. Jarvis, A.; Beavon, R., *Periodicity, Quantitative Equilibria and Gunctional Group Chemistry*. Nelson Thornes: 2001.

96. Zhou, G.-d., *Fundamentals of Structural Chemistry*. World Scientific: 1993.

97. Iqbal, M. S.; S.A.; Satake, M., *Chemistry of P-Block Elements*. Discovery Publishing House: 2003.

98. Howarter, J. A.; Youngblood, J. P.; Optimization of Silica Silanization by 3-Aminopropyltriethoxysilane. *Langmuir* **2006,** *22*, 11142-11147.

99. Aronsson, B. O.; Lausmaa, J.; Kasemo, B.; Glow Discharge Plasma Treatment for Surface Cleaning and Modification of Metallic Biomaterials. *J. Biomed. Mater. Res.* **1997,** *35*, 49-73.

100. Harrick-Plasma, *Applications Involving Plasma Treatments with Harrick Plasma Devices*. http://www.harrickplasma.com/applications_cleaning.php: 2010.

101. Ruiz, M., Cell Membrane: Detailed Diagram. In *http://en.wikibooks.org/wiki/File:Cell_membrane_detailed_diagram_en.svg* This work has been released into the public domain by the author. This applies worldwide. The author has granted anyone the right to use this work for any purpose, without any conditions.

102. Singer, S. J.; Fluid Lipid-Globular Protein Mosaic Model of Membrane Structure. *Ann. N.Y. Acad. Sci.* **1972,** *195*, 16-&.

103. Singer, S. J.; Nicolson, G. L.; Fluid Mosaic Model of Structure of Cell-Membranes. *Science* **1972,** *175*, 720-&.

104. Sackmann, E.; Supported Membranes: Scientific and Practical Applications. *Science* **1996,** *271*, 43-48.

105. Dietrich, C.; Bagatolli, L. A.; Volovyk, Z. N.; Thompson, N. L.; Levi, M.; Jacobson, K.; Gratton, E.; Lipid Rafts Reconstituted in Model Membranes. *Biophys. J.* **2001,** *80*, 1417-1428.

106. Simons, K.; Ikonen, E.; Functional Rafts in Cell Membranes. *Nature* **1997,** *387*, 569-572.

107. Simons, K.; Toomre, D.; Lipid Rafts and Signal Transduction. *Nat. Rev. Mol. Cell Biol.* **2000,** *1*, 31-39.

108. Morone, N.; Fujiwara, T.; Murase, K.; Kasai, R. S.; Ike, H.; Yuasa, S.; Usukura, J.; Kusumi, A.; Three-Dimensional Reconstruction of the Membrane Skeleton at the Plasma Membrane Interface by Electron Tomography. *J. Cell Biology* **2006,** *174*, 851-862.

109. Fujiwara, T.; Ritchie, K.; Murakoshi, H.; Jacobson, K.; Kusumi, A.; Phospholipids Undergo Hop Diffusion in Compartmentalized Cell Membrane. *J. Cell Biol.* **2002,** *157*, 1071-1082.

110. Kusumi, A.; Nakada, C.; Ritchie, K.; Murase, K.; Suzuki, K.; Murakoshi, H.; Kasai, R. S.; Kondo, J.; Fujiwara, T.; Paradigm Shift of the Plasma Membrane Concept from the Two-Dimensional Continuum Fluid to the Partitioned Fluid: High-Speed Single-Molecule Tracking of Membrane Molecules. *Annual Review of Biophysics and Biomolecular Structure* **2005,** *34*, 351-U54.

111. Morone, N.; Fujiwara, T.; Murase, K.; Kasai, R. S.; Ike, H.; Yuasa, S.; Usukura, J.; Kusumi, A.; Three-Dimensional Reconstruction of the Membrane Skeleton at the Plasma Membrane Interface by Electron Tomography. *J. Cell Biol.* **2006,** *174*, 851-862.

112. Ritchie, K.; Iino, R.; Fujiwara, T.; Murase, K.; Kusumi, A.; The Fence and Picket Structure of the Plasma Membrane of Live Cells as Revealed by Single Molecule Techniques. *Mol. Membr. Biol.* **2003,** *20*, 13-18.

113. Rose, W. G.; Synthesis of Cephalin. *J. Am. Chem. Soc.* **1947,** *69*, 1384-1387.

114. Slotboom, A. J.; Bonsen, P. P. M.; Recent Developments in Chemistry of Phospholipids. *Chem. Phys. Lipids* **1970,** *5*, 301-&.

115. Nagle, J. F.; Tristram-Nagle, S.; Structure of Lipid Bilayers. *Biochim. Biophys. Acta, Rev. Biomembr.* **2000,** *1469*, 159-195.

116. Pastor, R. W.; Venable, R. M.; Karplus, M.; Model for the Structure of the Lipid Bilayer. *PNAS* **1991,** *88*, 892-896.

117. Chandler, D.; Interfaces and the Driving Force of Hydrophobic Assembly. *Nature* **2005,** *437*, 640-647.

118. Israelachvili, J. N.; Mitchell, D. J.; Ninham, B. W.; Theory of the Self-Assembly of Lipid Bilayers and Vesicles. *Biochim. Biophys. Acta* **1977,** *470*, 185-201.

119. Wiener, M. C.; White, S. H.; Fluid Bilayer Structure Determination by the Combined Use of X-Ray and Neutron-Diffraction .1. Fluid Bilayer Models and the Limits of Resolution. *Biophys. J.* **1991,** *59*, 162-173.

120. Wiener, M. C.; White, S. H.; Structure of a Fluid Dioleoylphosphatidylcholine Bilayer Determined by Joint Refinement of X-Ray and Neutron-Diffraction Data .3. Complete Structure. *Biophys. J.* **1992,** *61*, 434-447.

121. Rodriguez, N.; Pincet, F.; Cribier, S.; Giant Vesicles Formed by Gentle Hydration and Electroformation: A Comparison by Fluorescence Microscopy. *Colloids Surf., B* **2005,** *42*, 125-130.

122. Marques, E. F.; Size and Stability of Catanionic Vesicles: Effects of Formation Path, Sonication, and Aging. *Langmuir* **2000,** *16*, 4798-4807.

123. Bresseleers, G. J. M.; Goderis, H. L.; Tobback, P. P.; Measurement of the Glucose Permeation Rate across Phospholipid-Bilayers Using Small Unilamellar Vesicles - Effect of Membrane-Composition and Temperature. *Biochim. Biophys. Acta* **1984,** *772*, 374-382.

124. Patty, P. J.; Frisken, B. J.; Extrusion Studies of Lipid Vesicles. *Biophys. J.* **2000,** *78*, 361Pos.

125. Macdonald, R. C.; Macdonald, R. I.; Menco, B. P. M.; Takeshita, K.; Subbarao, N. K.; Hu, L. R.; Small-Volume Extrusion Apparatus for Preparation of Large, Unilamellar Vesicles. *Biochim. Biophys. Acta* **1991,** *1061*, 297-303.

126. Hope, M. J.; Bally, M. B.; Webb, G.; Cullis, P. R.; Production of Large Unilamellar Vesicles by a Rapid Extrusion Procudure - Characterization of Size Distribution, Trapped Volume and Ability to Maintain a Membrane-Potential. *Biochim. Biophys. Acta* **1985,** *812*, 55-65.

127. Frisken, B. J.; Asman, C.; Patty, P. J.; Studies of Vesicle Extrusion. *Langmuir* **2000,** *16*, 928-933.

128. Bucher, P.; Fischer, A.; Luisi, P. L.; Oberholzer, T.; Walde, P.; Giant Vesicles as Biochemical Compartments: The Use of Microinjection Techniques. *Langmuir* **1998,** *14*, 2712-2721.

129. Estes, D. J.; Mayer, M.; Electroformation of Giant Liposomes from Spin-Coated Films of Lipids. *Colloid. Surf. B* **2005,** *42*, 115-123.

130. Montes, L. R.; Alonso, A.; Goni, F. M.; Bagatolli, L. A.; Giant Unilamellar Vesicles Electroformed from Native Membranes and Organic Lipid Mixtures under Physiological Conditions. *Biophys. J.* **2007,** *93*, 3548-3554.

131. Heimburg, T., *Thermal Biophysics of Membranes*. Wiley-VCH: 2007.

132. Garrett, R.; Grisham, C. M., *Biochemistry*. Cengage Learning: 2010.

133. Janiak, M. J.; Small, D. M.; Shipley, G. G.; Nature of the Thermal Pre-Transition of Synthetic Phospholipids - Dimyristoyllecithin and Dipalmitoyllecithin. *Biochem.* **1976,** *15*, 4575-4580.

134. Mueller, P.; Rudin, D. O.; Tien, H. T.; Wescott, W. C.; Reconstitution of Cell Membrane Structure in Vitro and Its Transformation into an Excitable System. *Nature* **1962,** *194*, 979.

135. Mueller, P.; Wescott, W. C.; Rudin, D. O.; Tien, H. T.; Methods for Formation of Single Biomolecular Lipid Membranes in Aqueous Solution. *J. Phys. Chem.* **1963,** *67*, 534.

136. Bamberg, E.; Alpes, H.; Apell, H. J.; Bradley, R.; Harter, B.; Quelle, M. J.; Urry, D. W.; Formation of Ionic Channels in Black Lipid-Membranes by Succinic Derivaties of Gramicidin-A. *Journal of Membrane Biology* **1979,** *50*, 257-270.

137. Bamberg, E.; Apell, H. J.; Alpes, H.; Gross, E.; Morell, J. L.; Harbaugh, J. F.; Janko, K.; Lauger, P.; Ion Channels Formed by Chemical Analogs of Gramicidin-A. *Federation Proceedings* **1978,** *37*, 2633-2638.

138. Gomezlagunas, F.; Pena, A.; Lievano, A.; Darszon, A.; Incorporation of Ionic Channels from Yeast Plasma-Membranes into Black Lipid-Membranes. *Biophys. J.* **1989,** *56*, 115-119.

139. Van Gelder, P.; Dumas, F.; Winterhalter, M.; Understanding the Function of Bacterial Outer Membrane Channels by Reconstitution into Black Lipid Membranes. *Biophys. Chem.* **2000,** *85*, 153-167.

140. Alonsoromanowski, S.; Gassa, L. M.; Vilche, J. R.; An Investigation by Eis of Gramicidin Channels in Bilayer-Lipid Membranes. *Electrochim. Acta* **1995,** *40*, 1561-1567.

141. Aguilella, V. M.; Rostovtseva, T. K.; Vodyanoy, I.; Bezrukov, S. M.; Parsegian, V. A.; Streaming Potential in Mitochondrial Porin, Vdac. *Biophys. J.* **1999,** *76*, A208-A208.

142. Stelzle, M.; Miehlich, R.; Sackmann, E.; 2-Dimensional Microelectrophoresis in Supported Lipid Bilayers. *Biophys. J.* **1992,** *63*, 1346-1354.

143. Johnson, J. M.; Ha, T.; Chu, S.; Boxer, S. G.; Early Steps of Supported Bilayer Formation Probed by Single Vesicle Fluorescence Assays. *Biophys. J.* **2002,** *83*, 3371-3379.

144. Cremer, P. S.; Boxer, S. G.; Formation and Spreading of Lipid Bilayers on Planar Glass Supports. *J. Phys. Chem. B* **1999,** *103*, 2554-2559.

145. Egawa, H.; Furusawa, K.; Liposome Adhesion on Mica Surface Studied by Atomic Force Microscopy. *Langmuir* **1999,** *15*, 1660-1666.

146. Tamm, L. K.; McConnell, H. M.; Supported Phospholipid-Bilayers. *Biophys. J.* **1985,** *47*, 105-113.

147. Lagerholm, B. C.; Starr, T. E.; Volovyk, Z. N.; Thompson, N. L.; Rebinding of Ige Fabs at Haptenated Planar Membranes: Measurement by Total Internal Reflection with Fluorescence Photobleaching Recovery. *Biochem.* **2000,** *39*, 2042-2051.

148. Hubbard, J. B.; Silin, V.; Plant, A. L.; Self Assembly Driven by Hydrophobic Interactions at Alkanethiol Monolayers: Mechanism of Formation of Hybrid Bilayer Membranes. *Biophys. J.* **1999,** *76*, A431-A431.

149. Meuse, C. W.; Krueger, S.; Majkrzak, C. F.; Dura, J. A.; Fu, J.; Connor, J. T.; Plant, A. L.; Hybrid Bilayer Membranes in Air and Water: Infrared Spectroscopy and Neutron Reflectivity Studies. *Biophys. J.* **1998,** *74*, 1388-1398.

150. Kalb, E.; Frey, S.; Tamm, L. K.; Formation of Supported Planar Bilayers by Fusion of Vesicles to Supported Phospholipid Monolayers. *Biochim. Biophys. Acta* **1992,** *1103*, 307-316.

151. Plant, A. L.; Supported Hybrid Bilayer Membranes as Rugged Cell Membrane Mimics. *Langmuir* **1999,** *15*, 5128-5135.

152. Plant, A. L.; Brighamburke, M.; Petrella, E. C.; Oshannessy, D. J.; Phospholipid Alkenethiol Bilayers for Cell-Surface Receptor Studies by Surface-Plamon Resonance. *Anal. Biochem.* **1995,** *226*, 342-348.

153. Kastl, K.; Ross, M.; Gerke, V.; Steinem, C.; Kinetics and Thermodynamics of Annexin A1 Binding to Solid-Supported Membranes: A Qcm Study. *Biochem.* **2002,** *41*, 10087-10094.

154. Rao, N. M.; Plant, A. L.; Silin, V.; Wight, S.; Hui, S. W.; Characterization of Biomimetic Surfaces Formed from Cell Membranes. *Biophys. J.* **1997,** *73*, 3066-3077.

155. Rao, N. M.; Silin, V.; Ridge, K. D.; Woodward, J. T.; Plant, A. L.; Cell Membrane Hybrid Bilayers Containing the G-Protein-Coupled Receptor Ccr5. *Anal. Biochem.* **2002,** *307*, 117-130.

156. Koper, I.; Insulating Tethered Bilayer Lipid Membranes to Study Membrane Proteins. *Mol. Biosyst.* **2007,** *3*, 651-657.

157. Naumann, R.; Schiller, S. M.; Giess, F.; Grohe, B.; Hartman, K. B.; Karcher, I.; Koper, I.; Lubben, J.; Vasilev, K.; Knoll, W.; Tethered Lipid Bilayers on Ultraflat Gold Surfaces. *Langmuir* **2003,** *19*, 5435-5443.

158. Schiller, S. M.; Naumann, R.; Lovejoy, K.; Kunz, H.; Knoll, W.; Archaea Analogue Thiolipids for Tethered Bilayer Lipid Membranes on Ultrasmooth Gold Surfaces. *Angew. Chem. Int. Ed.* **2003,** *42*, 208-211.

159. Sackmann, E.; Tanaka, M.; Supported Membranes on Soft Polymer Cushions: Fabrication, Characterization and Applications. *Trends in Biotechnol.* **2000,** *18*, 58-64.

160. Tanaka, M.; Sackmann, E.; Polymer-Supported Membranes as Models of the Cell Surface. *Nature* **2005,** *437*, 656-663.

161. Glazier, S. A.; Vanderah, D. J.; Plant, A. L.; Bayley, H.; Valincius, G.; Kasianowicz, J. J.; Reconstitution of the Pore-Forming Toxin Alpha-Hemolysin in Phospholipid/18-Octadecyl-1-Thiahexa(Ethylene Oxide) and Phospholipid/N-Octadecanethiol Supported Bilayer Membranes. *Langmuir* **2000,** *16*, 10428-10435.

162. Elender, G.; Kuhner, M.; Sackmann, E.; Functionalisation of Si/Sio2 and Glass Surfaces with Ultrathin Dextran Films and Deposition of Lipid Bilayers. *Biosens. Bioelectron.* **1996,** *11*, 565-577.

163. Hillebrandt, H.; Wiegand, G.; Tanaka, M.; Sackmann, E.; High Electric Resistance Polymer/Lipid Composite Films on Indium-Tin-Oxide Electrodes. *Langmuir* **1999,** *15*, 8451-8459.

164. Kugler, R.; Knoll, W.; Polyelectrolyte-Supported Lipid Membranes. *Bioelectrochem.* **2002,** *56*, 175-178.

165. Renner, L.; Osaki, T.; Chiantia, S.; Schwille, P.; Pompe, T.; Werner, C.; Supported Lipid Bilayers on Spacious and Ph-Responsive Polymer Cushions with Varied Hydrophilicity. *J. Phys. Chem. B* **2008,** *112*, 6373-6378.

166. Naumann, C. A.; Knoll, W.; Frank, C. W.; Hindered Diffusion in Polymer-Tethered Membranes: A Monolayer Study at the Air-Water Interface. *Biomacromolecules* **2001,** *2*, 1097-1103.

167. Naumann, C. A.; Prucker, O.; Lehmann, T.; Ruhe, J.; Knoll, W.; Frank, C. W.; The Polymer-Supported Phospholipid Bilayer: Tethering as a New Approach to Substrate-Membrane Stabilization. *Biomacromolecules* **2002,** *3*, 27-35.

168. Han, X. J.; Studer, A.; Sehr, H.; Geissbuhler, I.; Di Berardino, M.; Winkler, F. K.; Tiefenauer, L. X.; Nanopore Arrays for Stable and Functional Free-Standing Lipid Bilayers. *Adv. Mater.* **2007,** *19*, 4466-4470.

169. Mey, I.; Stephan, M.; Schmitt, E. K.; Muller, M. M.; Ben Amar, M.; Steinem, C.; Janshoff, A.; Local Membrane Mechanics of Pore-Spanning Bilayers. *J. Am. Chem. Soc.* **2009,** *131*, 7031-7039.

170. Schmitt, E. K.; Vrouenraets, M.; Steinem, C.; Channel Activity of Ompf Monitored in Nano-Blms. *Biophys. J.* **2006,** *91*, 2163-2171.

171. Romer, W.; Lam, Y. H.; Fischer, D.; Watts, A.; Fischer, W. B.; Goring, P.; Wehrspohn, R. B.; Gosele, U.; Steinem, C.; Channel Activity of a Viral Transmembrane Peptide in Micro-Blms: Vpu(1-32) from Hiv-1. *J. Am. Chem. Soc.* **2004,** *126*, 16267-16274.

172. Romer, W.; Steinem, C.; Impedance Analysis and Single-Channel Recordings on Nano-Black Lipid Membranes Based on Porous Alumina. *Biophys. J.* **2004,** *86*, 955-965.

173. Pfeiffer, I.; Petronis, S.; Koper, I.; Kasemo, B.; Zach, M.; Vesicle Adsorption and Phospholipid Bilayer Formation on Topographically and Chemically Nanostructured Surfaces. *J. Phys. Chem. B* **2010,** *114*, 4623-4631.

174. Pfeiffer, I.; Seantier, B.; Petronis, S.; Sutherland, D.; Kasemo, B.; Zach, M.; Influence of Nanotopography on Phospholipid Bilayer Formation on Silicon Dioxide. *J. Phys. Chem. B* **2008,** *112*, 5175-5181.

175. Worsfold, O.; Voelcker, N. H.; Nishiya, T.; Biosensing Using Lipid Bilayers Suspended on Porous Silicon. *Langmuir* **2006,** *22*, 7078-7083.

176. Im, H.; Wittenberg, N. J.; Lesuffleur, A.; Lindquist, N. C.; Oh, S. H.; Membrane Protein Biosensing with Plasmonic Nanopore Arrays and Pore-Spanning Lipid Membranes. *Chem. Sci.* **2010,** *1*, 688-696.

177. Jonsson, P.; Jonsson, M. P.; Hook, F.; Sealing of Submicrometer Wells by a Shear-Driven Lipid Bilayer. *Nano Lett.* **2010,** *10*, 1900-1906.

178. Cunin, F.; Milhiet, P. E.; Anglin, E.; Sailor, M. J.; Espenel, C.; Le Grimellec, C.; Brunel, D.; Devoisselle, J. M.; Continuous Planar Phospholipid Bilayer Supported on Porous Silicon Thin Film Reflector. *Ultramicroscopy* **2007,** *107*, 1048-1052.

Chapter 2

Methods, Materials, Instruments: Extended Experimental

2.1. Anodic Aluminum Oxide (AAO) Membranes

2.1.1. Structure and Physical Properties of AAO

Anodic aluminum oxide (AAO) is a self-organized nanoporous material that possesses non-intersecting, close-packed, cylindrical pores running straight through the film thickness, as illustrated in figure 1A. The preparation of this porous material has been carried out through by the electrochemical anodization of Al metal since the 1970's.[1] In the 1990's, growing interest in manipulating nanoscale structures revived the interest in this material. A number of research groups have mapped out the experimental conditions that allow the preparation of AAO with a desired monodisperse pore diameters ranging from 10-420 nm in size.[2-4] Under the presence of an electrolyte, Al metal is converted to Aluminum oxide through an applied voltage, according to eq. (2.1).

$$\textit{At anode:}\ 2\ Al^{3+} + 3\ H_2O \rightarrow Al_2O_3 + 6\ H^+ + 6\ e^- \qquad \text{equation (2.1a)}$$

$$\textit{At cathode:}\ 6\ H^+ + 6\ e^- \rightarrow 3\ H_2 \qquad \text{equation (2.1b)}$$

AAO membranes have a thin uniform oxide layer (5-200 nm), that is located next to the metal, *i.e.* the barrier layer, and an outer porous layer that can extend from several tens of nm to several μm. Within the porous layer, cylindrical pores, with monodisperse diameters that can be adjusted (d_0 = 10-420 nm), are orientated normal to the metal and extend from the barrier layer to the porous film surface.[2, 5] The porous AAO membrane is composed of locally close packed and equally sized hexagonal unit cells with lattice constant $\lambda_{C\text{-}C}$. Every hexagonal cell has a central pore that is open atop and closed by an hemispherical shaped base near the barrier layer. Unit cell dimensions, as well as the barrier layer thickness are proportional to anodizing voltages. The thickness of the barrier layer depends on the

anodization voltage (2.8 $nm \cdot V^{-1}$).[1] The unit cell dimensions depend on the thickness of the Al_2O_3 inter-pore walls (t_{walls}), which is directly related to the barrier layer thickness ($t_{barrier}$): $t_{wall} \approx 2 \cdot t_{barrier}$. The porous region thickness depends on the amount of charge passed during the anodizing period, and can be adjusted to a desired thickness (nm to μm). Stresses during the porous film growth, which are relieved through the porous structure formation, directly lead to a self-ordering hexagonal pore arrangement. A schematic of the AAO structure and an SEM image of the samples produced are shown in figure 1.

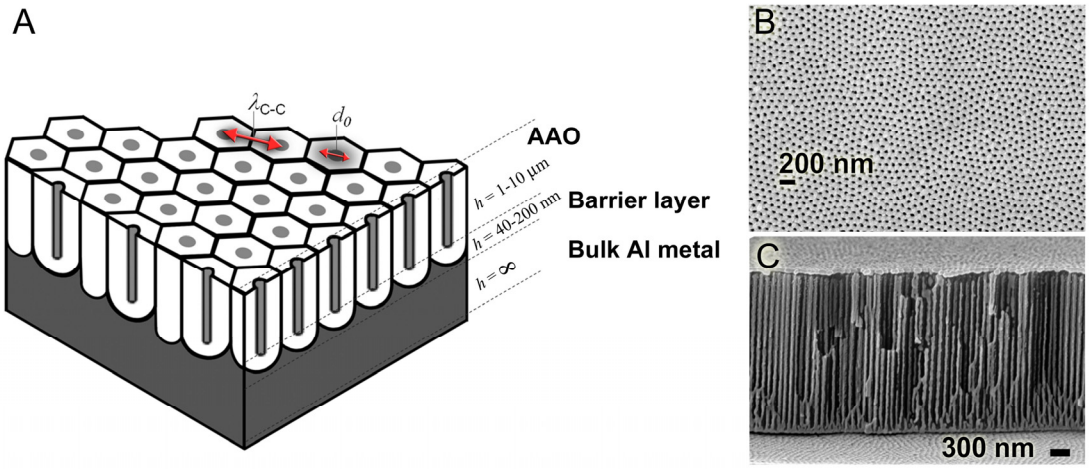

Figure 2.1. (**A**) 3D schematic of the self-ordered anodic aluminum oxide (AAO) material that is produced by electrochemical anodization of bulk Al metal. Anodization conditions control the parameters: lattice constant (λ_{C-C}) and pore diameter (d_0). (**B**) SEM image (*c.a.* 50 nm of Au evaporated for imaging) shows the ordered pores AAO, $d_0 \sim 55$ nm. (**C**) SEM image of AAO film showing parallel cylindrical nanopores.

AAO growth occurs because of ionic transport at the barrier layer located at the pore bottoms, while ionic transport is negligible at the pore walls. Ionic migration involves mainly Al^{3+} ions outward and O^{2-} ions inward.[6] The porous oxide film grows because of the O^{2-} migration because Al^{3+} ions reaching the barrier-solution interface are dissolved. Water is then the main source of oxygen in the films.[6] The chemical composition of the AAO oxide strongly depends on the conditions under which the anodization is carried out. AAO has an amorphous structure and has been shown to have significant incorporation of both hydroxide and hydrate oxide,[3, 7] as well as the conjugate base anion of the acid electrolyte,[3, 7-11] and was proposed to replace some of the O^{2-} anion in the oxide structure.[3, 8] The AAO oxide formed has a lower density than crystalline Al_2O_3 due in part to incorporated electrolyte anionic species ($\varepsilon = 2.68$ *vs* $\varepsilon = 2.76$ for pure Al_2O_3). The degree of acid anion incorporation depends on the electrolyte used: H_2SO_4 > $(COOH)_2$ > H_3PO_4. Higher incorporation has been found at higher anodization voltages. For H_2SO_4, 8 wt.%,[7] 10 wt.%[8] and even 20 wt.%[3] anion incorporation have been reported.

AAO growth is mainly controlled by voltage (U), and hence resulting current density (J), employed for anodizing. Temperature, pH and nature of the electrolyte as well as the electrolyte concentration also contribute to the final AAO structure. The interplay between these parameters determines the extent of chemical interaction that converts the underlying metal to the porous anodic aluminum oxide material.[11] The conversion efficiency of Al metal into the amorphous oxide increases with increasing applied voltages. The volume expansion increases the compressive mechanical stress incorporated into the oxide layer that is formed under anodization. The generated mechanical stress actually provides the main driving force for the formation and hexagonal ordering of the porous structure. The pores effectively eliminate stress concentrations, which gives rise to uniform hexagonal pore arrangement. Under an appropriate U and choice of electrolyte, the compressive stress associated with the Al metal to AAO volume expansion is achieved (from 1.2-1.4) and promotes long range hexagonal ordering of the pore array.[2, 4, 12-13] Furthermore, higher U's and therefore higher volume expansion can improve pore ordering in some cases.[9, 14-15] The anodization voltage controls $\lambda_{C\text{-}C}$, while d_0 can be adjusted by subsequent isotropic pore widening that slowly dissolves the exposed oxide pore walls. Each electrolyte has a critical U, above which acid burning occurs. Therefore, in practice, anodization in specific acids and voltages, together with pore-widening, are employed to generate optimally ordered pore arrays with a given $\lambda_{C\text{-}C}$ and a range of $d_{native} < d_0 < \lambda_{C\text{-}C}$.[4, 16]

The anodization of Aluminum metal to the nanoporous oxide occurs in different characteristic steps, before reaching steady-state oxide growth (figure 2B, steps **I-IV**). At the beginning of the anodization, an oxide film forms on the polished aluminum that is essentially flat, thin and of uniform thickness (step **I**). This occurs within the first minute and is characterized by a drop in the current density, $J \rightarrow 0$ mA/cm^2. Barrier layer growth is sustained and Aluminum species are lost to the electrolyte by field-assisted ejection of Al^{3+} ions[11, 17] (Step **II**). Step **II** is characterized by an increase in J, during which the oxide layer thickness increases. The continued uniform oxide growth eventually becomes unsustainable under the applied constant voltage conditions and all outward migrating Al^{3+} ions are retained. Perturbations in the surface topography lead to local increases of the electric field.[11] The perturbations become self-sustaining, resulting in the initiation of pores (step **III**). Step **III** is characterized by a rise in current until a maximum value is attained, corresponding to the pore initiation occurring in order to reestablish outward Al^{3+} migration. The initial pores are relatively fine, may branch and terminate or develop into the major pores that are characteristic of steady-state oxide growth.

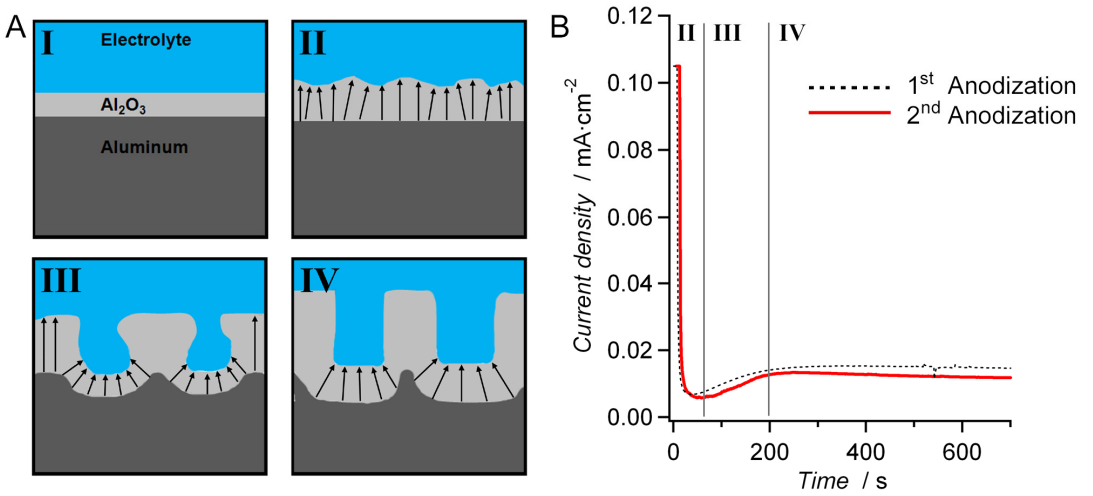

Figure 2.2. (**A**) Schematic of the initial steps leading to steady-state AAO growth with uniform cylindrical pore structure. (**B**) Current density (*J*) as a function of anodization time during the 1st anodization (---) of a polished Al surface and for the 2nd (–) anodization of a pre-textured Al surface (first 1000 s).

After the initiation of pores during the period of increasing *J vs* time, major pore formation, those of interest, takes place (Step **IV**). During step **IV**, the pores grow at a constant rate, characterized by a slow decrease in *J* towards a relatively constant value over the remainder of the anodization process. Any deviation from this ideal *J vs t* curve is indicative of a problematic anodization and the anodization should be repeated after stripping of the AAO. Deviations may take the form of high noise, random variation in *J*, drops in current, unusually high anodization current densities and will generate non-uniform AAO. Typical problems include a leak that exposes the Pt anode to the Cu cathode base and solution impurities. Constant voltage (25-200 V) anodization of Al metal generally produces AAO with a native porosity of approximately 10%.[4]

To obtain a highly ordered porous AAO substrate, a pre-texturing step is required. This involves a 2-step anodization, where the first anodized layer acts as a sacrificial layer. Pore initiation at the original Al metal surface is initially random in nature and pore ordering only occurs at the pore growth front, as the Al metal is converted to Al_2O_3. The highly ordered hexagonal ordering of the cylindrical nanopores, beyond the nearest neighbor, begins to be observed only when the pore depth *vs* d_{native} ratio is > 100.[3] In 2-step anodizations,[18-20] a thick (5-50 μm) sacrificial layer AAO with a well-developed pore ordering is first grown and then removed by chemical dissolution in either 5 vol % H_3PO_4 or with added chromic acid acting as a catalyst for the Al_2O_3 dissolution. The surface left behind is scalloped from the first oxide growth. Subsequent anodization of this pre-textured Al surface directs pore initiation at the centre of the pore-textured depressions and the optimal pore-ordering is rapidly established.

2.1.2. AAO preparation

Experimentally, AAO was prepared in a 3-step process that ensures a nanoporous film growth with uniform properties: (1) Surface cleaning and polishing, (2) Surface pre-texturing and (3) final oxide film growth. Steps (2) and (3) have been described above and summarized in figure 2, and are straightforward because they involve the simple anodization in an acid electrolyte under constant *U* and temperature. However, step (1) requires significant attention since the uniform structure and overall quality of the thin AAO films that are gown, 1-10 μm, is directly dependent on the initial metal surface. The Al has to be made extremely smooth and defect-free. Ideally, mirror surfaces (distortion-free reflection) with no traces of surface inhomogeneities must be attained. The oxide film has an atop-interface that is highly dependent on the initial Al metal surface. Since the atop-interface is used in experiments, and not the bottom barrier-layer, it is crucial that polishing be optimal such as to ensure that the low surface roughness of the metal layer is reproduced on AAO surface.

Al metal preparation/polishing. Aluminum 99.999% was either used as received from Good Fellow (Huntington, UK) or annealed at 500°C overnight. The AAO grown from non-annealed Al metal has $\lambda_{C\text{-}C}$ = 90-95 nm. The annealing process allows highly ordered AAO to be formed with $\lambda_{C\text{-}C}$ = 95-105 nm, but has the disadvantage of creating domains delimited by grain-boundaries formed during the annealing, which are on the order of a hundred of μm to a few mm in size, which varies from sample to sample. These are sometimes problematic for waveguide studies because the AAO thickness varies slightly on different domains, leading to a mixed spectrum composed of overlapping spectra, as shown in figure 2.3. Since the laser spot is at least 1.5-2.0 mm wide, many of these domains are typically probed at once. OWS is still possible with these substrates, but these potential problems should be kept in mind.

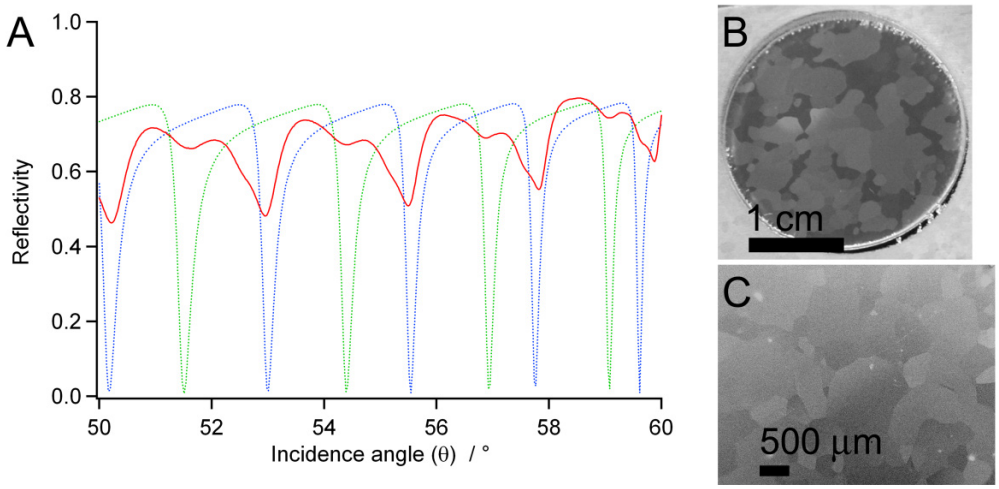

Figure 2.3. (**A**) Optical waveguide spectrum of AAO from Al annealed at 500°C. Double-peaks are because of domains of different height (*c.a.* 300 nm difference), simultaneously probed by the laser spot; green line is the result of the fit for 3670 nm thickness, while the blue line is for 3960 nm. (**B**) Photography of light reflecting off an annealed Al disk with large domains. (**C**) SEM images of a sample with domains taken with the secondary electron detector.

Mechanical polishing of Aluminum. This technique was only used for experiments in Chapter 3, given that the instrumentation was only available at the Max-Planck Institute for Polymer Research (Mainz, Germany). All other preparation were performed without any mechanical polishing. All polishing consumables, abrasive disks and diamond slurry solutions, were purchased from Buehler (Lake Bluff, IL, USA), as well as the rotating-disk polishing machine *Vector Power Head, Beta variable speed*. Mechanical polishing was performed in 4 steps. 99.999 % Al disks (20 mm diameter x 1 mm thick) from Goodfellow (Bad Nauheim, Germany) were firstly treated with abrasive SiC paper for 5 min on both sides, making the disk flat, and of even thickness. This was followed with a 9 µm diamond suspension polishing for 6 min on a polymer abrasive disk. Afterwards, the polishing was continued with 1 µm diamond suspension for 4 min on a finer polymer acrylic brush disk. Finally, the polishing was finished with a 0.2 µm silicate solution for 2 min on a foam pad. The mirror finish disks were electrochemically polished in perchloric acid for 5 min, before anodizing the polished metal. The sequence was followed, as recommended by Buehler.

Electrochemical polishing of Aluminum. In this process the Al surface is removed by field-assisted electrochemical dissolution in strong acids, under constant *U*, using a Pt electrode as a cathode. The sole purpose of this step is to make the metal as smooth and uniform as possible by rapid Al metal dissolution, improving the uniformity and lowering the surface roughness. 4 Al plates (squares 25 x 25 x 0.5 mm) were washed with Ethanol and inserted in a 4-hole Teflon chamber with a Cu base. The polishing solution made from concentrated H_3PO_4/H_2SO_4 acids was added: 250 g of H_2O, 250 g of 85% H_3PO_4 and 250 g

of H_2SO_4. The chamber was warmed to 70°C. A Pt wire as an anode mounted on a Teflon chamber cover was installed and a constant voltage of 25 V was applied. The electrochemical dissolution of Al was continued until the surface became reflective, such that the first layer of impurities was removed (3-5 min). The acid solution was changed and the polishing continued until the surface reflectivity and surface was as close to "mirror-like" as possible (15-20 min). The Al plates were removed and left in 5 vol. % H_3PO_4 solution until the white Al_2O_3 thin-film was dissolved (30-60 min). The Al plates were then electrochemically polished with perchloric acid in an identical Teflon chamber, but that is solely dedicated to perchloric acid polishing. Polishing chambers must not be mixed: this will contaminate both types of electrochemical polishing and generate deep surface pits and grains that cannot be removed. A 1:4 *v/v* perchloric acid: *p.a.* ethanol solution was poured in the anodization chamber, cooled to near 0°C on ice, under stirring attached to the chamber cover (with cathode Pt wire). For 5 min, a 20 V current was applied to the plates. The solution was changed, cooled, the rotation reversed and the Al electrochemically polished at 25 V for another 5 min. The process further smoothens out visible surface inhomogeneities.

AAO membrane growth. In a typical procedure, the electrochemically polished Al plates were assembled in a plastic anodization chamber, which is harder than Teflon and provides a tighter seal. For $\lambda_{C\text{-}C}$ = 100 nm, 0.3 M oxalic acid was cooled under stirring at 1.0°C on a cooling block equipped with a Peltier element. A first anodization was carried out for 2-3 hr to pre-texture the surface. The oxide layer was removed using 5 *vol.*% H_3PO_4 solution over 2-3 hrs and the samples are verified frequently to ensure that only the Al metal remains and no white oxide film is visible upon sample drying. If the samples are left for longer times in the acid, amorphous oxide forms and the samples must then be re-polished. The anodization was repeated under the same conditions for a controlled amount of time, which determines the AAO thickness, typically 90 min provides a sample 3.5 μm thick. Following the established porosity rule of 10%[4]; AAO produced in 0.3 M oxalic acid at 40 V gives $\lambda_{C\text{-}C} \approx$ 100 nm and $d_0 \approx$ 25 nm. The following anodization conditions have been used in this work:

AAO with lattice constant 100 nm: 0.3 M oxalic acid, 40 V, 1.0°C; growth ~2.5 μm/hr.

AAO with lattice constant of 60 nm: 0.3 M H_2SO_4, 25 V, 1.0°C; ~2 μm/hr

AAO with lattice constant of ~150 nm: 0.3 M oxalic acid, 60 V, 1.0°C; ~9 μm/hr.

AAO with lattice constant of ~180 nm: 0.05 M oxalic acid, 80 V, 1.0°C; ~10 μm/hr.

2.1.3. Mounting AAO Thin-Films on Solid Supports

AAO mounting for optical waveguiding. The AAO was surrounded with thin 1 mm thick strips of double sided mirror-mounting tape from Tesa (Hamburg, Germany). The Al plate was placed AAO-side towards a glass slide such that the tape provided a 1 mm gap. Lines were drawn on the reverse of the Al disk to delimit the AAO-Al boundary. The periphery of the Al disk was then covered with fast curing 2 min. epoxy UHU (Bühl, Germany) up to the estimated boundary line, as well as the gap between the glass and the disk. This produces a seal that protects the AAO from the etching solution, used to dissolve the Aluminum metal. Therefore part of the AAO has to be sacrificed such that it remains partly attached to the Al metal, providing a support that will allow the AAO membrane to remain free-standing. Once the epoxy was cured (1-2 hr), the substrate was immersed in a $CuCl_2$ solution (Sigma Aldrich, St-Louis, MO, USA) (8.5 g of $CuCl_2$, 250 mL of H_2O and 250 mL of 37 M HCl). The solution was cooled in a glass petri dish on ice (1-5°C). The reaction was left to proceed, during which the Cu metal formed was removed by gently flowing continuously the solution across the surface with a Pasteur pipet. The Al metal removal is catalyzed by *in-situ* oxidation-reduction reactions where $Al^0 \rightarrow Al^{3+}$ and $Cu^+ \rightarrow Cu^0$. At this stage, an inadequate level of dexterity will result in rupture of the AAO membrane. AAO membranes below 1 μm in thickness can only be achieved over no more than a few mm^2. After some of the alumina became visible, the sample was transferred to a fresh $CuCl_2$ solution and ethanol was added to reduce the surface tension of the solution, preventing bubbles from rupturing the thin membrane. Once a sufficiently large area had its Al metal removed, the slide was dipped in deionized water and then carefully rinsed with water and *p.a.* ethanol and dried under a slow N_2 stream towards one single direction, in such a way that the AAO barrier layer remained free of drying stains. These stains are due to remaining electrolyte salts, and will prevent proper Cr/Au adhesion. The metal layer may thus not act as an ideal waveguide mode selector: weak and/or distorted waveguide modes are hence observed. Large pieces of the AAO were removed and placed on a glass slide, with the tips of the AAO pieces held under a piece of vacuum-safe tape (3M, USA). The AAO on the slide were O_2 plasma cleaned for 2 min. 2 nm of Cr and 25 nm of Au are then evaporated onto the AAO barrier-side. 3 drops of UV-curable optical adhesive (NOA 83H) were dissolved in 1 mL of THF, from Norland Products (Cranbury, NJ, USA) was spin-coated on a LaSFN9 glass slide. A large enough (5 mm diameter) AAO template piece was carefully broken off from the main piece with sharp tweezers (as used for TEM grids) and meticulously deposited, gold side towards the glue, in order to avoid air bubble formation

between the AAO and the adhesive. 5-10 waveguide substrates can typically be prepared from a 20 mm diameter AAO piece.

Pore widening of AAO. All anodizations of Al metal produce AAO with ~10% porosity. Pore diameters ranging from the native oxide diameter to about 80-90% of the lattice constant can be achieved by slow dissolution of the oxide in 5% *vol.* H_3PO_4 (Merck, USA), prepared using a volumetric flask to ensure reproducible concentrations. The pore widening occurs at ~0.75 nm/min. For AAO anodized at 40 V in oxalic acid, Eq. (2.2) is used to estimate the final pore diameter; where d_0 is the enlarged pore diameter and t is time in min.

$$d_0 \approx (0.75 \cdot t + 25)\ \text{nm} \qquad \text{equation (2.2)}$$

Before pore widening, samples were immersed in *p.a.* Ethanol and left under vacuum for 1-2 min to remove any air that may have remained trapped within the pores. The samples were then immersed in the 5% H_3PO_4 solution to the desired $d_{native} < d_0 < \lambda_{C\text{-}C}$.

2.1.4. Preparation of AAO from Sputtered Al Thin-Films on LaSFN9 Glass

LaSFN9 glass substrates (Hellma Optik, GMbH) were ultrasonically cleaned in 2 vol. % Hellmanex solution (Hellma Optik, GMbH) followed by a final rinse in absolute ethanol. The metal layer, used to generate the AAO film was formed by first depositing a 3 nm Cr film onto the substrate, followed by 1 μm Al (99.999% Alfa Aesar). The Al metal was deposited by electron beam evaporation (Edwards, Auto306). Cr was deposited by thermal evaporation (R-DEC Co., Ltd., Japan). To generate AAO, the Al films were anodized by connecting the edges of the substrate with conductive Cu tape (1 mm wide) and covering these conductive parts with nail polish to protect them from the solution such that only the Al surface was conductive. The sample was then placed in a beaker of 0.3 M oxalic acid solution at 2-5 °C opposite a Pt mesh counter electrode. The Al was anodized at a constant potential of 40 V. After about 30 min, the anodization was complete and a laser was used to estimate when the transmitted intensity was sufficiently large such that only about 20-30 nm of Al remained beneath the AAO. The laser beam intensity was only allowed to increase to 5% of the maximum value, measured without the substrate in the laser path. After complete anodization, the pores were widened by immersing the samples in 5 *wt. %* H_3PO_4 for an allotted amount of time. Such substrates were then mounted for OWS studies. Its important to mention that high quality Al metal films cannot typically exceed 10^2-10^3 nm in thickness and thus, 1 μm Al films will typically produce a 1.4 μm thick AAO. When a two step

anodization is performed to increase the order of the second AAO layer, as is the case for the samples used in the chapters 3 and 4, the final AAO thickness is decreased to below 0.8-1.0 μm. The process of pore initiation on vacuum deposited Al is identical to that of bulk Al. More recent methods of depositing thicker Al films by electrochemical deposition methods could be explored as a useful alternative to vacuum deposition and to produce much thicker AAO films by Al surface anodization.

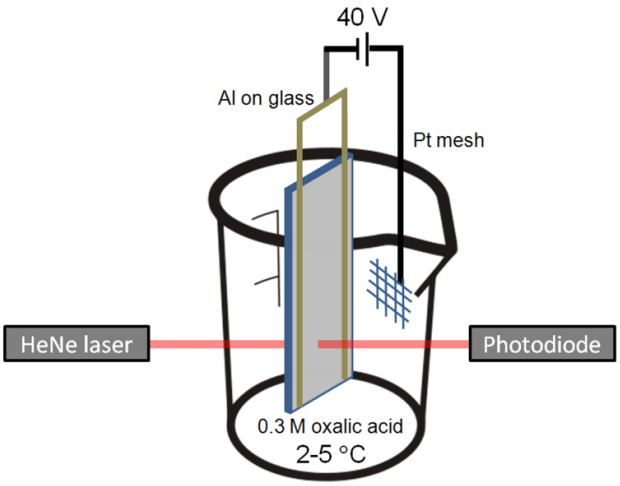

Figure 2.4. Anodization of Al metal on glass slides. The final Al layer thickness is controlled by a laser photodiode measuring the laser light (633 nm) transmission passing across the glass/Al/AAO structure.

2.2. AAO Dielectric Constant: Effective Medium Theory Approximation

Porous materials can essentially be considered as materials composed of different discrete domains that may appear as distinct at the nanoscale, but that are effectively homogeneous when observed at larger length scales, such as when probed with light of visible wavelengths. For domain sizes that are smaller than the scattering limit of the incident radiation (~1/10 λ_{light}), the porous material is effectively continuous with a dielectric response (ε) that is related to some average value lying in between the dielectric properties of its micro-phases. The dielectric response should therefore be a function of the microdomain volume fraction and the spatial arrangement and shape of these domains. The optical properties of different nanostructured materials have been studied by effective medium theory (EMT) approximations of their dielectric constants. These include polymer nanorod arrays,[21] nanocrystalline TiO_2 films,[22] Block-copolymer self-assembled thin-films[23-24] and nanoporous anodic aluminum oxide,[25-28] which is presented here. An EMT approach approximates the dielectric constant ($\varepsilon = n^2$) of optically transparent materials,[29] such that their properties and optical response can be characterized by optical measurements. In its simplest form, a direct EMT approximation of a porous material's

effective dielectric response ($\varepsilon_{\text{effective}}$) can be a weighted average of the individual properties of the materials 1 and 2 that compose the porous material, described by: $\varepsilon_{\text{effective}} = \varepsilon_1 \cdot f_1 + \varepsilon_2 \cdot (1 - f_1)$, where $\varepsilon_{1,2}$ is the dielectric response of materials 1 or 2, and f_1 is the f_{pore} of material 1. The AAO anisotropy requires a more refined EMT approach.

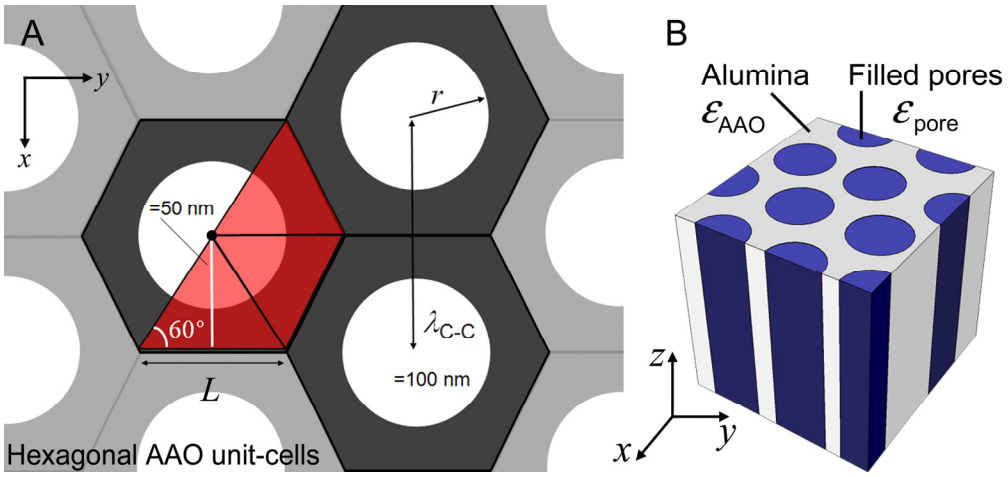

Figure 2.6. (**A**) AAO unit-cell and pertinent dimensions used to estimate porosity: pore radius (r), lattice constant ($\lambda_{\text{C-C}}$ = 100 nm). (**B**) Schematic of domains embedded in a matrix for AAO.

The 3D volume fraction of AAO is equal to the 2D pore fraction (f_{pore}) since the pores are cylindrical. For AAO with hexagonal unit cells, shown in figure 2.6A, the pore fraction (f_{pore}) is the ratio of the pore area (A_{pore}) to the unit cell area (A_{Hexagon}):

$$f_{\text{pore}} = A_{\text{pore}} / A_{\text{Hexagon}} \qquad \text{equation (2.4)}$$

where A_{pore} is simply the area of a circle given by the pore radius (r) as:

$$A_{\text{pore}} = \pi R_{\text{pore}}^2 \qquad \text{equation (2.5)}$$

and A_{Hexagon} is the area of the unit-cell:

$$A_{\text{Hexagon}} = \frac{3\sqrt{3}}{2} L_{\text{apex}}^2, \qquad \text{equation (2.6)}$$

where the unit-cell side dimension L_{apex} is obtained using from the known inner 60° angle formed by the unit cell apexes and $\lambda_{\text{C-C}}/2$ = 50 nm for the length of the bisecting line going from the center of the pore to the edge of the hexagonal unit-cell:

$$L_{\text{apex}} = \frac{50\ \text{nm}}{\sin(60^\circ)}. \qquad \text{equation (2.7)}$$

A more refined EMT approach can be applied to analyzing the dielectric properties of AAO,[25-26] as well as phase separated and nano morphologies.[23-24, 30-31] The Maxwell-Garnett

(MG) formula[29, 32-33] derives the $\varepsilon_{effective}$ based on the microscopic properties of porous materials. MG was derived from the Clausius-Mossotti relation,[32, 34] by considering the polarizability of a macroscopically small but atomically large inclusion (*i.e.* the nanodomain) in the presence of an external field:[32, 34] For AAO, the nanodomains are the cylindrical nanopores.

$$\frac{\varepsilon_{effective}-\varepsilon_{matrix}}{\varepsilon_{matrix}+\left(\varepsilon_{effective}-\varepsilon_{matrix}\right)\cdot P}=f_{domain}\frac{\varepsilon_{domain}-\varepsilon_{matrix}}{\varepsilon_{matrix}+\left(\varepsilon_{domain}-\varepsilon_{matrix}\right)\cdot P} \qquad \text{equation (2.8a)}$$

$$\varepsilon_{effective}=\varepsilon_{matrix}\frac{\varepsilon_{matrix}+\left(f_{domain}+f_{matrix}\cdot P\right)\cdot\left(\varepsilon_{domain}-\varepsilon_{matrix}\right)}{\varepsilon_{matrix}+f_{matrix}\cdot\left(\varepsilon_{domain}-\varepsilon_{matrix}\right)\cdot P} \qquad \text{equation (2.8b)}$$

where nanodomains with ε_{domain}, occupy a volume fraction f_{domain}, and are embedded in material considered to be a continuous matrix (ε_{matrix}). The pore volume fraction is therefore $f_{domain} = 1 - f_{matrix}$. The depolarization factor (P) is a parameter that biases $\varepsilon_{effective}$ based on the shape and orientation of the nanodomains ($0 \leq P \leq 1$),[35] the details of which are discussed further. For porous materials, the nanodomains are considered as pores, but for other materials the nanodomains may be a second material embedded into another, such a phase-separated block-copolymer blend, or an array of free-standing nanorods.

Eq. (2.8b) expresses the effective dielectric response of a nanostructured optically transparent material. If certain parameters can be determined, such as P and f_{domain}, by scanning electron microscopy techniques for example, then the changes of $\varepsilon_{effective}$ can be used to deduce and calculate nanostructural dimensions and physical changes such as molecular deposition or physical loss of material. In the case of cylindrical domains it has been determined that $P_x = P_y = 0.5$, while $P_z = 0$.[36-38]

Table 2.1. Depolarization factors (P) along principle axes of an optically transparent nanostructured thin-film.

	P_x	P_y	P_z	$\sum_i (P_i)$
Orientation to E field	Perpendicular	Perpendicular	Parallel	**1**
Cylindrical parallel domains perpendicular to surface.	**1/2**	**1/2**	**0**	**1**
Isotropic spherical domains	**1/3**	**1/3**	**1/3**	**1**

Therefore $\varepsilon_{effective}$ in the x- and y-directions, *i.e.* $\varepsilon_x = \varepsilon_y$, is given from eq. (2.8b) when $P_x = P_y = 0.5$. Solving eq. (2.8b) for $P_z = 0$ provides $\varepsilon_{effective}$ in the z-direction. In figure 2.7A, the pore fraction is given as a function of pore diameter for an hexagonally packed array of

nanopores with $\lambda_{C\text{-}C}$ = 100 nm. From these porosity values the effective dielectric constants were calculated, $\varepsilon_x = \varepsilon_y$ and ε_z, and are shown in figure 2.7B as a function of pore diameter. The dielectric function of Al_2O_3 (ε_{matrix}) in eq. (2.8), was taken as ε_{matrix} = 2.68, previously shown.[25-26, 28]

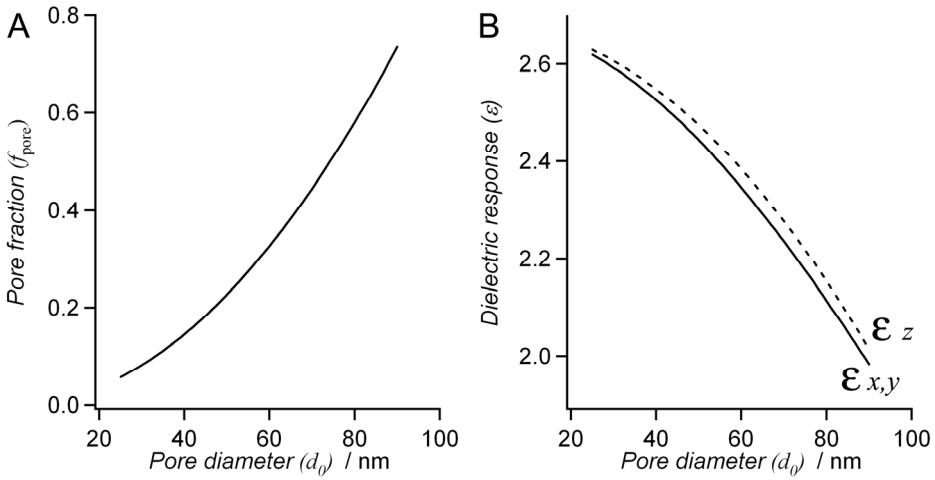

Figure 2.7. (**A**) Pore fraction as a function of AAO pore diameter (d_0) for $\lambda_{C\text{-}C}$ = 100 nm, following eq. (2.4-2.6) using $\varepsilon_{Al_2O_3}$ = 2.68. (**B**) The anisotropic dielectric responses estimated for AAO in water as a function of pore diameter ($\lambda_{C\text{-}C}$ = 100 nm), eq. (2.8b).

When adsorption of molecular species takes place within the interior-surface of the cylindrical nanopores, such as a functionalized silane monolayer or adsorbed proteins, the overall refractive index of the pore interior increases because these molecular species have a higher refractive index than the buffer or air that is displaced. The organic layer thickness ($t_{organic}$) is then related to the fraction of organic material ($f_{deposited\ material}$) and the initial pore diameter under the assumption that the organic film formed a conformal layer on the inner-pore surface:

$$t_{organic} = \frac{d_{pore}}{2}\left(1 - \sqrt{1 - f_{deposited\ material}}\right). \qquad \text{equation (2.9)}$$

The dielectric response for the pore-interior ($\varepsilon_{effective}^{pore}$) can be approximated by an EMT approach that consists in applying the MG equations (eq. (2.8b)) to the two component system in the cylindrical pores consisting of the empty part (buffer) and the adsorbed material, as described in eq. (2.10).

$$\varepsilon_{effective}^{pore} = \varepsilon_{unfilled\ pore}\frac{\varepsilon_{unfilled\ pore} + \left(f_{deposited\ material} + f_{unfilled\ pore}\cdot P\right)\cdot\left(\varepsilon_{deposited\ material} - \varepsilon_{unfilled\ pore}\right)}{\varepsilon_{unfilled\ pore} + f_{unfilled\ pore}\cdot\left(\varepsilon_{deposited\ material} - \varepsilon_{unfilled\ pore}\right)\cdot P}$$

equation (2.10)

$\varepsilon_{\text{unfilled pore}}$ is the dielectric constant of the bulk solution (buffer, $\varepsilon_{\text{buffer}}$ = 1.775), $\varepsilon_{\text{deposited material}}$ is the dielectric constant of the adsorbed material to the AAO pore-walls and $f_{\text{deposited material}}$ is the volume fraction of the deposited material which is assumed to be a conformal film of uniform thickness. $f_{\text{unfilled pore}}$ is the volume fraction of the remaining void volume (*i.e.* 1-$f_{\text{deposited material}}$). Recursively applying eq. (2.10), using $\varepsilon_{\text{effective}}^{\text{pore}}$ (eq. (2.10)) to describe the increased dielectric constant of the pores after molecular adsorption, provides an effective dielectric constant for the entire AAO film ($\varepsilon_{\text{effective}}^{\text{AAO film}}$) as given by eq. (2.11), where P=0.5 describes ε_x and ε_y, while for ε_z, P=0.

$$\varepsilon_{\text{effective}}^{\text{AAO film}} = \varepsilon_{Al_2O_3} \frac{\varepsilon_{Al_2O_3} + \left(f_{\text{pore}} + f_{Al_2O_3} \cdot P\right) \cdot \left(\varepsilon_{\text{effective}}^{\text{pore}} - \varepsilon_{Al_2O_3}\right)}{\varepsilon_{Al_2O_3} + f_{Al_2O_3} \cdot \left(\varepsilon_{\text{effective}}^{\text{pore}} - \varepsilon_{Al_2O_3}\right) \cdot P} \qquad \text{equation (2.11)}$$

When the deposited material layer thickness (t) increases because of molecular adsorption, the volume fraction of the deposited material also increases. In figure 2.8A, the effective dielectric constant of the AAO membrane as a function of the deposited layer thickness is shown (eq. (2.9-2.11)).

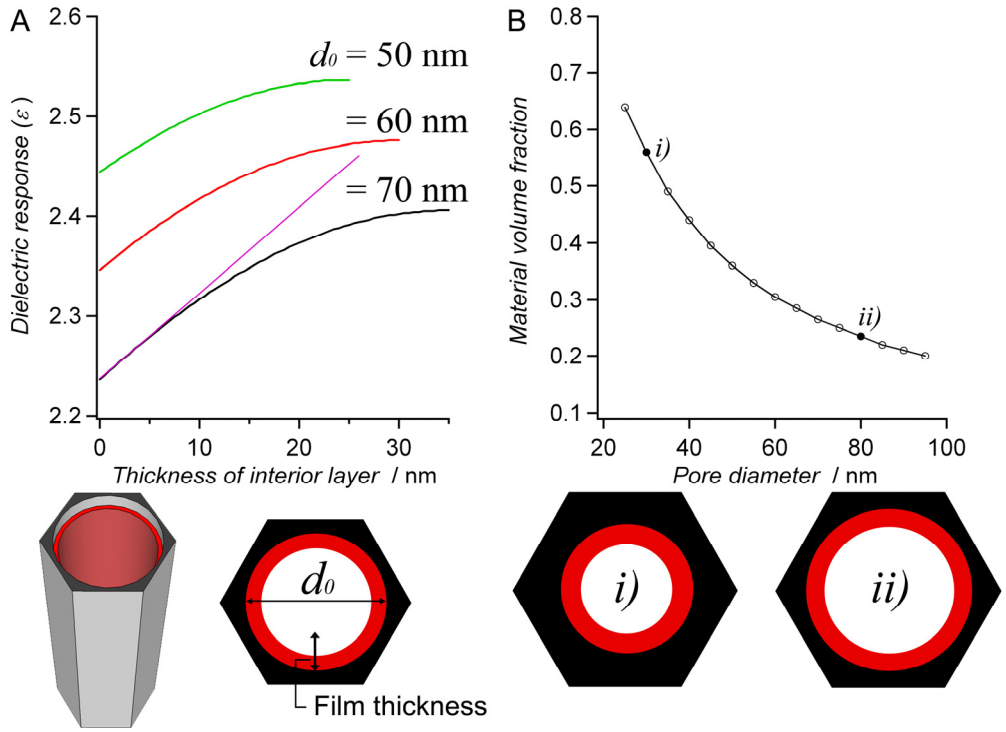

Figure 2.8. (**A**) Dielectric constant ($\varepsilon_{x,y}$) of AAO when a material (ε = 2.1) deposits uniformly within the entire depth of the cylindrical nanopores: thicknesses ranging from empty pores (t = 0 nm) until the pores are completely filled (t = d_0/2). Below: schematic of the hexagonal unit cell of the cylindrical AAO nanopores being filled with a uniform film with thickness t. A 3D schematic is shown to illustrate the uniform conformal layer that is assumed for the deposited material. (**B**) Volume fraction occupied in AAO having different d_0 by a 5 nm film of material deposited on the pore-walls.

As a consequence of the non-linearity of the dielectric constant with respect to the deposited thickness, the observed kinetics are only valid for the first deposited 5-8 nm. However, if the film thickness is built in by a Layer-by-Layer fashion, the recorded kinetics of each step, recorded individually, are approximately valid if each deposited layer as an optical thickness $t < 5$ nm.

The volume fraction occupied by deposited material is an important consideration. Typically, molecules or macromolecules are deposited within the AAO pores, forming 0.5-10 nm thick films. The ratio of particle size to pore diameter can be used to estimate at which point steric hindrance becomes a dominant factor, especially for $d_0 < 100$ nm. In figure 2.8B, as the pore diameter increases, the volume fraction occupied by a 5 nm thick film ($\varepsilon = 2.1$) is approximately 25% for $d_0 = 65$-80 nm, while this values increases over 60% for pore $d_0 < 30$ nm. This is of significant importance for steric effects that can hinder the macrolecular transport within the pore-interior; if the volume fraction occupied by a layer of macromolecules is sufficiently large, transport of further protein along the vertical z-axis of the nanopores can become sterically hindered or even inhibited.

For larger pores, $d_0 > 50$ nm, the kinetics are linearly proportional to the dielectric response variation up to $t = 5$-8 nm (figure 2.8A), in terms of optical thickness (not equal to actual protein thickness). The kinetics therefore do not need to be corrected for molecular adsorption (peptides, fluorophores, small molecules) or even macromolecular adsorption (proteins, polyelectrolytes, nanoparticles) in larger AAO pores. The optical thickness obtained from the EMT approach follows the assumption that the deposited film is homogeneous and contiguous. In reality, deposited films, especially for macromolecules such as proteins, are not dense homogeneous layers and therefore will typically give rise to lower measured film thicknesses than the actual macromolecular dimensions.

As discussed previously, AAO produced from annealed Al metal plates grows highly ordered with a lattice constant approaching the ideal C-C = 100-105 nm. However, AAO grown from as received Al metal plates exhibits a lower degree of order and translates into an overall lower value of C-C = 90 nm. This is clearly observed during the pore-widening process, where the AAO from annealed Al can be pore-widened for a significantly longer period of time (maximum 80-85 min), in comparison to non-annealed AAO (maximum ~ 65-70 min), to obtain 10-15 nm larger pore diameters, before the entire AAO structure is excessively dissolved leading to complete loss of waveguide properties.

Table 2.2. Dielectric constant of AAO grown from annealed and non-annealed Al metal.

	Non-Annealed AAO			Annealed AAO		
Pore-widening time (min)	$\varepsilon_{x,y}$	***Estimated diameter, EMT*** (nm)	***Pore diameter SEM*** (nm)	$\varepsilon_{x,y}$	***Estimated diameter, EMT*** (nm)	***Pore diameter SEM*** (nm)
0	2.58	20	19 ± 5	2.61	25	24 ± 4
10	2.53	35				
15	2.51	39	35 ± 6	2.57	33	
25	2.44	46	43 ± 5	2.49	44	
35	2.34	55	50 ± 7	2.42	52	50 ± 5
45	2.24	63	61 ± 5	2.39	56	58 ± 6
55	2.12	71				
60				2.17	71	72 ± 8
65	2.00	80				
70	1.88	85				

Optical waveguide TM-spectra of AAO substrates after different pore-widening duration, obtained from annealed Al, show that the waveguiding properties are lost after about 85 min where pore-interpenetration occurs and leads to structural failure. For example, after 35 min pore-widening, the highly ordered AAO has ε_x = 2.41 in buffer, while the non-annealed sample was determined to have ε_x = 2.34. Because the $\lambda_{C\text{-}C}$ is slightly smaller in non-annealed samples, the pore-fraction is slightly higher and ε is accordingly lower, for the same pore diameter. SEM analysis of the interpore spacing gave a value of $\lambda_{C\text{-}C}$ = 93 ± 8 nm for the AAO obtained from non-annealed metal, while the AAO from annealed Al had $\lambda_{C\text{-}C}$ = 98 ± 5 nm. If the proper value of $\lambda_{C\text{-}C}$ is not selected, this differences causes ~10% error when evaluating pore diameter sizes using EMT. The dielectric constants determined at different anodization times, as well as d_0 evaluated from EMT, are shown in Table 2.2.

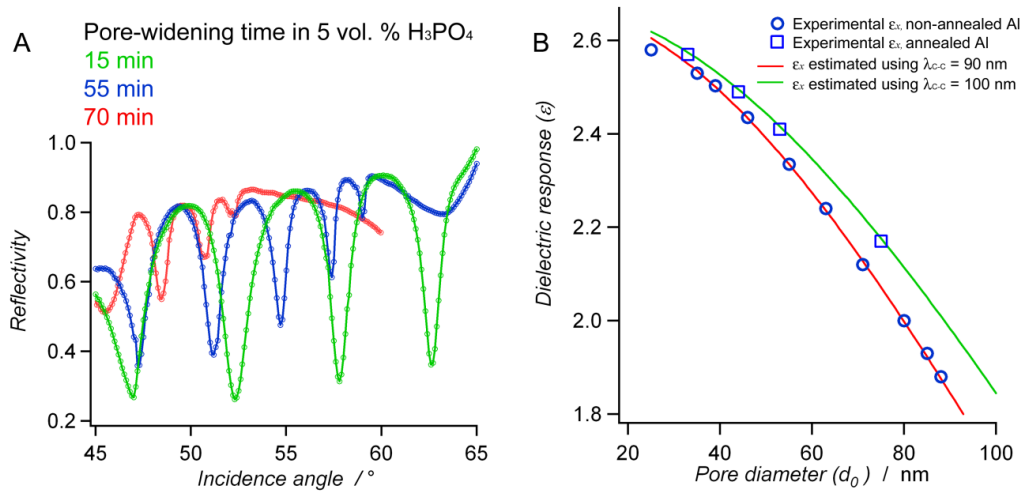

Figure 2.9. (**A**) OWS TM-polarization spectra of AAO pore-widened for different times; AAO from non-annealed metal. (**B**) Measured values of ε_x for non-annealed and annealed AAO for samples pore-widened for different times (Table 2.2). Also shown is the EMT approximation in water of ε_x using either $\lambda_{C\text{-}C}$ = 90 or 100 nm. AAO from annealed Al metal is highly ordered and better agrees if $\lambda_{C\text{-}C}$ = 100 nm is assumed.

2.3. Total Internal Reflection Techniques

Maxwell's equations can be used to describe the transmission, reflection and absorption of light at the interface between two optically transparent media.

$$\nabla \times \mathbf{H} = \frac{\partial D}{\partial t} \qquad \nabla \times \mathbf{E} = -\frac{\partial B}{\partial t} \qquad \text{equation (2.12)}$$

$$\nabla \cdot \mathbf{H} = 0 \qquad \nabla \cdot \mathbf{E} = 0 \qquad \text{equation (2.13)}$$

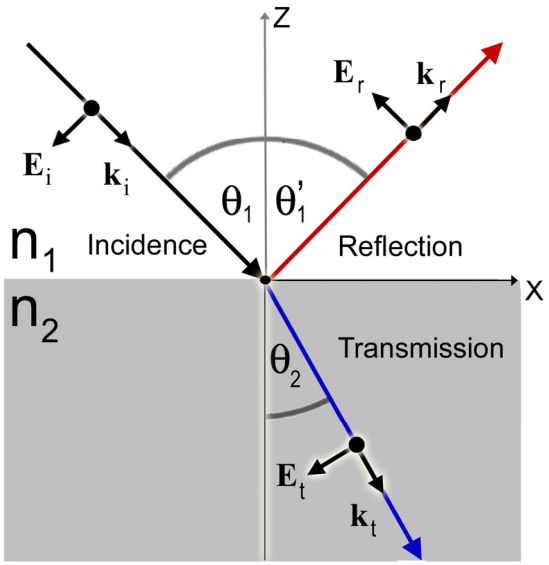

Figure 2.10. Reflection and transmission of p-polarized light at the interface between two optically transparent media, $n_2 > n_1$. Plane of incidence is the *x*-*z* plane and **H** is polarized perpendicular to it (TM). Subscripts *i* refer to incidence, *r* refer to reflected and *t* refers to transmitted.

The electric field and magnetic field, represented by **E** and **H** respectively, are related to an electric displacement **D** and magnetic flux density **B**:

$$\mathbf{D} = \varepsilon\varepsilon_0\mathbf{E} \qquad \text{equation (2.14)}$$

$$\mathbf{B} = \mu\mu_0\mathbf{H} \qquad \text{equation (2.15)}$$

where ε is the relative dielectric constant of the material and ε_0 is the dielectric constant of vacuum, while μ and μ_0 are the relative magnetic susceptibility and its value in vacuum, respectively. Propagating electromagnetic waves can be expressed as:

$$\mathbf{E} = \mathrm{E}_0\, e^{i(\mathbf{kr}-\omega t)} \qquad \mathbf{H} = \mathrm{H}_0\, e^{i(\mathbf{kr}-\omega t)} \qquad \text{equation (2.16)}$$

where E_0 and H_0 are the electric field and magnetic field amplitudes, respectively, while **k** is the wavevector, **r** is the position vector, ω is radiation's angular frequency and t is time. The frequency as a function of **k** in optical media, typically referred to as the dispersion relation, can be expressed as:

$$\frac{\omega^2}{|\mathbf{k}|^2} = \frac{1}{\mu\mu_0\varepsilon\varepsilon_0} \qquad \text{equation (2.17)}$$

where the amplitude of the wavevector is represented by:

$$|\mathbf{k}| = \frac{\omega}{c}\sqrt{\varepsilon}, \qquad \text{equation (2.18)}$$

$c = 1/\sqrt{\mu_0\varepsilon_0}$ being the velocity of light in vacuum.

Transverse magnetic- (TM-) or p-polarized light corresponds to the magnetic field being polarized perpendicular to the plane of incidence such that the components $E_z = E_x = 0$ and $H_y = 0$. Transverse electric- (TE-) or s-polarized light has electric field components perpendicular to the plane of incidence with vanishing components: $H_z = H_x = 0$ and $E_y = 0$. Reflection and transmission of light is shown in figure 2.10. Light is reflected from the surface with the same angle as that of the incidence light with the normal to the surface, such that $\theta_1' = \theta_1$. Transmitted light into a higher refractive index material follows Snell's law:

$$n_1 \sin\theta_1 = n_2 \sin\theta_2, \qquad \text{equation (2.19)}$$

where n_1 and n_2 are the refractive indices of each medium (figure 2.10). Total internal reflection (TIR) occurs when light passes through a medium 1 of refractive index n_1 and is subsequently reflected at the interface with medium 2, which is of lower refractive index n_2. If the incidence angle increases above a certain critical value $\theta_c = n_2/n_1$, only reflection occurs; all light is reflected for $\theta \geq \theta_c$. Above the critical angle, a plane wave travels along the interface between the two media and gives rise to an evanescent wave. The resulting evanescent field decays exponentially from the surface. This decay length (b) is given as a function of wavelength (λ), the refractive indices of the media (n_1, n_2) and the angle of incidence (θ):

$$b = \frac{\lambda}{2\pi}\left(\frac{n_1^2}{n_2^2}\sin^2\theta - 1\right)^{-1/2}. \qquad \text{equation (2.20)}$$

The limited size of this illumination field (< 500 nm) near the TIR interface is fundamental for a number of measurement techniques that specifically rely on having only the area near the surface being illuminated by the incident radiation.

2.3.1. Surface Plasmon Resonance Spectroscopy (SPR)

Surface plasmon resonance (SPR) spectroscopy relies on the phenomenon of attenuated total internal reflection to excite surface plasmons (SP) at the surface of a thin metal layer (Au, Ag, Cu, Cr, Al) through coupling of the evanescent wave that occurs at the total internal reflection interface. Surface plasmons (SPs) are collective oscillations of the electrons of a metal and propagate laterally at the metal-dielectric interface (figure 2.11A). Since the excitation conditions are dependent on the dielectric medium properties, changes that occur near the interface are directly detectable with subnanometer sensitivity. The ability to detect molecular events occurring at planar interfaces is the basis for surface plasmon-based biosensing[39-40] and its frequent use as a versatile surface characterization technique.

Maxwell's equations for surface plasmons therefore involve metals, which have dielectric constants with complex components:

$$\varepsilon_1 = \varepsilon_1' + i\,\varepsilon_1'' \qquad \varepsilon_2 = \varepsilon_2' + i\,\varepsilon_2'' . \qquad \text{equation (2.21)}$$

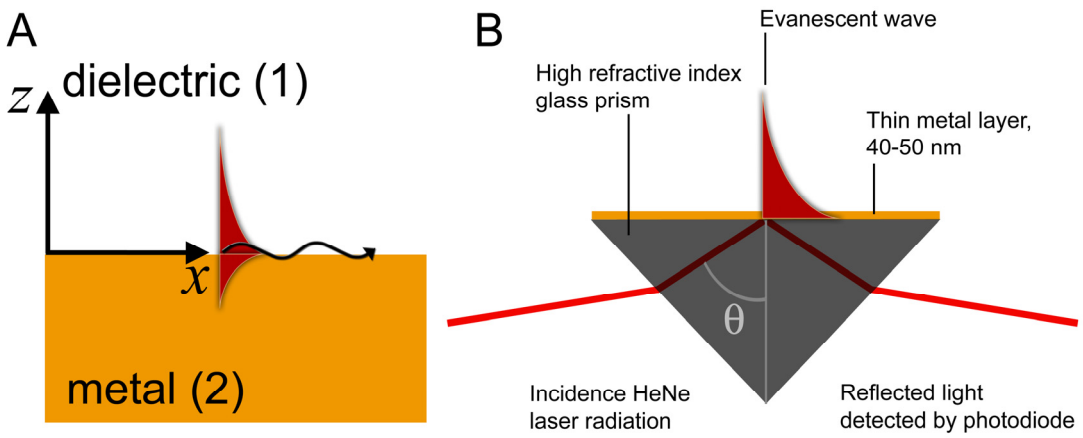

Figure 2.11. (**A**) Propagation of a SP at the metal-dielectric interface. (**B**) Attenuated total-internal reflection Kretschmann configuration used to study surface phenomena using surface plasmon resonance spectroscopy.

Dielectric media have $\varepsilon' > 0$, while metals have $\varepsilon' < 0$. The dielectric constant is related to the refractive index (n) as such: $(n + i\nu)^2 = \varepsilon_1' + i\,\varepsilon_1''$, where ν is the absorption coefficient of the material, describing the damping of the propagating EM waves because of interactions with the material. The EM surface wave propagates along the x-direction and decays exponentially into the metal (2), as well as into the dielectric (1) (figure 2.11A). The **E** and **H** field vectors that describe the exponential decay into each media are described by:

$$\mathrm{E}_{1,2} = \begin{pmatrix} E_{x_{1,2}} \\ 0 \\ E_{z_{1,2}} \end{pmatrix} e^{i\left(k_{x_{1,2}}x + k_{z_{1,2}}z - \omega t\right)} \qquad \mathrm{H}_{1,2} = \begin{pmatrix} 0 \\ H_{y_{1,2}} \\ 0 \end{pmatrix} e^{i\left(k_{x_{1,2}}x + k_{z_{1,2}}z - \omega t\right)}, \quad \text{equation (2.22)}$$

where the subscripts denote each medium, *i.e.* the metal (2) for $z \leq 0$, and the dielectric (1) for $z \geq 0$. At the interface, continuity relations imply that both field vectors **E** and **H** must satisfy the boundary conditions, where the tangential components must be continuous, as well as the normal components such that:

$$E_{\mathrm{x}_1} = E_{\mathrm{x}_2} \qquad \text{and} \qquad H_{\mathrm{y}_1} = H_{\mathrm{y}_2}. \qquad \text{equation (2.23)}$$

In which case, $k_{\mathrm{x}1} = k_{\mathrm{x}2} = k_{\mathrm{x}}$. The magnetic field components are related to the electric field as such:

$$k_{z_1} H_{y_1} - \frac{\omega}{c}\varepsilon_1 E_{x_1} = 0 \qquad k_{z_2} H_{y_2} - \frac{\omega}{c}\varepsilon_2 E_{x_2} = 0 \qquad \text{equation (2.24)}$$

which has the solution:

$$\frac{k_{z_1}}{k_{z_2}} = -\frac{\varepsilon_1}{\varepsilon_2} \qquad \text{equation (2.25)}$$

where $k_{\mathrm{z}1}$ and $k_{\mathrm{z}2}$ are positive real numbers and therefore, one of the dielectric constants of the two media must be negative to excite SPs. Metals have negative dielectric constants, which is why Au, Ag or Cu are typically used in SPR. Eq. 2.26 is described as the dispersion relation of the SPs that propagate along the metal-dielectric interface. The component of the wavevector **k** that is parallel to the surface k_{x}, can be expressed in terms of the dielectric properties of both media and essentially describes the momentum required to excite the SPs (k_{SP}):

$$k_{\mathrm{x}} = \frac{\omega}{c}\sqrt{\frac{\varepsilon_1\varepsilon_2}{\varepsilon_1 + \varepsilon_2}}. \qquad \text{equation (2.26)}$$

If we consider the dispersion relation of a free photon k_{photon} propagating in a medium with dielectric constant ε_1:

$$k_{\mathrm{photon}} = \frac{\omega}{c}\sqrt{\varepsilon_1}, \qquad \text{equation (2.27)}$$

then the momentum of the light will always be smaller than is required to excite the SP such that:

$$k_{\text{photon}} < k_{\text{SP}} . \qquad \text{equation (2.28)}$$

Because a high refractive index material can increase the wavenumber, attenuated total internal reflection method is used to excite SPs, as shown in figure 2.11B. The plasmon coupling condition (eq. (2.29)) is achieved by excitation with the evanescent field on the TIR prism surface, where the metal lies. Both the Otto and the Kretschmann configurations can be used, but for practical purposes only the Kretschmann configuration (figure 2.11B) allows chemistry to be performed on the Au surface. When incident is totally reflected at the bottom of the prism, an evanescent field occurs and excites the SPs at the metal-dielectric interface. Using a high refractive index prism makes it possible to increase the wavenumber of the incident light to reach k_{SP}. The wavenumber of light in a prism is ($\omega / c\sqrt{\varepsilon_{\text{prism}}}$) and the projection on surface is:

$$k_{\text{x}} = \frac{\omega}{c}\sqrt{\varepsilon_{\text{prism}}}\sin\theta = k_{\text{SP}} , \qquad \text{equation (2.29)}$$

where matching of the wavenumber's projection (k_{x}) ensures SP excitation. The dispersion relations are shown in figure 2.12 for a free photon propagating in either a dielectric or a prism and for SPs on a metal-dielectric interface. The figure serves to illustrate that momentum matching using a prism is required to excite SPs.

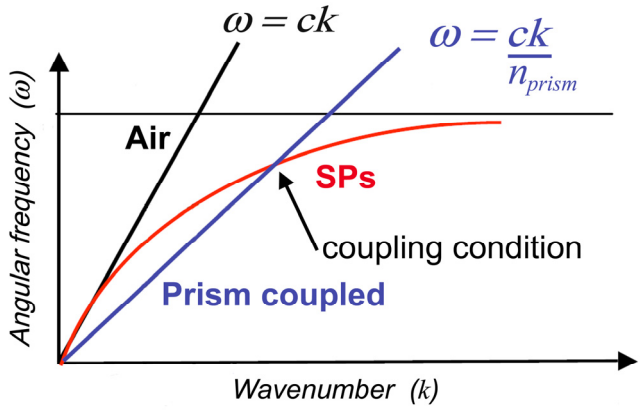

Figure 2.12. Dispersion relation of free photons in air and propagating in a coupling prism, in comparison to the dispersion relation for SPs at the metal-dielectric interface. Momentum matching only occurs with prism coupling.

Changes in the dielectric environment of the SPs, modifies the wavevector which results in a change in plasmon resonance angle θ. Adsorption and desorption of molecules to/from the surface can therefore be measured by following the resonance condition changes with time. The θ shift is proportional to the adsorbed layer thickness (d) and refractive index (n).

$$\Delta\theta \approx n \cdot d \qquad \text{equation (2.30)}$$

As shown in figure 2.13, the plasmon resonance angle shifts to higher values for a 10 nm deposited layer of a material with $\varepsilon_{\text{deposited material}}$ = 2.1. If only thickness information is required, only the angular scans before and after adsorption can be used. The Winspall program[41] has been developed for the purpose of analyzing and simulating reflectivity spectra by solving Fresnel's equations for infinite 2D films. To obtain the kinetics of an adsorption process, the reflectivity change at a specific angle is monitored as function of time, with up to 10 ms resolution. The angle is chosen before the SPR minimum, such that the adsorption process follows the linear profile of the surface plasmon reflectivity curve.

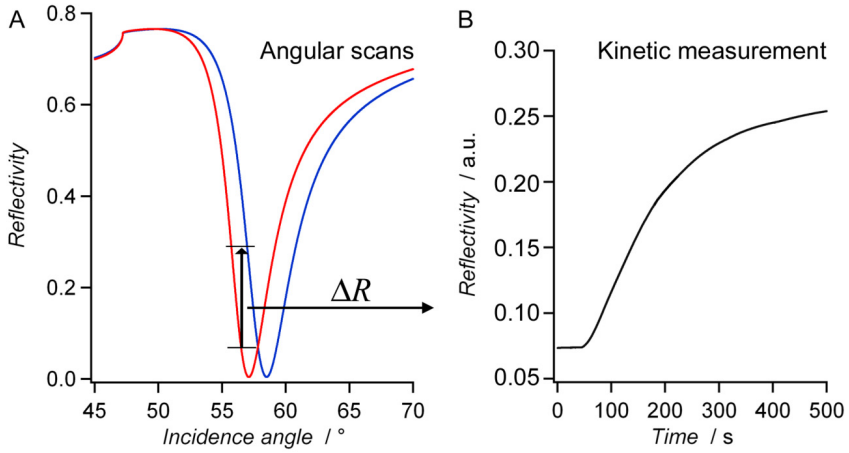

Figure 2.13. (**A**) SPR angular reflectivity spectra in buffer before and after adsorption onto a 50 nm Au film on high refractive index glass. (**B**) Kinetic adsorption measurements measured by tracking the reflectivity change as a function of time.

2.3.2. Optical Waveguide Spectroscopy (OWS)

Optical waveguide spectroscopy (OWS) is an experimental technique that is used to analyze the optical waveguide modes that are excited in a thin-film slab waveguide.[24, 42-45] A slab waveguide is a planar dielectric thin-film (layer (2)) that is surrounded by two lower refractive index cladding layers (layers: substrate (1) and bulk (3)), as depicted in figure 2.14A, such that $n_1 < n_2 > n_3$. This condition ensures that light propagates laterally within the waveguide by total internal reflection at the interfaces with the cladding media.[45-46] The method allows the independent characterization of the thickness and the dielectric constant, *i.e.* refractive index ($n = \sqrt{\varepsilon}$), of optically transparent thin-films at a chosen wavelength. The ε subscript *s* stands for substrate, *w* stands for waveguide thin-film and *b* for bulk.

The momentum of the incident radiation required for light propagation within a waveguide planar structure is described by Maxwell's equations. The waveguide mode propagation constant (ξ), together with the film thickness (h), dictate the phase matching conditions that allow light propagation. ξ depends on the dielectric constant of the waveguide film described by $\sqrt{\varepsilon}\omega/c$, which is the momentum of freely traveling light in a material with a dielectric constant ε. The ε of AAO is described in section 2.2. The light may be polarized parallel to the surface (TE), or perpendicular to the surface (TM). Similarly to SPR, different waveguide propagating modes can be represented in terms of the electric and magnetic field components, **E** and **H**. For TE modes **E** = (0, E_y, 0) or **H** = (H_x, 0, H_z) and for TM modes **E** = (E_x, 0, E_z) or **H** = (0, H_y, 0).

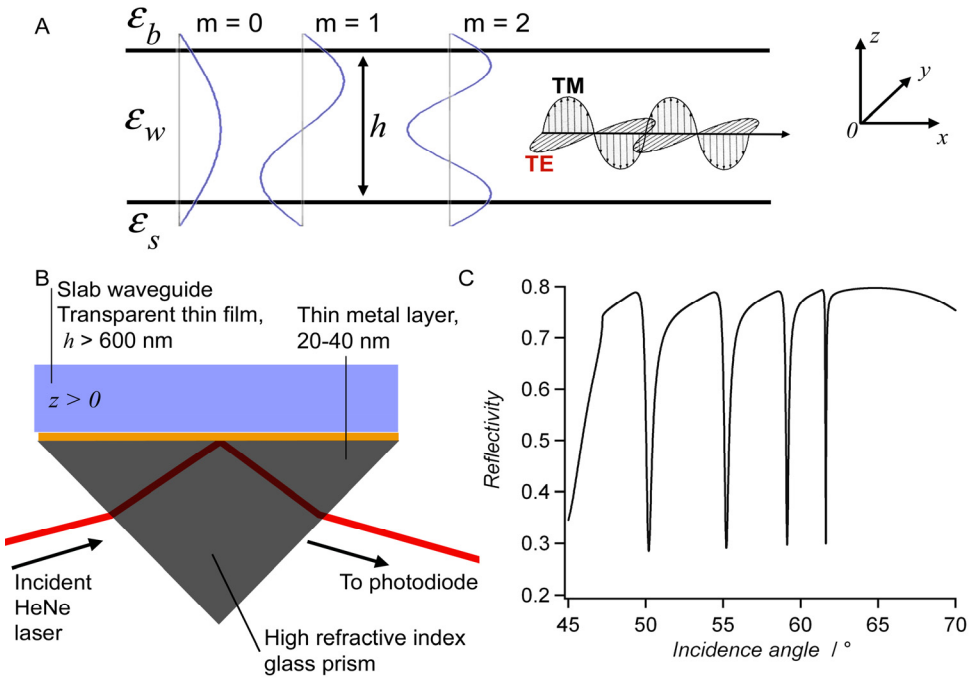

Figure 2.14. (**A**) Light propagation in a thin-film of thickness h; z = 0 is the metal-slab waveguide interface. E-field intensity of the first three modes is schematically shown. (**B**) Attenuated total-internal reflection Kretschmann configuration used for optical waveguide spectroscopy studies of slab waveguide films that are >600 nm in thickness. (**C**) Example of an OWS spectrum showing TM-modes occurring at different incidence angles for a 2 μm thick glass film (ε = 2.25) on Au.

For planar slab waveguides, the guided light is confined within a z = 0 to z = h thickness. The field solutions of the propagation modes are given by Eq. (2.31), where A stands for either E (TE modes) or H (TM modes). These solution are for the general case of a slab waveguide. At the waveguide-dielectric interfaces, the fields decay exponentially into the bulk and the substrate.

$$A_y = A_b\, e^{-\alpha_b (z-h)} \qquad \alpha_b = \sqrt{\xi^2 - \varepsilon_b\, \omega^2 / c^2} \qquad for\ z \geq h \qquad \text{equation(2.31)}$$

$$A_y = A_w \cos\left(\kappa_w z + \phi\right) \qquad \kappa_w = \sqrt{\varepsilon_w \omega^2 / c^2 - \xi^2} \qquad for\ 0 \leq z \leq h$$

$$A_y = A_s\, e^{\alpha_s z} \qquad \alpha_s = \sqrt{\xi^2 - \varepsilon_s\, \omega^2 / c^2} \qquad for\ z \leq 0$$

where subscripts *b, w* and *s* stand for bulk, waveguide and substrate, respectively. α and κ stand respectively for the decay and propagation constants in the *y*-direction, while ϕ is the phase shift and ξ is the waveguide mode propagation constant. The solutions are met when equating the fields at z=0 and z=h. The phase shift across the waveguide film thickness occurs for multiples of π.

Eq. (2.32) generally describes which waveguide mode (m) is allowed with respect to film thickness (h) and dielectric constants of the waveguide substrate and bulk, which are contained within the values of ϕ_s *and* ϕ_b that stand for the phase shifts at the substrate and bulk interfaces, respectively.

$$\kappa_w h - \phi_s - \phi_b = \mathrm{m}\pi \qquad (\mathrm{m} = 0, 1, 2, \ldots) \qquad \text{equation (2.32)}$$

For TE-modes: $\phi_s = \tan^{-1}\dfrac{\alpha_s}{\kappa_w}$ and $\phi_b = \tan^{-1}\dfrac{\alpha_b}{\kappa_w}$

For TM-modes: $\phi_s = \tan^{-1}\dfrac{\varepsilon_w}{\varepsilon_s}\dfrac{\alpha_s}{\kappa_w}$ and $\phi_b = \tan^{-1}\dfrac{\varepsilon_w}{\varepsilon_b}\dfrac{\alpha_b}{\kappa_w}$

Eq. (2.32) shows that for a certain combination of ε_w, ε_s, ε_b and h, only discrete values of the propagation constant ξ are allowed. These different ξ values (ξ_{m}) correspond to the different modes that are experimentally observed such that: $\xi_{\mathrm{m}} = \sqrt{\varepsilon} \cdot \omega / c \cdot \sin\phi_{\mathrm{m}}$. Waveguide modes are annexed according to m as such: TM_0, TM_1 … TM_n. Thicker films also give rise to a greater number of waveguide modes.

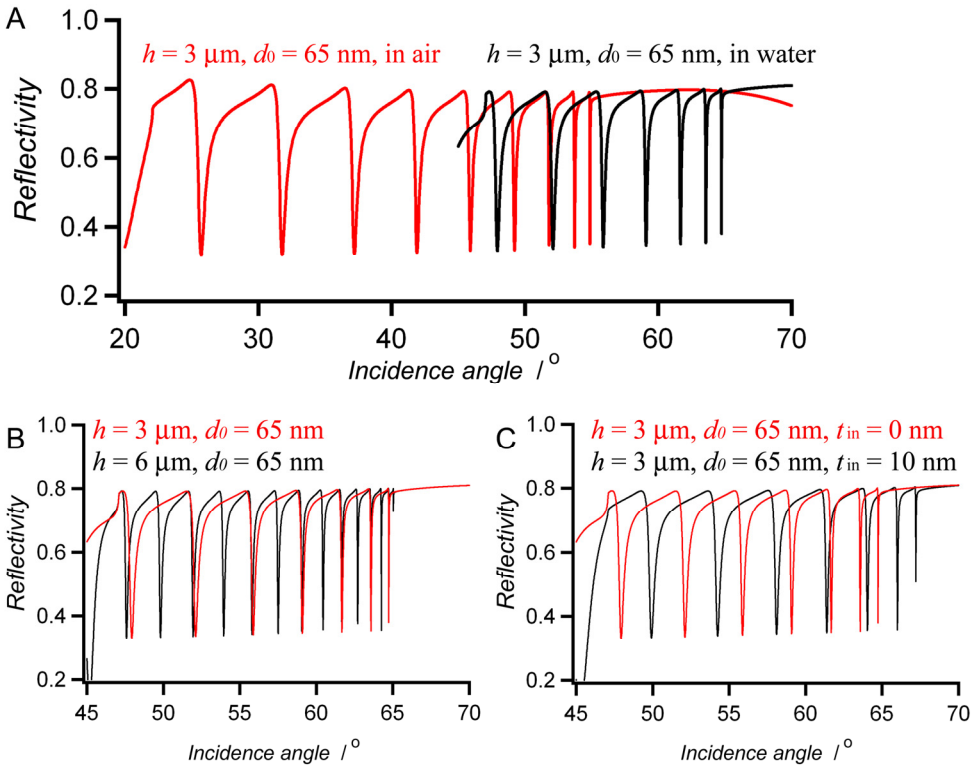

Figure 2.15. OWS TM-spectra simulations for substrates with different AAO parameters (28 nm Au coupling film). (**A**) Change in the bulk medium: air *vs* water. (**B**) Change in AAO thickness for samples at constant d_0 = 65 nm. (**C**) Difference in spectra for the adsorption of 10 nm thick film (t_{in}) on the inner AAO nanopore walls.

The OWS measurements were carried out in the Kretschmann configuration (figure 2.14B). A prism coupling device, similarly to SPR, is required to increase the momentum of the incident light in order to match the permitted values of ξ and excite the waveguide modes. A high refractive index glass prism ($\varepsilon_{prism} > \varepsilon_w$) is used to couple the incident light into the waveguide and similarly to SPR, the wavenumber's parallel projection ($k_x = k \cdot sin\theta$) of the incident light is modulated by the incidence angle θ, in the Kretschmann configuration. At specific θ values where k_x matches the waveguide propagation condition, light from the TIR evanescent field is channeled into the dielectric waveguide instead of being reflected through the use of a thin semi-transparent metal layer, 20-40 nm thick. The waveguide modes are experimentally accessed by recording the reflectivity (R) *vs* θ angular scans (figure 2.14C), where sharp dips occur at the waveguide coupling conditions $k_{prism} \cdot \sin\theta$. In most cases, the waveguide slab structure layer is assembled on a glass slide to facilitate handling and then joined to the prism using index-matching oil for OWS measurements.

The experimentally measured R *vs* θ angular scans are analyzed using Fresnel equations, solved for a multilayer systems lying atop the base of the prism. Fresnel equations are solutions to Maxwell's equations to calculate the expected reflectivity as a function of the

multilayer film composition, where each infinite 2D layer has a specific value of ε and h. The reflectivity for such a multilayer system is given by:[47-48]

$$R = \left|r_{0123\ldots q}\right|^2 = \left|\frac{r_{01} + r_{123\ldots q}\, e^{i2h_1k_1}}{1 + r_{01}\, r_{123\ldots q}\, e^{i2h_1k_1}}\right|^2 \quad ; \quad r_{ij} = \frac{n_j^{2\gamma}k_i - n_i^{2\gamma}k_j}{n_j^{2\gamma}k_i + n_i^{2\gamma}k_j} \qquad \text{equation (2.33)}$$

$$n_i \sin\theta_i = n_j \sin\theta_j \quad ; \quad k_i = \frac{\omega}{c} n_i \cos\theta_i$$

$\gamma = 0$ TE-modes

$\gamma = 1$ TM-modes

The numbered subscripts 0, 1, 2, 3… describe the multilayer systems (up to q layers) that rests on the surface of a 90° prism in the Kretschmann configuration. The prism is layer 0, while q refers to the infinite bulk layer (air or buffer). r_{ij} is the amplitude reflection coefficient between layers i and j, n is the refractive index and k is the wavevector component in z-direction. Values of ε_i and h_i can be substituted in eq. (2.33) to simulate a R *vs* θ angular scan for both TM- and TE-polarization. These simulations, carried out by Fresnel calculations, are implemented with the WINSPALL program,[41] which allows to specify parameters for individual layers of the multilayer film. The experimentally acquired OWS spectra can then be compared to the simulations in order to determine the best fitting parameters. Similar fitting procedures are used to analyze SPR spectra. The OWS measurements unambiguously provide independent values of ε and h for the dielectric thin-film slab waveguide. At least as many modes as free parameters, for each polarization, are required for a reliable fitting process (at least > 2). The actual interpolation of the thin-film nanostructure (pore diameter, porosity, etc), as well any molecular deposition processes occurring within the film are derived from interpreting the changes in the dielectric constant, using the EMT approach presented in section 2.2. Atop deposition can be modeled by simulating an additional ad-layer atop the waveguide.

2.4. Fluorescence Microscopy

Molecular fluorescence describes the emission of electromagnetic radiation from organic molecules, following their excitation to higher electronic energy levels because of the absorption of higher frequency radiation. Absorption is followed by energy losses because of internal conversion and the emitted radiation is always of longer wavelength. This process can be exploited for both high selectivity and sensitivity because the fluorescence

signal has, in principle, a zero background.[49-50] Organic fluorophores are excited and emit under visible wavelengths: λ=200-800 nm. The conjugated p-orbitals of fluorophores allow π-electrons delocalization, which lowers the transition energy required to reach excited electronic states.

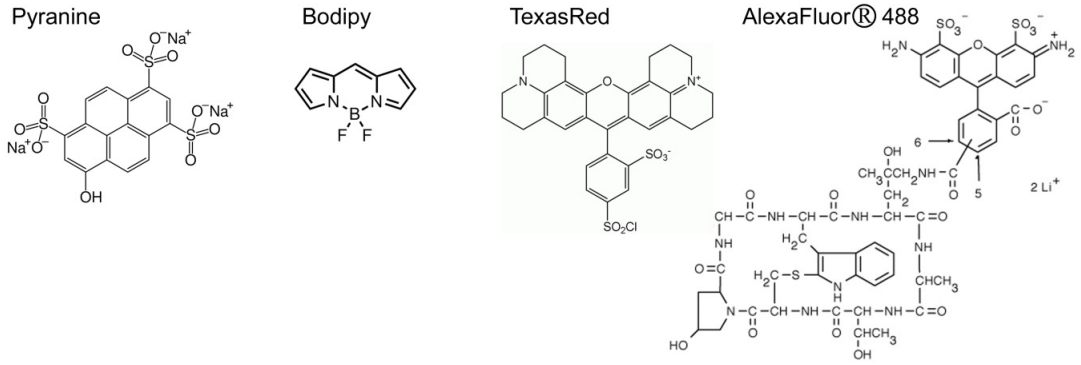

Figure 2.16. The chemical structures of the 4 molecular fluorophores used.

Electronic transitions can classically be described by the Franck-Condon principle. Compared to nuclear motion, electronic transitions occur instantaneously, without changes in the positions of fluorophore atoms. For the electronic transition to be allowed, vibrational levels of the excited state must be instantaneously compatible, with respect to both the nuclear positions and the momentum of the vibrational levels of the molecule in the ground electronic state. Consequently, excitation transitions are higher in energy than emission transitions. The Perrin-Jablonski diagram, shown in figure 2.17, summarizes the different radiative and non-radiative processes that a molecule can undergo after excitation.

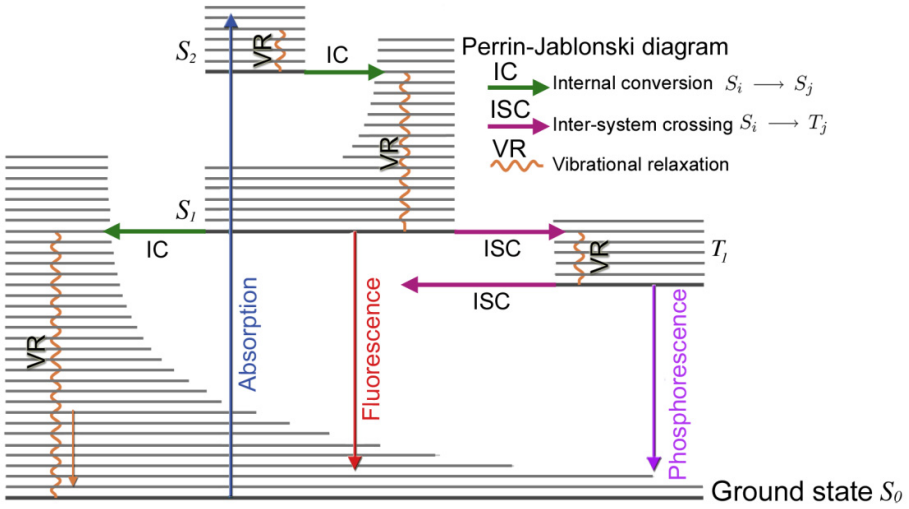

Figure 2.17. The Perrin-Jablonski diagram summarizes the radiative and non-radiative energy loss processes to return to the ground electronic state.

2.4.1. Upright Fluorescence Microscopy

Fluorescence can be used to selectively reveal and localizing underlying structural features in 3-dimensional space, within optically transparent samples, such as the plasma membranes, the cytoskeleton or the cellular nuclei of cells. Fluorescence instruments are designed to study the emission signal from fluorophores, without interference from excitation radiation. Fluorescence microscopes provide a mechanism for specimen excitation, followed by isolation of the much weaker fluorescence emission using a second filter that enables image formation on a dark background (figure 2.18A). Emission brightness can be 3-6 orders of magnitude lower than that of the illumination. The fundamental challenge is therefore to produce high-efficiency illumination of the specimen, while simultaneously capturing weak fluorescence emission that is effectively separated from the much more intense illumination band. Fluorescence set-ups include an illumination source, an excitation filter that select a single $\lambda_{emission}$, a dichromatic mirror that lets $\lambda_{emission}$ through while reflecting $\lambda_{excitation}$, an emission filter that further filters out only a narrow λ range and a detector that records the fluorescence.

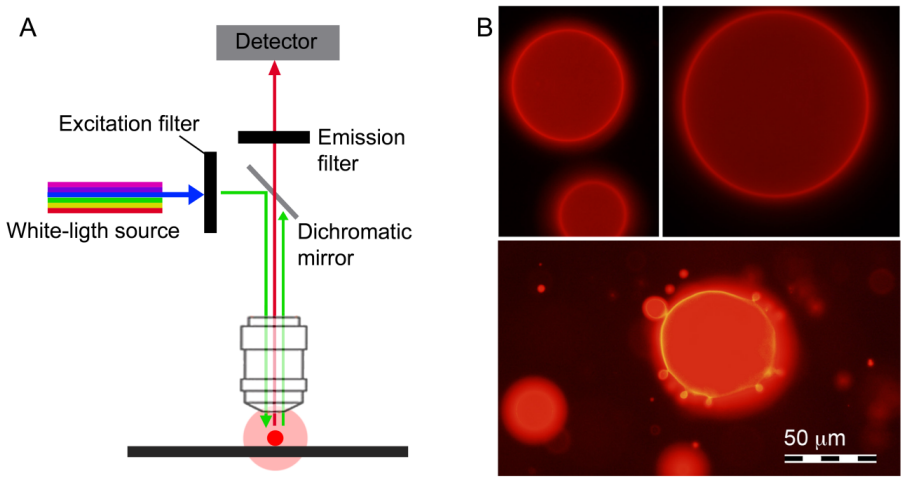

Figure 2.18. (**A**) Experimental schematic of an upright epifluorescent microscope. (**B**) Epifluorescence images of giant unilamellar vesicles made from DPhPC phospholipids doped with 1 mol % TexasRed labeled DHPE. The dye allows the visualization of the 3-dimensional vesicle. Scale bar valid for all images.

The upright epifluorescence microscope used was from Olympus Germany (Hamburg, Germany) model BX-51. The microscopy was equipped with water immersion objectives 10x (N.A.), 40x (N.A.), 100x (N.A.) magnification; 40x was used, unless noted otherwise. In Figure 2.18B, Epi-fluorescence of giant liposomes illustrates the type of samples studied. The detector records fluorescence originating from the entire vesicle and therefore the technique has low axial resolution. Traditional widefield epi-fluorescence microscope

objectives focus a wide cone of illumination over a large volume of the specimen, which is uniformly and simultaneously illuminated. A majority of the fluorescence emission directed back towards the microscope is gathered by the objective (depending upon the numerical aperture) and projected into the detector. Nevertheless, rapid sample visualization and real-time videomicroscopy (30 frames s^{-1}) make this technique useful for simple and rapid image acquisition.

2.4.2. Confocal Laser Scanning Microscopy (CLSM)

The laser illumination source in confocal microscopy is first expanded to fill the objective rear aperture, and then focused by the lens system to a very small spot at the focal plane. The size of the illumination point ranges from approximately 0.25-0.8 μm in diameter (depending on objective's N.A.) and 0.5-1.5 μm deep at the brightest intensity. Confocal spot size is determined by the microscope design, wavelength of incident laser light, objective characteristics, scanning unit settings, and the specimen.[51] The resolution in the *x*-*y* plane is on the order of the point spread function (PSF) of a confocal microscope (200 nm diameter in the *x*-*y* plane).[51] Resolution is worse in the *z*-direction because of a more diffuse PSF and is typically to 900 nm resolution at N.A.=1 for the water-immersion 63× objective used.

In CLSM, the fluorescence image is generated by scanning the focused beam across a defined area in a raster pattern, controlled by two high-speed oscillating mirrors driven by galvanometer motors in the *x*-*y* plane.[52] After each single scan along the *x*-axis, the beam is transported back to the starting point and shifted along the *y*-axis (flyback). During flyback, image information is not collected. As each scan line passes along the specimen in the lateral focal plane, fluorescence emission is collected by the objective and passed back through the confocal optical system. After leaving the scanning mirrors, the fluorescence emission passes directly through the dichromatic mirror and is focused at the detector pinhole aperture. Fluorescence emission that is passed through the pinhole aperture is converted into an analog electrical signal by the photomultiplier. The confocal image of a specimen is reconstructed, point by point, from the photomultiplier and electronics. The image itself never exists as a real image, observable through the microscope eyepieces.

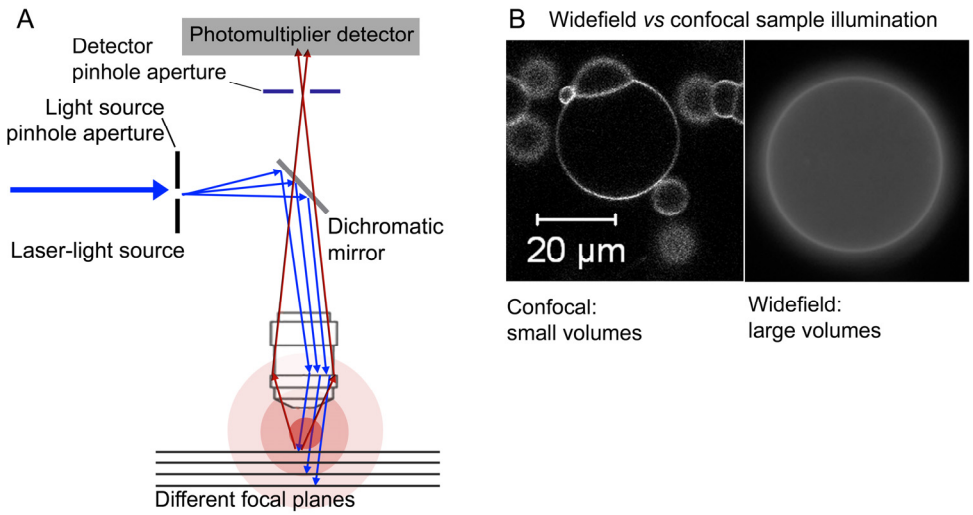

Figure 2.19. (**A**) Schematic of a confocal laser scanning microscope (CLSM). (**B**) Difference between GUV images acquired using Epi and Confocal fluorescence. Confocal collects fluorescence from small volume focal planes. Scale bar valid for both images.

A particularly useful application of confocal microscopy, termed z-stack, consists in reconstituting 3-dimensional images of samples by taking multiple single *x*-*y* focal plane images in the *z*-direction and reconstituting them into a composite 3-dimensional projection. Figure 2.20A illustrates the concept of a-stack measurements, and an example is shown of a 3D image of fluorescent labeled GUVs. Deconvolution softwares, such as Huygens, can be used to obtain better spatial *z*-direction resolution, through numerical image processing.

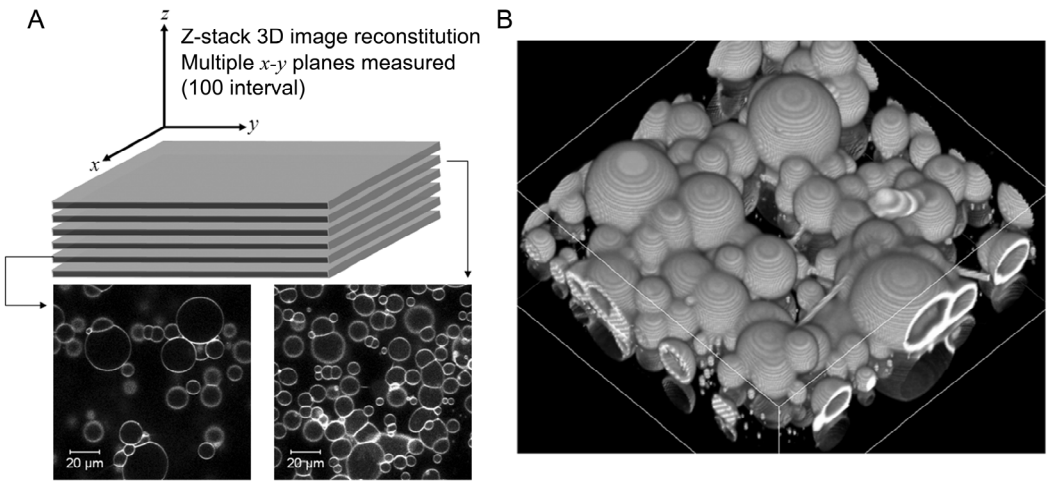

Figure 2.20. (**A**) Schematic of the z-stack principle behind 3-dimensional image reconstitution using confocal laser scanning microscopy. (**B**) Example of a 3D reconstituted image of giant liposomes lying on native AAO.

2.4.3. Fluorescence Recovery after Photobleaching (FRAP)

FRAP is a method developed to measure the diffusion of labeled molecules in two-dimensions. For lipid membranes, the diffusion of labeled proteins or lipids can be measured.[53] Irreversible photobleaching[54] of organic fluorophores occurs after repeated excitation, where the fluorophores undergo an intersystem-crossing into a triplet state, chemically react with oxygen species in solution and are deactivated because of the loss of π-conjugation. Only fluorophores that are easily deactivated are used for photobleaching experiments. Bleaching has to occur rapidly (< 2 s) in comparison to the diffusion time of labeled species within the bleached area (few μm). Bodipy, perylene or carboxy-fluorescein are easily photobleached at high laser intensities. Atto® dyes and Alexa Fluor® dyes, are particularly stable and not easily photobleached.

The measurement consists in monitoring the fluorescence intensity of a sample area using an attenuated light excitation source. Typically, several *x*-*y* frames are recorded each second. The light emission intensity is raised several folds, focused onto a circular region of interest (ROI), for a short time (1-2 s), and the subsequent fluorescence intensity is recorded as a function of time. The exposed fluorophores within the ROI are permanently deactivated. If the system under investigation is mobile, the fluorescent molecules surrounding the photobleached area diffuse within the ROI and the depleted fluorescence recovers with a speed that is characteristic of the diffusion coefficient (*D*) of the labeled molecule. If the labeled molecules are immobile, then the fluorescence within the photobleached area never recovers. Finally, if certain parts are mobile and certain parts are immobile, then the fluorescence recovery will only be proportional to the mobile fraction within the sample. The recovery signal is typically normalized to a reference fluorescence area that only undergoes loss of fluorescence because of repeated imaging. In figure 2.21A, the fluorescence recovery of the ROI is shown after bleaching. In figure 2.21B, the intensity as a function of time for the reference and the ROI are shown. The reference decreases steadily, while the fluorescence of the ROI is completely lost after bleaching and recovers slowly over seconds. In figure 2.21C, a normalized FRAP curve is shown with mobile and immobile fractions identified. Normalization consists in dividing the ROI intensity by the reference intensity. Ideally, a ROI should have a clear-cut, complete, loss of fluorescence in a short period (< 2 s) to obtain a well-defined Gauss radius. The reference must be taken sufficiently far from the ROI such that the bleaching process does not affect the area.

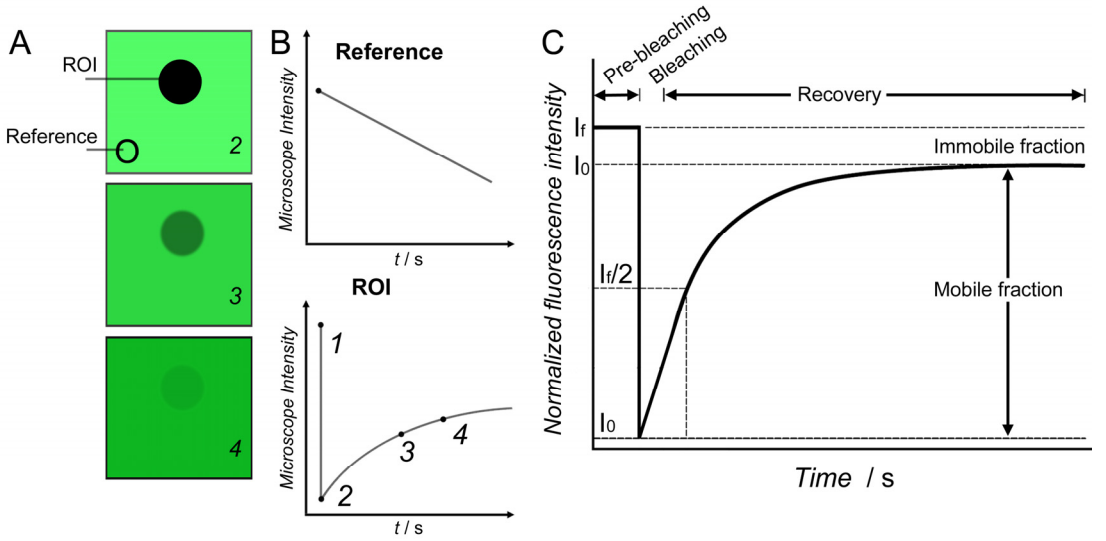

Figure 2.21. (**A**) Schematic of the typical recovery observed in a bleached ROI, after a SSM is bleached. (**B**) Examples of microscope intensity values obtained from analyzing the fluorescence intensity of the reference area and from the ROI. (**C**) Schematic of a typical normalized FRAP curve with important parameters identified. The ROI intensity was normalized to the reference area.

When diffusion proceeds in an ordered fashion according to Fick's diffusion equation, the diffusion coefficient (D) of the labeled molecule is given by:[53]

$$D = \frac{G_r^2}{4\,t_{1/2}}, \qquad \text{equation (2.34)}$$

where G_r is the Gauss radius of the circular bleached ROI and $t_{1/2}$ is the time required for half the fluorescence to recover (figure 2.21C). Lipid diffusion coefficients for SSMs have been reported with values of 1-4 $\mu m^2/s$. FRAP can also be performed on cells[55-56] to determine D of proteins.

2.5. Scanning Electron Microscopy (SEM)

By using the wave properties of electrons, resolutions on the order of 1 nm can be achieved. SEM requires a dry vacuum environment and sufficiently conductive samples. The magnification in an SEM can be controlled over 6 orders of magnitude to investigate samples with features of 10^{-3}-10^{-9} m. Although the working principle is analogous to optical microscopy, the components differ since electrons require magnetic lenses that condense the charged particle beam.[57-58] An electron gun equipped with an electron-producing source generates a constant flow of electrons, which is continuously extracted by magnetic coils and accelerated through 1 or 2 condensor lenses under a high applied voltage. A series of condensor lenses are then used to focus and stabilize the electron beam onto the sample. The function of the condensers is to focus the beam to a narrow diameter spot and the

rastering is controlled through a current supplied to *x, y* scanning coils. The narrower the focused electrons are, the greater the resolution power. The e-beam typically has an energy that can be varied from 0.5 keV to 40 keV, and is focused by condenser lenses to a spot about 1 nm in diameter. Magnification results from the ratio of the dimensions of the raster spot to the specimen raster region.

SEM measurements are conducted under mbar pressures. High resolution is in practice only achievable for inorganic metal samples. For soft materials and organic samples, a metal (Cr, Au, Ag) must be evaporated onto the sample. This conductive coating helps remove the accumulated static electric charge during electron irradiation. However, this may unfortunately mask nm features. Metal surface coatings can also improve topographic contrast and resolution of the sample's surface because backscattered and secondary electron emissions are improved near the high density surface of the thin metal layer. In-lense detectors capture surface features with high resolution. Scattered secondary electrons are collected with a back-scattering detector, revealing topographical features and material density variations. The Göttingen University physics department is equipped with a LEO supra-35 SEM microscope (Zeiss, Jena, Germany) based on a Tungsten filament emission, max. emission of 25 eV. The SEM is equipped with in-lens and secondary scattering detectors.

2.6. References

1. O'Sullivan, J. P.; Wood, G. C.; The Morphology and Mechanism of Formation of Porous Anodic Films on Aluminium. *Proc. R. Soc. Lond. A* **1970,** *317*, 511-543.

2. Li, A. P.; Muller, F.; Birner, A.; Nielsch, K.; Gosele, U.; Hexagonal Pore Arrays with a 50-420 Nm Interpore Distance Formed by Self-Organization in Anodic Alumina. *J. Appl. Phys.* **1998,** *84*, 6023-6026.

3. Li, F. Y.; Zhang, L.; Metzger, R. M.; On the Growth of Highly Ordered Pores in Anodized Aluminum Oxide. *Chem. Mater.* **1998,** *10*, 2470-2480.

4. Nielsch, K.; Choi, J.; Schwirn, K.; Wehrspohn, R. B.; Gosele, U.; Self-Ordering Regimes of Porous Alumina: The 10% Porosity Rule. *Nano Lett.* **2002,** *2*, 677-680.

5. Keller, F.; Hunter, M. S.; Robinson, D. L.; Structural Features of Oxide Coatings on Aluminum. *J. Electrochem. Soc.* **1953,** *100*, 411-419.

6. Siejka, J.; Ortega, C.; Perriere, J.; Rigo, S.; Study of Ion Movement During Anodic-Oxidation of Al and of Al and Nb Superimposed Layers by O-18 and Mev Ion-Beam Techniques. *J. Electrochem. Soc.* **1977,** *124*, C100-C100.

7. Diggle, J. W.; Downie, T. C.; Goulding, C. W.; Anodic Oxide Films on Aluminum. *Chem. Rev.* **1969,** *69*, 365-&.

8. Ono, S.; Masuko, N.; The Duplex Structure of Cell-Walls of Porous Anodic Films Formed on Aluminum. *Corrosion Science* **1992,** *33*, 503-505.

9. Ono, S.; Saito, M.; Ishiguro, M.; Asoh, H.; Controlling Factor of Self-Ordering of Anodic Porous Alumina. *J. Electrochem. Soc.* **2004,** *151*, B473-B478.

10. Thompson, G. E.; Porous Anodic Alumina: Fabrication, Characterization and Applications. *Thin Solid Films* **1997,** *297*, 192-201.

11. Thompson, G. E.; Xu, Y.; Skeldon, P.; Shimizu, K.; Han, S. H.; Wood, G. C.; Anodic-Oxidation of Aluminum. *Philosophical Magazine B-Physics of Condensed Matter Statistical Mechanics Electronic Optical and Magnetic Properties* **1987,** *55*, 651-667.

12. Jessensky, O.; Muller, F.; Gosele, U.; Self-Organized Formation of Hexagonal Pore Arrays in Anodic Alumina. *Appl. Phys. Lett.* **1998,** *72*, 1173-1175.

13. Jessensky, O.; Muller, F.; Gosele, U.; Self-Organized Formation of Hexagonal Pore Structures in Anodic Alumina. *J. Electrochem. Soc.* **1998,** *145*, 3735-3740.

14. Chu, S. Z.; Wada, K.; Inoue, S.; Isogai, M.; Yasumori, A.; Fabrication of Ideally Ordered Nanoporous Alumina Films and Integrated Alumina Nanotubule Arrays by High-Field Anodization. *Adv. Mater.* **2005,** *17*, 2115.

15. Lee, W.; Ji, R.; Gosele, U.; Nielsch, K.; Fast Fabrication of Long-Range Ordered Porous Alumina Membranes by Hard Anodization. *Nat. Mater.* **2006,** *5*, 741-747.

16. Li, A. P.; Muller, F.; Gosele, U.; Polycrystalline and Monocrystalline Pore Arrays with Large Interpore Distance in Anodic Alumina. *Electrochem. Solid-State Lett.* **2000,** *3*, 131-134.

17. Xu, Y.; Thompson, G. E.; Wood, G. C.; Bethune, B.; Anion Incorporation and Migration During Barrier Film Formation on Aluminum. *Corrosion Science* **1987,** *27*, 83-&.

18. Masuda, H.; Hasegwa, F.; Ono, S.; Self-Ordering of Cell Arrangement of Anodic Porous Alumina Formed in Sulfuric Acid Solution. *J. Electrochem. Soc.* **1997,** *144*, L127-L130.

19. Masuda, H.; Yamada, H.; Satoh, M.; Asoh, H.; Nakao, M.; Tamamura, T.; Highly Ordered Nanochannel-Array Architecture in Anodic Alumina. *Appl. Phys. Lett.* **1997,** *71*, 2770-2772.

20. Kriha, O.; Zhao, L. L.; Pippel, E.; Gosele, U.; Wehrspohn, R. B.; Wendorff, J. H.; Steinhart, M.; Greiner, A.; Organic Tube/Rod Hybrid Nanoribers with Ad Ustable Segment Lengths by Bidirectional Template Wetting. *Adv. Funct. Mat.* **2007,** *17*, 1327-1332.

21. Gitsas, A.; Yameen, B.; Lazzara, T. D.; Steinhart, M.; H., D.; Knoll, W.; Polycyanurate Nanorod Arrays for Optical Waveguide-Based Biosensing. *Nano Lett.* **2010,** *10*, 2173-2177.

22. Peic, A.; Staff, D.; Risbridger, T.; Menges, B.; Peter, L. M.; Walker, A. B.; Cameron, P. J.; Real-Time Optical Waveguide

Measurements of Dye Adsorption into Nanocrystalline Tio2 Films with Relevance to Dye-Sensitized Solar Cells. *J. Phys. Chem. C* **2011,** *115*, 613-619.

23. Kim, D. H.; Lau, K. H. A.; Joo, W.; Peng, J.; Jeong, U.; Hawker, C. J.; Kim, J. K.; Russell, T. P.; Knoll, W.; An Optical Waveguide Study on the Nanopore Formation in Block Copolymer/Homopolymer Thin Films by Selective Solvent Swelling. *J. Phys. Chem. B* **2006,** *110*, 15381-15388.

24. Kim, D. H.; Lau, K. H. A.; Robertson, J. W. F.; Lee, O. J.; Jeong, U.; Lee, J. I.; Hawker, C. J.; Russell, T. P.; Kim, J. K.; Knoll, W.; Thin Films of Block Copolymers as Planar Optical Waveguides. *Adv. Mater.* **2005,** *17*, 2442.

25. Lau, K. H. A.; Duran, H.; Knoll, W.; In Situ Characterization of N-Carboxy Anhydride Polymerization in Nanoporous Anodic Alumina. *J. Phys. Chem. B* **2009,** *113*, 3179-3189.

26. Lau, K. H. A.; Tan, L. S.; Tamada, K.; Sander, M. S.; Knoll, W.; Highly Sensitive Detection of Processes Occurring inside Nanoporous Anodic Alumina Templates: A Waveguide Optical Study. *J. Phys. Chem. B* **2004,** *108*, 10812-10818.

27. Lazzara, T. D.; Lau, K. H. A.; Abou-Kandil, A. I.; Caminade, A. M.; Majoral, J. P.; Knoll, W.; Polyelectrolyte Layer-by-Layer Deposition in Cylindrical Nanopores. *Acs Nano* **2010,** *4*, 3909-3920.

28. Lazzara, T. D.; Lau, K. H. A.; Knoll, W.; Mounted Nanoporous Anodic Alumina Thin Films as Planar Optical Waveguides. *J. Nanosci. Nanotechnol.* **2010,** *10*, 4293-4299.

29. Choy, T. C., *Effective Medium Theory: Principles and Applications* Oxford University Press: New York, 1999.

30. Green, P. F.; Limary, R.; Block Copolymer Thin Films: Pattern Formation and Phase Behavior. *Adv. Colloid Interface Sci.* **2001,** *94*, 53-81.

31. Lipic, P. M.; Bates, F. S.; Matsen, M. W.; Non-Equilibrium Phase Behavior of Diblock Copolymer Melts and Binary Blends in the Intermediate Segregation Regime. *J. Polym. Sc. B* **1999,** *37*, 2229-2238.

32. Aspnes, D. E.; Optical-Properties of Thin-Films. *Thin Solid Films* **1982,** *89*, 249-262.

33. Aspnes, D. E.; Local-Field Effects and Effective-Medium Theory - a Microscopic Perspective. *Am. J. Phys.* **1982,** *50*, 704-709.

34. Choy, T. C., *Effective Medium Theory: Principles and Applications*. 1st ed.; Oxford University Press: New York, 1999; Vol. 102.

35. Foss, C. A.; Hornyak, G. L.; Stockert, J. A.; Martin, C. R.; Template-Synthesized Nanoscopic Gold Particles - Optical-Spectra and the Effects of Particle-Size and Shape. *J. Phys. Chem.* **1994,** *98*, 2963-2971.

36. Foss, C. A.; Tierney, M. J.; Martin, C. R.; Template Synthesis of Infrared-Transparent Metal Microcylinders: Comparison of Optical Properties with the Predictions of Effective Medium Theory. *J. Phys. Chem.* **1992,** *96*, 9001-9007.

37. García-Vidal, F. J.; Pitarke, J. M.; Pendry, J. B.; Effective Medium Theory of the Optical Properties of Aligned Carbon Nanotubes. *Phys. Rev. Lett.* **1997,** *78*, 4289-4292.

38. Maldovan, M.; Bockstaller, M. R.; Thomas, E.; Carter, W. C.; Validation of the Effective Medium Approximation for Dielectric Permittivity of Nanoparticle Filled Materials. *Appl. Phys. B* **2003,** *76*, 877-884.

39. Liedberg, B.; Lundstrom, I.; Stenberg, E.; Principles of Biosensing with an Extended Coupling Matrix and Surface-Plasmon Resonance. *Sens. Actuators, B* **1993,** *11*, 63-72.

40. Schuck, P.; Use of Surface Plasmon Resonance to Probe the Equilibrium and Dynamic Aspects of Interactions between Biological Macromolecules. *Ann. Rev. Biophys. Biomol. Struct.* **1997,** *26*, 541-566.

41. Scheller, A. *Winspall*, 3.01; Max-Planck Institute for Polymer Research: Mainz, Gernany.

42. Kovacs, G. J.; Scott, G. D.; Attenuated Total Reflection Angular Spectra and Associated Resonant Electromagnetic Oscillations of a Dielectric Slab Bounded by Ag Films. *Appl. Opt.* **1978,** *17*, 3314-3322.

43. Aust, E. F.; Knoll, W.; Electrooptical Wave-Guide Microscopy. *J. Appl. Phys.* **1993,** *73*, 2705-2708.

44. Hickel, W.; Knoll, W.; Optical Wave-Guide Microscopy. *Appl. Phys. Lett.* **1990,** *57*, 1286-1288.

45. Knoll, W.; Interfaces and Thin Films as Seen by Bound Electromagnetic Waves. *Annu. Rev. Phys. Chem.* **1998,** *49*, 569-638.

46. Li, H. G.; Cao, Z. Q.; Lu, H. F.; Shen, Q. S.; Free-Space Coupling of a Light Beam into a Symmetrical Metal-Cladding Optical Waveguide. *Appl. Phys. Lett.* **2003,** *83*, 2757-2759.

47. Born, M.; Wolf, E.; Bhatia, A. B., *Principles of Optics, Electromagnetic Theory of Propagation, Interference and Diffraction of Light*. 7th ed.; Cambridge university press.

48. Debruijn, H. E.; Altenburg, B. S. F.; Kooyman, R. P. H.; Greve, J.; Determination of Thickness and Dielectric-Constant of Thin Transparent Dielectric Layers Using Surface-Plasmon Resonance. *Opt. Commun.* **1991,** *82*, 425-432.

49. Lakowicz, J. R., *Principles of Fluorescence Spectroscopy*. Springer: 2006.

50. Rost, F. W. D., *Fluorescence Microscopy*. Cambridge University Press: 1992.

51. Müller, M., *Introduction to Confocal Fluorescence Microscopy*. SPIE Press: 2006.

52. Pawley, J. B., *Handbook of Biological Confocal Microscopy*. Springer: 2006.

53. Axelrod, D.; Koppel, D. E.; Schlessinger, J.; Elson, E.; Webb, W. W.; Mobility Measurement by Analysis of Fluorescence Photobleaching Recovery Kinetics. *Biophys. J.* **1976,** *16*, 1055-1069.

54. Song, L. L.; Varma, C.; Verhoeven, J. W.; Tanke, H. J.; Influence of the Triplet Excited State on the Photobleaching Kinetics of Fluorescein in Microscopy. *Biophys. J.* **1996,** *70*, 2959-2968.

55. Lippincott-Schwartz, J.; Snapp, E.; Kenworthy, A.; Studying Protein Dynamics in Living Cells. *Nat. Rev. Mol. Cell Biol.* **2001,** *2*, 444-456.

56. Weiss, M.; Challenges and Artifacts in Quantitative Photobleaching Experiments. *Traffic* **2004,** *5*, 662-671.

57. Echlin, P., *Handbook of Sample Preparation for Scanning Electron Microscopy and X-Ray Microanalysis*. Springer: 2009.

58. Reimer, L., *Scanning Electron Microscopy: Physics of Image Formation and Microanalysis*. Springer: 1998.

Chapter 3

Mounted Nanoporous Anodic Alumina Thin Films as Planar Optical Waveguides

by

Thomas D. Lazzara, [1, †] *K.H. Aaron Lau*, [2, †] *Wolfgang Knoll* [3, †]

Published in: *Journal of Nanoscience and Nanotechnology* (2010) **10**, 4293-4299

[1] Institute for Organic and Biomolecular Chemistry, University of Göttingen, Göttingen, Germany.
[2] Department of Biomedical Engineering, Northwestern University, Evanston, Illinois, USA.
[3] Austrian Institute of Technology, Donau City Strasse 1, 1220 Vienna, Austria.
[†] Max Planck Institute for Polymer Research, Ackermannweg 10, D55128, Mainz, Germany.

Abstract

Solid-supported thin films of self-organized nanoporous anodic aluminum oxide (AAO) have been widely employed for the template preparation of nanostructured functional materials. Recently, the use of nanoporous AAO thin films in optical waveguide spectroscopy (OWS) has been explored for high sensitivity, *in situ* monitoring of processes occurring within these nanoporous templates. In this contribution, we demonstrate a strategy for mounting bulk anodized AAO thin films on heterogeneous solid-supports suitable for waveguide sensing experiments. Unlike conventional preparations of AAO thin films by anodization of vacuum- or electrochemically deposited Al thin films, the full range of techniques available to anodize bulk Al may potentially be applied with the present method. Moreover, we show that the AAO thin films mounted on glass substrates can have superior waveguide coupling properties compared to conventionally prepared samples. Furthermore, comparison between scanning electron microscope images and the pore dimensions calculated from an effective medium theory (EMT) analysis of the film refractive index measured by OWS, shows that the nanostructure of the AAO can be well characterized by an EMT-OWS analysis. Finally, using a curved metallic substrate as an example, we show that our mounting technique can be used as a general strategy to functionalize objects with nanoporous AAO films.

3.1. Introduction

Porous anodic aluminum oxide (AAO) membranes have been widely demonstrated as versatile templates for the preparation of nanostructured functional materials by virtue of their self-organized nanoporous structure that is composed of well-ordered, cylindrical pores that run straight through the membrane thickness.[1-5] AAO membranes may be prepared by anodization of bulk Al at voltages of 20~200 V to generate pores 10~400 nm in diameter.[6-8] Thin, solid substrate-supported AAO films may also be prepared. These have attracted great interest for use as nano-patterning masks of the underlying substrates.[2, 9] Moreover, the application of nanoporous AAO thin films as surface plasmon[10] and planar optical waveguide sensors[11, 12] have been demonstrated, and the investigation of nanoporous waveguides prepared from various materials has followed.[13-17]

The preparation of AAO thin films on non-Al solid supports conventionally requires the anodization of a layer of high quality Al deposited by vacuum[2, 18-20] or electrochemical[21] techniques. However, due to grain microstructure development,[22] the deposition of high purity Al films > 0.5~1 μm thick with low surface roughness may be technically demanding,[21, 23] but is required for spatially uniform pore initiation during anodization. In addition, the deposition of even thicker films required for pore ordering by 2-step anodization,[9] typical in bulk Al anodization, is a resource-intensive process. Although pore ordering by mechanical or lithographic pre-texturing of the Al thin film surface is possible,[24, 25] the pre-texturing process generally requires e-beam or ion-beam lithography and sample areas are limited. Furthermore, depending on the mechanical and electrochemical stability of the interface between the deposited Al film and the substrate, high voltage anodization for producing interpore distances > 100 nm,[6] or for hard anodization,[26] becomes problematic.

In this contribution, we report a method for mounting free-standing AAO thin films anodized from bulk Al metal on heterogeneous substrates. Conventional anodization of bulk Al circumvents many of the aforementioned problems associated with anodizing Al thin films. Free-standing AAO films were produced by chemical etching of the excess bulk Al. In particular, special attention was paid to the interface surface tension between the ambient and the etching solution. Previous demonstrations of mounted free-standing AAO templates have required the mechanical stabilization of the brittle AAO thin film by filling the pores with a polymer matrix during sample preparation,[27] have been mostly restricted to small samples,[28-30] or have required a technically demanding atomic layer deposition step.[11] In

contrast, our method avoids pore contact with any organic material, and provides large areas of AAO films suitable for chemical functionalization of the alumina surface. Furthermore, we demonstrate that AAO thin films mounted on glass can function as optical slab waveguides, and can exhibit better optical coupling properties than AAO films prepared from vacuum deposited Al. Optical waveguide spectroscopy (OWS), which is a simple but powerful technique for measuring the thickness and refractive index of optically transparent thin films,[31, 32] was used for characterizing the AAO waveguides. The pore nanostructure of the high quality AAO films was also found to be well-described by effective medium theory[33, 34] derived using the Maxwell-Garnett approach.[35, 36] Finally, we show that the proposed method can be extended to mounting AAO membranes on different substrate systems, including curved metallic surfaces.

3.2. Experimental Details

Preparation of mounted AAO thin films. AAO thin films mounted on solid-supports were prepared according to figure 3.1. First, anodization was performed following common procedures for bulk Al.[6] Briefly, 99.9999 % Al disks (20 mm x 1 mm; Goodfellow, Germany) were first mechanically[37] and then electrochemically polished (20V, 1°C, 5 min in 1:4 $HClO_4$:C_2H_5OH) to give a smooth surface suitable for optical measurements. We then employed anodization in oxalic acid (30~45 min) to produce AAO films (1~1.5 μm thick) with a pore lattice constant of ~100 nm, so as to conduct optical waveguide measurements at a wavelength available to our setup (see discussion further below). After anodization, the unreacted Al was selectively etched to obtain free-standing AAO films (up to 10 mm in diameter). The pores of the AAO were prevented from coming into contact with the etching solution (figure 3.1, step 2) by securing the AAO/Al disk on a glass slide, barrier layer[8] side up, using an o-ring spacer and fast curing epoxy (UHU brand). Al was etched by immersion in 3.4 wt.% $CuCl_2$ in 1:1 H_2O:10 M HCl at 1°C. Crucially, when the Al was completely etched away over a small area of the sample such that some AAO became visible (after ~30 min etching), the solution was diluted with an equal volume of ethanol. This reduced the surface tension and prevented AAO film rupture by the hydrogen produced during acid etching. After the etching was completed, the sample was carefully rinsed with ethanol and dried. Finally, large area samples were prepared by placing the secured, pure AAO membrane (figure 3.1, step 3), barrier layer side down, over a substrate coated with an adhesive (NOA 83H, Norland Products, USA; spin-coated: 3000 rpm, 60 s) using sharp tweezers.

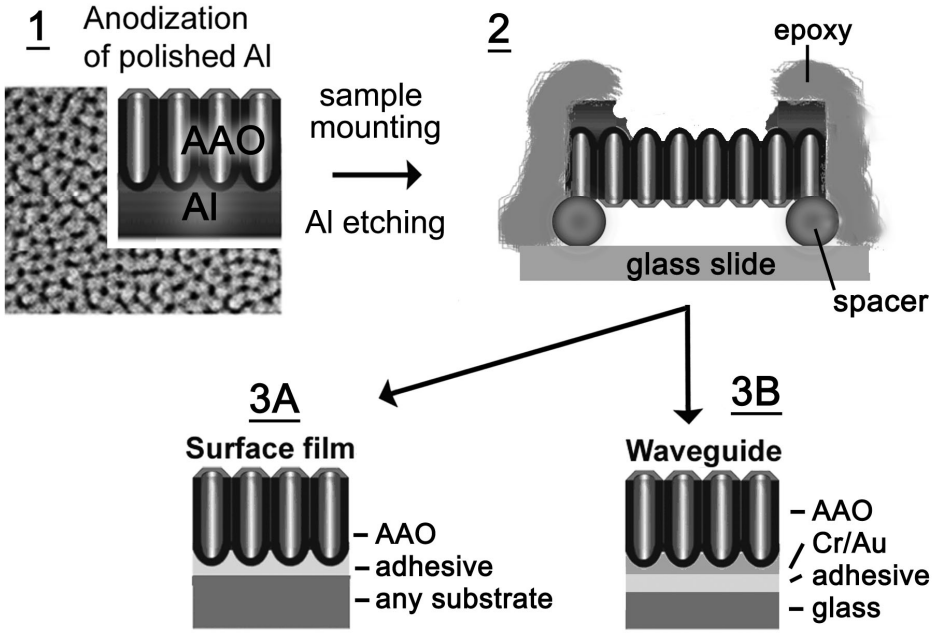

Figure 3.1. Preparation scheme for AAO thin film preparation on different surfaces.

For optical waveguide measurements (see below), a glass substrate was used (LaSFN9, Helma Optik, Germany), and 35 nm of Au (with 2 nm Cr for adhesion) was deposited for optical coupling onto the AAO barrier layer by thermal evaporation (Auto300, BOC Edwards, U.K.). Before deposition, an opening was made through the epoxy/o-ring to allow pressure equalization across the two sides of the free-standing AAO film during evacuation of the vacuum deposition chamber.

Optical waveguide spectroscopy (OWS) was performed on a purpose-built setup.[31, 32] In our measurements, a laser beam (λ = 632.8 nm) reflecting off the Cr/Au optical coupling layer (figure 3.1) was scanned over a range of incidence angles (θ). At specific θ's, determined by the thickness and effective refractive index of the nanoporous film, the laser could couple into the film and sharp minima (i.e. waveguide modes) in the reflectivity vs. θ (R vs. θ) scan could be observed. Scattering of the light being guided in the nanoporous structure is minimized by choosing pore sizes much smaller (e.g. 1/10) than the laser wavelength (see results and discussion).[12, 34] Measurement of the pore diameter from SEM images gives an average value of ~20 nm (see below), thus the requirement for efficient waveguiding was satisfied in the present experiment.

Scanning Electron Microscopy (SEM) was performed on a LEO Gemini 1530 instrument. Electron acceleration voltages between 1 and 6 kV was used.

3.3. Results and Discussion

Figure 3.2 shows a 1 μm thick AAO film with straight cylindrical pores mounted onto a glass substrate via a ~15 μm thick polymeric adhesive layer. Without surface tension control during the Al etching process, only films thicker than 10~30 μm retained sufficient mechanical strength to be readily handled. Also, mechanical polishing of the Al disks prior to anodization was found to enable free-standing AAO films < 2 μm to be reliably prepared. It is likely that the macroscale inhomogeneities over an AAO film prepared without mechanical polishing could induce stress concentrations that weaken a free-standing AAO film (figure 3.1, step 2). Anodization of bulk Al is a mature technique. Thus the present method allows one to apply this technical knowledge to prepare AAO thin films of a uniform thickness with few defects on heterogeneous substrates. This surface homogeneity is expected to yield improved waveguide coupling properties, as shown below.

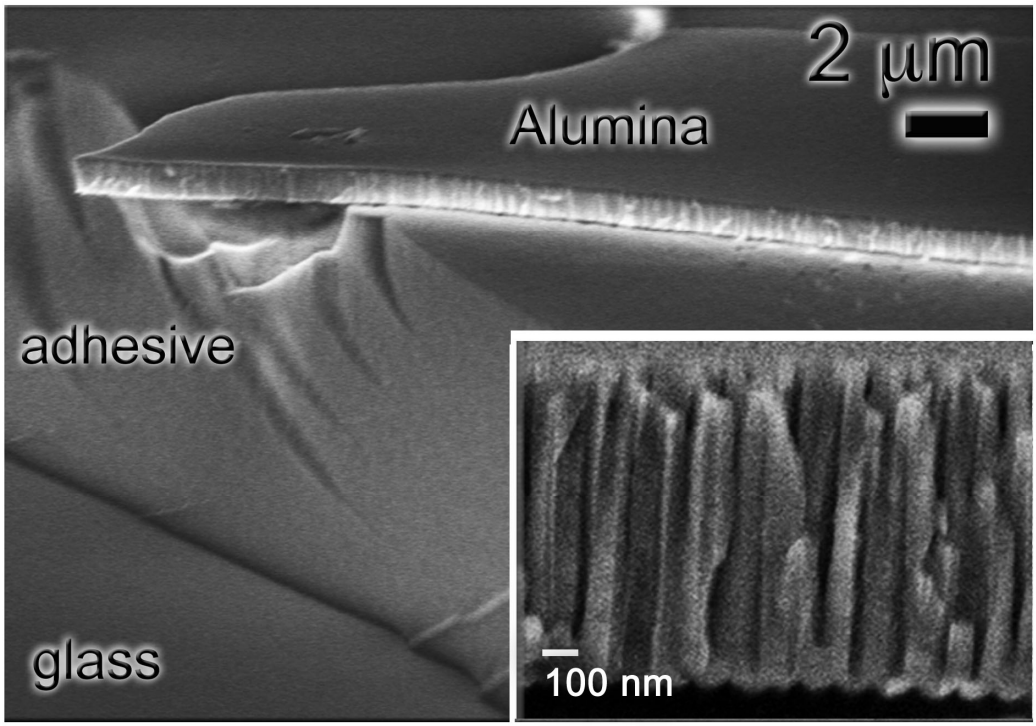

Figure 3.2. SEM cross-section of an AAO film mounted as a slab waveguide on glass using a polymeric adhesive. Inset: Magnified view showing close-packed straight pores with lattice constant ~100 nm.

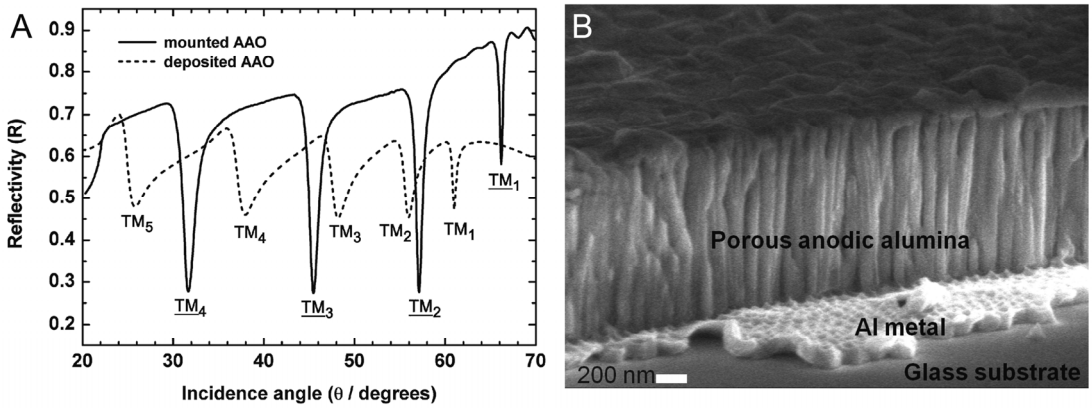

Figure 3.3. (**A**) Optical waveguide R vs. θ spectra in air for a mounted alumina film, about 1.35 microns thick (see figure 3.4) and for a sample prepared from vacuum deposited Al. Laser coupling into the AAO occurs where the minima appeared. The underlined modes correspond to the mounted AAO. (**B**) SEM image showing the cross-sectional view of an AAO waveguide substrate prepared from the anodization of a 1 μm sputtered Al metal film.

Figure 3.3 compares the OWS reflectivity spectra of the mounted AAO thin film waveguide (mounted AAO) with a conventional sample prepared from vacuum deposited Al (deposited AAO).[12] The result of the conventional sample is taken from reference 12. The magnetic field polarization of the incidence laser was set to be parallel to the film surface, thus transverse magnetic (TM) modes were excited. Moreover, as seen in figure 3.3, multiple minima were observed, indicating that the thin film constituted a multimode waveguide. The modes were labeled by the number of nodes in the optical field distributions.[31] In particular, the amplitude of the waveguide mode minima relative to the reflectivity baseline in between the minima indicates the amount of light coupled into the AAO thin film, as opposed to being reflected away to the detector. That is, higher relative amplitudes indicate more efficient waveguide coupling, and figure 3.3 shows that higher relative amplitudes were obtained for the mounted AAO thin film than the conventional sample prepared from deposited Al ("deposited AAO"). Specifically, the relative amplitudes for the mounted AAO waveguide ranged from 0.34 for TM_1 to 0.63 for TM_2 through TM_4. These were almost twice as high as the relative amplitudes for the conventional sample, which ranged from 0.26 for TM_1 to 0.32 for TM_5. Another criterion for comparing the two waveguides is the ratio between the mode's relative amplitude and its full-width-half-minimum (FWHM), with higher ratios indicating sharper modes. Accordingly, the ratios for the mounted AAO were between 0.40 for TM_4 to 0.83 for TM_1, significantly higher than those for the conventional sample: 0.04 for TM_5 to 0.52 for TM_1.

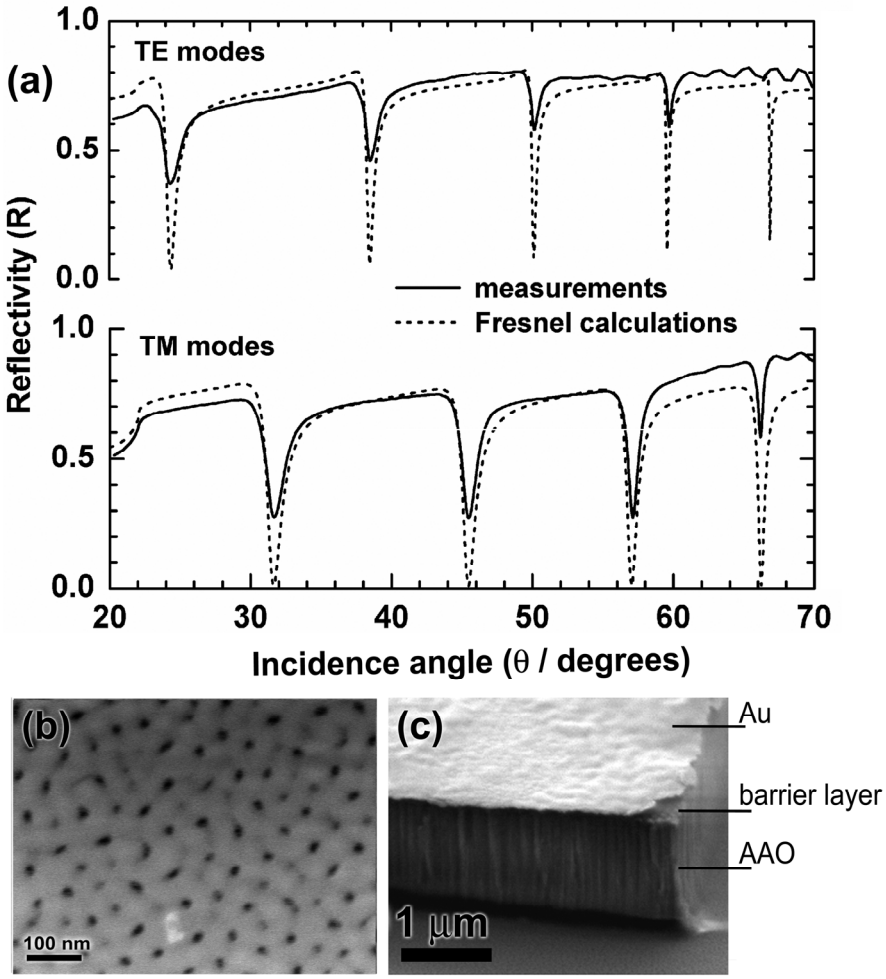

Figure 3.4. (**A**) R vs. θ spectra of a mounted AAO thin film (–) and Fresnel calculations (---). The TM mode spectrum obtained from the OWS measurement is duplicated from figure 3.3. (**B**)/(**C**) SEM images of the top and cross-section of the AAO thin film used for the waveguide. Note that in B, only the larger, darker pore openings spaced ~100 nm apart indicate actual pore channels. The lighter-colored openings reflect failed pore initiation sites that do not satisfy the 100 nm spacing intrinsic to the anodization process used.

Ideally, very sharp minima with high minima relative amplitudes should be observed in the case of atomically sharp waveguide surfaces[38] and for appropriately chosen metal coupling layers.[31, 32] Broadening of the minima may be caused by non-uniformity in the thickness and optical properties of the AAO thin film, because the observed spectra were obtained as an averaged response over an area probed by the incident laser (beam width was ~2 mm). Furthermore, surface roughness, physical defects, and optical damping of the metal coupling layer cause broadening of the waveguide coupling conditions. Importantly, broader minima reduce the sensitivity in determining the angle shifts of waveguide mode minima if processes were to occur within the pores (e.g. material deposition).[12, 31] Cr/Au coupling layers with optimized thicknesses were used for both the mounted and the "deposited" AAO waveguides, and the theoretical coupling minima should ideally reach zero for both samples. Therefore the higher quality peaks observed for the mounted AAO

indicates that high overall geometric and optical homogeneity may be obtained with the thin film mounting strategy.

The OWS measurements were analyzed with the Fresnel equations, which are the solutions to Maxwell's equations describing the angle-dependent intensity of the light reflecting off the AAO-substrate multilayer system. This standard OWS analysis matches the angle positions of the measured reflectivity minima with those calculated from the Fresnel equations based on trial values of a waveguiding film's thickness and (anisotropic) refractive index value(s).[31, 32] For the anodic alumina nanostructure, the ~60 nm thick barrier layer consisting of solid alumina[8] was treated separately from the nanoporous AAO film structure.[39] The measurements and the Fresnel calculations are compared in figure 3.4, and both the TM modes and the spectrum measured in the orthogonal polarization (transverse electric (TE) modes) are shown. The analysis gave a film thickness of 1.34 μm and effective refractive indices of 1.596 and 1.609 in the directions parallel and normal to the substrate surface, respectively. Comparison of the thickness obtained from the SEM characterization shows that the optical thickness is consistent with the actual film (figure 3.4C). It has been shown that variations in the optical properties through the thickness of a waveguiding thin film causes the angle positions of the reflectivity minima to shift by different amounts.[40] Therefore the excellent match in angle positions between the reflectivity minima of the measured spectra and the Fresnel calculations, which assume layers with homogenous optical properties, shows that the mounted AAO thin film also possesses homogenous optical properties. However, the interference fringes observed at high incidence angles (> 65° for TM modes and > 60° for TE modes), and a restricted range in θ due to total internal reflection at the adhesive/substrate interface (θ_{max} = 69° for the adhesive used), are disadvantages of introducing a polymer layer for mounting the AAO thin film. Also, Fresnel calculations indicate that the reflectivity minima for the AAO waveguide, which has optimized Cr/Au coupling layer thicknesses, should ideally reach close to zero. However the measured values were higher (figure 3.4). Nonetheless, the minima corresponding to the "deposited" AAO (figure 3.3) had even lower relative amplitudes. This non-ideal behavior reflects the issues of surface roughness and macroscale inhomogeneities discussed earlier.

The use of glass substrates and anodization in oxalic acid had been motivated by the application of the mounted AAO thin film to OWS studies. Our OWS setup employed a λ=633 nm laser, thus we prepared pore features below 1/10 λ to limit scattering effects and enable a quasi-static effective medium theory (EMT) analysis of the AAO's dielectric

response.[33, 34] Nonetheless, films with larger pores may also be studied by OWS at a longer wavelength. Importantly, the proposed procedure enables the application of the techniques developed for bulk Al anodization, including 2-step anodization[24] and high-voltage "hard" anodization[26, 41] to produce highly ordered AAO.

The anisotropic optical response measured by OWS is a result of the anisotropic AAO nanostructure composed of straight cylindrical pores aligned along the direction normal to the film surface.[12] Furthermore, the refractive indices measured are effective values because the optical response of the AAO derives from contributions of both the alumina matrix and the air filling the pores. We have previously clarified[12] the origin of the larger film effective dielectric constant (equal to the square of the refractive index) in the direction normal to the substrate surface ($\varepsilon_{\perp}$) as compared to the value in the direction parallel to the substrate ($\varepsilon_{//}$) using the Wiener upper and lower bounds:[34]

$$\varepsilon_{\perp} = f_{pore}\varepsilon_{pore} + (1 - f_{pore})\varepsilon_{anod.} \qquad \text{Eq. (3.1A)}$$

$$\varepsilon_{//}^{-1} = f_{pore}\varepsilon_{pore}^{-1} + (1 - f_{pore})\varepsilon_{anod.}^{-1} \qquad \text{Eq. (3.1B)}$$

where f_{pore} is the volume fraction of the pores within the AAO film, $\varepsilon_{anod.}$ is the dielectric constant of the anodic alumina, and $\varepsilon_{\text{pore}} = \varepsilon_{\text{air}} = 1$. To more accurately describe the dielectric response of the AAO film nanostructure, an EMT result following the Maxwell-Garnett (MG) approach[34] may be applied. This is the appropriate EMT model for describing the nanoporous AAO structure because it assumes domains (i.e. the cylindrical pores) that are completely isolated from each other by a continuous matrix (i.e. the alumina). Martin *et al.* has previously shown that the optical properties of gold-filled AAO templates may be described by a MG model that approximates the cylindrical pores as infinite prolate spheroids.[42, 43] Here we apply an approximation that also follows the MG approach and which directly takes into account the cylindrical pore geometry, validated experimentally[35] and by numerical calculations:[36]

$$\varepsilon_{\perp} = f_{pore}\varepsilon_{pore} + (1 - f_{pore})\varepsilon_{anod.} \qquad \text{Eq. (3.2A)}$$

$$\varepsilon_{//} = \varepsilon_{anod.} + \varepsilon_{anod.}\frac{f_{pore}(\varepsilon_{pore} - \varepsilon_{anod.})\beta}{\varepsilon_{anod.} - \tfrac{1}{2} f_{pore}(\varepsilon_{pore} - \varepsilon_{anod.})\beta} \;;\; \beta = \frac{2}{\varepsilon_{pore}/\varepsilon_{anod.} + 1} \qquad \text{Eq. (3.2B).}$$

Since the anodized alumina is considered to be non-crystalline and different amounts of acid anions are incorporated into the oxide structure depending on the exact anodization conditions,[44] $\varepsilon_{anod.}$ is expected to be lower than the value for crystalline Al_2O_3 (e.g. $\varepsilon_{sapphire}$ =

3.1[45]). The exact value of f_{pore} is also not known a priori without the benefit of an independent characterization technique such as SEM. On the other hand, $\varepsilon_{anod.}$ and f_{pore} may be obtained by solving equations 3.2A and 3.2B simultaneously using the measured values of $\varepsilon_{\perp}$ and $\varepsilon_{//}$. Accordingly, $\varepsilon_{anod.}$ = 2.67 and f_{pore} = 0.051. Given an average inter-pore distance of 100 nm for anodization in oxalic acid[6] and a corresponding pore density, ρ_{pore} = 1.15 x 10^{14} m^{-1}, the pore diameter (d_{pore}) can be calculated from $d_{\text{pore}} = 2\sqrt{f_{pore}/\pi\rho_{pore}}$ = 23 nm. SEM characterization of the top view of the AAO waveguide (figure 3.4B) shows that the actual pore diameter is ~20 nm (the SEM resolution is limited to a few nanometers). An identical pore diameter can also be measured from the SEM cross-section of the sample shown in figure 3.2, which was anodized under the same conditions. In contrast, calculations based on the Wiener bounds (Equation 3.1) gave a significantly smaller pore diameter (11 nm) and alumina dielectric constant (2.61). Therefore the nanoporous structure of the mounted AAO film appears to be described well by analysis of the OWS measurements with the EMT approximation derived from the MG approach.

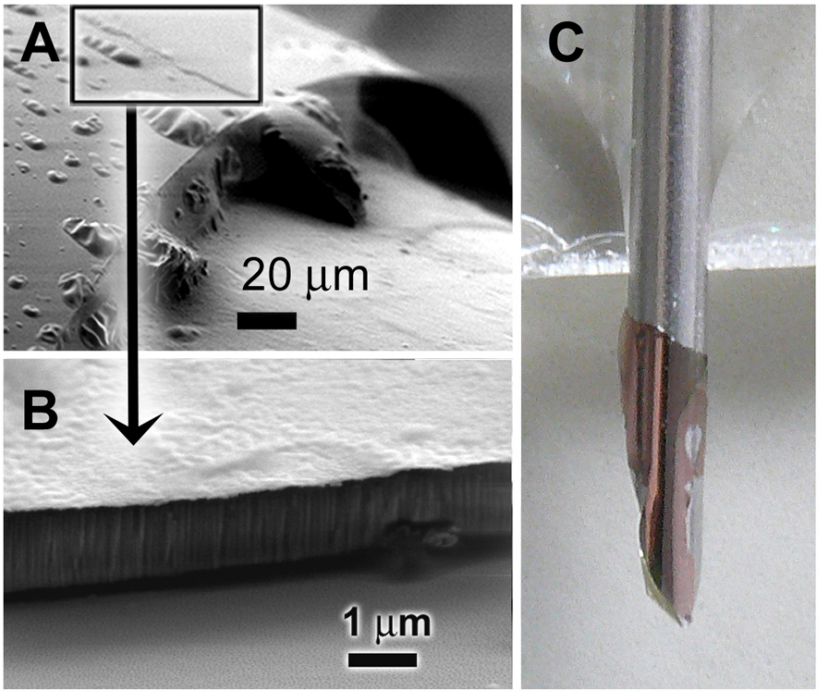

Figure 3.5. Characterization of a 1.4 μm thick AAO membrane mounted on the curved metallic surface of a steel syringe needle, 1 mm in diameter. (**A**) SEM cross section image of the ~30 microns thick polymer adhesive layer bonding the AAO membrane on the steel surface. The AAO is the smooth, thin, top layer along the upper portion of the image; its edge is highlighted within the boxed area. (**B**) The SEM shows the corresponding cross section of the AAO membrane. The striations normal to the film surface are the AAO pores. A thin Au layer was evaporated on the top surface of the AAO to give a smooth appearance, and to give a distinctive color to the membrane for identification in the optical image (**C**). The cross sections were generated by brittle fracture of the layer structure.

The thin film mounting procedure can also be applied to virtually any substrate. As an example, a 1.4 μm thick AAO sample was mounted on the curved, steel surface of a syringe needle (figure 3.5). Note that the thin film format enabled the brittle AAO layer to conform to the curved surface without fracture, since the low AAO film thickness implied only small bending strains within the AAO film, even though the surface curvature was relatively large at 2000 m^{-1} (radius = 0.5 mm). In comparison, uniform Al vacuum deposition on non-planar surfaces for direct anodization is difficult, although a cylindrical AAO structure prepared from the anodization of Al wires has been demonstrated.[46] Notwithstanding, direct anodization of Al deposited on metal substrates may be complicated by electrochemical dissolution. In addition, a suitable choice of the bonding material, including ceramic adhesives,[47] may extend the chemical stability of the mounted AAO thin films to a wide range of environments. Thus the "surface functionalization" of surfaces with free-standing AAO thin films may be implemented in a wide variety of applications.

3.4. Conclusion

A method suitable for preparing AAO thin films on heterogeneous solid supports is presented. Bulk Al disks were anodized to produce thin AAO layers, and the unreacted Al was selectively etched to produce free-standing AAO films. In particular, intact AAO thin films with thickness ~1 μm were reliably prepared by controlling the surface tension at the gas/etchant interface. The nanoporous thin films were mounted on glass substrates and used as planar optical waveguides. These mounted AAO thin film waveguides were shown to have improved optical coupling properties compared to AAO waveguides anodized from vacuum-deposited Al metal films. The nanostructure of the mounted AAO film is also well-described by an effective medium theory approximation, such that the pore diameter of the AAO film may be characterized by measurement of the film's anisotropic refractive index. Decoration of a curved metal surface with an AAO thin film was also demonstrated. The proposed procedure circumvents the technically demanding steps of depositing high quality Al thin films, the limitations associated with anodizing such deposited films, and enables the application of the techniques developed for conventional anodization of bulk Al to the preparation of AAO thin films on a variety of surfaces.

3.5. References

1. O. Kriha, L. Zhao, E. Pippel, U. Gösele, R. B. Wehrspohn, J. H. Wendorff, M. Steinhart, and A. Greiner, *Adv. Funct. Mater.* 17, 1327 (**2007**)

2. Y. Lei, W. Cai, and G. Wilde, *Prog. Mater Sci.* 52, 465 (**2007**)

3. H. Hillebrenner, F. Buyukserin, M. Kang, M. O. Mota, J. D. Stewart, and C. R. Martin, *J. Am. Ceram. Soc.* 128, 4236 (**2006**)

4. I. Mikulskas, S. Juodkazis, R. Tomasiunas, and J. G. Dumas, *Adv. Mat.* 13, 1574 (**2001**)

5. C. R. Martin, *Science* 266, 1961 (**1994**)

6. K. Nielsch, J. Choi, K. Schwirn, R. B. Wehrspohn, and U. Gosele, *Nano Lett.* 2, 677 (**2002**)

7. H. Masuda and K. Fukuda, *Science* 268, 1466 (**1995**)

8. J. P. O'Sullivan and G. C. Wood, *Proc. R. Soc. London, Ser. A* 317, 511 (**1970**)

9. H. Masuda and M. Satoh, *Jpn. J. Appl. Phys.* 35, L126 (1996)

10. S. G. Cloutier, A. D. Lazareck, J. Xu, Applied Physics Letters 88, 013904 (2006)

11. L. K. Tan, H. Gao, Y. Zong, and W. Knoll, *J. Phys. Chem. C* 112, 17576 (**2008**)

12. K. H. A. Lau, L. S. Tan, K. Tamada, M. S. Sander, and W. Knoll, *J. Phys. Chem. B* 108, 10812 (2004)

13. P. J. Cameron, A. T. A. Jenkins, W. Knoll, F. Marken, E. V. Milsom, and T. L. Williams, *Chem. Mater*. 18, 4304 (**2008**)

14. K. Awazu, C. Rockstuhl, M. Fujimaki, N. Fukuda, J. Tominaga, T. Komatsubara, T. Ikeda, and Y. Ohki, *Opt. Express* 15, 2592 (**2007**)

15. M. Fujimakia, C. Rockstuhla, X. Wanga, K. Awazua, J. Tominagaa, T. Ikedab, Y. Ohkib, and T. Komatsubarac, *Microelectron. Eng.* 84, 1685 (**2007**)

16. E. Reimhult, K. Kumar, and W. Knoll, *Nanotechnol*. 18, 275303 (**2007**)

17. D. H. Kim, K. H. A. Lau, J. W. F. Robertson, O. J. Lee, U. Jeong, J. I. Lee, C. J. Hawker, T. P. Russell, J. K. Kim, and W. Knoll, *Adv. Mat.* 17, 2442 (**2005**)

18. O. Rabin, P. R. Herz, Y. M. Lin, A. I. Akinwande, S. B. Cronin, and M. S. Dresselhaus, *Adv. Funct. Mat*. 13, 631 (**2003**)

19. S. Z. Chu, K. Wada, S. Inoue, and S. Todoroki, *J. Electrochem. Soc.* 149, B321 (**2002**)

20. D. Crouse, Y.-H. Lo, A. E. Miller, and M. Crouse, *Appl. Phys. Lett*. 76, 49 (**2000**)

21. S. Biring, K.-T. Tsai, U. K. Sur, Y.-L. Wang, Nanotechnology 19, 015304 (2008)

22. J. A. Thornton, *J. Vac. Sci. Technol. A* 3059 (**1986**)

23. A. E. Lita, J. J. E. Sanchez, *J. Appl. Phys*. 85, 876 (**1999**)

24. H. Masuda, H. Yamada, M. Satoh, H. Asoh, M. Nakao, and T. Tamamura, *Appl. Phys. Lett.* 71, 2770 (**1997**)

25. C. Y. Liu, A. Datta, and Y. L. Wang, *Appl. Phys. Lett.* 78, 120 (**2001**)

26. S.-Z. Chu, K. Wada, S. Inoue, M. Isogai, A. Yasumori, Advanced Materials 17, 2115 (**2005**)

27. Y. Lei, W.-K. Chim, Chemistry of Materials 17, 580 (**2005**)

28. G. Q. Ding, M. J. Zheng, W. L. Xu, W. Z. Shen, Nanotechnology 16, 1285 (**2005**)

29. M. Tian, S. Xu, J. Wang, N. Kumar, E. Wertz, Q. Li, P. M. Campbell, M. H. W. Chan, T. E. Mallouk, Nano Letters 5, 697 (**2005**)

30. C.-S. Toh, B. M. Kayes, E. J. Nemanick, N. S. Lewis, Nano Letters 4, 767 (**2004**)

31. W. Knoll, Annual Review of Physical Chemistry 49, 569 (**1998**)

32. H. Raether, *Surface-Plasmons on Smooth and Rough Surfaces and on Gratings*, Vol. 111, Springer, Berlin / Heidelberg, (**1988**)

33. T. C. Choy, *Effective Medium Theory: Principles and Applications* Vol. 102, Oxford University Press, New York, (**1999**)

34. D. E. Aspnes, Thin Solid Films 89, 249 (**1982**)

35. F. J. García-Vidal, J. M. Pitarke, J. B. Pendry, Physical Review Letters 78, 4289 (1997)

36. M. Maldovan, M. R. Bockstaller, E. L. Thomas, W. C. Carter, Applied Physics B: Lasers and Optics 76, 877 (**2003**)

37. B. L. USA, Buehler Ltd. USA, Lake Bluff, USA.

38. R. Lawall, W. Knoll, Journal of Applied Physics 76, 5764 (**1994**)

39. A. C. Galca, E. S. Kooij, H. Wormeester, C. Salm, V. Leca, J. H. Rector, B. Poelsema, Journal of Applied Physics 94, 4296 (**2003**)

40. P. W. Beines, I. Klosterkamp, B. Menges, U. Jonas, W. Knoll, Langmuir 23, 2231 (**2007**)

41. W. Lee, R. Ji, U. Goesele, K. Nielsch, Nature Materials 5, 741 (2006)

42. C. A. Foss, G. L. Hornyak, J. A. Stockert, C. R. Martin, J. Phys. Chem 98, 2963 (**1994**)

43. G. L. Hornyak, C. J. Patrissi, and C. R. Martin, *J. Phys. Chem. B* 101, 1548 (1997)

44. G. E. Thompson, G. C. Wood, *Nature* 290, 230 (**1981**)

45. M. E. Thomas and W. J. Tropf, in *Handbook of Optical Constants of Solids*, edited E. D. Palik, Academic Press, Orlando, **1998**, Vol. III, p. 653.

46. R. Sanz, M. Hernández-Vélez, Kleber R. Pirota, J. L. Baldonedo, and M. Vázquez, *Small* 3, 434 (**2007**)

47. P. Wagner, M. Hegner, H.-J. Guentherodt, and G. Semenza, *Langmuir* 11, 3867 (**1995**)

Acknowledgements Thomas D. Lazzara acknowledges the award of a scholarship from *le Fonds Québécois de la Recherche sur la Nature et les Technologies*. We thank Gunnar Glasser at the Max Planck Institute for Polymer Research (MPIP) for electron microscopy. We thank Akihiro Sato at the MPIP and, in particular, Dr. Martin Steinhart and Kornelia Sklarek for their help with anodization and etching techniques.

Chapter 4

Polyelectrolyte Layer-by-Layer Deposition in Cylindrical Nanopores

by:
Thomas D. Lazzara,[†,∂] *K. H. Aaron Lau,*[*,†,‡] *Ahmed I Abou-Kandil,*[†] *Anne-Marie Caminade,*[‡] *Jean-Pierre Majoral,*[‡] *Wolfgang Knoll*[†,§]

Graphical abstract:

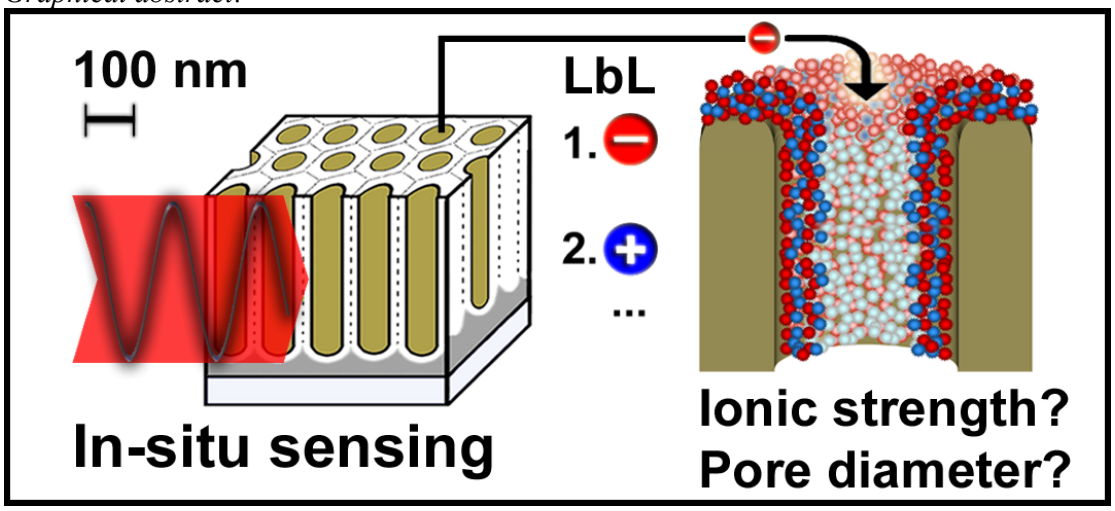

Published in: *ACS Nano* (2010) **4**, 3909-3920

[†] Max Planck Institute for Polymer Research, Ackermannweg 10, D55128, Mainz, Germany.
[‡] Laboratoire de Chimie de Coordination du CNRS, 205 route de Narbonne, F-31077, Toulouse cedex 04, France.
[∂] Institute for Organic and Biomolecular Chemistry, Tamannstr. 2, 37077, Göttingen, Germany.
[‡] Department of Biomedical Engineering, Northwestern University, Sheridan Road, Evanston, IL 60202, USA.
[§] Austrian Institute of Technology, Donau City Strasse 1, 1220 Vienna, Austria.

Abstract

Layer-by-layer (LbL) deposition of polyelectrolytes within nanopores in terms of the pore size and the ionic strength was experimentally studied. Anodic aluminum oxide (AAO) membranes, which have aligned, cylindrical, non-intersecting pores, were used as a model nanoporous system. Furthermore, being prepared as thin films on glass substrates, the AAO membranes were employed as planar optical waveguides so as to monitor, *in situ*, the LbL process within the nanopores by optical waveguide spectroscopy (OWS). Structurally well-defined N,N-disubstituted hydrazine phosphorous-containing dendrimers of the fourth generation, with peripherally charged groups and diameters of approximately 7 nm, were used as the model polyelectrolytes. The pore diameter of the AAO was varied between 30-116 nm and the ionic strength was varied over 3 orders of magnitude. The dependence of the deposited layer thickness on ionic strength within the nanopores is significantly stronger than LbL deposition on a planar surface. Furthermore, deposition within the nanopores can become inhibited even when the pore diameter is much larger than the diameter of the G4-polyelectrolyte, and when the screening length is insignificant relative to the dendrimer diameter at high ionic strengths. Our results and experimental approach may be used to test theories regarding the partitioning of nano-objects within nanopores where electrostatic interactions are a dominating force. Furthermore, we show that the strong dependence of polyelectrolyte transport within the nanopores on the solution ionic strength could be used to selectively deposit a multilayer LbL membrane atop the pores of an AAO substrate.

Keywords: porous substrates, cylindrical pores, polyelectrolytes, dendrimers, layer-by-layer self-assembly, optical lightmode waveguide spectroscopy

4.1. Introduction

Layer-by-Layer (LbL) assembly is a versatile technique to create multilayered structures by the alternating deposition of polycationic and polyanionic species. The technique has inherent advantages towards the nanoscale control of the layered material.[1-7] Multilayer formation is governed by electrostatic self-assembly of oppositely charged species and therefore, as long as the LbL building blocks are charged, the size, structure and nature of the building blocks can be modified to impart different functionalities to the LbL film. Technologically relevant functional films have been produced by the homogeneous or heterogeneous layered mixing of polyelectrolyte polymers[8-11] of various structures (linear, branched, dendritic, degree of hydrophobicity) and with different types of suitably charged

nanoparticles[12-17] and proteins[18, 19]. A number of methods, such as x-ray diffraction, ellipsometry and surface plasmon resonance, are now available to characterize planar LbL structures. However, advanced LbL structures formed inside porous systems, such as within films of colloidal particles or cylindrical nanoporous membranes,[20-28] cannot be easily characterized as with those formed on planar surfaces.

Nanoporous anodic aluminum oxide (AAO) films have been widely employed as versatile templates for the preparation of nano-structured functional materials.[13, 14, 20-23, 25, 27, 28] It is a self-organized material that possesses non-intersecting, close-packed, cylindrical pores running straight through the film thickness. The pore diameters can be conveniently adjusted,[24, 26, 29, 30] and the AAO can be prepared with minimum equipment requirements. Studies involving thin AAO films have attracted significant interest for their potential use in non-destructive, high sensitivity assays such the selective separation of drug enantiomers[31, 32] or DNA oligomers[33] and the development of on-chip biosensors[34-37] where miniaturization, device performance and efficiency are required. Two dominant factors affecting macromolecular transport in the cylindrical geometry are steric effects and the electrostatic interactions with the pore surfaces.[38]

Dendrimers are macromolecules that typically have a spherical or globular shape originating from a regular 3-dimensional branching and have a highly defined molecular weight. Their compact size, uniformity and tunability are significant advantages for applications such as gene delivery agents, drug carriers and molecular sensors[39-42]. Polyelectrolyte dendrimers are dendritic structures with ionizable groups. In particular, water-soluble, globular N,N-disubstituted hydrazine phosphorus-containing dendrimers developed by Majoral and Caminade *et al.* have been extensively used to create multilayer LbL dendrimer films.[43] These dendrimers have been used as building blocks for functional systems[40] such as nanotubes,[14, 44] capsules[45] and energy-cascade sensor architectures.[13] Multilayers prepared from these polyelectrolyte dendrimers on a planar surface show a monotonic increase in layer thickness with the number of LbL deposition steps.[43, 45] Additionally they have a lower degree of inter-layer penetration than multilayers formed from linear polyelectrolytes because of their well-defined peripherally charged surface and their rigid internal hydrophobic structure.[40, 46] Such structural properties make these dendrimers suitable model polyelectrolytes to study the LbL deposition process in nanoporous substrates.

The study of charged macromolecule and colloid transport within cylindrical pores has been of interest both on a theoretical[38, 47-53] and a practical level.[54, 55] Although diffusion through cylindrical pores for dilute systems of rigid neutral spheres is relatively well understood, this is not the case for systems of charged particles through charged nanopores. Comprehensive theoretical modeling of these systems is complex due to the electrostatic contributions and charge regulation in the confined nanopore geometry.[52] The partitioning of charged analytes inside and outside cylindrical pores is not simply described by a reduction in the Debye screening length (λ_{Debye}) at decreasing ionic strengths.[48-51, 53, 56, 57] Calculations based on spherical charged particles and infinite cylindrical pores have shown that electrostatic interactions continue to significantly influence transport properties even at ionic strengths approaching 1 M, where $\lambda_{Debye} << 1$ nm, and in cases where pore diameters is much larger than the size of the particles.[49, 53] To facilitate the description of, respectively, the particle diameter (d) relative to the pore diameter (D_0) and relative to λ_{Debye}, the normalized parameters $\alpha = d/D_0$ and $\tau = D_0/2\lambda_{Debye}$, are often used.

A number of experimental studies have focused on measuring the apparent diffusion constants in nanoporous membranes[58, 59] and studies related to electro-osmotic transport[60, 61] and Coulter counters[62-64] have been previously reviewed. More recently, indirect measurement of the filling by polyelectrolyte multilayers of nanopores ranging from 100-500 nm has been carried out in the dried state by gas-flow porometry.[65] Nonetheless, direct investigation of surface processes occurring within nanoscale pores has been hampered by the limited availability of *in situ*, high-sensitivity, surface characterization techniques that can probe inside nanoporous morphologies.

Optical Waveguide Spectroscopy (OWS) is a highly sensitive yet experimentally simple technique for independently characterizing the thickness and refractive index of optically transparent thin films.[66, 67] In recent years, OWS has also been explored for *in situ* monitoring of processes occurring within AAO[68-70] and other nanoporous templates[14, 71-75] at sub-nanometer sensitivities.[68, 69] The nano-porosity ensures that scattering loses are minimal for optical waveguiding at visible or longer wavelengths, and that effective medium theory (EMT) can be applied to quantify processes occurring within the nanoporous AAO structure based on refractive index responses.[68, 76, 77] In this regard, the ordered cylindrical pore morphology of AAO membranes lends itself to a simple EMT description using the Maxwell-Garnett approach.[68, 70, 77]

In this contribution, the LbL deposition of dendrimer polyelectrolytes within the nanopores of AAO was investigated by *in situ* OWS and EMT analysis, and the limiting conditions in terms of pore size and ionic strength were explored. The diameter of the AAO pores was varied between 30-116 nm, which corresponds to 4~17 times of the diameter of the dendrimers used (~7 nm).[45, 78-80] The ionic strength was controlled by the addition of NaCl, with the lowest concentration set by the polyelectrolytes dissolved in ultrapure water, and the highest at 900 mM NaCl. In our experiments, LbL deposition within the nanopores occurred simultaneously on the internal pore surfaces and atop the AAO membrane on the planar surfaces between openings of the cylindrical nanopores. As proposed in earlier studies,[68, 70] the depositions atop and within the AAO membrane were independently measured by OWS. Depositions on the AAO were compared with surface plasmon resonance (SPR) measurements of LbL deposition on a planar surface. In addition, *ex situ* scanning electron microscopy (SEM) was employed to corroborate the *in situ* OWS results. Electrostatic hindrance to LbL deposition of polyelectrolytes within a nanoporous structure is not unexpected. However, our results indicate that dependence of the deposited layer thickness on ionic strength within the nanopores was significantly stronger than deposition on a planar surface. In particular, LbL deposition could be completely inhibited within the nanopores even when the pore diameter was much larger than the diameter of the dendrimer polyelectrolyte, and increased ionic strengths was unable to compensate for this effect. Finally, the enhanced ionic strength effect was utilized to selectively deposit, hence suspend, a polyelectrolyte membrane atop a nanoporous AAO substrate.

4.2. Results and Discussion

4.2.1. LbL Deposition Within and Atop Nanoporous AAO Membranes.

The structures of the polyelectrolyte dendrimers used, N,N-disubstituted hydrazine phosphorus containing dendrimers of the fourth generation (G4), are shown in figure 4.1A. Each dendrimer has 96 peripheral charged groups, which are either all cationic or all anionic in nature (G4(+) = $G_4(NH^+Et_2Cl^-)_{96}$, M_w = 32361; G4(-) = $G_4(CHCOO^-Na^+)_{96}$, M_w = 35625).

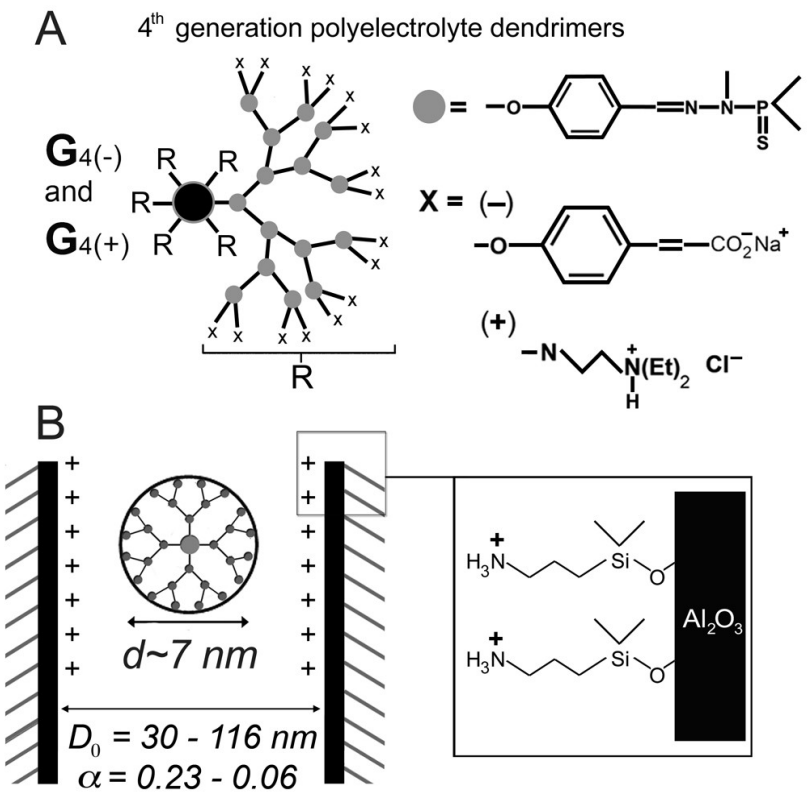

Figure 4.1. (**A**) Chemical structure of the N,N-disubstituted hydrazine phosphorus-containing dendrimers of the fourth generation (G4-polyelectrolyte) used in the LbL experiments. (**B**) Schematic illustrating the geometry of the polyelectrolyte multilayer experiments carried out within cylindrical nanopores of different diameters (α), involving the interaction of charged dendrimers with a positively charged surface obtained by silanization with APDMES.

At low ionic strengths, akin to unbranched polyelectrolytes, the counter-ions of most charged groups remain close to the dendrimers (counterion condensation) and the ionized groups are weakly screened. Since these groups are located on the periphery of the G4-polyelectrolyte, to minimize repulsive electrostatic interactions, the dendrimers adopt a more extended conformation that is commensurate with the dendrimer's symmetry. The theoretical diameter of the dendrimers in a fully extended conformation is ~10 nm. At higher ionic strengths, enhanced charge screening allows an increase in the degree of dissociation and the diameter of the G4 dendrimers in solution has been measured to be ~7 nm.[45, 79, 80]

G4-polyelectrolyte LbL depositions were initiated on the nanoporous AAO membrane with an aminopropyl-dimethylethoxysilane (APDMES) surface layer that provided a positive surface charge. The AAO membranes were prepared with a thickness of ~1 μm and a range of average pore diameters (D_0) of 30-117 nm. The pores are open only on the top side of the AAO membrane. On the APDMES-functionalized AAO substrates, LbL multilayer formation occurred *via*: 1) deposition on the internal surface of the cylindrical

pores, and 2) deposition atop the nanoporous membrane on the surfaces between individual pore openings. G4-polyelectrolyte depositions were performed starting from immersion in 1 mg/mL G4(-) dissolved in ultrapure water solution, followed by immersion in a 1 mg/mL G4(+) solution, and so forth, with a rinsing step in between every immersion. The ionic strength was controlled by the addition of NaCl. As previously reported, the AAO membranes were prepared on glass substrates that acted as optical waveguides.[68, 70, 81] This allowed *in situ* monitoring of the LbL deposition using optical waveguide spectroscopy (OWS).[66] In OWS, the intensity minima in reflectivity *vs* incidence angle measurements indicate conditions at which light is coupled through the prism into the AAO membrane (figure 4.2). The deposited dendrimers have a higher dielectric constant ($\varepsilon_{dendrimer}$ = 2.25)[45] than the liquid they displace (ε_{water} = 1.774). Consequently, G4-polyelectrolyte deposition increases the overall dielectric constant inside the pores (ε_{pore}) and hence the dielectric constant of the entire AAO membrane waveguide (ε_{AAO}). Increases in ε_{AAO} cause the waveguide mode minima to shift to higher angles.[68, 70, 81] Each deposition step was allowed to proceed until no further change was observed in the OWS signal (typically 30 min). Figure 4.3A shows the shifts in the waveguide mode minima for the transverse magnetic (TM) modes after successive LbL deposition steps on an AAO membrane (D_0 = 65 nm) using polyelectrolytes solutions with 100 mM NaCl.

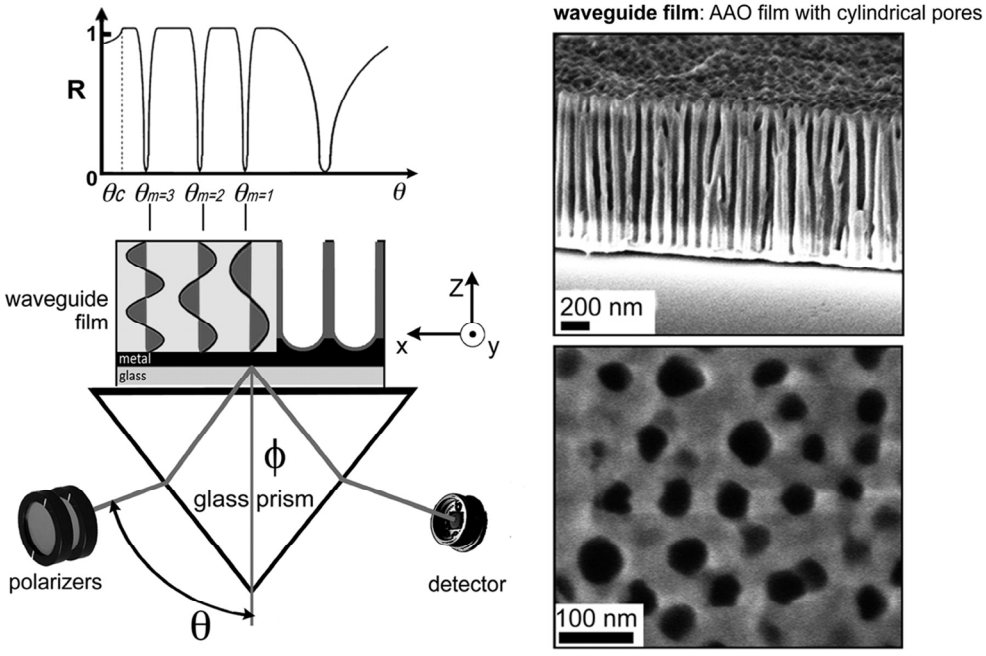

Figure 4.2. Schematic of the OWS set-up used to measure waveguide modes, from which ε_{AAO}, t_{in} and t_{atop} were measured. The reflectivity (R) is measured as a function of the incidence angle (θ). The idealized field distributions of several guided modes are shown. The excitation of these modes is detected as sharp minima in the R *vs* θ measurements. Also shown are SEM images of the cross-section and the top view of an AAO waveguide membrane.

Figure 4.3B shows the cumulative angle shifts of the TM mode minima after each LbL step for the experiment in 3A, and also that of a transverse electric (TE_0) mode. It was observed that the cumulative angle shifts for all modes increased linearly up to 5 layers. However, the angle increase and deposition slowed thereafter, but at different rates for the different modes. Indeed, from the seventh layer on, the angle shifts for TE_0 became negligible, the TM_1 mode shifts became small, and only the TM_2 mode shifts were still obvious. In the waveguide, the electromagnetic fields of the different modes are distributed transversely in and around the AAO membrane with specific nodal patterns (figure 4.2). In particular, higher order modes (*e.g.* TM_2 *vs* TM_1) have larger fractions of their fields distributed towards the edges of the AAO membrane and are more sensitive to processes occurring atop the membrane.[66] Furthermore, TE modes have electric fields polarized in the plane of the membrane and are less sensitive than TM modes to processes atop the membrane. Deposition atop the pores contributes to increases in the AAO waveguide film thickness. Therefore, as discussed in previous reports,[68, 70] the higher shifts of higher order modes (figure 4.3) showed that LbL deposition atop the AAO proceeded continuously but that G4-polyelectrolyte deposition within the nanopores stopped after 3 bilayers.

The changes in ε_{AAO} was derived from the angle changes in the waveguide modes using conventional OWS Fresnel multilayer analysis,[66] and the thickness change on the interior pore surfaces (t_{in}) was in turn calculated from ε_{AAO} using an effective medium theory (EMT)[82] model.[68, 70, 81] The atop thickness (t_{atop}) was also obtained from Fresnel analysis that is constrained by an EMT calculated value of ε_{atop} commensurate with the porosity indicated by ε_{AAO} (figure 4.S1). The thickness values obtained from both the OWS and EMT analyses are the averaged thicknesses of the polyelectrolyte layers, which have finite roughnesses and may have incomplete surface coverage.

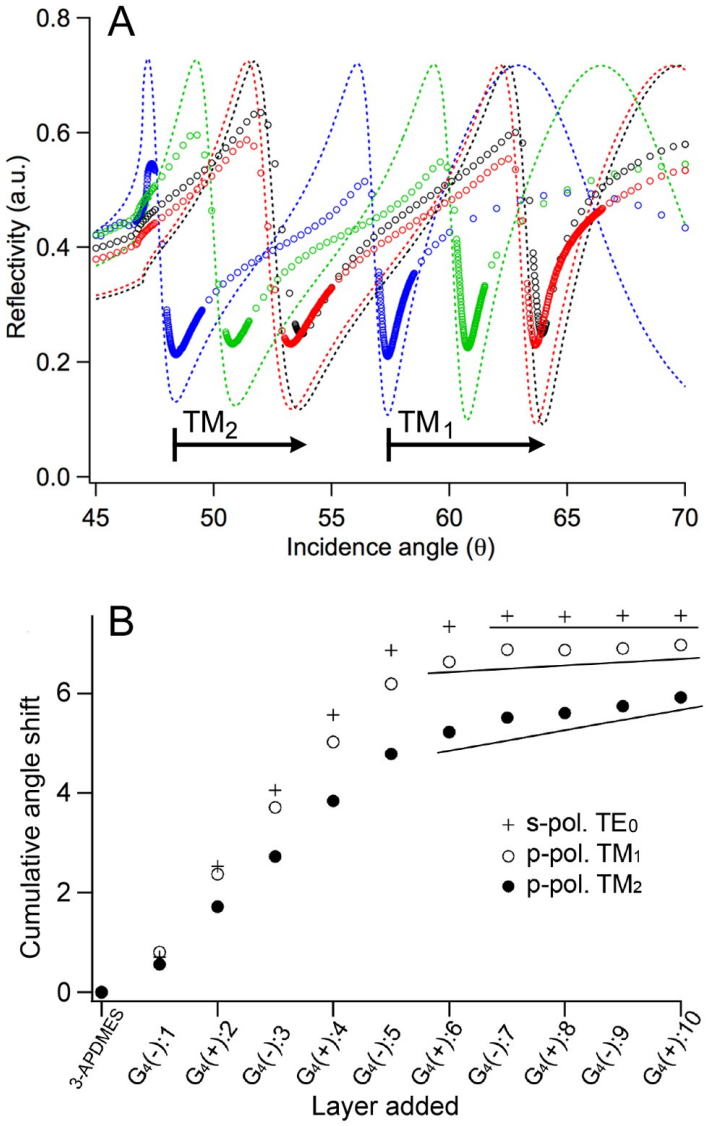

Figure 4.3. (**A**) Optical waveguide measurements (circles) with Fresnel calculations (----) for an APDMES-functionalized AAO waveguide with D_0 = 65 nm in water and after 3, 6 and 9 G4-polyelectrolyte deposition steps from 100 mM NaCl solutions. The waveguide mode minima shift to higher angles as G4-polyelectrolytes deposit within and atop the pores. (**B**) The corresponding angle shifts of the minima of the each TM mode and the TE_0 mode *vs* the number of LbL deposition steps.

Figure 4.4 shows both t_{in} and t_{atop} *vs* deposition steps (n) of the G4-polyelectrolyte film deposited for membranes with a range of different pore diameters (D_0 = 30 – 97 nm). This set of experiments was performed using dendrimer solutions with a moderate NaCl concentration of 100 mM. It is seen that t_{in} initially increased following a common linear trend regardless of the pore diameter. The average increase in t_{in} per polyelectrolyte layer (t_{avg}) within the linear regime was 3.2 nm. This was smaller than the native G4-polyelectrolyte diameter of ~7 nm,[45, 79, 80] and could indicate some surface-induced compression of the dendrimer structure and incomplete dendrimer surface coverage. In

comparison, the thickness of a *dried* G4 dendrimer monolayer in air, measured by AFM, is ~2.5 nm thick[79] and the maximum thickness of our G4 layers measured on both a planar surface and within the pores is t_{max} ~4.5 nm (see discussion related to figure 4.7); t_{max} is consistent with the volume averaged thickness (as measured by OWS or SPR) of a random sequentially adsorbed layer (_55% coverage)[90] of a ~7 nm globular species, and one could relate the ratio t_{avg}/t_{max} ~70% to sub-monolayer coverage. However, the present optical techniques cannot independently measure surface coverage and the effects of surface-induced G4-polyelectrolyte compression and spreading, which is expected to contribute to the reduction in the layer thickness within the initial linear regime, as well as in subsequent deposition steps.

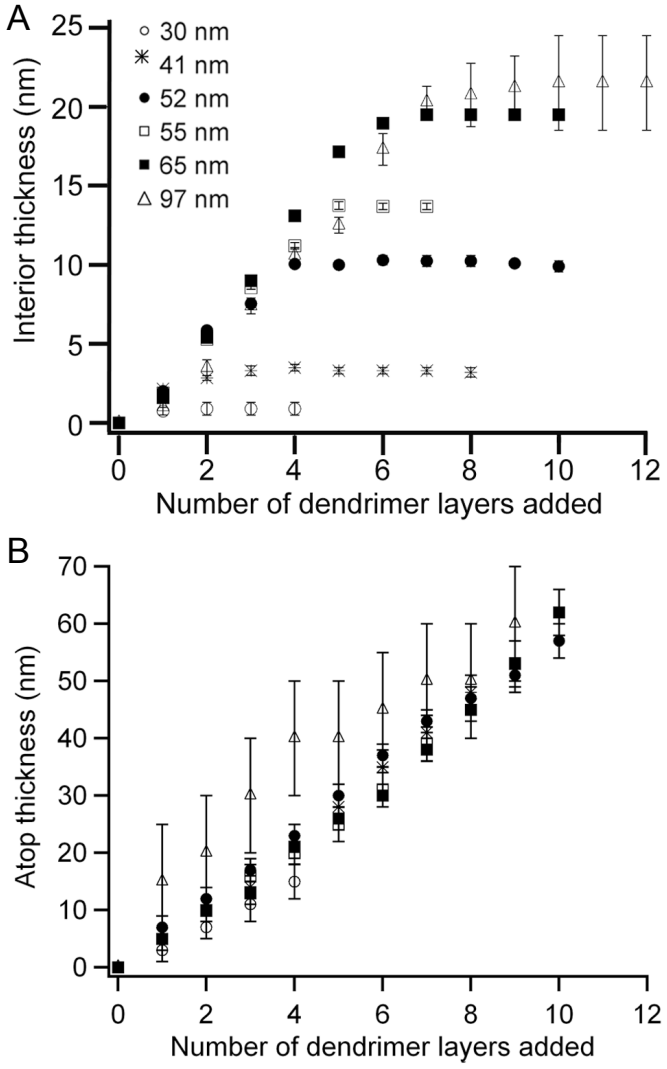

Figure 4.4. Thicknesses of the G4-polyelectrolyte layers deposited from 100 mM NaCl aqueous solutions, within (t_{in}, (**A**)) and atop (t_{atop}, (**B**)) nanoporous AAO membranes with various pore diameters.

As expected, t_{in} saturation values were higher for larger pore diameters. However, the pores were far from being completely filled at these saturation values. For example, with D_0 = 65 nm, t_{in} did not increase beyond 21.5 nm (after 6 LbL steps), while deposition within pores with D_0 = 30 nm immediately reached saturation during the first deposition step.

Figure 4.4B shows the cumulative thickness of G4-polyelectrolytes deposited atop the AAO membrane on surfaces between the pores (t_{atop}). Unlike t_{in}, t_{atop} increased uninterrupted for all deposition steps for all D_0 in a linear fashion. Furthermore, the rates of deposition for different D_0 were essentially coincident with each other, which shows that t_{atop} was unaffected by the presence of the pores (deposition on the inter-pore surface proceeded with the same rate as on a flat surface).[83]

As pointed out above, the interior of the pores were not completely filled even after t_{in} reached saturation values. The pore diameter that remained "open" after successive LbL deposition steps (*i.e. open-pore diameter*, $D_{open\text{-}pore}$) may be estimated from $D_{open\text{-}pore} = D_0 - 2t_{in}$. For example, for D_0 = 65 nm, t_{in} = 21.5 nm, and $D_{open\text{-}pore}$ = 22 nm. (Note that t_{in} measured by OWS, and hence $D_{open\text{-}pore}$, is also the value averaged over the entire length of the pore, since the guided light in the OWS setup had a λ = 633 nm and cannot resolve fine variations through the thickness of the AAO membrane).

The OWS data was also corroborated by *ex situ* scanning electron microscopy (SEM). Figure 4.5 shows that, after 10 deposition steps, the pores in the AAO membrane (D_0 = 65 nm) were not completely filled ($D_{open\text{-}pore}$ = 22 nm). In the AAO cross-section image (figure 4.5A) a layer of organic material can be observed on the pore walls. In the top view image (figure 4.5B), most of the pores are observed to remain open (there is a distribution in the diameters of the pore openings in the AAO prepared, so the smaller pores appeared obscured). Exact values of t_{in} and $D_{open\text{-}pore}$ may not be measured from SEM images as the vacuum environment in the SEM requires dried samples.[79]

The electrostatic screening length λ_{Debye} is < 1 nm at the experimental NaCl concentration of 100 mM. Therefore, one might not have expected the deposition within the pores to be electrostatically hindered when $D_{open\text{-}pore}$ = 22 nm was significantly larger than $d \sim 7$ nm,[45, 78-80] the diameter of the G4-polyelectrolytes. However, as a polyelectrolyte dendrimer enters a nanopore similar in size to itself, due to charge regulation, the electrostatic potential around the polyelectrolyte is altered and the local ion concentration, hence the local screening length, may deviate from bulk values.[52, 59] Furthermore, electrostatic repulsion

arising from polyelectrolytes already deposited near pore entrances within the same deposition step can significantly hinder the transport of same-charge G4-polyelectrolytes further into the pores.

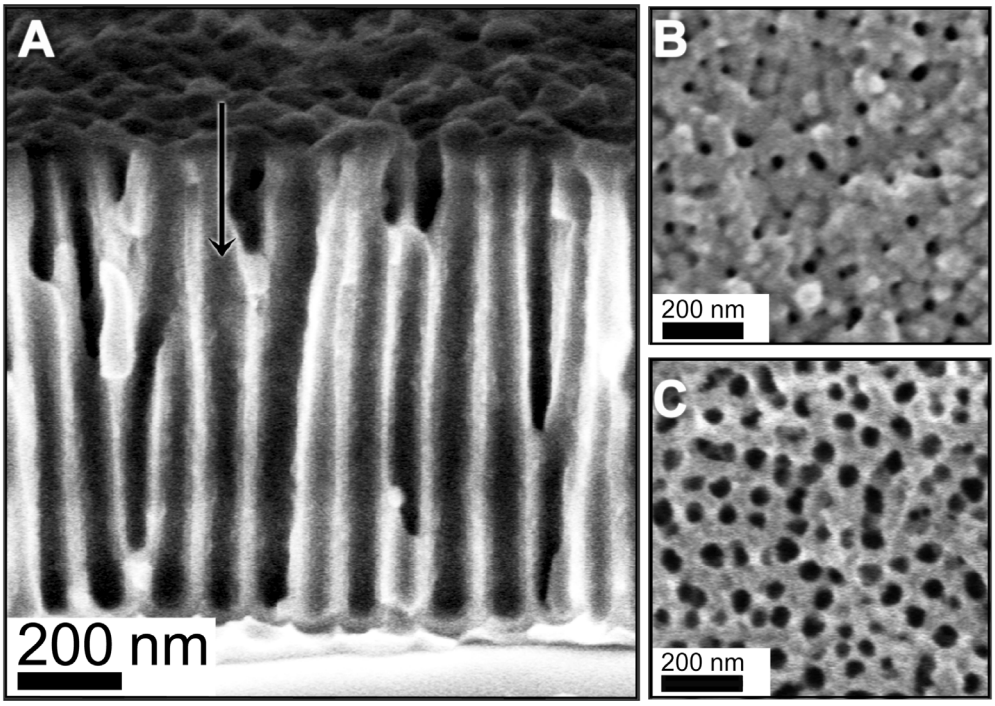

Figure 4.5. SEM images of (**A**) the interior and (**B**) atop the AAO membrane (D_0 = 65 nm) after 10 deposition steps from 100 mM NaCl aqueous solution. (**C**) SEM image of the top surface of the AAO (D_0 = 70 nm) after 6 depositions steps from ultrapure water solutions.

4.2.2. Ionic Strength and Charge Effects on LbL within Nanopores

At a low ionic strength, counterion condensation is predominant and only a fraction of the polyelectrolyte charged groups are dissociated.[84-86] G4 polyelectrolytes dissolved in ultrapure water corresponded to the minimum ionic strength possible in our experimental system. Under these conditions, transport into the pores was expected to be strongly hindered electrostatically due to large λ_{Debye}, and figure 4.6 shows that deposition of G4 polyelectrolyte dendrimer dissolved in ultrapure water within the pores was inhibited for all pore diameters D_0 = 30-116 nm (figure 4.6A). The cumulative layer thickness within the pores did not increase beyond ~1 nm, regardless of the number of deposition steps. Concurrently, the deposition atop the AAO membrane (figure 4.6B) proceeded in an approximately linear fashion with an average layer thickness of ~1.5 nm per deposition step. Accordingly, figure 4.5C (D_0 = 70 nm) shows that the pore diameter remained similar to the

original value even after 6 deposition steps. Compared with the deposition at 100 mM NaCl, t_{atop} without added NaCl was significantly decreased. This decrease with lowering of ionic strength is consistent with LbL deposition on flat homogeneous substrates (see figures 4.6, 4.S2).

Increasing the ionic strength increases the degree of dissociation, and by increasing the NaCl concentration in our G4-polyelectrolyte solutions, we were able to increase the per layer dendrimer thickness on both flat surfaces and within the nanoporous AAO membranes. Higher ionic strengths also induces a denser polyelectrolyte surface packing due to a decrease in the electrostatic screening length, which suppresses repulsion between surface-bound dendrimers and those in solution. However, comparison between figures 4.4 and 4.6 clearly shows that t_{in} was more strongly hindered than t_{atop} by the electrostatic interactions such that 1) G4-polyelectrolyte deposition within the pores was inhibited at low ionic strength for all D_0 tested, and 2) G4-polyelectrolyte per layer thickness was lower within than atop the pores even at 100 mM NaCl.

We further investigated the ionic strength effect by measuring the G4-polyelectrolyte layer thickness over a range of NaCl concentrations (0 – 900 mM). In figure 4.7, the thickness of the initial G4 layer within the pores is plotted, and AAO samples with D_o = 35 and 54 nm were compared with the deposition on a flat surface (measured by SPR).

With no NaCl added, deposition within the pores was almost completely suppressed, while the layer thickness was only ~1 nm on the flat surface. As the NaCl concentration increased, we observed that the G4-polyelectrolyte single layer thickness increased to a maximum of 1.2 nm within the smaller 35 nm pores, and to a maximum of 4.5 nm within both the larger 54 nm pores and on the flat surface. However, to obtain a G4-polyelectrolyte layer thickness within the 54 nm pores similar to that on the flat surface, greater salt concentrations were required. At the same time, at high NaCl concentrations, only a third of the thickness was deposited within the 35 nm pores as compared to within the 55 nm pores. Indeed, the differences between the thicknesses measured on the flat surface and within the pores represent the effect of the cylindrical nanoporous geometry on G4-polyelectrolyte deposition as a function of the pore diameter.

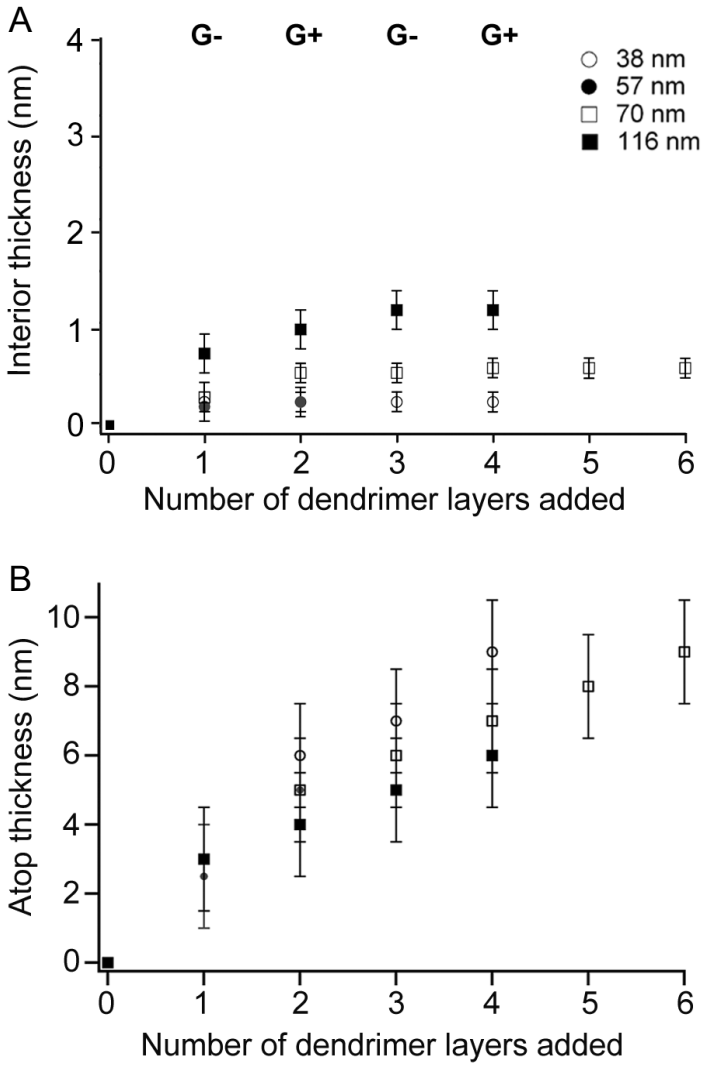

Figure 4.6. Thicknesses of the G4-polyelectrolyte layers deposited from ultrapure water solutions, within (t_{in}, (**A**)) and atop (t_{atop}, (**B**)) nanoporous AAO membranes with various pore diameters.

The nanoscale cylindrical geometry, even under optimal conditions, significantly contributes to hinder the surface adsorption density with respect to flat surfaces. In largest diameter pores, the average thickness of an adsorbed dendrimer layer is ~75% (~3.5 nm) of that on a flat surface (~4.5 nm). Additionally, as shown in figure 4.7, this value drops to ~25% for narrower pores < 40 nm diameter. Altogether, figure 4.7 suggests that the cylindrical nanopore geometry decreases the surface density of adsorbed polyelectrolyte species, and significantly more for pore diameters that are < 40 nm. A significant increase in the solution ionic strength, much greater than indicated by experiments on flat surfaces, is required to efficiently load molecules within the nanopores. Similarly, experiments with linear PAH/PSS polyelectrolytes have shown that increasing the ionic strength by adding 0.5 M NaCl to 100 mM acetate buffer solutions increased by 2-4x the thickness of the

deposited layers within the pores of track-etched polycarbonate membranes (100, 200 and 500 nm pore diameters)[65].

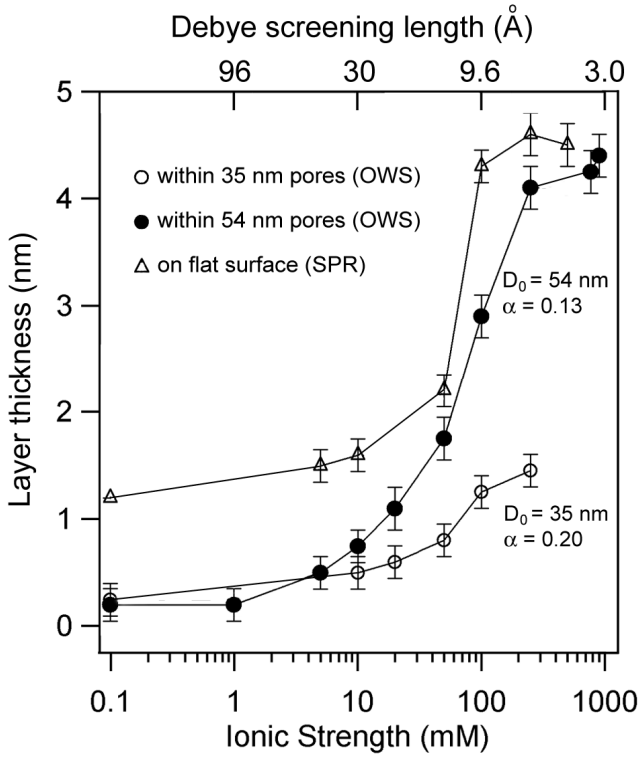

Figure 4.7. Initial G4-polyelectrolyte layer thickness deposited within AAO pores at increasing NaCl concentrations, in cylindrical pores D_0 = 35 and 54 nm (measured by OWS), and on a flat surface (measured by SPR). See figure 4.S5 for the data presented using a linear scale.

We examined in more detail the electrostatic nature of the enhanced hindrance to polyelectrolyte dendrimer transport that results in a large $D_{\text{open-pore}}$ to G4-polyelectrolyte diameter ratio. Figure 4.8A highlights the three regimes observed for the interior layer thickness (t_{in}) *vs* the number of deposition steps (n): 1) initial linear LbL deposition, 2) a transition regime, and 3) complete inhibition of the LbL process within the pores. As discussed in section II, the repulsive potential surrounding pore entrances created by the initial deposition of G4-polyelectrolytes and subsequent charge inversion in these locations likely contributed to the eventual inhibition of further deposition within the nanopores. The transition regime (2) observed is therefore a manifestation of the gradual build-up of an electrostatic barrier surrounding the pore entrances and as the deposition was more and more localized towards the pore openings, since the OWS measurements of t_{in} represents a value averaged over the entire length of the AAO pore. Consequently, the number of polyelectrolyte layers deposited near the pore openings may be more accurately described by the total number of deposition steps in regimes (1) and (2) before the deposition became

completely inhibited (n_{max}, figure 4.8B). Applying this assumption to calculating the local *open-pore diameter* near the pore entrances (D_{local}) yields:

$$D_{local} = D_0 - 2\, n_{max}\, t_{avg} \qquad \text{equation (4.1)}$$

where t_{avg} is the average layer thickness within the linear regime (1).

Figure 4.8C plots D_{local} against D_0 for the experiments performed at 100 mM NaCl. It is seen that D_{local} does not depend on D_0 and the pores became inhibited at an average D_{local} ~ 26 nm. Taken at face value, this represents a G4-polyelectrolyte diameter to screening length ratio $\tau_{local} = D_{local}/2\lambda_{Debye} \sim 14$, which is much larger than conventionally assumed (λ_{Debye} being interpreted as the length over which electrostatic interactions are screened to $1/e$ its full strength).

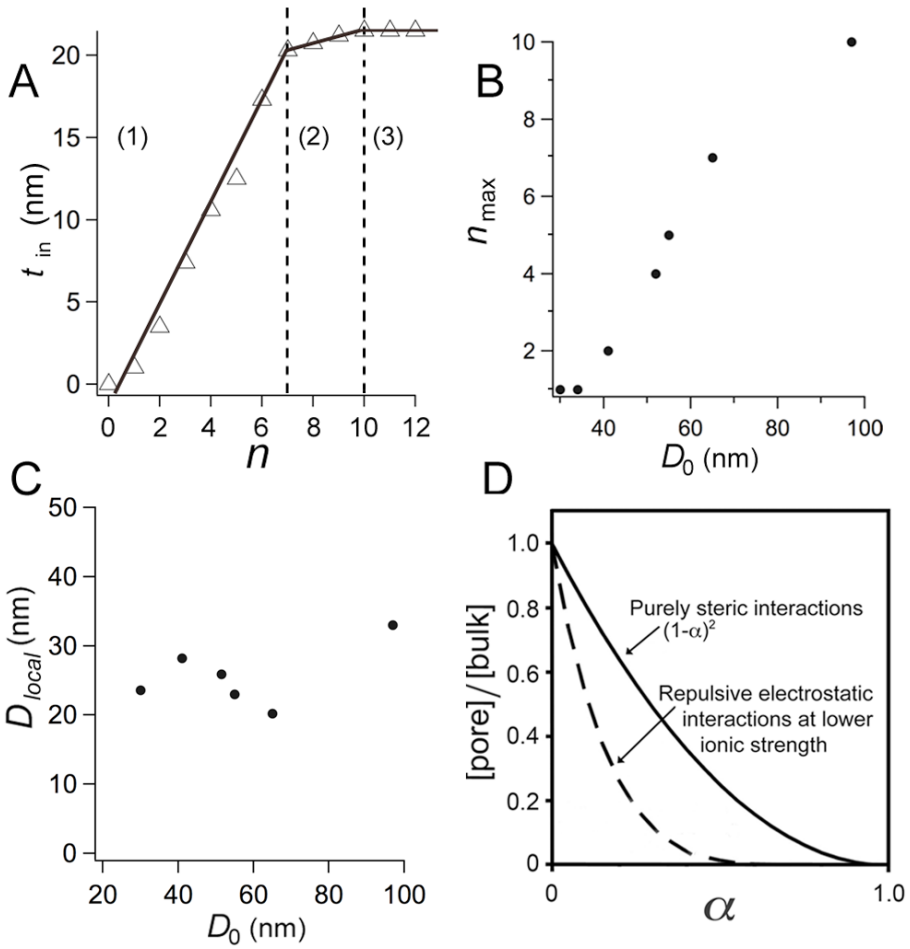

Figure 4.8. (**A**) Dendrimer deposition within D_0 = 97 nm pores from a 100 mM NaCl solution. Three regimes are defined: (1) linear increase with additional deposition steps (n); (2) a transition exhibiting hindered LbL deposition; and (3) inhibited LbL deposition due electrostatic effects in a confined geometry. (**B**) Replot of the data shown in figure 4.4A in terms of the maximum number (n_{max}) of dendrimer layers deposited (regimes (1) plus (2)) *vs* D_0. (**C**) D_{local} calculated from the data shown in figure 4.4A using Equation 4.1.) The partitioning of a charged particle inside cylindrical pores as a function of the relative particle diameter $\alpha = d/D_0$. (Adapted from ref.[57])

Typically, in neutral-charge systems, when the pore diameter ($D_{open\text{-}pore}$) is comparable to the diameter of a transported object (d), *i.e.* large $\alpha \sim 1 \sim d/D_{open\text{-}pore}$, the partitioning ($\Phi$) within cylindrical pores becomes sterically limited according to $\Phi = (1 - \alpha)^2$ (figure 4.8D).[59] Therefore, in the absence of electrostatic interactions, as the limit $\alpha \rightarrow 1$ is approached, dendrimer diffusion into nanopores would already become hindered. In the case of G4-polyelectrolytes, after initial dendrimer deposition around the pore entrances, the repulsive potential that is built up around the pore entrances causes the partitioning of the G4-polyelectrolyte to be even more strongly inhibited than the $(1 - \alpha)^2$ steric limit (figure 4.8D). Hence dendrimer partitioning and LbL deposition within a nanopore are strongly dependent on the electrostatic conditions and may already become negligible at $0 < \alpha << 1$. In fact, our data indicates a limiting value of $\alpha_{limit} = d/D_{local} = 0.27$ for G4-polyelectrolyte at 100 mM NaCl. When the NaCl concentration was halved (50 mM), we measured $D_{local} = 38$ nm and α_{limit} decreased to 0.18 (figure 4.S3). A comparable behavior is observed for a similar set of experiments involving PAH/PSS polyelectrolyte multilayers in track-etched polycarbonate membranes (100 nm diameter pores) under an ionic strength of 100 mM acetate buffer.[65]

If the polyelectrolytes were to be deposited deeper within the pore, the remaining pore entrance (D_{local}) must accommodate both the diameter of the diffusing G4-polyelectrolytes and the electrostatic double layers associated with both the diffusing and surface bound polyelectrolytes. This criterion may be expressed, as one examines the AAO pore geometry and as a first approximation:

$$D_{local} = d + 4\lambda_{local} \qquad \text{equation (4.2)}$$

where λ_{local} is the screening length locally modified in the pores due to charge regulation, and it is assumed that the local screening length is identical over the G4-polyelectrolyte in solution and on the polyelectrolyte covered pore surfaces. At 100 mM NaCl, λ_{local} was 4.75 nm. This local value is much larger than the bulk $\lambda_{Debye} = 0.96$ nm, which may explain the very large limiting values of D_{local} and τ_{local} measured experimentally, and highlights the considerations of charge regulation and local pore geometry that apply to LbL deposition within nanoporous systems.

4.2.3. Selective Formation of Polyelectrolyte Membranes Atop AAO

A polyelectrolyte membrane may be selectively formed atop the AAO membrane while maintaining negligible deposition within the pores, by taking advantage of the hindered polyelectrolyte deposition within the pore at a low ionic strength, and promoting the deposition of G4-polyelectrolytes atop the AAO pores. To begin, G4-polyelectrolytes LbL deposition was carried out with solutions of the dendrimers dissolved in ultrapure water. This was followed by LbL deposition of G4-polyelectrolytes dissolved in 100 mM NaCl or higher ionic strengths. As discussed in section III, the low salt conditions of the first deposition stage prevents deposition within the pores and promoted deposition around the pore openings on the top of the AAO membrane. This first deposition stage effectively narrowed the diameter near the pore openings and inhibited the deposition of additional polyelectrolyte material within the pores in the second stage.

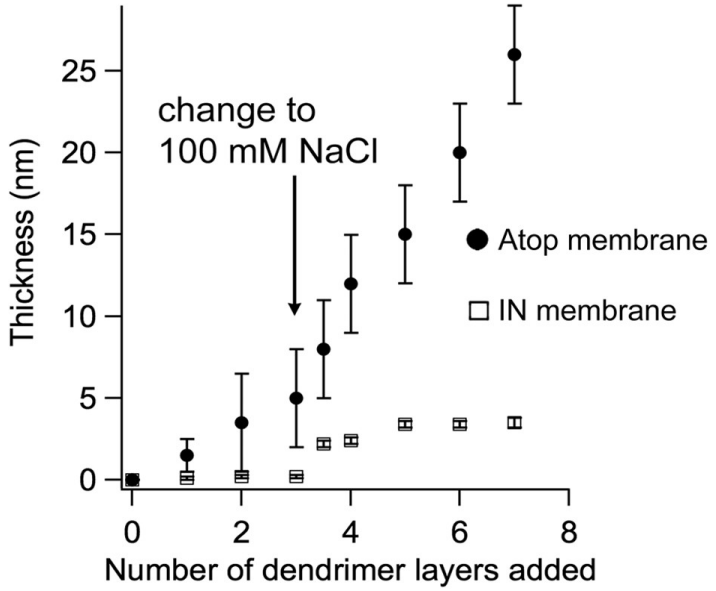

Figure 4.9. t_{atop} (circles) and t_{in} (squares) obtained by a 2-step protocol for selectively depositing a polyelectrolyte membrane atop empty pores: deposition of G4-polyelectrolytes first from an ultrapure water solution, followed by deposition from a solution with a high salt concentration. Deposition from a 100 mM NaCl is shown as an example.

Figure 4.9 shows the evolution of the inner and atop dendrimer film thickness for an AAO membrane with D_0 = 55 nm, for a deposition sequence beginning with ultrapure water solutions (3 layers), followed by a second stage deposition with G4-polyelectrolyte dissolved in solutions with 100 mM NaCl. At the end of the first deposition stage, it was observed that the pores remained essentially empty while the atop thickness grew to an average of ~5 nm. After the NaCl concentration was increased in the second stage, the slope

of the atop deposition curve increased and the atop thickness reached 26 nm at the end of the seventh step. In contrast, the layer thickness increase within the pores in the second high-salt deposition stage was minimal and quickly reached a saturation value. In comparison, a thickness of ~15 nm would be obtained in conventional one-stage deposition at 100 mM NaCl at an equivalent cylindrical pore diameters (see figure 4.4).

The deposition atop the AAO was observed to vary proportionally with the ionic strength and a thick multilayer film could also be deposited this way. Polyelectrolyte membranes have been prepared above porous substrates for applications in nano-filtration and separation applications[87], and also for other practical applications such as gas and chemical separation. The presented method is a simple and effective way to produce pore-spanning multilayer membranes and combines the advantageous properties of multi-component polyelectrolyte based membranes and permeable porous AAO solid supports.

4.3. Conclusion

The effects of pore size and ionic strength on the layer-by-layer (LbL) deposition of polyelectrolyte dendrimers within the cylindrical nanopores of anodic aluminum oxide (AAO) membranes were experimentally studied *in situ* by optical waveguide spectroscopy (OWS). The OWS results were corroborated by ex situ SEM characterization, and were also compared to regular LbL deposition on a planar surface characterized by surface plasmon resonance spectroscopy (SPR). Globular N,N-disubstituted hydrazine phosphorus containing dendrimer polyelectrolytes of the fourth generation (G4-polyelectrolyte) were used as the model deposition species. It was demonstrated that OWS could independently quantify the thickness of the LbL deposited layers within, and atop, the AAO membrane with high sensitivity.

The deposition atop the AAO on surfaces between the pore openings was observed to follow the behavior of linear LbL deposition on a regular planar surface. However, LbL deposition within the cylindrical nanopores, after an initial linear deposition regime, became completely inhibited when the pores were still significantly larger than the diameter of the G4-polyelectrolyte. In fact, the interior deposition was inhibited at all pore diameters investigated (D_0 = 30-116 nm) by adjusting the ionic strength of the deposition solution *via* the NaCl concentration. Unexpectedly, a significant increase in the solution ionic strength, much greater than indicated by experiments on flat surfaces, was required to efficiently load

the polyelectrolytes within the nanopores. Partitioning of dendrimers within the nanopores was already expected to be sterically hindered. Additionally, as deposition initially proceeded near the pore entrances before proceeding further within the pore, the initial charge inversion in the vicinity of the pore entrances created a repulsive potential that further inhibited partitioning of polyelectrolytes in the pores. For example, at 100 mM NaCl at which $\lambda_{Debye} = 1$ ($< d = 7$ nm), the limiting G4-polyelectrolyte to pore diameter ratio was $\alpha_{limit} = 0.27$, and halving the NaCl concentration decreased this to 0.18.

The electrostatic considerations governing macromolecular deposition within cylindrical pores are expected to be strongly influenced by the polyelectrolyte structure, its charge density, the chemical nature of the ionizable groups, as well as the nature and valency of the electrolyte used. The present experimental approach of in situ OWS characterization of the AAO system may be useful for investigating theories describing the transport of charged macromolecules in charged pores. Finally, by manipulating the sequence of LbL deposition at different ionic strengths, a 2-step method was demonstrated to selectively deposit multilayer polyelectrolyte films atop AAO membranes with negligible interior deposition. Such differentiated substrates could have applications in which the compartmentalization of the contents between, or the differential functionalization of the interior and exterior of a nanoporous membrane are required.

4.4. Experimental Section

Materials. Fourth generation N,N-disubstituted hydrazine phosphorus-containing dendrimers having 96 charged terminal groups were synthesized by Majoral *et al.* according to a previously reported protocol.[88] High purity 11-mercaptoundecanoic acid (MUA) and 3-aminopropyldimethylethoxysilane (APDMES) were purchased from Sigma-Aldrich and used as received. Oxalic acid, phosphoric acid, toluene and ethanol were of ACS reagent grade. Ultrapure deionized water (resistivity = 18.2 MΩcm) was obtained from a MilliPore filtration machine (Millipore, Schwalbach, Germany). High refractive index LaSFN9 glass substrates (ε=3.406 at 632.8 nm) were obtained from Hellma Optik (Halle, Germany). 99.999 % Al disks (20 mm x 1 mm) were purchased from Goodfellow (Bad Nauheim, Germany). The optical adhesive used (NOA 83H) was purchased from Norland Products (Cranbury, USA).

AAO waveguide membranes (figure 4.2). AAO membranes were prepared by two different protocols depending on the desired pore diameter. Membranes with pore diameters < 75 nm and lattice spacing = 100 nm, were prepared by anodization of 1 μm sputtered Al films in 0.3 M oxalic acid at 40 V with a 25 nm thick Al layer left un-anodized between the AAO membrane and the glass substrate for optical coupling, according to a previously reported method.[70] For AAO membranes with D_0 > 75 nm and 175 nm lattice spacing, 1.5 μm AAO anodized from bulk Al discs were mounted on LaSFN9 glass slides using an optical adhesive according to another previously reported technique[81]. The Al discs were anodized in 0.05 M oxalic acid at 80 V for 20 min. The pores for all AAO membranes were widened to the desired diameter by etching in 5% wt. phosphoric acid (etch rate = 0.3 nm/min). Furthermore, all AAO membranes were functionalized with a 1~2 nm thick APDMES layer *via* solution silanization by refluxing for 12-15 hours in a 2 vol.% APDMES solution in toluene.[84]

Surface plasmon resonance (SPR). SPR measurements were performed on a purpose-built setup operating at 632.8 nm in the Kretschmann configuration.[66] LASFN9 glass substrates coated with 2 nm Cr and 50 nm Au (by thermal evaporation using an Auto300, BOC Edwards, U.K.) were used. The Au-coated substrates were functionalized with MUA self-assembled monolayers by immersion in 5 mM MUA in ethanol for 3 hours followed by copious rinsing with ethanol.

Optical Waveguide Spectroscopy (OWS). OWS measurements of the AAO membranes prepared on glass slides were performed using the same setup as that used for SPR.[66] The glass-side of an AAO sample was attached to the base of a symmetric LaSFN9 glass prism by optical immersion oil. The laser (λ = 632.8 nm) was incident through the prism-substrate assembly and reflected off the thin metal coupling layer in between the AAO membrane and the glass substrate as the incidence angle (θ) was varied. At specific θ's determined by the thickness and the dielectric constant of the AAO membrane (ε_{AAO}), the laser was coupled into the membrane and such waveguide modes were measured as sharp minima in a reflectivity (R) *vs* θ scan (figure 4.2). Transverse electric (TE) and transverse electric (TM) modes were indexed according to the number of nodes in their electromagnetic field distributions.[66] ε_{AAO} and the thickness of the AAO film, as well as any overlayers on top of the AAO, were calculated from the angles of the waveguide mode reflectivity minima using Fresnel equations, which exactly describe the layered geometry of the AAO waveguide in the OWS setup;[66, 89] tracking the coupling angle of a mode enabled real time, *in situ* monitoring of changes in the thickness or the dielectric constant of the film.[66]

Effective Medium Theory Analysis. The ε_{AAO} measured by OWS includes contributions from both the alumina, the medium filling the pores (*e.g.* water), and any organic thin layer coating the pore surfaces (*i.e.* the G4 polyelectrolyte). Due to the anisotropic nature of the long, cylindrical AAO pores, ε_{AAO} also has an anisotropic component that is described by the infinite, prolate ellipsoid approximation within the Maxwell-Garnett theory:[76, 77]

$$\varepsilon_{AAO}^{\perp} = \varepsilon_{alumina} + f_{pore}(\varepsilon_{pore} - \varepsilon_{alumina}) \qquad \text{equation (4.2A)}$$

$$\varepsilon_{AAO}^{//} = \varepsilon_{alumina}\frac{\varepsilon_{alumina} + \tfrac{1}{2}(1+f_{pore})(\varepsilon_{pore} - \varepsilon_{alumina})}{\varepsilon_{alumina} + \tfrac{1}{2}(1-f_{pore})(\varepsilon_{pore} - \varepsilon_{alumina})} \qquad \text{equation (4.2B)}$$

where $\varepsilon_{AAO}^{\perp}$ and $\varepsilon_{AAO}^{//}$ are, respectively, the dielectric constant components normal and parallel to the AAO membrane surface, f_{pore} is the pore volume fraction within the AAO, $\varepsilon_{alumina} = 2.68$,[70] is the dielectric constant of bulk anodic alumina at λ=632.8 nm, and ε_{pore} is the (effective) dielectric constant within the pores. For a blank AAO film in water, $\varepsilon_{pore} = \varepsilon_{water} = 1.77$. With the addition of an organic film, $\varepsilon_{organic} = 2.25$.[45] on the internal pore surfaces (*e.g.* APDMES or G4-polyelectrolyte), the volume within the pores would be occupied by a combination of the organic material and the pore filling medium (*i.e.* air or solvent). ε_{pore} was then approximated by recursively applying equation 4.2 to the pore-organic film geometry:[68, 69]

$$\varepsilon_{pore}^{\perp} = \varepsilon_{water} + f_{organic}(\varepsilon_{organic} - \varepsilon_{water}) \qquad \text{equation (4.3A)}$$

$$\varepsilon_{pore}^{//} = \varepsilon_{water}\frac{\varepsilon_{water} + \tfrac{1}{2}(1+f_{organic})(\varepsilon_{organic} - \varepsilon_{water})}{\varepsilon_{water} + \tfrac{1}{2}(1-f_{organic})(\varepsilon_{organic} - \varepsilon_{water})} \qquad \text{equation (4.3B)}$$

where $f_{organic}$ is the volume fraction of the organic layer within the cylindrical pores and the organic layer thickness ($d_{organic}$) could then be calculated from $f_{organic}$ and the pore diameter by assuming that the organic film formed a conformal layer on the pore surfaces:

$$d_{organic} = \frac{D_{pore}}{2}(1 - \sqrt{1 - f_{organic}}). \qquad \text{equation (4.4)}$$

Scanning electron microscopy (SEM). SEM measurements were performed with a LEO Gemini 1530 SEM with acceleration voltages between 1 and 6 kV.

Polyelectrolyte dendrimer deposition. G4 polyelectrolyte concentrations were all 1 mg/mL, dissolved in ultrapure water. Different ionic strengths were obtained by directly adding μl aliquots of a 1 or 10 M NaCl stock solution to the prepared solutions. After 4 deposited layers, newly prepared dendrimer solutions were used to ensure that the polyelectrolyte concentration remained constant. The G4-polyelectrolytes were deposited by flowing the solutions through a liquid flow cell, until saturation was reached in the recorded signal (between 15-45 minutes). The samples were all rinsed with ultrapure water

before measuring the R *vs* θ waveguide spectra. A flow rate of 0.4 mL/min was used and the flow cell consisted of a 1 mm thick PDMS stamp with an 8 x 4 mm rectangular opening measuring. At near zero ionic strength, the interior deposition is negligible and all experiments without added salt were only carried out for a maximum of 6 deposited layers.

4.5. References

1. Decher, G.; Schlenoff, J. B., *Multilayer Thin Films: Sequential Assembly of Nanocomposite Materials*. Wiley-VHC: Weinheim, Germany, 2003.

2. Bertrand, P.; Jonas, A.; Laschewsky, A.; Legras, R., Ultrathin Polymer Coatings by Complexation of Polyelectrolytes at Interfaces: Suitable Materials, Structure and Properties. *Macromol. Rapid Commun.* **2000,** *21*, 319-348.

3. De Geest, B. G.; Sanders, N. N.; Sukhorukov, G. B.; Demeester, J.; De Smedt, S. C., Release Mechanisms for Polyelectrolyte Capsules. *Chem. Soc. Rev.* **2007,** *36*, 636-49.

4. Decher, G., Fuzzy Nanoassemblies: Toward Layered Polymeric Multicomposites. *Science* **1997,** *277*, 1232-1237.

5. Decher, G.; Hong, J. D.; Schmitt, J., Buildup of Ultrathin Multilayer Films by a Self-Assembly Process: III. Consecutively Alternating Adsorption of Anionic and Cationic Polyelectrolytes on Charged Surfaces. *Thin Solid Films* **1992,** *210*, 831-835.

6. Iler, R. K., Multilayers of Colloidal Particles. *J. Colloid Interface Sci.* **1966,** *21*, 569-&.

7. Joanny, J. F., Polyelectrolyte Adsorption and Charge Inversion. *Eur. Phys. J. B* **1999,** *9*, 117-122.

8. Anzai, J.; Kobayashi, Y.; Nakamura, N.; Nishimura, M.; Hoshi, T., Layer-by-Layer Construction of Multilayer Thin Films Composed of Avidin and Biotin-Labeled Poly(amine)s. *Langmuir* **1999,** *15*, 221-226.

9. Caruso, F.; Caruso, R. A.; Mohwald, H., Production of Hollow Microspheres from Nanostructured Composite Particles. *Chem. Mat.* **1999,** *11*, 3309-3314.

10. Dobrynin, A. V.; Rubinstein, M., Theory of Polyelectrolytes in Solutions and at Surfaces. *Prog. Polym. Sci.* **2005,** *30*, 1049-1118.

11. Hammond, P. T., Form and Function in Multilayer Assembly: New Applications at the Nanoscale. *Adv. Mat.* **2004,** *16*, 1271-1293.

12. Fendler, J. H., Self-Assembled Nanostructured Materials. *Chem. Mat.* **1996,** *8*, 1616-1624.

13. Feng, C. L.; Zhong, X. H.; Steinhart, M.; Caminade, A. M.; Majoral, J. P.; Knoll, W., Graded-bandgap quantum-dot-modified nanotubes: A sensitive biosensor for enhanced detection of DNA hybridization. *Adv. Mat.* **2007,** *19*, 1933.

14. Kim, D. H.; Karan, P.; Goring, P.; Leclaire, J.; Caminade, A. M.; Majoral, J. P.; Gosele, U.; Steinhart, M.; Knoll, W., Formation of Dendrimer Nanotubes by Layer-by-Layer Deposition. *Small* **2005,** *1*, 99-102.

15. Liu, Y. J.; Wang, Y. X.; Claus, R. O., Layer-by-Layer Ionic self-Assembly of Au Colloids into Multilayer Thin-Films with Bulk Metal Conductivity. *Chem. Phys. Lett.* **1998,** *298*, 315-319.

16. Caruso, F.; Schuler, C., Enzyme Multilayers on Colloid Particles: Assembly, Stability, and Enzymatic Activity. *Langmuir* **2000,** *16*, 9595-9603.

17. He, J. A.; Valluzzi, R.; Yang, K.; Dolukhanyan, T.; Sung, C. M.; Kumar, J.; Tripathy, S. K.; Samuelson, L.; Balogh, L.; Tomalia, D. A., Electrostatic Multilayer Deposition of a Gold-Dendrimer Nanocomposite. *Chem. Mat.* **1999,** *11*, 3268-3274.

18. Wang, Y.; Angelatos, A. S.; Caruso, F., Template Synthesis of Nanostructured Materials *via* Layer-by-Layer Assembly. *Chem. Mat.* **2008,** *20*, 848-858.

19. Zhang, J.; Senger, B.; Vautier, D.; Picart, C.; Schaaf, P.; Voegel, J.-C.; Lavalle, P., Natural Polyelectrolyte Films Based on Layer-by-Layer Deposition of Collagen and Hyaluronic Acid. *Biomaterials* **2005,** *26*, 3353-3361.

20. Hillebrenner, H.; Buyukserin, F.; Kang, M.; Mota, M. O.; Stewart, J. D.; Martin, C. R., Corking Nano Test Tubes by Chemical Self-Assembly. *J. Am. Chem. Soc.* **2006,** *128*, 4236-4237.

21. Hoyer, P.; Masuda, H., Electrodeposited Nanoporous TiO_2 Film by a Two-Step Replication Process from Anodic Porous Alumina. *J. Mater. Sci. Lett.* **1996,** *15*, 1228-1230.

22. Kriha, O.; Zhao, L. L.; Pippel, E.; Gosele, U.; Wehrspohn, R. B.; Wendorff, J. H.; Steinhart, M.; Greiner, A., Organic Tube/Rod Hybrid Nanoribers with ad Ustable Segment Lengths by Bidirectional Template Wetting. *Adv. Funct. Mat.* **2007,** *17*, 1327-1332.

23. Lei, Y.; Cai, W. P.; Wilde, G., Highly Ordered Nanostructures with Tunable Size, Shape and Properties: A New Way to Surface Nano-Patterning Using Ultra-Thin Alumina Masks. *Prog. Mater Sci.* **2007,** *52*, 465-539.

24. Martin, C. R., Nanomaterials - a Membrane-Based Synthetic Approach. *Science* **1994,** *266*, 1961-1966.

25. Masuda, H.; Fukuda, K., Ordered Metal Nanohole Arrays Made by a 2-Step Replication of Honeycomb Structures of Anodic Alumina. *Science* **1995,** *268*, 1466-1468.

26. Mikulskas, I.; Juodkazis, S.; Tomasiunas, R.; Dumas, J. G., Aluminum Oxide Photonic Crystals Grown by a New Hybrid Method. *Adv. Mat.* **2001,** *13*, 1574.

27. Schmid, G., Materials in Nanoporous Alumina. *J. Mater. Chem.* **2002,** *12*, 1231-1238.

28. Steinhart, M.; Wehrspohn, R. B.; Gosele, U.; Wendorff, J. H., Nanotubes by Template Wetting: A Modular Assembly System. *Angew. Chem. Int. Ed.* **2004,** *43*, 1334-1344.

29. O'Sullivan, J. P.; Wood, G. C., The Morphology and Mechanism of Formation of Porous Anodic Films on Aluminium. *Proc. R. Soc. Lond. A* **1970,** *317*, 511-543.

30. Nielsch, K.; Choi, J.; Schwirn, K.; Wehrspohn, R. B.; Gosele, U., Self-Ordering Regimes of Porous Alumina: The 10% porosity rule. *Nano Letters* **2002,** *2*, 677-680.

31. Lee, S. B.; Mitchell, D. T.; Trofin, L.; Nevanen, T. K.; Soderlund, H.; Martin, C. R., Antibody-Based Bio-Nanotube Membranes for Enantiomeric Drug Separations. *Science* **2002,** *296*, 2198-2200.

32. Mitchell, D. T.; Lee, S. B.; Trofin, L.; Li, N. C.; Nevanen, T. K.; Soderlund, H.; Martin, C. R., Smart Nanotubes for Bioseparations and Biocatalysis. *J. Am. Chem. Soc.* **2002,** *124*, 11864-11865.

33. Vlassiouk, I.; Krasnoslobodtsev, A.; Smirnov, S.; Germann, M., "Direct" Detection and Separation of DNA Using Nanoporous Alumina Filters. *Langmuir* **2004,** *20*, 9913-9915.

34. Chiem, N. H.; Harrison, D. J., Microchip Systems for Immunoassay: an Integrated Immunoreactor with Electrophoretic Separation for Serum Theophylline Determination. *Clin. Chem.* **1998,** *44*, 591-598.

35. Figeys, D.; Pinto, D., Lab-on-a-chip: A Revolution in Biological and Medical Sciences. *Anal. Chem.* **2000,** *72*, 330A-335A.

36. Stone, H. A.; Stroock, A. D.; Ajdari, A., Engineering Flows in Small Devices: Microfluidics Toward a Lab-on-a-Chip. *Ann. Rev. Fluid Mech.* **2004,** *36*, 381-411.

37. Wang, J., From DNA Biosensors to Gene Chips. *Nucleic Acids Res.* **2000,** *28*, 3011-3016.

38. Biesheuvel, P. M.; Stroeve, P.; Barneveld, P. A., Effect of Protein Adsorption and Ionic Strength on the Equilibrium Partition Coefficient of Ionizable Macromolecules in Charged Nanopores. *J. Phys. Chem. B* **2004,** *108*, 17660-17665.

39. Bosman, A. W.; Janssen, H. M.; Meijer, E. W., About Dendrimers: Structure, Physical Properties, and Applications. *Chem. Rev.* **1999,** *99*, 1665-1688.

40. Caminade, A. M.; Majoral, J. P., Nanomaterials Based on Phosphorus Dendrimers. *Acc. Chem. Res.* **2004,** *37*, 341-348.

41. Frechet, J. M. J.; Tomalia, D. A., *Dendrimers and Other Dendritic Polymers*. John Wiley & Sons: Chichester, UK, 2001.

42. Majoral, J. P.; Caminade, A. M., Dendrimers Containing Heteroatoms (Si, P, B, Ge, or Bi). *Chem. Rev.* **1999** *99*, 845–880.

43. Yu, Y.; Feng, C.; Caminade, A.-M.; Majoral, J.-P.; Knoll, W., The Detection of DNA Hybridization on Phosphorus Dendrimer Multilayer Films by Surface Plasmon Field Enhanced-Fluorescence Spectroscopy. *Langmuir* **2009,** *25*, 13680-13684.

44. Hou, S.; Harrell, C. C.; Trofin, L.; Kohli, P.; Martin, C. R., Layer-by-Layer Nanotube Template Synthesis. *J.Am. Chem. Soc.* **2004,** *126*, 5674-5675.

45. Kim, B. S.; Lebedeva, O. V.; Kim, D. H.; Caminade, A. M.; Majoral, J. P.; Knoll, W.; Vinogradova, O. I., Assembly and Mechanical Properties of Phosphorus Dendrimer / Polyelectrolyte Multilayer Microcapsules. *Langmuir* **2005,** *21*, 7200-7206.

46. Launay, N.; Caminade, A. M.; Lahana, R.; Majoral, J. P., A General Synthetic Strategy for Neutral Phosphorus-Containing Dendrimers. *Angew. Chem. Int. Ed.* **1994,** *33*,1589–1592.

47. Adler, P. M., Influence of Colloidal Forces on a Closely-Fitting Sphere in a Fluid-Filled Tube. *Physicochemical Hydrodynamics* **1983,** *4*, 1-10.

48. Bhattacharjee, S.; Sharma, A., Apolar, Polar, and Electrostatic Interactions of Spherical Particles in Cylindrical Pores. *J.Coll. Interf. Sc.* **1997,** *187*, 83-95.

49. Deen, W. M., Hindered Transport of Large Molecules in Liquid-Filled Pores. *AlChE J.* **1987,** *33*, 1409-1425.

50. Deen, W. M.; Bohrer, M. P.; Epstein, N. B., Effects of Molecular-Size and Configuration on Diffusion in Microporous Membranes. *AlChE J.* **1981,** *27*, 952-959.

51. Papadopoulos, K. D.; Kuo, C. C., The Van der Waals Interaction between a Colloid and Its Host Pore. *Colloids Surf.* **1990,** *46*, 115-125.

52. Pujar, N. S.; Zydney, A. L., Charge Regulation and Electrostatic Interactions for a Spherical Particle in a Cylindrical Pore. *J. Colloid Interface Sci.* **1997,** *192*, 338-349.

53. Smith, F. G.; Deen, W. M., Electrostatic Double-Layer Interactions for Spherical Colloids in Cylindrical Pores. *J. Colloid Interface Sci.* **1980,** *78*, 444-465.

54. Han, J. Y.; Fu, J. P.; Schoch, R. B., Molecular Sieving Using Nanofilters: Past, Present and Future. *Lab on a Chip* **2008,** *8*, 23-33.

55. Jiang, X. Q.; Mishra, N.; Turner, J. N.; Spencer, M. G., Diffusivity of Sub-1,000 Da Molecules in 40 nm Silicon-Based Alumina Pores. *Microfluid. Nanofluid.* **2008,** *5*, 695-701.

56. Keh, H. J.; Chiou, J. Y., Electrophoresis of a Colloidal Sphere in a Circular Cylindrical Pore. *AlChE J.* **1996,** *42*, 1397-1406.

57. Smith, F. G.; Deen, W. M., Electrostatic Effects on the Partitioning of Spherical Colloids between Dilute Bulk Solution and Cylindrical Pores. *J. Colloid Interface Sci.* **1983,** *91*, 571-590.

58. Causserand, C.; Lafaille, J. P.; Aimar, P., Transmission of Bio-Molecules through Porous Membranes Triggered by an External Electric-Field. *J. Controlled Release* **1994,** *29*, 113-123.

59. Deen, W. M.; Smith, F. G., Hindered Diffusion of Synthetic Poly-Electrolytes in Charged Microporous Membranes. *J. Membr. Sci.* **1982,** *12*, 217-237.

60. Verbrugge, M. W.; Schneider, E. W.; Conell, R. S.; Hill, R. F., The Effect of Temperature on the Equilibrium and Transport-Properties of Saturated Poly(Perfluorosulfonic Acid) Membranes. *J. Electrochem. Soc.* **1992,** *139*, 3421-3428.

61. Wong, C. T. A.; Muthukumar, M., Polymer Capture by Electro-Osmotic Flow of Oppositely Charged Nanopores. *J. Chem. Phys.* **2007,** *126*.

62. Bezrukov, S. M.; Vodyanoy, I.; Parsegian, V. A., Counting Polymers Moving

through a Single-Ion Channel. *Nature* **1994,** *370*, 279-281.

63. Chang, H.; Kosari, F.; Andreadakis, G.; Alam, M. A.; Vasmatzis, G.; Bashir, R., DNA-Mediated Fluctuations in Ionic Current through Silicon Oxide Nanopore Channels. *Nano Letters* **2004,** *4*, 1551-1556.

64. Saleh, O. A.; Sohn, L. L., Quantitative Sensing of Nanoscale Colloids Using a Microchip Coulter Counter. *Rev. Sci. Instrum.* **2001,** *72*, 4449-4451.

65. Roy, C. J.; Dupont-Gillain, C.; Demoustier-Champagne, S.; Jonas, A. M.; Landoulsi, J., Growth Mechanism of Confined Polyelectrolyte Multilayers in Nanoporous Templates. *Langmuir* **2010,** *26*, 3350-3355.

66. Knoll, W., Interfaces and Thin Films as Seen by Bound Electromagnetic Waves. *Annu. Rev. Phys. Chem.* **1998,** *49*.

67. Dürr, M.; Menges, G.; Knoll, W.; Yasuda, A.; Nelles, G., Direct Measurement of Increased Light Intensity in Optical Waveguides Coupled to a Surface Plasmon Spectroscopy Setup. *App. Phys. Lett.* **2007,** *91*, 021113-021115.

68. Lau, K. H. A.; Tan, L. S.; Tamada, K.; Sander, M. S.; Knoll, W., Highly Sensitive Detection of Processes Occurring Inside Nanoporous Anodic Alumina Templates: A waveguide optical study. *J. Phys. Chem. B* **2004,** *108*, 10812-10818.

69. Lau, K. H. A.; Cameron, P. J.; Duran, H.; Abou-Kandil, A. I.; Knoll, W., Nanoporous Thin Films as Highly Versatile and Sensitive Waveguide Biosensors; in *Surface Design: Applications in Bioscience and Nanotechnology*, Förch, R.; Schönherr, H.; Jenkins, A. T. A., Eds. Wiley-VCH Verlag: Weinheim, 2009; pp 383-401.

70. Lau, K. H. A.; Duran, H.; Knoll, W., In situ Characterization of N-carboxy Anhydride Polymerization in Nanoporous Anodic Alumina. *J. Phys. Chem. B* **2009,** *113*, 3179-3189.

71. Cameron, P. J.; Jenkins, A. T. A.; Knoll, W.; Marken, F.; Milsom, E. V.; Williams, T. L., Optical Waveguide Spectroscopy Study of the Transport and Binding of Cytochrome c in Mesoporous Titanium Dioxide Electrodes. *J. Mater. Chem.* **2008,** *18*, 4304-4310.

72. Awazu, K.; Rockstuhl, C.; Fujimaki, M.; Fukuda, N.; Tominaga, J.; Komatsubara, T.; Ikeda, T.; Ohki, Y., High Sensitivity Sensors Made of Perforated Waveguides. *Optics Express* **2007,** *15*, 2592-2597.

73. Fujimaki, M.; Rockstuhl, C.; Wang, X. M.; Awazu, K.; Tominaga, J.; Koganezawa, Y.; Ohki, Y.; Komatsubara, T., Silica-Based Monolithic Sensing Plates for Waveguide-Mode Sensors. *Optics Express* **2008,** *16*, 6408-6416.

74. Reimhult, E.; Kumar, K.; Knoll, W., Fabrication of Nanoporous Silicon Nitride and Silicon Oxide Films of Controlled Size and Porosity for Combined Electrochemical and Waveguide Measurements. *Nanotechnology* **2007,** *18*, 275303.

75. Kim, D. H.; Lau, K. H. A.; Joo, W.; Peng, J.; Jeong, U.; Hawker, C. J.; Kim, J. K.; Russell, T. P.; Knoll, W., An Optical Waveguide Study on the Nanopore Formation in Block Copolymer/Homopolymer Thin Films by Selective Solvent Swelling. *J. Phys. Chem. B* **2006,** *110*, 15381-15388.

76. Egan, W. G.; Aspnes, D. E., Finite-Wavelength Effects in Composite Media. *Thin Solid Films* **1982,** *89*, 249-262.

77. Foss, C. A.; Tierney, M. J.; Martin, C. R., Template Synthesis of Infrared-Transparent Metal Microcylinders: Comparison of Optical Properties With the Predictions of Effective Medium Theory. *J. Phys. Chem.* **1992,** *96*, 9001-9007.

78. Schmid, G.; Emmrich, E.; Majoral, J.-P.; Caminade, A.-M., The Behavior of Au55 Nanoclusters on and in Thiol-Terminated Dendrimer Monolayers. *Small* **2005,** *1*, 73-75.

79. Emmrich, E.; Franzka, S.; Schmid, G.; Majoral, J.-P., Monolayers of a Fourth-Generation Thiol-Terminated Dendrimer. *Nano Letters* **2002,** *2*, 1239-1242.

80. Leclaire, J.; Coppel, Y.; Caminade, A.-M.; Majoral, J.-P., Nanometric Sponges Made of Water-Soluble Hydrophobic Dendrimers. *J. Am. Chem. Soc.* **2004,** *126*, 2304-2305.

81. Lazzara, T. D.; Lau, K. H. A.; Knoll, W., Mounted Nanoporous Anodic Alumina Thin Films As Planar Optical Waveguides. *J. Nanosc. Nanotech.* **2010,** *10*, 4293-4299.

82. Choy, T. C., *Effective Medium Theory: Principles and Applications*. 1st ed.; Oxford University Press: New York, 1999; Vol. 102.

83. The agreement with the deposition atop the AAO membranes with D_0 = 97 nm was looser. This can likely be attributed to the modifications in AAO preparation conditions in order to produce membranes with such large pores, which also produced a wider spread in the distributions of pore diameters and average center-to-center distance ($\lambda_{C\text{-}C}$) between pores (see Experimental).

84. Glinel, K.; Moussa, A.; Jonas, A. M.; Laschewsky, A., Influence of Polyelectrolyte Charge Density on the Formation of Multilayers of Strong Polyelectrolytes at Low Ionic Strength. *Langmuir* **2002,** *18*, 1408.

85. Borisov, O. V.; Zhulina, E. B., Effects of Ionic Strength and Charge Annealing in Star-Branched Polyelectrolytes. *Eur. Phys. J. B* **1998,** *4*, 205-217.

86. Steitz, R.; Jaeger, W.; Klitzing, R., Influence of Charge Density and Ionic Strength on the Multilayer Formation of Strong Polyelectrolytes. *Langmuir* **2001,** *17*, 4471.

87. Bruening, M. L.; Dotzauer, D. M.; Jain, P.; Ouyang, L.; Baker, G. L., Creation of Functional Membranes Using Polyelectrolyte Multilayers and Polymer Brushes. *Langmuir* **2008,** *24*, 7663–7673.

88. Loup, C.; Zanta, M. A.; Caminade, A. M.; Majoral, J. P.; Meunier, B., Preparation of Water-Soluble Cationic Phosphorus-Containing Dendrimers As DNA Transfecting Agents. *Chem. Eur. J.* **1999,** *5*, 3644-3650.

89. Raether, H., *Surface-Plasmons on Smooth and Rough Surfaces and on Gratings*. Springer: Berlin/Heidelberg, 1988; Vol. 111.

90. Talbot, J.; Tarjus, G.; Van Tassel, P. R.; Viot, P. From CarParking to Protein adsorption: An Overview of Sequential Adsorption Processes. *Colloids Surf., A* **2000**, *165*, 287–324.

Acknowledgements. T. D. Lazzara acknowledges the award of a doctoral scholarship from FQRNT: *Le Fonds Québécois de la Recherche sur la Nature et les Technologies*. We thank Gunnar Glasser at the MPI for Polymer Research for electron microscopy. We also thank Stefan Schmidt and Dr. Peter Detemple at the Institut für Mikrotechnik Mainz for providing Al thin film deposition services.

Supporting Information Available. The supp. info. section includes additional experimental data on the SPR experiments for the LbL dendrimer multilayer formation on a flat surface. The atop *vs* interior deposition at 500 mM NaCl is compared with 50 and 100 mM concentrations; SEM images show the formation of a multilayer film atop and corresponding OWS data. Further details on the layer model used for Fresnel simulations and on the increase of the dielectric constant of the alumina layer are presented. This material is available free of charge via the Internet at http://pubs.acs.org.

4.6. Supporting information

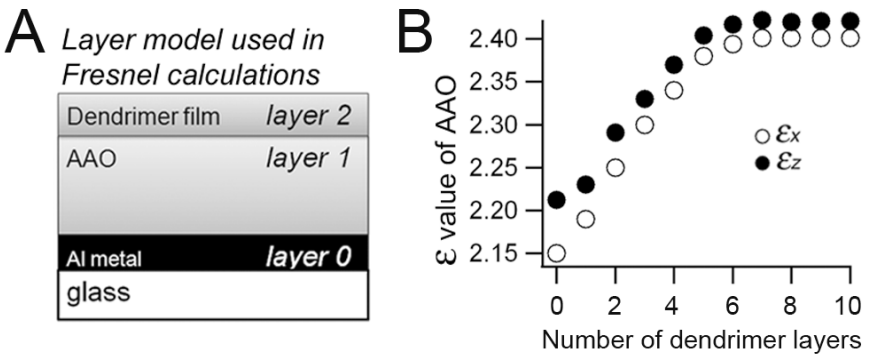

Figure 4.S1: (**A**) Layer model used for Fresnel calculations to obtain an interior (layer 1) and atop (layer 2) thickness from fitting the experimental waveguide modes spectra of LbL deposition on AAO. Both layers 1 and 2 are composite layers modeled by EMT: an alumina matrix interspersed with cylindrical pores in layer one; and a dendrimer matrix interspersed with cylindrical pores in layer two. For technical discussions of the calculations, please refer to the Experimental, and ref. 66. (**B**) Evolution of the dielectric constant of the alumina membrane after multiple LbL dendrimer depositions from 100 mM NaCl solutions, in D_0 = 65 nm.

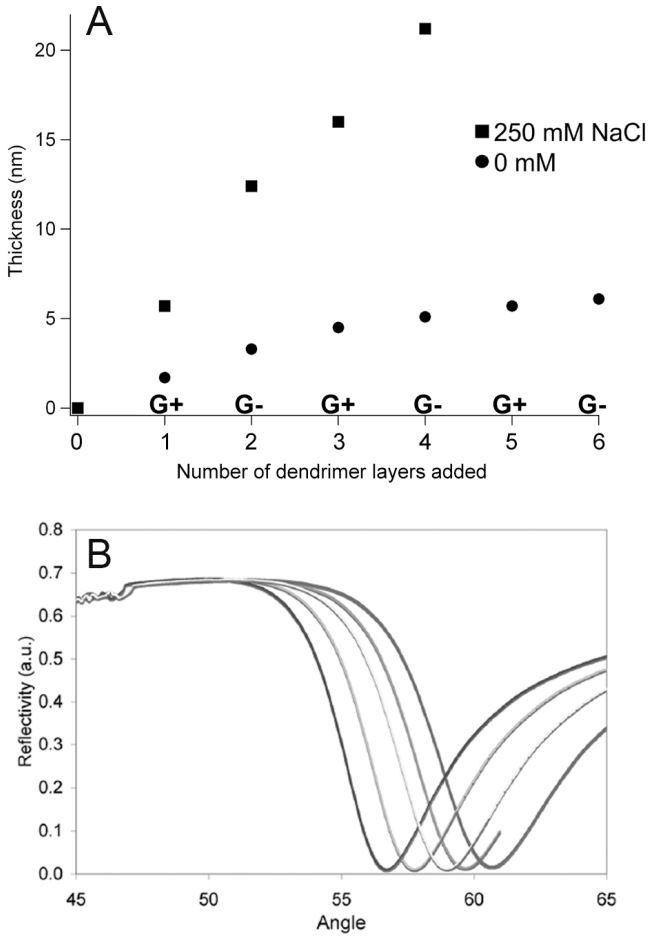

Figure 4.S2: (**A**) Optical thickness increase of polyelectrolyte dendrimer (ε=2.25) multilayers from depositions of dendrimers dissolved in deionized water and in 250 mM NaCl. (**B**) SPR curves after each polyelectrolyte dendrimer addition from 250 mM NaCl solutions.

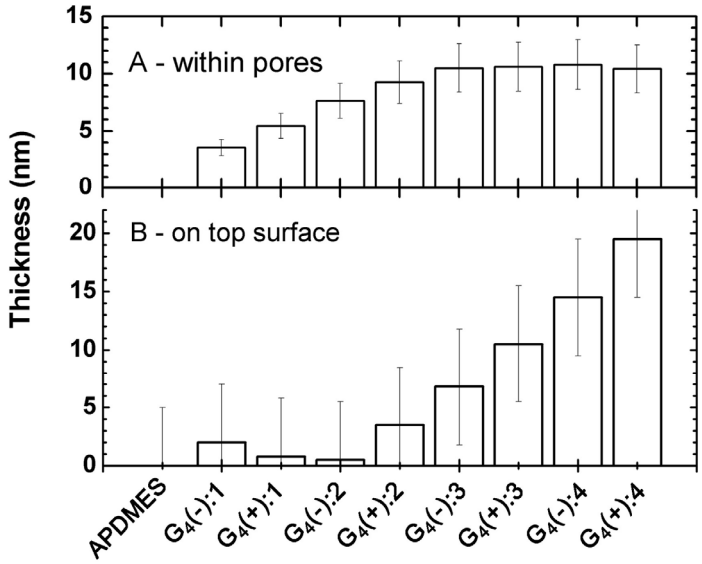

Figure 4.S3: Comparison of the LbL deposition (50 mM NaCl) process within the pores (**A**) and on the top surface of the AAO film (**B**). (A) was obtained by EMT fitting of ε_{AAO} measured from the R *vs* θ data and corresponding Fresnel calculations, while (B) was obtained directly from the change in film thickness obtained from the same Fresnel calculations using an EMT calculated t_{atop}. The uncertainty plotted in (A) is ~20%, and is ± 5 nm in (B).

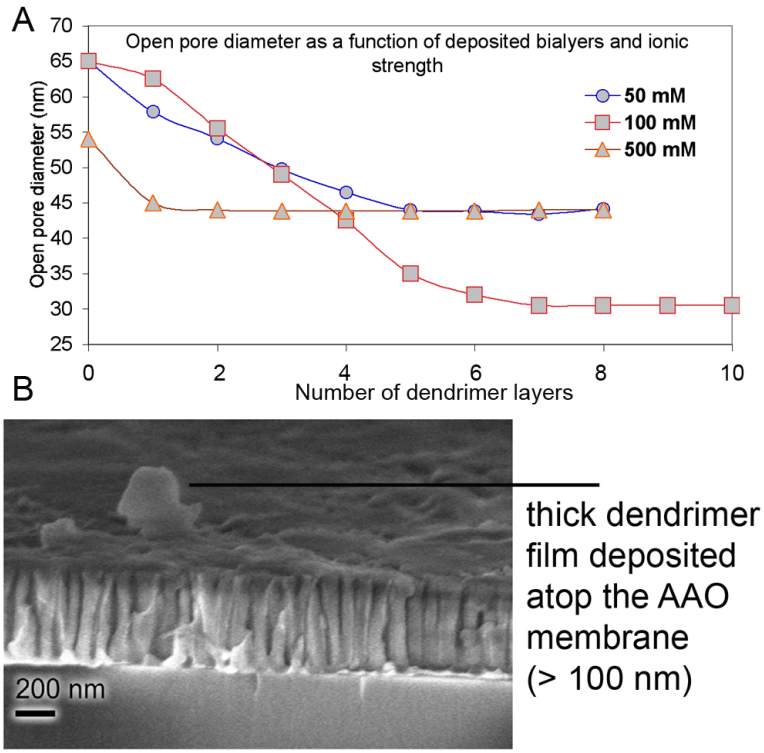

Figure 4.S4: (**A**) Open pore diameter reduction as the number of polyelectrolyte dendrimer layers increases. Because of excessive aggregation at high ionic strength, thick dendrimer films develop atop the alumina template (**B**). This limits the interior deposition of dendrimers and moderate salt concentrations are required to achieve maximum loading of the pore interior.

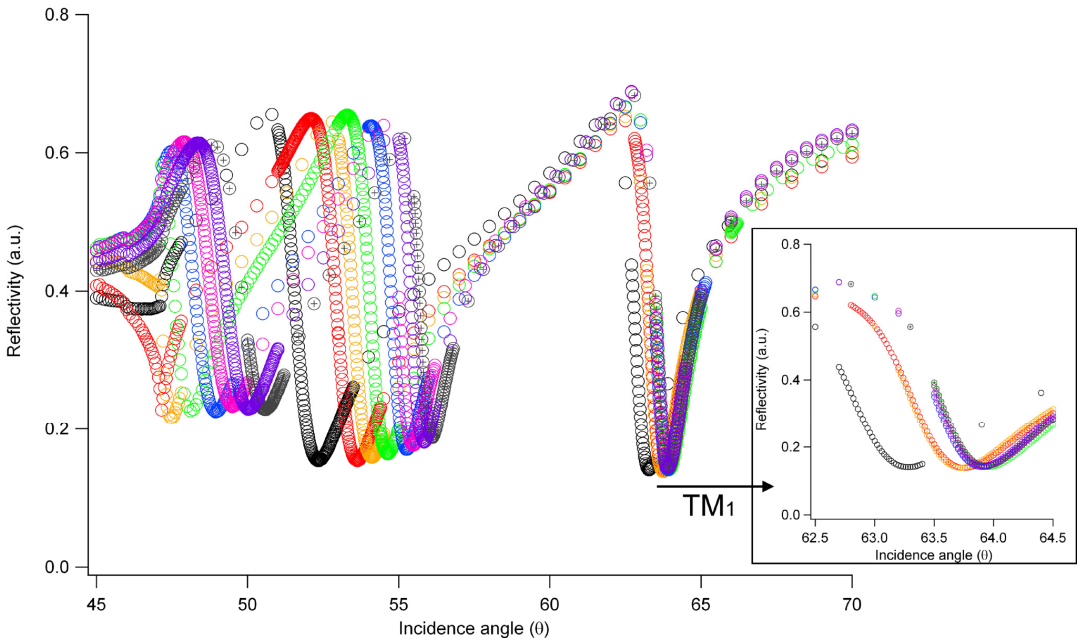

Figure 4.S5: Transverse magnetic waveguide modes for deposition on a 55 nm pore AAO membrane from 500 mM NaCl solutions of dendrimers (1 mg/mL). The saturation in TM1 mode (see inset) indicates that the pore interior remains void. On the other hand, the greater shifts in TM2 and TM3 indicate that a thick multilayer film deposits atop the AAO membrane as shown in the SEM image in figure 4.S4. The angular TM mode shifts should also be compared with Figure 4.3: dendrimer incorporation within the pores is observed as a positive angular shift, for all TM modes.

Chapter 5

The Importance of Macromolecular Shape and Interactions in Layer-by-Layer Assemblies within Cylindrical Nanopores

By:
Thomas D. Lazzara,[†] *K. H. Aaron Lau,*[‡] *Wolfgang Knoll,*[δ] *Andreas Janshoff,*[§] *Claudia Steinem*[†]

Graphical abstract:

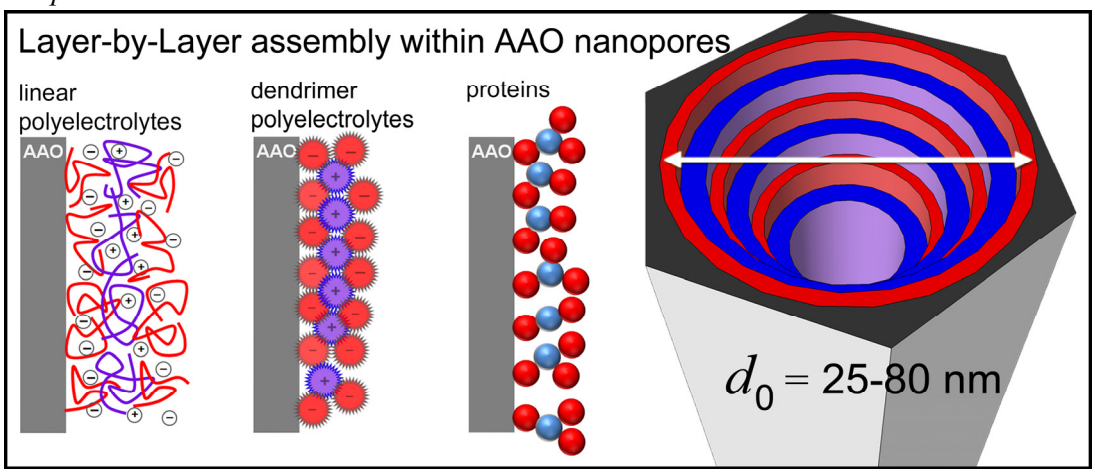

Manuscript prepared for submission

2011

[†] Institute of Organic and Biomolecular Chemistry, Tamannstrasse 2, 37077, Göttingen, Germany.
[‡] Department of Biomed. Eng., Northwestern University, 2145 Sheridan Road, Evanston, IL 60202, USA.
[§] Institute of Physical Chemistry, Tamannstrasse 6, 37077, Göttingen, Germany.
[δ] Austrian Institute of Technology, Donau City Strasse 1, 1220 Vienna, Austria.

Abstract

Layer-by-layer (LbL) deposition of macromolecules within the cylindrical nanopores of anodic aluminum oxide (AAO) membranes was experimentally studied. Avidin and biotinylated-bovine serum albumin proteins and linear polyelectrolytes (linear-PEs) were used, both species being of similar molecular weight (M_w). These results were compared to previous LbL of dendrimer polyelectrolytes (dendrimer-PEs). AAO has aligned cylindrical, non-intersecting pores and was prepared as thin-films on glass substrates. AAO was employed as a planar optical waveguide so as to monitor, *in situ*, the LbL process by optical waveguide spectroscopy (OWS). Studying the growth of LbL within the cylindrical AAO geometry for different pore diameters (d_0) was used to estimate the actual effective volume occupied by the deposited macromolecular species. LbL growth was inhibited at different maximum number of LbL steps (n_{max}), which varied depending on the macromolecular species; n_{max} was greatest for linear-PEs, while proteins had the lowest value. The cylindrical pore geometry imposes a physical limit to LbL growth; n_{max} was therefore strongly dependent on the overall internal structure of the LbL films. For all macromolecular species, deposition was inhibited in native AAO pore d_0 = 25-30 nm. Both OWS and electron microscopy showed that LbL growth became inhibited when approaching a local pore diameter (d_{local}) of 25-35 nm for linear-PEs, a similar size to that of native d_0 pores. Electrostatic LbL allowed for molecular rearrangement and compact layers such that optical thickness values provided a realistic approximation of the steric limit described by d_{local}. The size of the loosely packed protein multilayers was underestimated by the optical thickness, and a reasonable estimation of d_{local} was obtained by using the macromolecular diameter to evaluate the LbL film thickness. Our results and experimental approach may be used to further understand and improve the tailoring of the internal structure of macromolecular multilayer assemblies in nanoporous environments.

Keywords: nanoporous substrates, cylindrical nanopores, polyelectrolytes dendrimers, avidin-biotin, proteins, layer-by-layer self-assembly, optical lightmode waveguide spectroscopy

5.1. Introduction

Layer-by-Layer (LbL) is a versatile technique[1-2] to create functional films and consists in the sequential deposition of functional adsorbing components, to generate multilayered structures. LbL allows the incorporation of different functional materials within a single surface structure and is typically governed by electrostatic self-assembly[2-3] of components or molecular recognition pairs.[4-5] Therefore, as long an interaction is present between the LbL building blocks, species with different sizes and structures can be step-wise incorporated within functional thin-film structures. Homogeneous and heterogeneous layered mixing of nanometer sized species such as polyelectrolytes, proteins and nanoparticles has lead to various technologically functional surface coatings[6-10] and the preparation of capsules[11-12] and one-dimensional materials such as nanotubes by template-replication.[13-15] LbL structures on flat surfaces have been well characterized with sub-nanometer sensitivity using a number of surface analysis techniques such as surface plasmon resonance, ellipsometry or thin-film reflectometry.[16-18] LbL structures formed inside porous systems,[2] such as within films of colloidal particles or cylindrical nanoporous membranes, are not as easily characterized as on planar surfaces. Direct investigation of surface processes occurring within nano-sized pores has been hampered by the limited availability of *in situ*, high-sensitivity, surface characterization techniques that can probe changes occuring inside the nanoporous morphologies. However, optical waveguide spectroscopy[19-22] (OWS) and thin-film reflectometry[23-24] are two optical techniques that can used to independently characterize the thickness and refractive index of optically transparent thin dielectric films. OWS can be used for *in situ* monitoring of processes occurring within nanoporous templates with sub-nanometer sensitivities, through time-resolved measurement of the increasing dielectric constant. The nano-porosity ensures minimal scattering loses at visible or longer wavelengths, and an effective medium theory (EMT) approximation can be used to estimate the amount of macromolecular adsorbed material within the AAO nanopores in relation to the experimentally observed refractive index changes.

Nanoporous anodic aluminum oxide (AAO) is a nanoporous material that has been widely used due to its self-organized predictable structure that is composed of non-intersecting, hexagonally close-packed, cylindrical pores running straight through the AAO membrane thickness with conveniently adjustable monodisperse pore diameters, degree of lattice spacing, and membrane thickness.[25-27] AAO with highly ordered pores can be prepared with

minimal equipment requirements and relies on the simple anodization of Al metal under a constant applied potential, making it well suited as a model nanoporous system.[28-30]

We have shown in the past that macromolecular transport of polyelectroyte dendrimers in the cylindrical pore of AAO was hindered by steric effects at low pore sizes and inhibited by electrostatic repulsion at low ionic strengths.[20] The electrostatic hindrance can be overcome by sufficiently increasing the ionic strength above a certain threshold, > 100 mM NaCl for polyelectrolyte dendrimers. Obviously, many factors play a role in the multilayer growth process. The confined cylindrical nanoporous environment, in particular, imposes a physical barrier that limits the amount of material that can be step-wise incorporated. Confinement in nanoporous environments can lead to significantly different behaviors than observed on planar surfaces. For example, the apparent pKa values of cationic polymer brushes, *a priori* polymerized in 10-40 nm pore diameters, can be shifted more than a full pH unit lower due to a different chemical environment that affects the dissociation constant within the nanopores. Furthermore LbL formation of polyelectrolyte species within AAO has been shown to be strongly influenced by pH[13] and by ionic strength, [20] to such an extent that interior deposition can be completely inhibited due to electrostatic repulsion. For the fabrication of LbL structures under optimal charge screening conditions, considerations related to confinement are typically not observed given that the deposition process becomes hindered or terminates at the limit where these effects become important, for pore diameters around 20-30 nm.

Even under optimal pore-filling conditions, steric limitations to LbL growth in cylindrical nanopores is always present and parameters such as the macromolecular structure and shape of LbL building block, as well as the nature of the self-assembly interactions are factors that can directly influence the geometrical arrangement and shape of the growing multilayer film. In this contribution, the LbL deposition within AAO membranes of linear polyelectrolytes (linear-PEs) and proteins was contrasted to the previously studied behavior of dendrimer polyelectrolytes (dendrimer-PEs).[20] Deposition for AAO with d_0 = 63-66 nm, were first compared with surface plasmon resonance (SPR) measurements of LbL deposition on a planar surface gold surface. Then the LbL experiments were carried out in different d_0 pores, ranging from 25 to 80 nm, until the interior deposition became inhibited. The LbL growth in different d_0 was compared, allowing the determination of the average thickness of an LbL step, in terms of actual volume occupied, rather than the optical thickness that was estimated from effective medium theory (EMT) approximation. In such confined cylindrical geometry, the interior deposition is not limited by the actual surface

coverage of macromolecules, but is rather limited by the volume that macromolecules occupy, such that steric hindrance to interior pore-loading can occur sooner than expected, if only the optical thickness values are considered. The results are discussed in terms of local pore diameter (d_{local}), which describes the effective reduced pore diameter after LbL deposition terminates, essentially corresponding to the steric limit for macromolecular LbL deposition. For all macromolecular species, the estimated d_{local} was 20-35 nm, in agreement with macromolecules not depositing in AAO pores with d_0 = 25-30 nm. In addition, *ex situ* scanning electron microscopy (SEM) was employed to corroborate the *in situ* OWS results for the linear-PEs.

5.2. Results and Discussion

For our LbL studies of protein and linear-PE multilayers, as well as in our previous work on dendrimer-PE multilayes, we used anodic aluminum oxide (AAO), as a model nanoporous material. AAO was produced by anodizing aluminum in 0.3 M oxalic acid under a constant potential of 40 V. Two-step anodization process ensured highly ordered and low pore diameter (d_0) size distribution. The resulting AAO substrates had an inter-pore distance of p = 95-105 nm, pore diameters that were enlarged between d_0 = 25-80 nm and with a thickness of h = 3.2-3.8 μm. The AAO membranes were covered with a thin metal coupling layer, 2 nm Cr and 25 nm Au, on the aluminum oxide barrier side (bottom) and then mounted on glass supports using an optical adhesive[31] (scheme 1 shows SEM images of the AAO). This allows the characterization of the AAO refractive index and the monitoring, *in-situ*, of the macromolecular adsorption kinetics using optical waveguide spectroscopy (OWS).

We investigated the formation of protein multilayers on porous AAO substrates using molecular recognition of biotinylated-bovine serum albumin (b-BSA) by avidin proteins. Avidin has 4 biotin-binding sites while the b-BSA used had 13 biotin molecules per protein. The linear-polyelectrolyte molecules self-assembled into multilayers by electrostatic interactions between 70 kDa poly(sodium 4-styrene sulfonate) (PSS) and 50-65 kDa poly(allyl amine) hydrochloride (PAH). The polyelectrolyte dendrimers previously studied were N,N-disubstituted hydrazine phosphorus containing dendrimers of the fourth generation (G4). Each dendrimer has 96 peripheral charged groups, which are either all cationic or all anionic in nature (G4(+) = $G_4(NH^+Et_2Cl^-)_{96}$, M_w = 32.3 kDa; G4(-) = $G_4(CHCOO^-Na^+)_{96}$, M_w = 35.6 kDa). In all LbL steps, the adsorption process was continued

until the adsorption kinetics showed that saturation was reached. The ionic strength was kept sufficiently high to achieve optimal pore-loading conditions. Illustration of the LbL in AAO nanopores, a graphical representation of the internal structure of the LbL macromolecular films and SEM images of a typical AAO sample used are shown in scheme 5.1. The cumulative deposited layer thickness was estimated using Maxwell-Garnett effective medium theory (EMT) approximation and does not depend on pore depth for a uniform deposition.

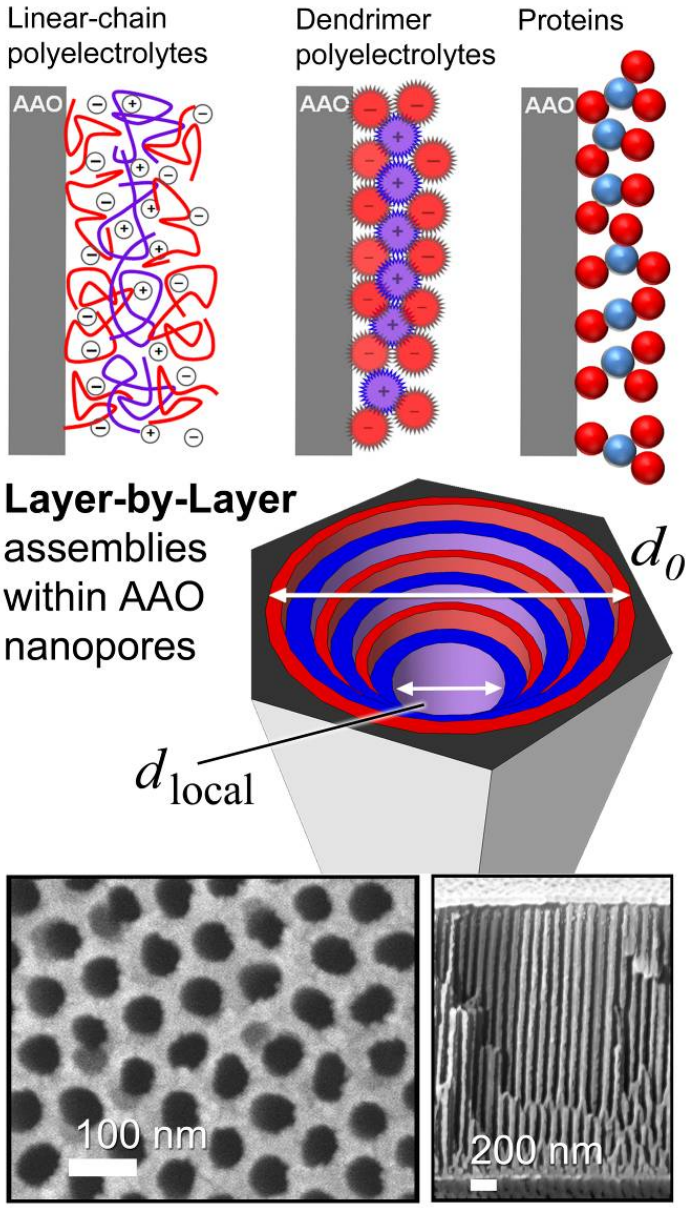

Scheme 5.1. Schematic of the layer-by-layer (LbL) structures for different types of macromolecules on the interior AAO pore-walls. Polyelectrolyte species (linear-chains and dendrimers) bind electrostatically, while the proteins bind by molecular recognition. The LbL process was performed until no further material could be incorporated within the AAO, reaching d_{local}. SEM of AAO used shown from top (left) and cross-section (right); 2 nm of Cr and 5 nm of Au were evaporated for imaging.

5.2.1. Layer-by-Layer Growth within AAO

The difference between LbL macromolecular growth on a flat surface vs within a porous AAO substrates having $d_0 \sim 65$ nm is shown in figure 5.1, for linear-PEs ($\varepsilon_{\text{linear-PEs}} = 2.15$),[32] proteins ($\varepsilon_{\text{proteins}} = 2.10$)[22] and dendrimre-PEs ($\varepsilon_{\text{dendrimer-PEs}} = 2.25$).[12, 20] The optical thickness (t_{optical}) of the deposited material was estimated using the same value of dielectric constant for both the planar and the porous surfaces. For the porous surface t_{optical} was obtained by fitting the experimentally observed dielectric constant changes to an average material thickness by an EMT approximation (see experimental). [20, 22]

The deposition of macromolecular species was measured by SPR on planar negatively charged gold surfaces, obtained from the self-assembly of a mercaptohexadecanoic acid. On a flat surface, for proteins, avidin was first adsorbed to the negatively charged surface, followed by b-BSA adsorption through molecular recognition. For both polyelectrolytes, the positive species were deposited first, followed by the negative ones. In the nanoporous AAO, protein multilayers were grown by first adsorbing avidin electrostatically on the untreated AAO surface. For the two polyelectrolyte species, the macromolecules were deposited on a positively charged surface obtained by silanization.

In figure 5.1, the cumulative t_{optical} is shown as a function of the number of added layers for dendrimer-PEs, linear-PEs and proteins on a flat surface and within AAO nanopores of approximately 65 nm diameter. The cylindrical geometry of the AAO pores imposes a steric limit that terminates the growth of the LbL film after a certain maximum number of deposition steps (n_{max}), unlike deposition on a flat surface that has in principle, no upper steric limit. For linear-PEs, $n_{\text{max}} = 9$, while this value was lower for dendrimer-PEs ($n_{\text{max}} = 7$) and proteins ($n_{\text{max}} = 3$). For the three different macromolecular species studied, the deposition in the cylindrical pores was characterized by 3 regimes, as can be observed in figure 5.1A to 5.1C. Firstly, the macromolecular deposition underwent a steady growth regime, similar to a flat surface. Secondly, after a certain number of deposition steps, a transition period proceeded for a few deposition steps, characterized by a reduction in the amount of deposited material per layer; more noticeable for the polyelectrolyte species. Finally, saturation was reached, where macromolecules could no longer be incorporated within the nanopores because steric hindrance prevented additional deposition.

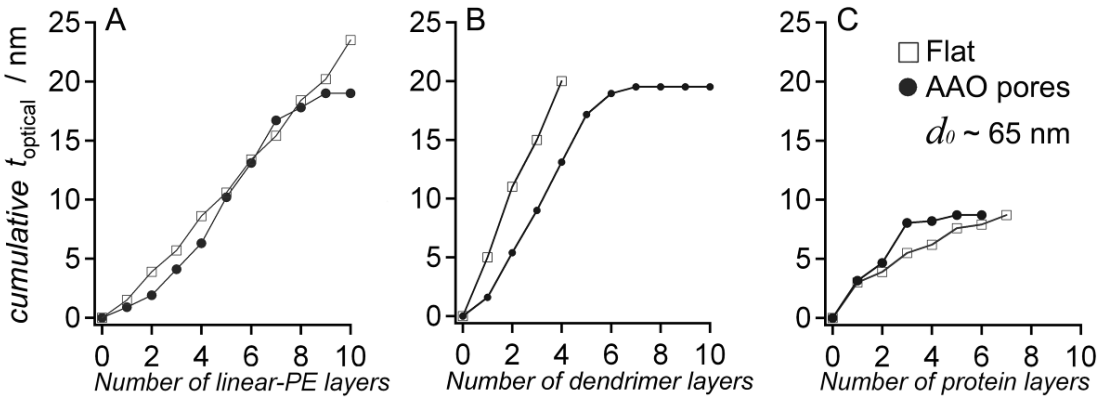

Figure 5.1. Flat vs porous behavior for linear-PEs (**A**), dendrimer-PEs (**B**) and proteins (**C**) in AAO with d_0 ~ 65 nm. The deposition behavior on a flat surface is similar than within the AAO pores: PE macromolecular deposition is approximately linear and protein LbL is non-monotonic. LbL growth becomes hindered in cylindrical nanopores after a certain number of deposited layers.

The overall deposition behavior on the flat surface was similar to the deposition behavior in the nanopores, until saturation was approached. Some deviations were observed for the initial deposition steps with the polyelectrolyte species due to differences in the initial surface charges, i.e., positively charged silane on alumina vs negatively charged thiols on gold. For polyelectrolytes, the deposition was approximately linear, while for proteins, the deposition was non-linear with b-BSA layers being about 1/3 thinner than the avidin layers,[33] observed on both flat and porous substrates.

Although these macromolecules were approximately the same size, each species saturated after at different n_{max}. This was clearly observed when comparing the LbL growth of proteins and linear-PEs over a range of pore diameters d_0 = 25-80 nm. The cumulative increase in $t_{optical}$ as a function of the number of added macromolecular layers is shown in figure 5.2 for proteins and linear-PEs in $25 < d_0 < 80$ nm.

For both proteins and linear-PE in figure 5.2, the LbL growth in the cylindrical nanopores only proceeded for a certain n_{max}, which was also observed for dendrimer-PEs.[20] In fact, a similar study involving the formation of polymer nanotubes by LbL of poly(acrylic acid) and PAH similarly showed that LbL terminates before complete pore-filling.[13] In general, from figure 5.2, we can observe that n_{max} increased with larger values of d_0 for both macromolecules. The striking difference between these two macromolecules is that saturation occurred at significantly lower n_{max} values for proteins, at similar d_0. For d_0 = 80 nm, only 5 protein LbL layers could be grown, while 11 layers of PSS and PAH were possible within d_0 = 69 nm pores. As we argue later on, these differences should in principle

be directly related to the structure of the LbL multilayer film that is grown within the cylindrical nanopores.

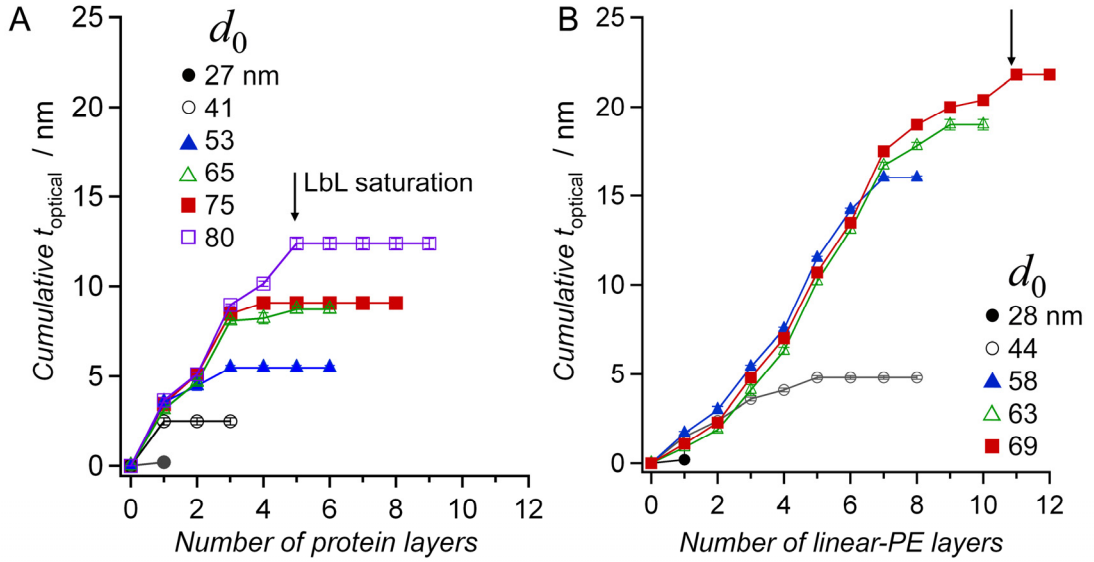

Figure 5.2. Optical thickness of the growing LbL multilayer film on the inner-surface of the AAO cylindrical nanopores for proteins (M_w ~ 65-68 kDa) and linear polyelectrolytes of similar size (M_w = 50-70 kDa), see scheme 1.

In figure 5.3, n_{max} is plotted as a function of d_0, for all three types of macromolecules that are discussed. Linear fits to the data are presented and illustrate that the number of possible LbL steps is significantly larger for linear-PEs, while the lowest number of LbL were achieved using proteins. For this data, no EMT assumptions were used, since only the number of possible LbL steps until saturation was considered. The parameters that affect the internal structure of the LbL film, and therefore the effective volume that it occupies, can be used to explain the observed behavior. While the size of the macromolecules was more or less similar, their structure, the nature of the LbL driving force and the interaction with the surface during adsorption significantly differed between each macromolecular species. The cylindrical geometry of AAO pores directly limits the number of LbL steps due to the shrinking volume that is available after each deposited step. Therefore, the structure of the LbL film can directly influence how much material can be incorporated within the nanopores, in contrast to flat surfaces where the deposition is in principle, not sterically hindered because of the absence of an upper physical boundary to deposition.

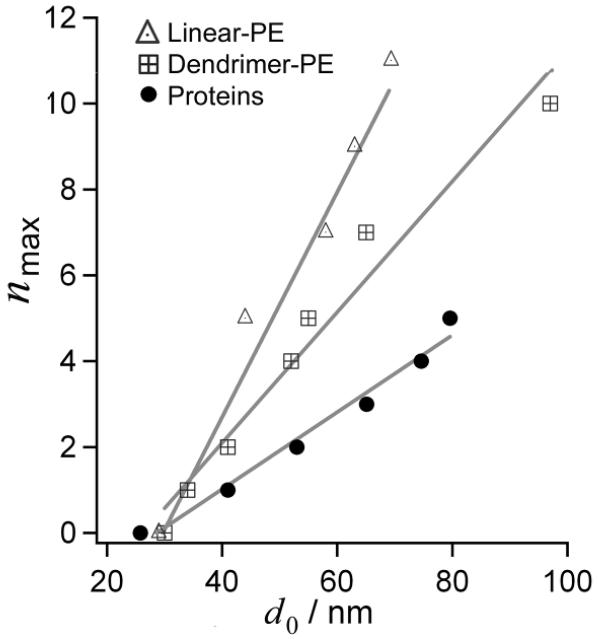

Figure 5.3. Maximum number of macromolecular LbL steps (n_{max}) for proteins, linear-PE and dendrimer-PE multilayers in AAO substrates as a function of initial d_0. Lines are linear fits to the data.

5.2.2. Estimation of the Steric Limit to LbL in Nanopores

During the LbL film growth in a cylindrical nanopore, each deposited macromolecular layer effectively shrinks the pore diameter that is available for additional particles to travel through in order to deposit within the remaining depth of the pores. As the number of LbL steps approaches saturation, i.e. n_{max}, the reduced diameter reaches a certain value where the available pore diameter is simply insufficiently large to allow unhindered diffusion of particles within the pores, which we refer to as d_{local}. The estimation of d_{local} is given by eq. (1), where t_{total} is the cumulative thickness within the pores after LbL growth saturates at n-max.

$$d_{local} = d_0 - 2 \cdot t_{total} \qquad \text{equation (1)}$$

The value of t_{total} can also be expressed as a sum of the different LbL steps in the case of heterogeneous LbL structures where LbL steps can have different optical thicknesses, as expressed in eq. (2):

$$d_{local} = d_0 - 2 \cdot \sum_{i}^{n_{max}} t\ (n_i) \qquad \text{equation (2)}$$

where $t\ (n_i)$ is the thickness of n_i^{th} macromolecular layer that describes the effective volume it occupies.

The value of t_{total} in eq. (1) represents a measure of the film thickness that physically limits macromolecular deposition in the pores. For compact LbL films, the size of t_{total} is closely related to the value obtained from the EMT approximations, which provides an optical thickness $t_{optical}$. However, as we will show later, $t_{optical}$ underestimates the actual volume occupied for loosely packed LbL films, which involve shape persistent molecules such as proteins for example. Therefore, additional considerations are required to estimate t_{total} based on estimations of the actual volume that loosely packed multilayer films occupy, which we refer to t_{volume}. In that sense, t_{volume} is an estimate of the maximal physical height of the LbL film. Ideally, for densely packed layers $t_{optical} = t_{volume}$. The above discussion is summarized in the schematics of scheme 2, where the reduced diameter ($d_{reduced}$) after the deposition of 2 layers of macromolecules illustrates the difference between dense and loosely packed layers on the available diameter for additional deposition.

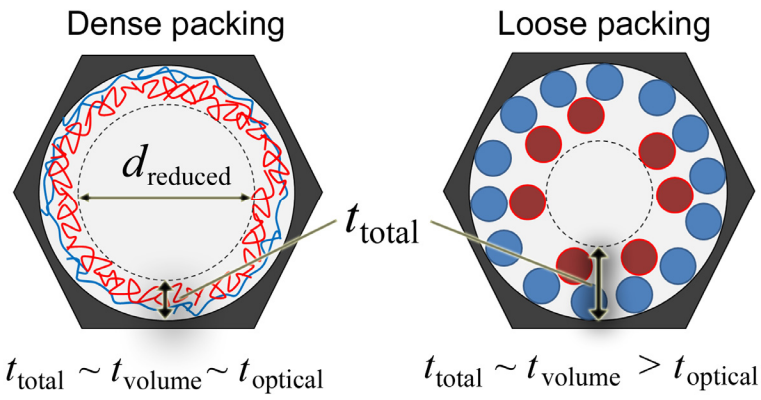

Scheme 2. The total volume occupied by a macromolecular layer directly influences t_{total} the available the pore diameter for additional macromolecular deposition within the depth of the pores, shown as the reduced diameter ($d_{reduced}$). The shape and interactions between macromolecules and with the surface changes the packing density and the volume that the layers occupy.

The value of $t_{optical}$, cumulative (eq. (1)) or for individual layers (eq. (2)) that we obtained from the EMT approximation is not necessarily a representation of the actual volume that restricts the entry of macromolecules within the AAO pores. For example, if we consider the results shown in figure 5.1, $n_{max} = 9$ for linear-PEs, while $n_{max} = 3$ for proteins. Both these species are of similar size in solution, but their interactions on the surface and between LbL layers differ. Polyelectrolytes can collapse and form densely interpenetrated films, while proteins form looser aggregates of shape-persistent molecules, as shown in several studies.[34-35] Furthermore, the $t_{optical}$ measured at saturation was about 19 nm for the polyelectrolytes, while it was only about 8.5 nm for the proteins for similar pore sizes of d_0

~ 65 nm. Obviously, eq. (1) gives unrealistic d_{local} values for proteins, if we assume $t_{total} = t_{optical}$. However, if we consider the actual protein diameters[36-38] to be t_{volume} ~ 5-6 nm in order to estimate t_{total} in eq. (1), then the value of d_{local} is properly estimated. We have compared the three macromolecular LbL systems, of similar size, in order to establish a reasonable method of approximating t_{total} in eq. (1). For polyelectrolytes, $t_{optical}$ appeared to be a reasonable approximation of t_{total}, but this assumption was unreasonable for proteins.

In summary, the steric hindrance to LbL formation in cylindrical nanopores can be understood by a model than takes into consideration the fact that macromolecules effectively occupy a defined volume, regardless of surface coverage. This effective volume, can be described by an estimated value t_{volume} for t_{total} in eq. (1). The estimation of t_{volume} has to take into account the shape, size and nature of the macromolecular interactions with other macromolecules and with the surface. Linear-PEs form compact layers that are well approximated by the layer thickness estimated from EMT. Dendrimer-PEs also formed compact interdigitated layers with a good agreement between t_{volume} and $t_{optical}$ for the estimation of $t_{total.}$ For proteins however, further considerations were required to accurately estimate the limit to steric hindrance for LbL formation in nanopores. Table 1 summarizes some of the macromolecules features and LbL films and the main points that have been discussed in relation to t_{total} in eq. (1). These parameters, as will be discussed later, are required to estimate the steric limitation (d_{local}) to macromolecular deposition in the cylindrical nanopore geometry. The protein,[36-39] linear-PE[40-42] and dendrimer[12, 43-44] sizes in solution have been taken from references.

Table 5.1. Details of the macromolecular species used and their deposition properties in AAO.

Macromolecule	Diameter / nm	Mw / kDa	Shape	LbL film structure	Optical t_{total} correlation	$t(n_i)$ used in Equation (2)
Dendrimers	~6-8	G4(+): 32.3 G4(–): 35.6	- Rigid ellipsoids - Hydrophobic core	- Close-packed, - Interdigitated layers	**good** $t_{total} \sim t_{optical}$ $t_{total} = t_{volume}$	*$t'_{optical}$ = 3.2 nm t = 3.5 nm
Linear-PE	~5-10	PAH: 50-65 PSS: 70	- Flexible - Random coil	- Compact, inter-penetrating layers	**Very good** $t_{total} = t_{optical}$ $t_{total} = t_{volume}$	$t = t'_{optical}$
Proteins	avidin: 5.5×4.0×6.0 BSA: 8.0 ×8.0×3.0	Avidin: 66-68 b-BSA: 67	- Shape-persistent - Secondary and tertiary structures	- Loosely packed - No reorganization	**Worse** $t_{total} > t_{optical}$ $t_{total} = t_{volume}$	Avidin: $t'_{optical}$ = 3.2 nm t = 5.3 nm b-BSA: $t'_{optical}$ = 1.1 nm t = 6.3 nm

* $t'_{optical}$ in this case is the optical thickness value, per layer

The d_{local} estimated for the macromolecules studied as a function of the initial AAO d_0, are shown in Figure 5.4 using the values of t_{total} calculated from the values of t (n_i) from table 1 and using eq. (2). The values of t (n_i) were estimated differently for each type of macromolecular species by taking into account the structure of the LbL film, such that t_{total} in eq. (1) was estimated by eq. (2). The estimation of t (n_i) was based on the actual volume that a macromolecular layer occupies, as described in Table 1. In the last column the per layer optical thickness ($t'_{optical}$) is compared to t (n_i) that was used.

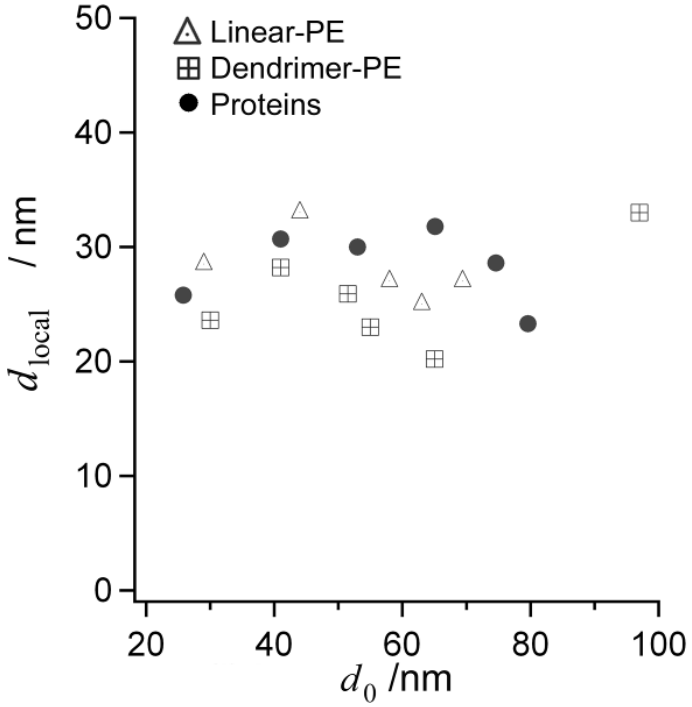

Figure 5.4. Estimated d_{local} as a function of d_0, for the studied linear-PEs, dendrimer-PEs and proteins. d_{local} represents the local reduced pore diameter (equation (2)) after multilayer LbL formation was obtained from the approximations made for t (n_i) in Table 1, in agreement with the hindered deposition for d_0 = 25-30 nm.

For polyelectrolyte species, the actual thickness was closely related to the optical thickness, while the volume occupied by the protein multilayer film was underestimated by $t_{optical}$ estimates. Based on our previous discussion, d_{local} was not necessarily accurately described by $t_{optical}$, due to the unknown parameters associated with the packing density that directly affect t_{volume}. The actual volume that a macromolecular layer occupies, based on the protein experiments, appears to be more relevant to estimate the steric limit of pore-filling in cylindrical geometry. In our previous dendrimer study, the actual value of t_{volume} was estimated by assuming that each layer was 3.5 nm thick ($t_{optical}$ = 3.2 nm per layer), which was about a half-dendrimer diameter in order to represent the structure of interdigitated

layers. This provided a reasonable value of d_{local} = 19-33 nm for different values of d_0. For the linear polyelectrolytes PSS/PAH studied here, no corrections were required to obtain similar values of d_{local} = 22-34 nm for the different d_0 tested, such that the cumulative thickness of figure 5.2B was directly used in eq.(1), $t_{total} = t_{optical} = t_{volume}$. However, using $t_{optical}$ with proteins to estimate t_{total} did not provide reasonably agreeable d_{local} values for the range of d_0 tested. For example, considering LbL in the d_0 = 80 nm sample of figure 5.2A, d_{local} would be 55 nm if the $t_{optical}$ was used to calculate t_{total}, which is incorrect since 3 full LbL steps were deposited in d_0 = 53 nm (figure 5.2A). Based on the argument that molecular recognition leads to static layers, and considering that proteins are rather shape-persistent rigid macromolecules, each protein layer should effectively be as thick as a macromolecular diameter. Even if surface coverage is low, as observed for b-BSA, incoming proteins are in reality strongly influenced by the effective volume that is occupied by the deposited proteins (see scheme 2) and not necessarily by the density of the LbL assembly. Since the proteins are shape-persistent macromolecules, the effective thickness that is seen by additional incoming proteins should be approximated by the volume that a protein occupies, i.e., by using the protein size (t_{volume}) as a realistic estimate of t_{total} in eq. (1). For this scenario, t_{volume} for avidin (5.3 nm) and b-BSA (6.3 nm) were estimated by taking the average of the 3 axial dimensions, which are 4.0×5.5×6.0 nm^3 for avidin and 8.0×8.0×3.0 nm^3 for BSA. Assuming these values for t_{total} in eq. (1) gives a d_{local} value that lies between 21-32 nm for all d_0 tested for proteins. The d_{local} = 20-35 nm values estimated from the assumption in Table 1 are shown in figure 5.4 and are in agreement with the observation in figure 5.2, that d_0 = 25-30 nm pores effectively inhibit macromolecular deposition.

Figure 5.5 shows an SEM image of AAO nanopores with d_0 = 69 nm before deposition and after the linear-PE deposition had become saturated (experiment from figure 5.2B). The initial diameter d_0 was reduced to d_{local} = 24 ± 6 nm, after macromolecular deposition saturated. Good agreement was observed between the SEM and OWS measurements presented between figures 5.2B and 5.5 for d_{local} since the EMT approximation assumes conformal linear-PE film formation on the AAO surface, which is well reproduced by the dense deposited polyelectrolytes. The evolution of the reduced pore diameter as a function of added linear-PE steps in d_0 = 69 nm pores, until d_{local} ~ 25 nm was reached, is shown in figure 5.5C, in agreement with the reduction in pore diameter observed by SEM, in figure 5.5B. In figure 5.2, deposition within narrow diameter pores d_0 = 25-30 nm was effectively

inhibited, which agrees with the observation that pore-filling saturates when the limit of d_{local} = 20-35 nm was reached (figure 5.4). An SEM of the narrow pores of AAO is shown in figure 5.3D.

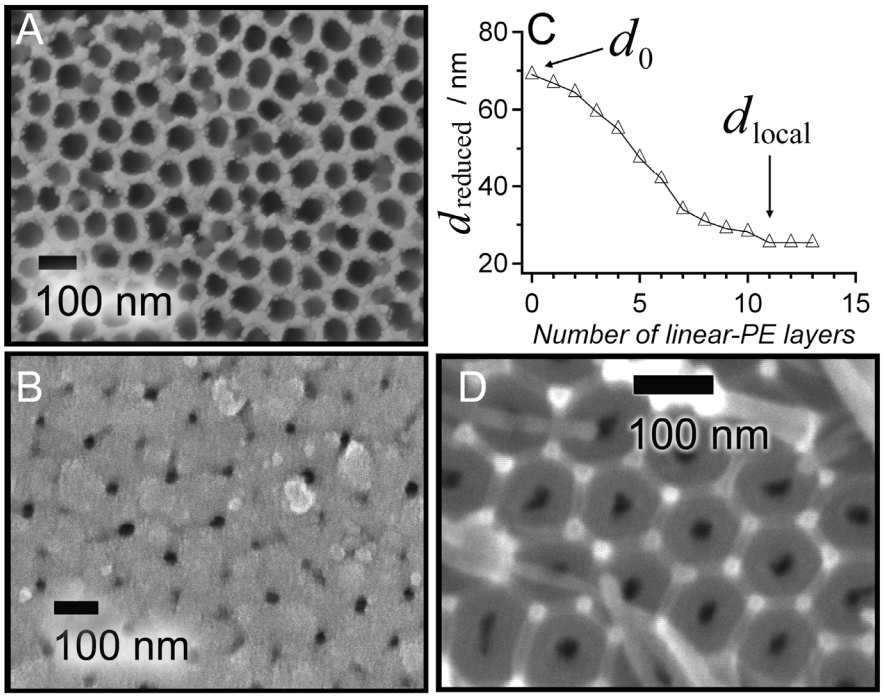

Figure 5.5. (**A**) SEM image of AAO with d_0 = 69 nm pores before deposition of linear-PEs. (**B**) SEM image of AAO after 13 PSS and PAH deposition steps in AAO pores of (A), based on the $t_{optical}$ estimated from EMT. After saturation, d_0 was reduced to d_{local} = 24 ± 6 nm (n = 50). (**C**) Reduced diameter as a function of the number of linear-PE LbL steps for (B). (**D**) SEM of AAO before pore widening, d_0 = 25-30 nm, in which deposition was hindered, see figure 5.2.

The difference in n_{max} for the different macromolecular species is shown in figure 5.3 and originates from the internal structure of LbL assemblies. In the cylindrical pore geometry, the multilayer film structure strongly influences the overall volume that is occupied by the LbL. This effective volume directly contributes to steric hindrance of macromolecular transport. The dendrimer species for example, have an internal rigid hydrophobic aromatic structure. Similarly, proteins have internal secondary and tertiary structures. These species are therefore not as flexible as random-coil linear-PEs. Dendrimer-PEs have been shown to form interdigitated layers, where quantum dots could be deposited in sufficiently defined ways to generate defined planar depositions.[45] Proteins however, tend to deposit more loosely because of molecular recognition that drives protein-protein interactions. Such is the case for the results presented for the LbL of b-BSA and avidin. The $t_{optical}$ of b-BSA layers was about 1/3 of the avidin layer thickness. We believe that the high degree of biotinylation of the BSA (13 biotin/protein) can allow for more than 1 avidin binding and that the

molecular recognition also immobilizes the b-BSA-avidin complexes in the orientation adopted upon adsorption, which can sterically hinder access to underlying biotin-binding sites. The proteins we studied form a static system, where macromolecules effectively become locked into the configuration adopted upon initial binding between proteins, with minimal, if any, further reorganization. The flexibility of linear-PE specifically allows for chain-interpenetration[46-47] and surface collapse of the polyelectrolyte structure on charged surfaces.[8, 48-50] Furthermore, polyelectrolyte films have the advantage of being dynamic self-assemblies, in the sense that the internal structure of the film can undergo rearrangement to achieve optimal packing density due to flexible electrostatic interactions. These differences therefore should be taken into consideration when estimating the limit of steric hindrance in LbL assemblies within nanopores. More importantly, these differences significantly affect how the optical thickness of the deposited LbL film that is experimentally obtained can be used to interpret what actually occurs within the confined nanoporous environment. For example, $t_{optical}$ obtained from tightly packed linear-PE can be interpreted as being a more realistic representation of the actual film thickness (t_{volume}) that has been deposited on the AAO pore walls than the value of $t_{optical}$ obtained for the protein multilayer system; for which case we assumed that t_{volume} was on the order of the protein size.

5.3. Concluding Remarks

Layer-by-layer (LbL) deposition of different macromolecular species within the cylindrical pores of anodic aluminum oxide (AAO) was strongly dependent on the size, on the shape and on the nature of the interactions with the surface and between molecules. The cylindrical pore geometry eventually becomes a physical barrier to LbL growth due to ever increasing confinement after each additional LbL step. When a local pore diameter (d_{local}) of approximately 20-35 nm was reached, deposition became inhibited. This was in agreement with hindered deposition within d_0 = 25-30 nm pores. AAO with different pore diameters were investigated to estimate the average volume that macromolecules occupy for dendrimers, linear-polyelectrolytes and proteins. The steric limit to macromolecular deposition was not necessarily reflected by simply considering the optical thickness. In fact, $t_{optical}$ could only be reliably used to calculate d_{local} for polyelectrolytes because they form tightly packed layers. For proteins, the multilayer LbL film thickness was approximated by using the average protein diameter as an estimate of layer thickness. For the cylindrical geometry, the effective volume occupied the macromolecular species is more relevant to

estimate how many LbL steps are possible before the deposition becomes sterically hindered. In this study we have only presented experimental results for the formation of homogeneous LbL assemblies, but the steric factors limiting the formation of heterogeneous self-assemblies can be similarly understood. Many investigations rarely have access to investigations tools such as OWS or other thin-film characterization techniques to analyse macromolecular deposition within the nanoporous matrix. Our results and experimental approach may be used to further understand and optimize the tailoring of the internal structure of multilayer assemblies in nanoporous environment towards generating multifunctional one-dimensional materials.

5.4. Experimental Section

Materials. Lyophilized avidin was purchased from Calbiochem (purity 12.9 units/mg). Biotinylated-BSA (b-BSA), Albumin Bovine-biotin, was purchased from Sigma Aldrich (St-Louis, MO, USA) with a 13 mol biotin/mol Albumin. Poly(sodium 4-styrene sulfonate) (PSS) with a molecular weight (M_w) of 70 kDa was purchased from Sigma Aldrich (St-Louis (MO), USA). Poly(allyl amine hydrochloride) PAH with a M_w of 50-65 kDa was purchased from Sigma Aldrich (Milwaukee, WI, USA). Al foil (0.25 mm thick, purity: 99.999 %) were purchased from Goodfellow (Huntington, UK). Oxalic acid dihydrate was purchased from AppliChem (Darmstadt, Germany). Phosphoric acid 85% and was purchased from Acros Chemicals (New Jersey, USA). High refractive index LaSFN9 glass substrates (ε=3.406 at 632.8 nm) were obtained from Hellma Optik (Halle, Germany). The UV-curable optical adhesive (NOA 83H) was purchased from Norland Products (Cranbury, NJ, USA). 16-mercaptohexadecanoic acid (90%) was purchased from Sigma Aldrich (St-Louis, MO, USA). Ethanol was p.a. grade (VWR, France). The water used was ion exchanged and filtered using a Millipore system (MilliQ System from Millipore, Molsheim, France; specific resistance R > 18 MΩ cm^{-1}, pH ~ 5.5). $CuCl_2$, and sodium chloride were purchased from Sigma Aldrich (St-Louis, MO, USA). Aminopropyltriethoxysilane (APTES) was purchased from Fluka (Steinheim, Germany).

Au evaporation. Au and Cr were evaporated on a Bal-Tec MCS610 evaporator equipped with a Bal-Tec QSG100 quartz film thickness monitor. For the metal layer at the AAO bottom, 2 nm of Cr and 25 nm of Au were evaporated on the AAO barrier layer. 1 nm Cr and 4 nm Au were evaporated on SEM samples for imaging purposes.

AAO membranes on planar glass supports. AAO anodized from bulk aluminum foils were mounted on microscope glass slides using an optical adhesive according to a previously reported technique.[31] Briefly, AAO membrane thin films were fabricated by electrochemical anodization of aluminum foils, which were annealed at 500 °C overnight. Al foils were electrochemically polished first in a solution of concentrated H_2SO_4 (250 g), 85% H_3PO_4 (250 g) and deionized water (250 g) at 25V. Secondly, the Al foils were polished in a solution of perchloric acid/ethanol (1:4 *v*/*v*) for 15 min, 0 °C at 20 V. They were then anodized for 2 h in 0.3 M oxalic acid, 1 °C at 40 V. The alumina was removed with a 5 vol. % phosphoric acid solution for 2-3 h. Al foils were then anodized a second time for 1 h 35 min to obtain the desired thickness of 3.5 μm or for 2 h to obtain 5 μm thick AAO. Al was removed from the anodized foil by immersion of the anodized Al foil in a 17 g/L $CuCl_2$ in HCl/H_2O (1:1, 37 M stock HCl solution: H_2O) solution until the AAO became visible and no metal remained. Prior to Al removal, the AAO side was isolated from solution by immobilization onto a glass slide and sealed using epoxy adhesive. 2 nm of Cr and 25 nm of Au were evaporated onto the barrier layer of the AAO membranes. The metal does not enter the pores and lies under the AAO barrier layer. The metal serves as a useful positioning tool to locate the transparent alumina using the microscope. Norland 83H adhesive was diluted in THF (1:10) and spin-coated on LASFN9 glass slides at 20 rpm for 2-3 s. The Au-coated AAO was glued, barrier side down, onto the glass side and UV-cured for 2 hr with a UV hand lamp, with both lamps on (λ = 254 + 354 nm, 4 W) from Herolab (Wiesloch, Germany). The pore diameter (d_0) for all AAO membranes was widened to the desired diameter by etching in 5 vol. % phosphoric acid (Δd_0 ~0.75 nm·min^{-1}).

AAO silanization with APTES. This step was only used with the linear-PEs, with avidin adsorbed on the unfunctionalized surface. AAO substrates were O_2 plasma cleaned for 2 min immediately prior to gas-phase silanization to increase the surface density of OH groups. The glass slide substrates to be silanized were inserted into a glass staining jar and 50 μl of (APTES) were added in a glass test tube, inside the chamber. The container was covered with its glass cover and sealed using Scotch vacuum tape from 3M (St-Paul, MN, USA), left in the oven at 130 °C for 5 min to warm, followed by 3 h under continuous vacuum. The functionalized samples were cooled.

Surface plasmon resonance (SPR). SPR measurements were performed on a setup operating at 632.8 nm in the Kretschmann configuration.[16] The negatively charged gold surface was obtained by immersion of an O_2 plasma cleaned gold surface into a 10 mM mercaptohexadecanoic acid ethanolic solution for 3 h.

Optical waveguide spectroscopy (OWS). OWS measurements of the AAO membranes prepared on glass slides were performed on a purpose-built setup.[16] The glass-side was attached to the base of a symmetric LaSFN9 glass prism by optical immersion oil ($\varepsilon = 2.89$). The laser (λ = 632.8 nm) was incident through the prism-substrate assembly and reflected off the thin metal coupling layer in between the AAO and the optical adhesive as the incidence angle (θ) was varied. At specific θ's determined by the thickness and the dielectric constant of AAO (ε_{AAO}), the laser was coupled into the AAO film and these waveguide modes were recorded as sharp minima in a reflectivity R vs. θ scan. Transverse electric (TE) and transverse electric (TM) modes were indexed according to the number of nodes in their electromagnetic field distributions. ε_{AAO} and the thickness of the AAO film, were obtained by fitting the angles of the waveguide mode reflectivity minima using Fresnel simulations carried out with Winspall program.[51] Tracking the coupling angle of a mode enables real time, *in situ* monitoring of changes in the dielectric constant of the film, i.e. adsorption kinetics.

Effective medium theory analysis. The dielectric constant of AAO (ε_{AAO}) that is measured by OWS includes contributions from the alumina, the pore-filling medium (e.g. buffer), and any organic thin layer coating the pore surfaces (i.e. the LbL multilayer film). The dielectric constant is related to the refractive index by: $\varepsilon = n^2$. ε_{AAO} has an anisotropic components that are described by the infinite, prolate ellipsoid approximation within the Maxwell-Garnett theory, and well-described elsewhere:[22, 52-53]

$$\varepsilon_{AAO}^{\perp} = \varepsilon_{alumina} + f_{pore}(\varepsilon_{pore} - \varepsilon_{alumina}) \qquad \text{equation (3)}$$

$$\varepsilon_{AAO}^{//} = \varepsilon_{alumina} \frac{\varepsilon_{alumina} + \tfrac{1}{2}(1 + f_{pore})(\varepsilon_{pore} - \varepsilon_{alumina})}{\varepsilon_{alumina} + \tfrac{1}{2}(1 - f_{pore})(\varepsilon_{pore} - \varepsilon_{alumina})} \qquad \text{equation (4)}$$

where $\varepsilon_{AAO}^{\perp}$ and $\varepsilon_{AAO}^{//}$ are, respectively, the dielectric constant components normal and parallel to the AAO membrane surface, f_{pore} is the pore volume fraction within the AAO, $\varepsilon_{alumina} = 2.68$[22] is the dielectric constant of bulk anodic alumina at λ = 632.8 nm, and ε_{pore} is the (effective) dielectric constant within the pores. For a blank AAO film in water, $\varepsilon_{pore} = \varepsilon_{buffer} = 1.78$. With the addition of an organic film of proteins or linear-PEs ($\varepsilon_{proteins} = 2.1$ or $\varepsilon_{linear\text{-}PEs} = 2.15$) on the internal pore surfaces, the volume within the pores is occupied by a combination of the organic material and the pore filling buffer. Recursively applying equations (3) and (4) for the organic-filled AAO pores, using a new effective ε'_{pore} for the pore interior, provides ε_{AAO} after molecular adsorption.

Protein and Linear-PE adsorption experiments. Avidin was dissolved in phosphate buffer (20 mM NaH_2PO_4/Na_2HPO_4, pH = 7, with 100 mM NaCl) to obtain 1 mg/ml solutions and further diluted to obtain 0.1 mg/ml solution, about 1.5 μM concentration. The b-BSA solutions were similarly prepared with a 0.1 mg/ml concentrations. PSS and PAH solutions were prepared with 0.1 mg/ml concentrations using 500 mM NaCl in deionized water. For both macromolecules, higher ionic strength than required were used to significantly reduce the Debye screening length, such that optimal pore-loading was achieved. The flow cell was rinsed with ethanol, followed by the buffer. Kinetics were monitored by following the change in a high order waveguide TM-mode. The solution was passed through the flow cell ($15\times7.5\times0.5$ mm^3) until 1.4× the dead-volume was washed out, and then the solution was re-circulated using a peristaltic pump. The flow rate was kept constant at 0.4 ml/min.

5.5. References

1. Hammond, P. T.; Form and function in multilayer assembly: New applications at the nanoscale. *Adv. Mater.* **2004,** *16*, 1271-1293.

2. Ali, M.; Yameen, B.; Cervera, J.; Ramirez, P.; Neumann, R.; Ensinger, W.; Knoll, W.; Azzaroni, O.; Layer-by-Layer Assembly of Polyelectrolytes into Ionic Current Rectifying Solid-State Nanopores: Insights from Theory and Experiment. *J. Am. Chem. Soc.* **2010,** *132*, 8338-8348.

3. Lvov, Y.; Ariga, K.; Ichinose, I.; Kunitake, T.; Assembly of Multicomponent Protein Films by Means of Electrostatic Layer-by-Layer Adsorption. *J. Am. Chem. Soc.* **1995,** *117*, 6117-6123.

4. Cui, X. Q.; Pei, R. J.; Wang, X. Z.; Yang, F.; Ma, Y.; Dong, S. J.; Yang, X. R.; Layer-by-layer assembly of multilayer films composed of avidin and biotin-labeled antibody for immunosensing. *Biosens. Bioelectron.* **2003,** *18*, 59-67.

5. Cassier, T.; Lowack, K.; Decher, G.; Layer-by-layer assembled protein/polymer hybrid films: nanoconstruction via specific recognition. *Supramol. Sci.* **1998,** *5*, 309-315.

6. Bertrand, P.; Jonas, A.; Laschewsky, A.; Legras, R.; Ultrathin polymer coatings by complexation of polyelectrolytes at interfaces: suitable materials, structure and properties. *Macromol. Rapid Commun.* **2000,** *21*, 319-348.

7. Crespo-Biel, O.; Dordi, B.; Reinhoudt, D. N.; Huskens, J.; Supramolecular layer-by-layer assembly: Alternating adsorptions of guest- and host-functionalized molecules and particles using multivalent supramolecular interactions. *J. Am. Chem. Soc.* **2005,** *127*, 7594-7600.

8. Yoo, D.; Shiratori, S. S.; Rubner, M. F.; Controlling Bilayer Composition and Surface Wettability of Sequentially Adsorbed Multilayers of Weak Polyelectrolytes. *Macromolecules* **1998,** *31*, 4309-4318.

9. Kotov, N. A.; Dekany, I.; Fendler, J. H.; Layer-by-Layer Self-Assembly of Polyelectrolyte-Semiconductor Nanoparticle Composite Films. *J. Phys. Chem.* **1995,** *99*, 13065-13069.

10. Tang, Z. Y.; Wang, Y.; Podsiadlo, P.; Kotov, N. A.; Biomedical applications of layer-by-layer assembly: From biomimetics to tissue engineering. *Advanced Materials* **2006,** *18*, 3203-3224.

11. Chen, Y.; Zheng, X.; Qian, H.; Mao, Z.; Ding, D.; Jiang, X.; Hollow Core−Porous Shell Structure Poly(acrylic acid) Nanogels with a Superhigh Capacity of Drug Loading. *Acs Appl. Mater. Interfaces* **2010,** *2*, 3532-3538.

12. Kim, B. S.; Lebedeva, O. V.; Kim, D. H.; Caminade, A. M.; Majoral, J. P.; Knoll, W.; Vinogradova, O. I.; Assembly and mechanical properties of phosphorus dendrimer/polyelectrolyte multilayer microcapsules. *Langmuir* **2005,** *21*, 7200-7206.

13. Cho, Y.; Lee, W.; Jhon, Y. K.; Genzer, J.; Char, K.; Polymer Nanotubules Obtained by Layer-by-Layer Deposition within AAO-Membrane Templates with Sub-100-nm Pore Diameters. *Small* **2010,** *6*, 2683-2689.

14. Li, J. B.; Cui, Y.; Template-synthesized nanotubes through layer-by-layer assembly under charge interaction. *J. Nanosc. Nanotechnol.* **2006,** *6*, 1552-1556.

15. Hou, S. F.; Wang, J. H.; Martin, C. R.; Template-synthesized protein nanotubes. *Nano Lett.* **2005,** *5*, 231-234.

16. Knoll, W.; Interfaces and Thin Films as Seen by Bound Electromagnetic Waves. *Annu. Rev. Phys. Chem.* **1998,** *49*, 569-638.

17. McCrackin, F. L.; Passaglia, E.; Stromberg, R. R.; Steinber.Hl; Measurement of Thickness and Refractive Index of Very Thin Films and Optical Propoerties of Surfaces by Ellipsometry. *J. Res. Nat. Bur. Stand.* **1963,** *A 67*, 363.

18. Porter, M. D.; Bright, T. B.; Allara, D. L.; Chidsey, C. E. D.; Spontaneously Organized Molecular Assemblies .4. Structural Characterization of Normal-Alkyl Thiol Monolayers on Gold by Optical Ellipsometry, Infrared-Spectroscopy, and Electrochemistry. *J. Am. Chem. Soc.* **1987,** *109*, 3559-3568.

19. Kovacs, G. J.; Scott, G. D.; Attenuated Total Reflection Angular Spectra and Associated Resonant Electromagnetic Oscillations of a Dielectric Slab Bounded by Ag Films. *Appl. Opt.* **1978,** *17*, 3314-3322.

20. Lazzara, T. D.; Lau, K. H. A.; Abou-Kandil, A. I.; Caminade, A. M.; Majoral, J. P.; Knoll, W.; Polyelectrolyte Layer-by-Layer Deposition in Cylindrical Nanopores. *Acs Nano* **2010,** *4*, 3909-3920.

21. Peic, A.; Staff, D.; Risbridger, T.; Menges, B.; Peter, L. M.; Walker, A. B.; Cameron, P. J.; Real-Time Optical Waveguide

Measurements of Dye Adsorption into Nanocrystalline TiO2 Films with Relevance to Dye-Sensitized Solar Cells. *J. Phys. Chem. C* **2011,** *115*, 613-619.

22. Lau, K. H. A.; Tan, L. S.; Tamada, K.; Sander, M. S.; Knoll, W.; Highly Sensitive Detection of Processes Occurring Inside Nanoporous Anodic Alumina Templates: A Waveguide Optical Study. *J. Phys. Chem. B* **2004,** *108*, 10812-10818.

23. Alvarez, S. D.; Li, C. P.; Chiang, C. E.; Schuller, I. K.; Sailor, M. J.; A Label-Free Porous Alumina Interferometric Immunosensor. *Acs Nano* **2009,** *3*, 3301-3307.

24. Mun, K. S.; Alvarez, S. D.; Choi, W. Y.; Sailor, M. J.; A Stable, Label-free Optical Interferometric Biosensor Based on TiO2 Nanotube Arrays. *Acs Nano* **2010,** *4*, 2070-2076.

25. Li, A. P.; Muller, F.; Birner, A.; Nielsch, K.; Gosele, U.; Hexagonal pore arrays with a 50-420 nm interpore distance formed by self-organization in anodic alumina. *J. Appl. Phys.* **1998,** *84*, 6023-6026.

26. Li, F. Y.; Zhang, L.; Metzger, R. M.; On the growth of highly ordered pores in anodized aluminum oxide. *Chem. Mater.* **1998,** *10*, 2470-2480.

27. Nielsch, K.; Choi, J.; Schwirn, K.; Wehrspohn, R. B.; Gosele, U.; Self-ordering regimes of porous alumina: The 10% porosity rule. *Nano Lett.* **2002,** *2*, 677-680.

28. O'Sullivan, J. P.; Wood, G. C.; The Morphology and Mechanism of Formation of Porous Anodic Films on Aluminium. *Proc. R. Soc. Lond. A* **1970,** *317*, 511-543.

29. Thompson, G. E.; Porous anodic alumina: Fabrication, characterization and applications. *Thin Solid Films* **1997,** *297*, 192-201.

30. Thompson, G. E.; Xu, Y.; Skeldon, P.; Shimizu, K.; Han, S. H.; Wood, G. C.; Anodic-Oxidation of Aluminum. *Philosophical Magazine B-Physics of Condensed Matter Statistical Mechanics Electronic Optical and Magnetic Properties* **1987,** *55*, 651-667.

31. Lazzara, T. D.; Lau, K. H. A.; Knoll, W.; Mounted Nanoporous Anodic Alumina Thin Films as Planar Optical Waveguides. *J. Nanosci. Nanotechnol.* **2010,** *10*, 4293-4299.

32. Feldoto, Z.; Varga, I.; Blomberg, E.; Influence of Salt and Rinsing Protocol on the Structure of PAH/PSS Polyelectrolyte Multilayers. *Langmuir* **2010,** *26*, 17048-17057.

33. Chen, H. M.; Lin, C. W.; Hydrogel-coated streptavidin piezoelectric biosensors and applications to selective detection of Strep-Tag displaying cells. *Biotechnol. Progr.* **2007,** *23*, 741-748.

34. Ram, M. K.; Bertoncello, P.; Ding, H.; Paddeu, S.; Nicolini, C.; Cholesterol Biosensors Prepared by Layer-by-Layer Technique. *Biosens Bioelectron* **2001,** *16*, 849-856.

35. Edmiston, P. L.; Saavedra, S. S.; Molecular Orientation Distributions in Protein Films. 4. A Multilayer Composed of Yeast Cytochrome C Bound through an Intermediate Streptavidin Layer to a Planar Supported Phospholipid Bilayer. *j. Am. Chem. Soc.* **1998,** *120*, 1665-1671.

36. Klajnert, B.; Stanislawska, L.; Bryszewska, M.; Palecz, B.; Interactions between PAMAM Dendrimers and Bovine Serum Albumin. *Biochim. Biophys. Acta, Proteins Proteomics* **2003,** *1648*, 115-126.

37. Livnah, O.; Bayer, E. A.; Wilchek, M.; Sussman, J. L.; 3-Dimensional Structures of Avidin and the Avidin-Biotin Complex. *PNAS* **1993,** *90*, 5076-5080.

38. Pugliese, L.; Coda, A.; Malcovati, M.; Bolognesi, M.; 3-Dimensional Structure of the Tetragonal Crystal Form of Egg-White Avidin in its Functional Complex with Biotin at 2.7 Angstrom Resolution. *J. Mol. Biol.* **1993,** *231*, 698-710.

39. Anzai, J.; Hoshi, T.; Nakamura, N.; Construction of Multilayer Thin Films Containing Avidin by a Layer-by-Layer Deposition of Avidin and Poly(anion)s. *Langmuir* **2000,** *16*, 6306-6311.

40. Drifford, M.; Dalbiez, J. P.; Effect of Salt on Sodium Polystyrene Sulfonate Measured by Ligth-Scattering. *Biopolymers* **1985,** *24*, 1501-1514.

41. Ball, V.; Voegel, J. C.; Schaaf, P.; Effect of thiocyanate counterion condensation on poly(allylamine hydrochloride) chains on the buildup and permeability of polystyrenesulfonate/polyallylamine polyelectrolyte multilayers. *Langmuir* **2005,** *21*, 4129-4137.

42. Jachimska, B.; Jasinski, T.; Warszynski, P.; Adamczyk, Z.; Conformations of Poly(Allylamine hydrochloride) in electrolyte solutions: Experimental measurements and

theoretical modeling. *Colloids Surf., A* **2010,** *355*, 7-15.

43. Schmid, G.; Emmrich, E.; Majoral, J.-P.; Caminade, A.-M.; The Behavior of Au55 Nanoclusters on and in Thiol-Terminated Dendrimer Monolayers. *Small 1*, 73-75.

44. Emmrich, E.; Franzka, S.; Schmid, G.; Monolayers of a fourth-generation thiol-terminated dendrimer. *Nano Lett.* **2002,** *2*, 1239-1242.

45. Feng, C. L.; Zhong, X. H.; Steinhart, M.; Caminade, A. M.; Majoral, J. P.; Knoll, W.; Graded-bandgap quantum-dot-modified nanotubes: A sensitive biosensor for enhanced detection of DNA hybridization. *Adv. Mater.* **2007,** *19*, 1933.

46. Schmitt, J.; Grunewald, T.; Decher, G.; Pershan, P. S.; Kjaer, K.; Losche, M.; Internal Structure of Layer-by-Layer Adsorbed Polyelectrolyte Films - A Neutron and X-Ray Reflectivity Study. *Macromolecules* **1993,** *26*, 7058-7063.

47. Liu, G. M.; Zhao, J. P.; Sun, Q. Y.; Zhang, G. Z.; Role of chain interpenetration in layer-by-layer deposition of polyelectrolytes. *J. Phys. Chem. B* **2008,** *112*, 3333-3338.

48. Xie, A. F.; Granick, S.; Local Electrostatics within a Polyelectrolyte Multilayer with Embedded Weak Polyelectrolyte. *Macromolecules* **2002,** *35*, 1805.

49. Dobrynin, A. V.; Rubinstein, M.; Theory of polyelectrolytes in solutions and at surfaces. *Prog. Polym. Sci.* **2005,** *30*, 1049-1118.

50. Castelnovo, M.; Joanny, J. F.; Formation of polyelectrolyte multilayers. *Langmuir* **2000,** *16*, 7524.

51. Scheller, A. *Winspall*, 3.01; Max-Planck Institute for Polymer Research: Mainz, Gernany.

52. Kim, D. H.; Lau, K. H. A.; Joo, W.; Peng, J.; Jeong, U.; Hawker, C. J.; Kim, J. K.; Russell, T. P.; Knoll, W.; An optical waveguide study on the nanopore formation in block copolymer/homopolymer thin films by selective solvent swelling. *J. Phys. Chem. B* **2006,** *110*, 15381-15388.

53. Kim, D. H.; Lau, K. H. A.; Robertson, J. W. F.; Lee, O. J.; Jeong, U.; Lee, J. I.; Hawker, C. J.; Russell, T. P.; Kim, J. K.; Knoll, W.; Thin Films of Block Copolymers as Planar Optical Waveguides. *Adv. Mater.* **2005,** *17*, 2442.

Acknowledgements. A.J. and C.S. gratefully acknowledge financial support from the DFG (JA 963/8-1 and STE 884/9-1 as well as the SFB 803). T.D.L. acknowledges the award of a doctoral scholarship from *le Fonds Québécois de la Recherche sur la Nature et les Technologies* (FQRNT) and additional financial support from the Göttingen Graduate School for Neurosciences and molecular Biosciences (GGNB).

Chapter 6

Benefits and Limitations of Porous Substrates as Biosensors for Protein Adsorption

By:
Thomas D. Lazzara,[†] *Ingo Mey*,[†] *Claudia Steinem*,[†] *Andreas Janshoff*[§]

Graphical abstract:

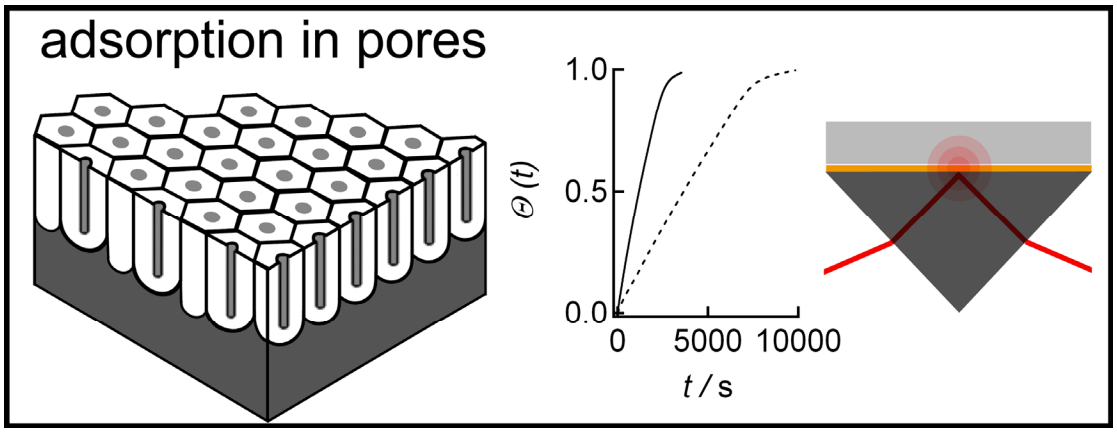

Manuscript submitted to:
Analytical Chemistry (ACS)
2011

[†] Institute of Organic and Biomolecular Chemistry, Tammannstrasse 2, Göttingen, 37077, Germany.
[§] Institute of Physical Chemistry, Tammannstrasse 6, Göttingen, 37077, Germany.

Abstract

Porous substrates have gained widespread interest for biosensor applications based on molecular recognition. Thus, there is a great demand to systematically investigate the parameters that limit the transport of molecules towards and within the porous matrix as a function of pore geometry. Finite elements simulations (FES) and time-resolved optical waveguide spectroscopy (OWS) experiments were used to systematically study the transport of molecules and their binding on the inner surface of a porous material. OWS allowed us to measure the kinetics of protein adsorption within porous anodic aluminum oxide membranes composed of parallel-aligned, cylindrical pores with pore radii of 10-35 nm and pore depths of 2-8 μm. FES showed that protein adsorption on the inner surface of a porous matrix is almost exclusively governed by the flux into the pores. The pore-interior nearly acts as a perfect sink for the macromolecules. Neither diffusion within the pores nor adsorption on the surface are rate limiting steps, except for very low rate constants of adsorption. While adsorption on the pore walls is mainly governed by the stationary flux into the pores, desorption from the inner pore walls involves the rate constants of desorption and adsorption, essentially representing the protein-surface interaction potential. FES captured the essential features of the OWS experiments such as the initial linear slopes of the adsorption kinetics, which are inversely proportional to the pore depth and linearly proportional to protein concentration. We show that protein adsorption kinetics allows for an accurate determination of protein concentration, while desorption kinetics could be used to capture the interaction potential of the macromolecules with the pore walls.

Keywords: biosensor, finite elements simulations, macromolecular transport, macroporous substrate, optical waveguide spectroscopy, protein adsorption kinetics

6.1 Introduction

Biosensors based on the specific binding of proteins on receptor-functionalized surfaces are among the most widespread analytical tools in biorecognition research.[1-5] The goal is either to quantify the interaction with the surface in terms of rate constants (adsorption and desorption rate) or association/dissociation constants (adsorption isotherms) to determine the protein concentration in the bulk phase. In either case, knowledge of mass transport limitations is pivotal to obtain reliable data, allowing the determination of biologically relevant interaction parameters.[6-7] Among the many available experimental techniques to measure rate constants and adsorption isotherms, surface plasmon resonance (SPR)

spectroscopy,[8-9] acoustic resonators such as the quartz crystal microbalance,[3] thin-film reflectometry and optical waveguide methods[10-11] are the most common ones.

While the adsorption behavior of molecules and macromolecules at planar interfaces is well described[7,12-14] and has been extensively experimentally characterized for practical purposes,[15-16] the growing number of applications involving mesoporous and macroporous substrates requires a comprehensive investigation of the factors governing macromolecular adsorption within functionalized porous substrates.[17-21] Porous TiO_2, SiO_2 or Al_2O_3 have recently been investigated as sensor devices to detect protein adsorption on functionalized pore-walls.[17,22-27] A particularly relevant material is anodic aluminum oxide (AAO), which has non-intersecting, hexagonally ordered cylindrical pores that run straight through the film thickness with adjustable pore diameter.[28-31] AAO has been used in selective separation of drug enantiomers,[32] and DNA oligomers[33] and in the development of on-chip biosensors for protein detection.[22] Some studies have provided insight into how various parameters, such as ionic strength,[34] particle size[35-36] and porosity[10] modify the binding efficiency and the transport within porous substrates. However, there is a fundamental need to elucidate which parameters are accessible from a biosensor readout based on porous substrates.

Here, we focused on the protein adsorption kinetics in a porous material using a representative flow cell geometry and solving the convective-diffusion equation with adsorptive boundary conditions employing finite elements simulations (FES). FES results were compared with optical waveguide spectroscopy (OWS) experiments on AAO substrates exposed to avidin solutions. We show that the dominant linear behavior of the time-resolved change in surface concentration can be explained in terms of boundary layer theory,[35,37] i.e., adsorption kinetics are predominately driven by the flux into the pores. Consequently, the large porous surface area behaves as a perfect sink for protein binding, which results in a depletion of the solution and produces a stationary Lévêque boundary layer.[37] This makes porous surfaces suitable for potential sensor applications to determine bulk protein concentrations with high accuracy, but inadequate to determine the rate constant of adsorption from measuring the surface concentration with time, unless the rate constants are very small.

6.2. Theory

6.2.1. Mass Balance on a Flat Surface

In this section, we describe the advection-diffusion equation of an adsorbent carrying liquid with laminar flow perpendicular to a flat adsorbing surface. For the sake of simplicity, we assume a fully developed flow profile in a 1-dimensional rectangular channel (figure 6.1A/B). The flow velocity $u_x(y) = \gamma y\left(1 - y/b\right)$ in *x*-direction is parabolic across the thickness (2*b*) of the flow cell. γ is the wall shear rate ($\gamma = 2u_{\max}/b$), and $u_{\max}$ the maximum velocity of the flow in the center of the channel at $y = b$. Ignoring diffusion in the direction of the flow (*x*-direction), the transient convective diffusion equation governing the adsorption on a flat surface is given as:

$$\frac{\partial c(x,y,t)}{\partial t} + \gamma y\left(1 - \frac{y}{b}\right)\frac{\partial c(x,y,t)}{\partial x} = D\frac{\partial^2 c(x,y,t)}{\partial y^2}, \quad 0 \le y \le b \qquad \text{equation (1)}$$

with the following initial and boundary conditions:

at $t = 0$, $c = 0$ for all $x, y > 0$ equation (2a)

at $x = 0$, $c = c_b$ for all y, t equation (2b)

at $y = b/2$, $c = c_b$ equation (2c)

at $y = 0$, $\frac{d\Gamma(x,t)}{dt} = D\frac{\partial c(x,0,t)}{\partial y} = k_{ad}c(x,0,t)\left(\Gamma_{\max} - \Gamma(x,t)\right) - k_{des}\Gamma(x,t)$ equation (2d)

and assuming a stationary, fully developed plane Poiseuille flow implying $\frac{\partial c(x,b/2,t)}{\partial t} = 0$.

D is the diffusion constant of the protein, $c(x,y,z)$ the concentration of the protein, and c_b the bulk concentration of the protein far away from any surface. $\Gamma(x,t)$ denotes protein surface concentration, $\Gamma_{\max}$ is the maximum surface concentration, k_{ad} and k_{des} the rate constants of adsorption and desorption, respectively.

6.2.2. Porous Surfaces

The geometry of the flow cell and the porous media used for simulations and experiments is illustrated in figure 6.1. where eq. (1) describes the mass balance in the flow cell, while absence of convection is assumed inside the pores. At the inner pore walls, adsorptive boundary conditions (eqs. (2a-d)) are assumed, while reflective boundary conditions are assigned to the pore rims capturing only adsorption within the porous matrix. The boundary condition given in eq. (2d) takes care of the mass balance at the surface assuming a first order Langmuir kinetics.

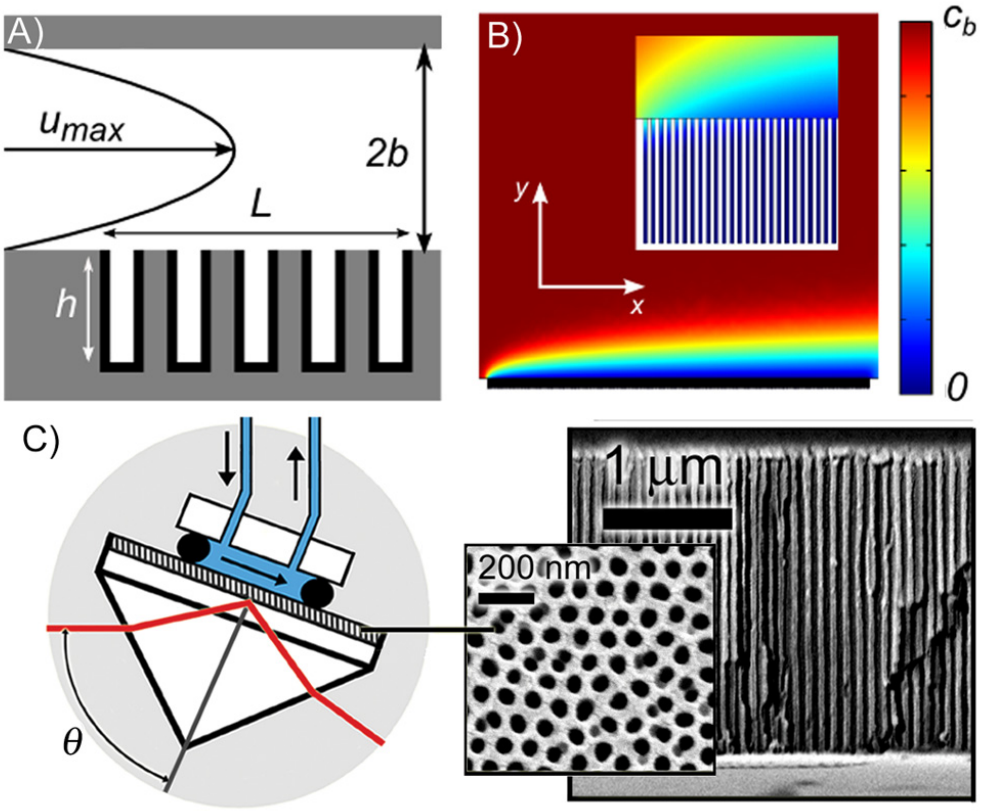

Figure 6.1. (**A**) Flow cell geometry used for FES and OWS studies of protein adsorption. For the simulations, equally spaced pores with R_{pore} = 25 nm and h = 3,2 µm along a distance of L = 120 µm. The flow chamber has a height of $2b$ = 0.5 mm with a maximum flow velocity of u_{max}. (**B**) Stationary concentration profile taken after 60 s. (**C**) Schematic of the OWS set-up with SEM images of porous AAO with R_{pore} = 28 nm.

The SEM images (figure 6.1C, right hand side) depict the top view and cross-section of AAO, showing the ordered cylindrical porous structure of the material. The number of pores per unit area is constant throughout. The membranes have hexagonally packed pores with inter-pore distances of p = 90-100 nm. The pore radius of the samples can, however be adjusted between R_{pore} = 10-40 nm by isotropic pore widening in phosphoric acid. The pore depth h is controlled by the duration of the anodization.

6.2.3. Simplified Adsorption Kinetics in Porous Media

Assuming that entry into the pores is the rate limiting step of protein adsorption on the pore walls, a stationary boundary layer will be established, as found for perfect sink conditions ($c(y = 0) = c_{wall} = 0$) on flat surfaces (supplementary information, figure 6.S1). This assumes that proteins experience numerous surface contacts, once entering the pores, which increases the apparent rates of adsorption and justifies approximate 'perfect sink' conditions for porous media.

FES show the validity of boundary layer theory for 'perfect sink' conditions with a large parameter space. Only at very low rate constants ($k_{ad} < 10^{-3}$ $m^3mol^{-1}s^{-1}$), the flux becomes non-stationary and adsorption follows Langmuir kinetics. At the end ($x = L$) of the adsorption area, the constant flux into the pores can be estimated to be approximately:

$$j = D\left(\frac{\partial c(L,0)}{\partial y}\right)_{wall} = \frac{D}{\delta(L)}\left(c_b - c_{wall}\right) = \frac{D}{\delta(L)}c_b \qquad \text{equation (3)}$$

with the diffusion layer thickness δ at $x = L$:

$$\delta(L) = 1.475\left(\frac{DbL}{u_{max}}\right)^{\frac{1}{3}}. \qquad \text{equation (4)}$$

The corresponding average diffusion layer thickness is:

$$\langle\delta\rangle = \frac{1}{L}\int_0^L 1.475\left(\frac{Dbx}{u_{max}}\right)^{\frac{1}{3}} dx\,. \qquad \text{equation (5)}$$

Consequently, the surface concentration at $x = L$ and the corresponding average surface concentration $\langle\Gamma(t)\rangle$ as a function of time is:

$$\frac{d\Gamma(L,0,t)}{dt} = D\left(\frac{\partial c(L,0)}{\partial y}\right)_{wall}\frac{\pi R_{pore}^2}{2\pi h R_{pore} + \pi R_{pore}^2} \cong \frac{D}{1.475\left(\frac{DbL}{u_{max}}\right)^{\frac{1}{3}}}c_b\frac{R_{pore}}{2h} \qquad \text{equation (6a)}$$

$$\Gamma(L,0,t) \cong 0.68\left(\frac{u_{max}D^2}{bL}\right)^{\frac{1}{3}}\frac{R_{pore}}{2h}c_b t \qquad \text{equation (6b)}$$

$$\left\langle \Gamma(t) \right\rangle \cong \frac{D}{\langle \delta \rangle} \frac{R_{\text{pore}}}{2h} c_{\text{b}} t \approx 0.92 \left(\frac{u_{\max} D^2}{bL} \right)^{\frac{1}{3}} \frac{R_{\text{pore}}}{2h} c_{\text{b}} t \qquad \text{equation (6c)}$$

The area ratio between pore entry area (πR^2_{pore}) and overall surface area of a single pore ($2\pi R_{\text{pore}} h$) needs to be taken into account because the flux into the pores (molecules per *pore-area* and time) relates to a different area than the rate of adsorption (molecules per *wall-area* and time). This explains why the kinetics are generally slower with increasing surface area. Essentially, eq. (6c) predicts that the change in surface concentration for $t \to 0$ will be linear with respect to bulk protein concentration c_{b}, and inversely proportional to the pore length h.

6.3. Results and Discussion

All FES were carried out using COMSOL™ within an experimentally accessible parameter space. A standard parameter set was used if not indicated otherwise (range given in brackets): maximum velocity $u_{\max}$ = 10^{-3} m·s^{-1} (10^{-5}-10^{-1} m·s^{-1}), bulk concentration c_{b} = 10^{-3} mol·m^{-3} (10^{-4}-10^{-2} mol·m^{-3}), k_{des} = 0, k_{ad} = 10^{3} m^3·mol^{-1}·s^{-1} (10^{-4}-10^{4} m^3·mol^{-1}·s^{-1}), D = 10^{-11} m^2·s^{-1} (10^{-13}-10^{-8} m^2·s^{-1}), number of pores = 1200, pore radius R_{pore} = 25 nm, interpore distance p = 100 nm, length h = 3.2 µm (0.8-9.6 µm).

6.3.1. Simulating Protein Adsorption Kinetics on Flat Surfaces

We first investigated to what extent the rate constant of adsorption (k_{ad}) can be regained from FE-simulations by fitting the integrated form of eq. (2) to the FES data, assuming $c(x,0,t) = c_{\text{b}}$ (figure 6.2A):

$$\frac{\Gamma(x,t)}{\Gamma_{\max}} = \frac{k_{\text{ad}} c_{\text{b}}}{k_{\text{ad}} c_{\text{b}} + k_{\text{des}}} \left(1 - \exp\left\{ \frac{t}{\left(k_{\text{ad}} c_{\text{b}} + k_{\text{des}} \right)^{-1}} \right\} \right) \qquad \text{equation (7)}$$

For small k_{ad}, mass transport is not rate limiting, since $c(x,0,t) \cong c_{\text{b}}$ and kinetics are entirely governed by eq. (7).

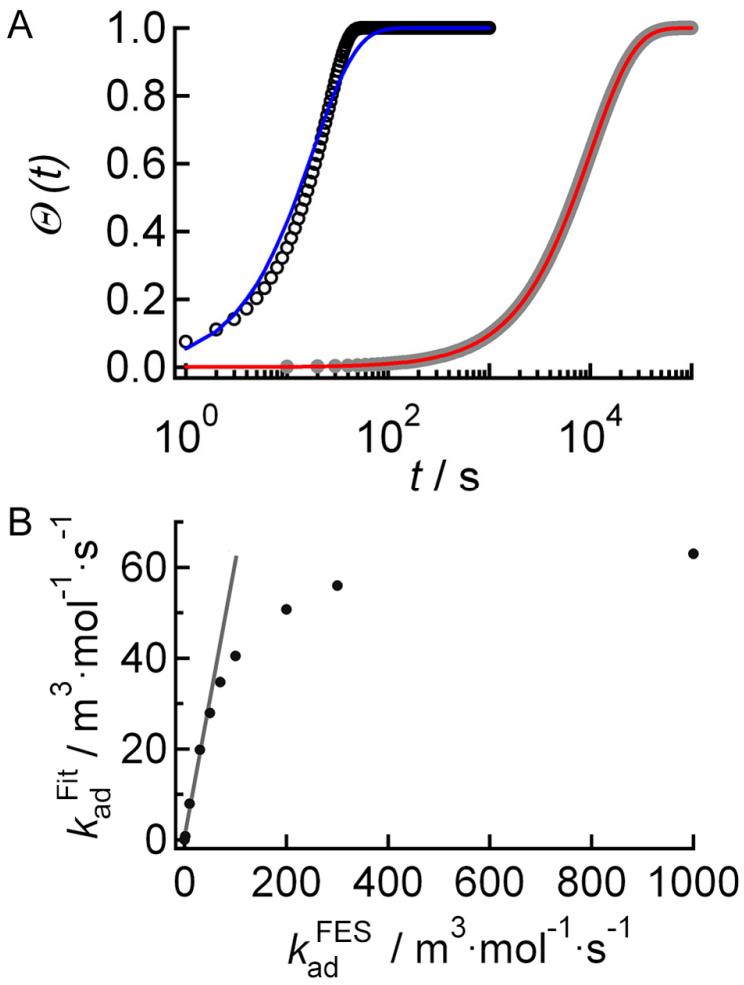

Figure 6.2. FES of the adsorption process on a flat surface. (**A**) FES with $k_{ad} = 3\times10^{2}$ m^3 mol^{-1} s^{-1} (open circles) and $k_{ad} = 10^{-1}$ m^3 mol^{-1} s^{-1} (filled circles). The solid lines (blue and red) are the results of fitting eq. (7) to the simulations providing k_{ad}^{Fit}. (**B**) Correlation between k_{ad}^{Fit} and k_{ad}^{FES}, the latter rate used as input parameter for FES. The solid line represents 100% correlation.

Albeit adsorption kinetics with larger adsorption rates (k_{ad} > 10 m^3 mol^{-1} s^{-1}) can apparently be modeled with Langmuir adsorption kinetics, the rate constants obtained deviate substantially from the given k_{ad} values in the simulations.

Figure 6.2B shows a correlation between the given k_{ad}^{FES} and fitted k_{ad}^{Fit} using eq. (7). It becomes obvious that k_{ad}^{Fit} is greatly underestimated due to mass transport limitations, which create an almost stationary depletion layer over the surface (supplementary information, figure 6.S1).

6.3.4. Simulating Protein Adsorption Kinetics in Porous Media

One might assume that the 1-dimensional diffusion of proteins within pores that display a high aspect ratio ($R_{pore}/h < 10^{-3}$), might be the rate limiting step of adsorption (for $h \leq 10$ μm). In fact, pore dimensions become only relevant on much larger length scales with h >>10 μm than considered in this study. Assuming that diffusion is restricted to the y-axis, which is justified by the small radii of the pores ($R_{pore} < 50$ nm), a protein would cover the distance of 1 μm in less than 0.1 s according to $\tau = \langle y^2 \rangle / D$ with $\langle y^2 \rangle$ the mean square displacement. More sophisticated numerical analysis confirms that this hands-on argument holds for the pores used in this study (supplementary information, figure 6.S2). The impact of pore radius on the diffusion constant of the protein has been neglected since hindered diffusion only becomes relevant if the pore radius is very close to the hydrodynamic radius of the protein,[38] in our case for $R_{pore}/R_{protein} < 10$.

Generally, we found that the presence of pores slows down the adsorption kinetics with increasing number of pores as compared to a flat surface with the same set of parameters (figure 6.3A). Importantly, the adsorption kinetics ($\Gamma(t)$) becomes almost linear over a long time period with increasing number of pores associated with a stationary flow into the pores due to a diffusion boundary layer produced by the adsorption capacity of the pores (figure 6.1B and figure 6.2). An infinite number of pores essentially represent a perfect sink for surface approaching proteins which is discussed in the previous section. In order to keep numeric calculations at a manageable level, we used 1200 pores in a 2D geometry (supplementary information, figure 6.S3) throughout the study, which produce a stationary boundary layer similar to that of a reactive wall (supplementary information, figure 6.S4 and S5).

For very low adsorption rate constants ($k_{ad} < 10^{-3}$ m^3 mol^{-1} s^{-1}), eq. (8) can safely be used to fit the simulated data reproducing the rates (k_{ad}^{FES}) used for the simulation (figure 6.3B). For larger k_{ad} the system behaves mass transport controlled, which results in a constant flux into the pores and a stationary concentration profile above the pores (supplementary information, figure 6.S5).

Figure 6.3B demonstrates to what extent the adsorption kinetics in porous media deviates from rate limitation. The linear initial slope S_i ($S_i = d\Theta/dt|_{t\to 0}$) obtained from FES is plotted as a function of the adsorption rate k_{ad} used as an input for FES. For very low rate constants

the slope is proportional to k_{ad} but deviates already for $k_{ad} > 10^{-3}$ m^3 mol^{-1} s^{-1} leading to a much slower adsorption of proteins than expected for rate limiting adsorption (supporting information, figure 6.S6). Figure 6.3C confirms that the initial slope S_i of $\Gamma(t)$ essentially follows eqs. (7b) and (7c) and becomes independent of k_{ad} for $k_{ad} > 1$ m^3 mol^{-1} s^{-1}. Notably, k_{ad} is usually in the range of > 100 m^3 mol^{-1} s^{-1} for most molecular recognition events. For instance, low affinity antigen-antobidy interactions are reported to exhibit a k_{ad} in the range of 1 m^3 mol^{-1} s^{-1}, while high affinity antigen-antibody or biotin-avidin reactions display rate contacts larger than 10,000 m^3 mol^{-1} s^{-1}.[39, 40]

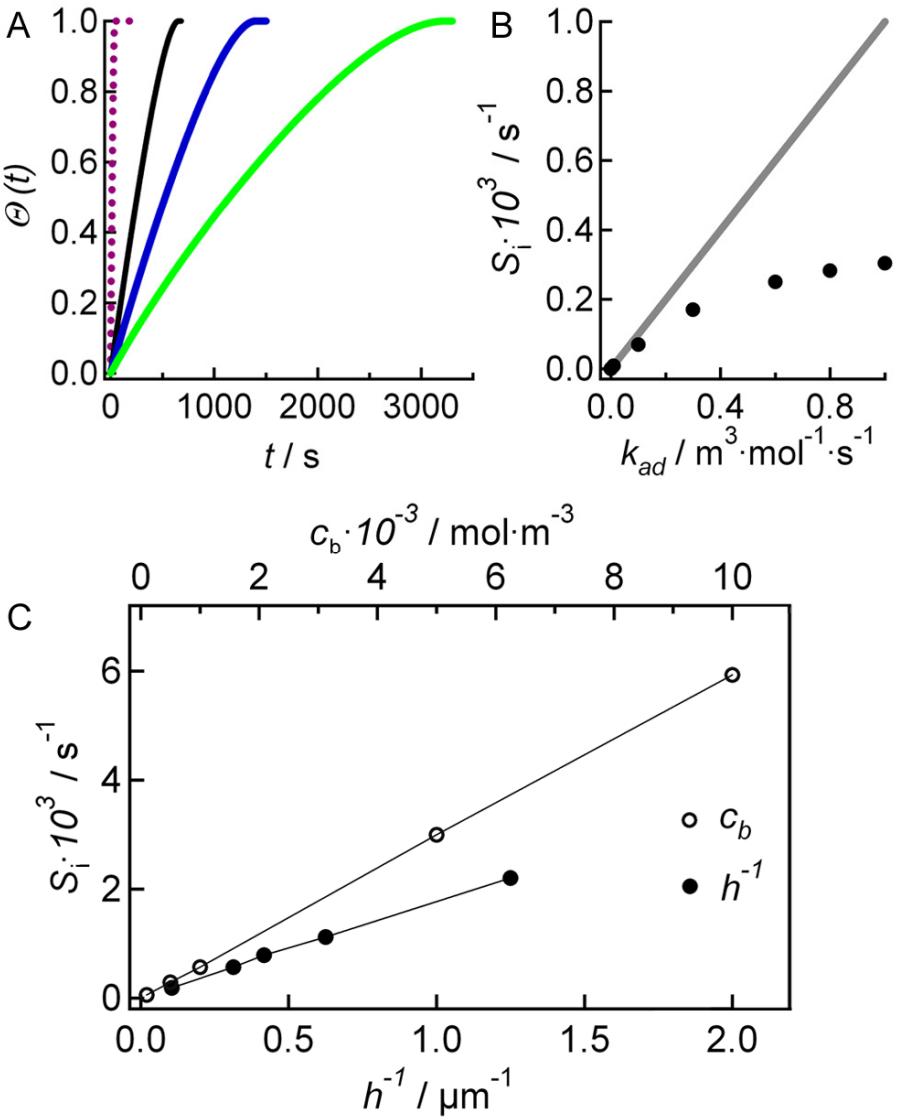

Figure 6.3. (**A**) Surface coverage as a function of time for different pore lengths, h = 0.8 µm (black), h = 1.6 µm (blue), h = 3.2 µm (green); the dashed purple line shows the result obtained on a flat surface. (**B**) Correlation between k_{ad} used in FES and the resulting initial slope (S_i). The solid line corresponds to $S_i = k_{ad}c_b$. (**C**) Linear dependency of S_i on protein concentration (c_b) and reciprocal pore depth (h^{-1}).

In conclusion, replacing the flat adsorbing surface with porous media has one important consequence for kinetics of protein adsorption on the pore walls. The walls of the pores essentially act as a reacting wall (perfect sink), which produces a stationary concentration profile (depletion layer) that renders adsorption entirely controlled by mass transport into the pores. Porous media are essentially a realization of a perfect sink with respect to boundary layer theory producing the identical concentration profile expected for a flat surface with adsorbing boundary conditions. As a consequence, rate constants of adsorption can only be determined for very low affinity to the pore walls (for $k_{ad} < 10^{-3}$ m^3 mol^{-1} s^{-1}).

6.3.5. Adsorption Kinetics of Avidin Binding to Porous AAO

Verification of the theoretical considerations was obtained from protein adsorption experiments on AAO. A rectangular flow cell configuration under laminar flow was used in OWS experiments (figure 6.1C). The experimental adsorption surface has about 10^7 pores/mm^2, with cylindrical pores adjusted to a desired pore radius $R_{pore} \geq 10$ nm (figure 6.1C). By monitoring the change in the AAO dielectric response, we recorded the electrostatically[41] driven adsorption kinetics of avidin on the AAO pore walls. With an isoelectric point near pH 4, positively charged avidin binds to AAO at pH > 5, while it desorbs at pH < 3 (supplementary information, figure 6.S7). Kinetics were obtained by following the angular shift of a high order TM waveguide mode[11] (supplementary information, figure 6.S8). Generally, we found substantially slower kinetics in comparison to flat surfaces (figure 6.4). The adsorption of avidin (c_b = 1.5 μM) under similar conditions on a planar gold surface functionalized with negatively charged mercaptohexadecanoic acid, measured by surface plasmon resonance (SPR) takes about 10 s, which translates into $k_{ad} \approx$ 200 m^3 mol^{-1}·s^{-1}, while adsorption within a porous substrate (R_{pore} = 35 nm, h = 3.2 μm) takes about 60 times longer (figure 6.4). Using c_b = 1.5 μM avidin solution, the change in surface concentration with time is approximately linear over a long time period (500-600 s) until the pore wall surfaces start to become saturated with protein and thus the signal slowly levels off over the following 100-200 s. As argued in the previous section, the almost linear regime is predominately governed by the constant flux of protein molecules into the pores due to a stationary diffusion boundary layer that forms as a result of protein depletion. We estimated the avidin flux into an individual pore to be only a few proteins per pore per second. The increase in refractive index in the saturation regime corresponds to an overall protein layer thickness of 2.8 ± 0.5 nm, averaged over several experiments (n = 20) and

assuming $\varepsilon_{protein}$ = 2.1. This corresponds to about 50% surface coverage with avidin with dimensions of 4.0 × 5.5 × 6.0 nm^3.[42]

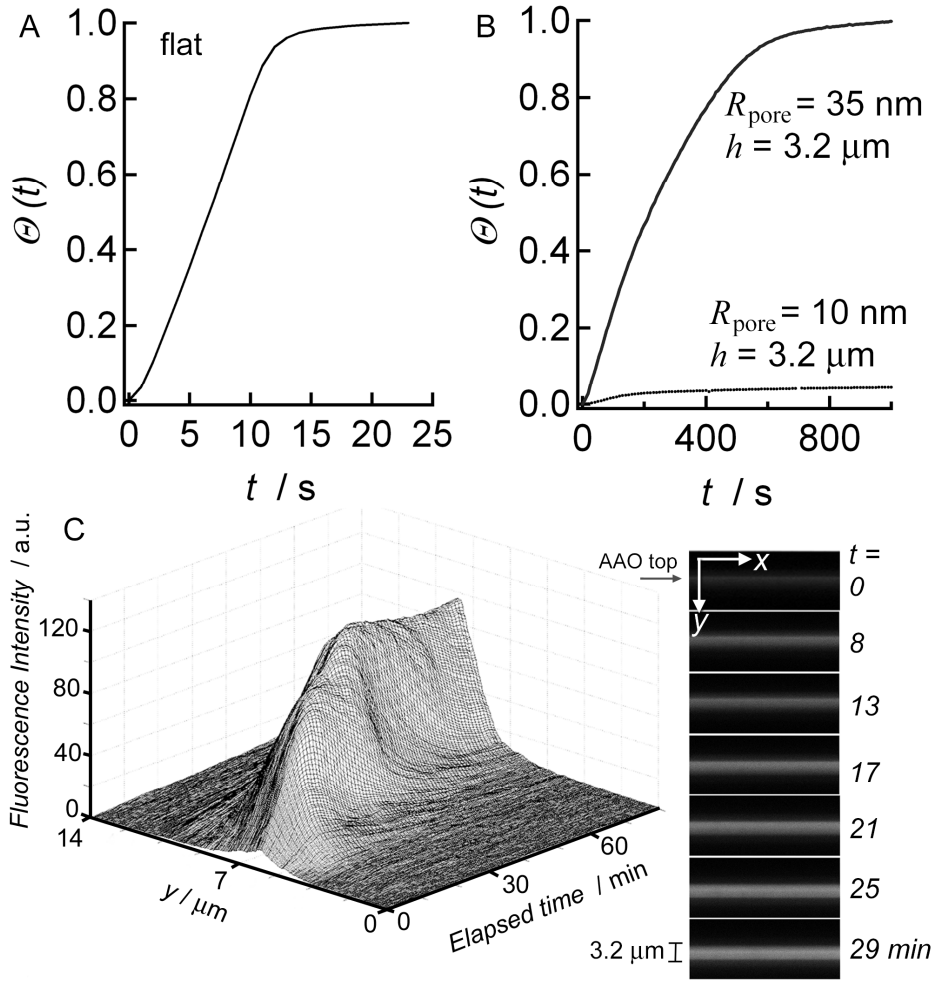

Figure 6.4. (**A**) Adsorption kinetics of avidin (c_b = 1.5 µM) on a flat negatively charged gold surface measured by SPR. (**B**) Avidin adsorption kinetics on AAO (c_b = 1.5 µM) as a function R_{pore}. Pores with R_{pore} = 10 nm are not filled with avidin due to a combined steric and electrostatic hindrance. (**C**) Time evolution of fluorescence, across the *y*-direction, of avidin (c_b = 0.45 µM) adsorbing onto AAO (R_{pore} = 32.5 nm, h = 3.2 µm). Right-hand side: vertical slices (*y*-direction) taken at different times showing the fluorescence increasing across the AAO thickness.

We corroborated the OWS adsorption kinetics (figure 6.4A/B) with time-resolved confocal laser scanning fluorescence microscopy. This was possible since AAO thin-films are sufficiently transparent with low background fluorescence. We imaged a cross-sectional portion of the AAO by taking sequential slices in the *z*-direction to study the evolution and distribution of the fluorescence signal arising from the adsorption of fluorescently Alexa-488 labeled avidin within AAO (R_{pore} = 32.5 nm, h = 3.2 µm). The fluorescence increase (*y*-direction) with time was essentially linear (figure 6.4C), as observed for the adsorption

kinetics measured by OWS. By varying the pore radii we found that the pore radius needed to be adjusted to R_{pore} > 20 nm, in order to ensure non-hindered pore entry and thus enable pore-filling.

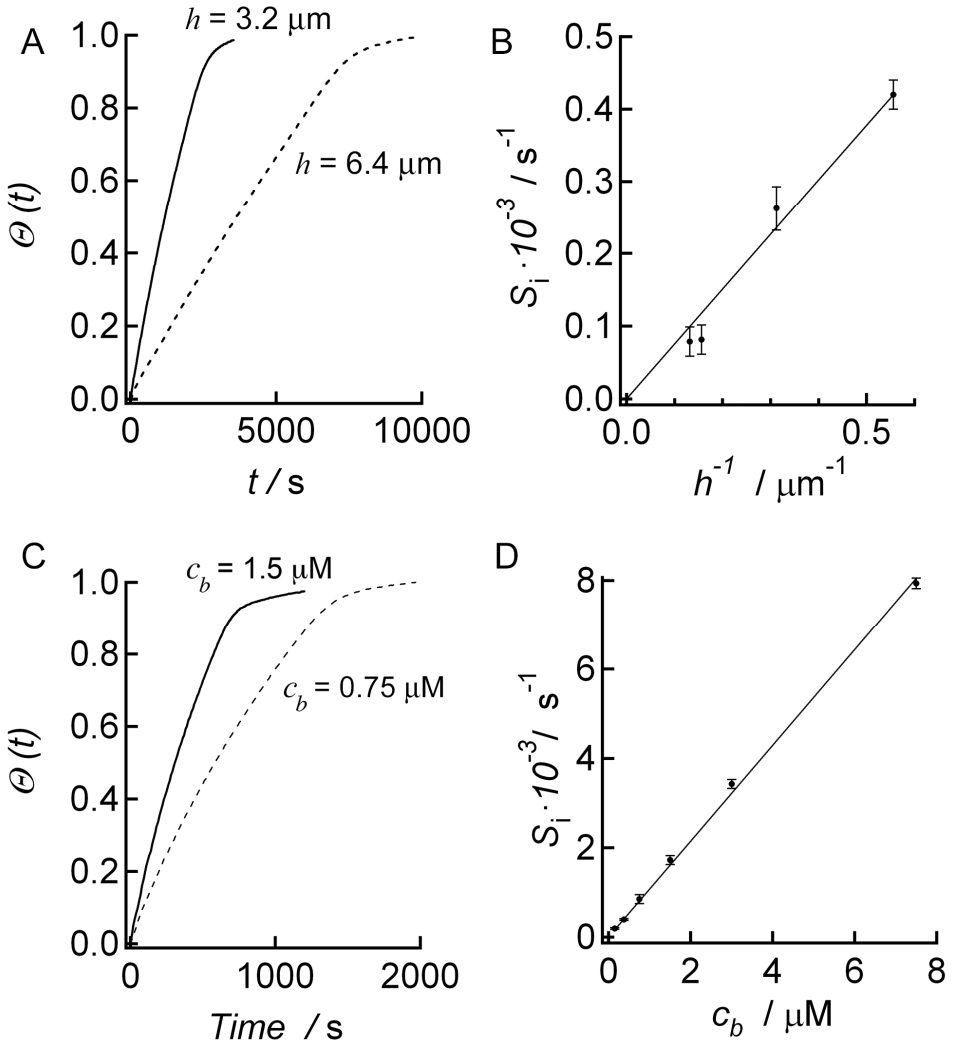

Figure 6.5. (**A**) Adsorption kinetics of avidin (c_b = 0.45 µM) on AAO (R_{pore} = 32.5 nm) with two different pore depths. (**B**) Experimentally determined S_i for avidin adsorption (c_b = 0.45 µM) on AAO (R_{pore} = 32.5 nm) as a function of the inverse pore depth h^{-1}. (**C**) Adsorption kinetics of avidin on AAO (h = 3.2 µm, R_{pore} = 35 nm) for two different bulk protein concentrations c_b. (**D**) S_i for avidin adsorption on AAO (h = 3.2 µm, R_{pore} = 35 nm) measured at different protein concentrations c_b.

Figure 6.4B shows that pores with R_{pore} = 10 nm are not filled with avidin on our experimental time scale. The early onset of adsorption is attributed to adsorption on the pore rims. Considering that the protein has a hydrodynamic radius of around 3.7 nm[43] the local pore radius is substantially reduced to about 5 nm and electrostatic repulsion and steric hindrance in the pore-entrance proximity significantly reduces the entrance probability, i.e. the flux into the pores. Therefore, all following experiments were carried out with AAO having pore radii of R_{pore} = 30-35 nm. In figure 6.5, the adsorption kinetics of avidin on

AAO substrates as a function of pore depth h and bulk avidin concentration c_b are shown. In good agreement with equation (7c) and figure 6.3C the slope depends linearly on c_b and h^{-1}. We obtained S_i by fitting the initial slope of the normalized adsorption kinetics, where the angular shift was converted into coverage ($\Theta(t) = \Gamma(t)/\Gamma_{max}$).

6.3.5. Desorption of Proteins from Porous Walls

Adsorption kinetics of proteins in porous media is almost exclusively governed by the stationary flux into the pores. It is valid to say that each protein that enters a pore immediately adsorbs on the pore wall because of the many surface contacts of the diffusing macromolecule and thus the increased interaction probability compared to a flat substrate. Until the surface coverage becomes nearly saturated, the rate constants of adsorption and desorption do not influence the deposition kinetics significantly. A different situation arises if the flow cell is flushed with fresh buffer that is devoid of proteins to measure desorption kinetics. We investigated this situation by simulating the release of proteins from a single pore to demonstrate the essential features of this process (figure 6.6). Initially, we assumed that the bulk concentration was everywhere zero ($c(y,t = 0) = 0$), while the coverage of the pore walls was maximal ($\Gamma(t = 0) = \Gamma_{max}$). Moreover, we assumed that at the pore entrance, $c(y = 0,t) = 0$, consistent with fast flushing. The boundary conditions at the pore walls remained $\dot{\Gamma}(t) = k_{ad} c_{wall}(t)\left(\Gamma_{max} - \Gamma(t)\right) - k_{des}\Gamma(t)$. Figure 6.6 shows the desorption kinetics ($\Gamma(t)$), and also the flux J at $y = 0$ from the pores into the flow cell for different k_{ad}. The kinetics are considerably slowed down by an increasing rate of adsorption, which can be attributed to rebinding of the released proteins to free surface sites. This reduces the bulk concentration of proteins in the pores and therefore also reduces the gradient that drives the proteins out of the pore. This is contrary to a flat surface where rebinding of released proteins to the surface is negligible if convection in x-direction flow is fast enough. More surface contacts due to longer pores increase the probability of sticking after release and therefore reduce the release kinetics accordingly. As opposed to adsorption, the flux out of the pores is time dependent since the concentration gradient changes with time and displays a maximum. At short times ($t \rightarrow 0$), the desorption kinetics is solely driven by k_{des}: $\Gamma(t) = \Gamma_{max} \exp\{-k_{des} t\}$. The flux increases with time since the bulk concentration in the pore increases due to the growing number of proteins desorbing from the pore walls. However, the decreasing number of molecules leads to a vanishing gradient. Consequently, the flux reaches a maximum that is strongly influenced by the adsorption rate (figure 6.6D).

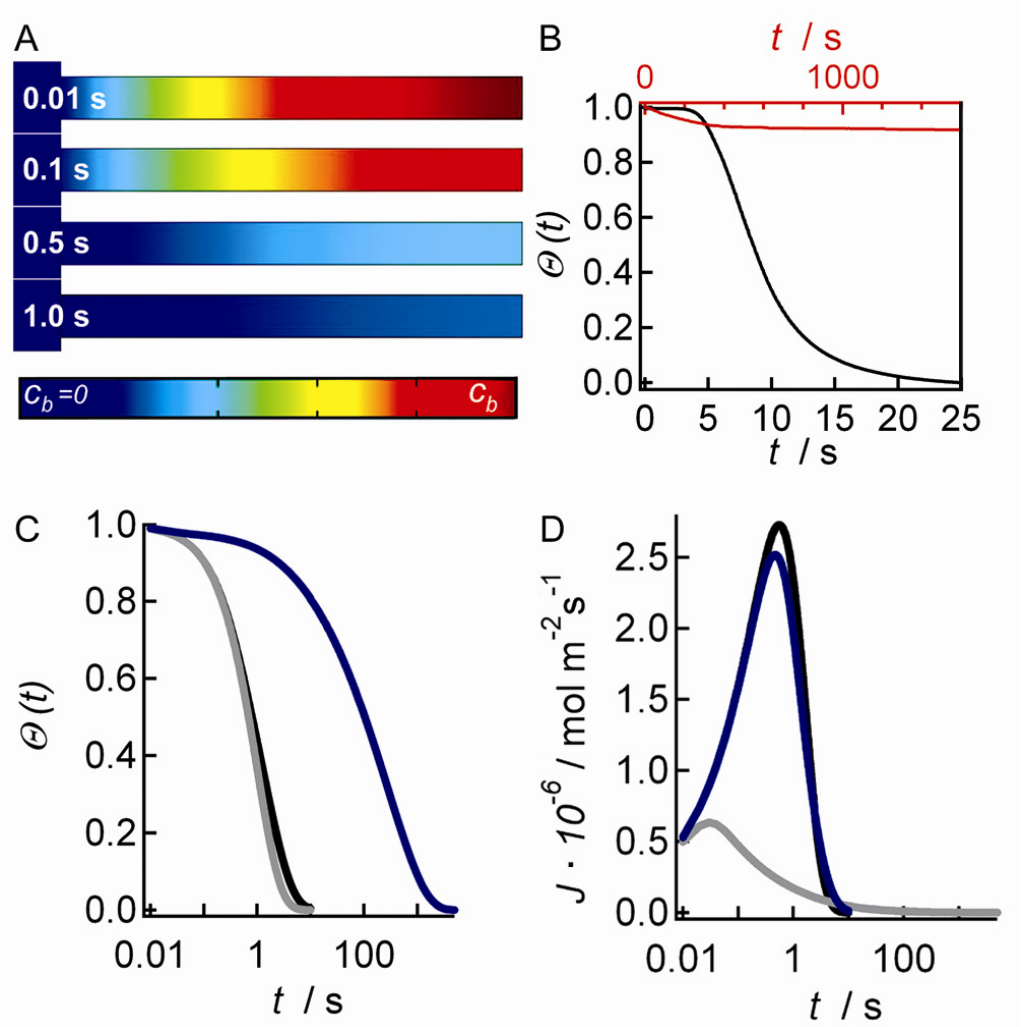

Figure 6.6. Desorption kinetics of proteins initially covering a single pore. (**A**) Simulated bulk concentration profile in a single pore at different times. (**B**) Experimentally measured surface coverage as a function of time for: i) the complete desorption of avidin from the porous surface by reduction of pH to values smaller than 3 (black curve) and ii) the incomplete desorption when protein-free buffer is flushed onto the AAO after saturation of the avidin adsorption process (red curve). (**C**) Simulated desorption kinetics as a function of k_{ad} ($k_{ad} = 10^3$ m^3 mol^{-1} s^{-1} (blue), $k_{ad} = 1$ m^3 mol^{-1} s^{-1} (grey), $k_{ad} = 10^{-3}$ m^3 mol^{-1} s^{-1} (black)) with $k_{des} = 1$. (**D**) Flux $J(t)$ of proteins across $z = 0$, the entrance of the pore, as a function of k_{ad} (color coding as in (C)).

In summary, desorption kinetics bears much richer physics and allows, in principle, to obtain both, k_{ad} and k_{des} from flushing the surface with protein-free buffer solution. It requires, however, numeric solutions of the governing mass balance equation due to the absence of a stationary gradient. Experimentally, we observed desorption of avidin from the porous surfaces by lowering the pH to 2.7 below the isoelectric point of the AAO surface (figure 6.6B). While the loading kinetics of a 1.5 µM avidin solution on AAO (R_{pore} = 32.5 nm, h = 3.2 µm) took 600 s, the release of avidin from the pore-walls devoid of affinity to avidin finished in less than 20 s. Conceivably, sensing schemes that rely on pore exit in response to external stimuli can be an effective method of utilizing the advantages of a nanoporous substrate for practical applications.

6.4. Concluding Remarks

The increasing interest in the applications of nanoporous media in biosensor research motivated our studies of the adsorption/desorption kinetics of proteins in porous AAO. Kinetics were investigated as a function of flow properties, pore geometry, and protein concentration both theoretically by means of finite elements simulations and experimentally using time-resolved optical waveguide spectroscopy.

We found that adsorption is mainly governed by the rate of protein entrance into the pores giving rise to a linear dependence of surface concentration with time consistent with boundary layer theory. This limits the usage of porous media as transducer or matrices, but bears an overlooked potential. While adsorption rates are out of reach, nanopores can act as a gate and time scales of adsorption can be easily shifted by producing pores of different lengths. Since the surface concentration is strictly proportional to the bulk concentration over very long time, nanoporous matrices are highly suitable for measuring bulk protein concentrations with high accuracy, almost regardless of the adsorption rates. This can be rationalized by a microscopic picture, in which proteins or any other molecule class with a finite stickiness adsorbs on the surface almost irreversibly due to the large number of surface contacts and the low surface coverage. Essentially, every protein which enters a pore with a high aspect ratio goes through a series of collisions with an almost uncovered surface, until the macromolecule finally adsorbs to the surface. Desorption leads to subsequent rebinding which in turn increases the dwell time of the protein inside the pores. The high surface area of the porous media and the small entrance area are responsible for this effect. Flushing the flow cell with protein-free buffer, inevitably leads to net desorption and protein release from the porous media. As opposed to the adsorption kinetics, the release from the pores strongly depends on the rate of adsorption (k_{ad}) since the resident time of the proteins is governed by the rebinding probability. In conclusion, the release kinetics compile both, rate of adsorption and rate of desorption. Albeit displaying richer physics, desorption and release are essentially more cumbersome to be described in terms of simple equations since fluxes are nonlinear and time dependent.

6.5. Experimental Section

AAO waveguide membranes. AAO membrane thin films (figure 6.1C) were fabricated by anodization of Al foils in 0.3 M oxalic acid, 40 V, at 1 °C. The Al was then removed, 2 nm of Cr and 25 nm of Au were evaporated on the AAO barrier side, and the AAO was finally mounted on LaSFN9 glass slides using an optical adhesive.[44] AAO thickness was controlled by the anodization time. The pores for all AAO membranes were widened to the desired radius R_{pore} in 5 vol. % H_3PO_4 (85%).

Surface plasmon resonance (SPR). SPR measurements were performed on a setup operating at 632.8 nm in the Kretschmann configuration.[45]

Optical waveguide spectroscopy (OWS). OWS measurements of AAO membranes mounted on LaSFN9 glass slides were performed on an SPR setup operating at λ = 632.8 nm.[34,45-46]

Fluorescence microscopy. CLSM measurements were performed on an upright confocal microscope from Carl Zeiss MicroImaging GmbH (LSM 710, Jena, Germany) with a 63× water immersion objective (WPlan-APO-CHROMAT (N.A.=1.0)).

Protein adsorption experiments. Avidin was dissolved in 20 mM phosphate buffer, 100 mM NaCl, pH = 7 (PBS) to obtain 1 mg/ml stock solutions. The flow cell was rinsed with ethanol, followed by PBS. Kinetics were monitored by following the change in a high order waveguide TM-mode. The 1 ml solution was passed through the flow cell (15 × 7.5 × 0.5 mm^3) until 1.4× the dead-volume was washed out, and then the solution was re-circulated using a peristaltic pump. The flow rate was kept constant at 0.4 ml/min.

Finite elements simulations. Calculations were performed with COMSOL Multiphysics 4.1. The models combine a 2D diffusion-convection equation with a 1D Langmuir-type surface adsorption equation. Adsorption occurs only at the inner pore-walls. Laminar flow was implemented as a time-constant parabolic velocity field in the flow chamber, above the pores.

6.6. References

(1) Casero, E.; Vazquez, L.; Parra-Alfambra, A. M.; Lorenzo, E. *Analyst* **2010**, *135*, 1878-1903.

(2) Endo, T.; Kerman, K.; Nagatani, N.; Takamura, Y.; Tamiya, E. *Anal. Chem.* **2005**, *77*, 6976-6984.

(3) Janshoff, A.; Galla, H. J.; Steinem, C. *Angew. Chem. Int. Ed.* **2000**, *39*, 4004-4032.

(4) McPhillips, J.; Murphy, A.; Jonsson, M. P.; Hendren, W. R.; Atkinson, R.; Hook, F.; Zayats, A. V.; Pollard, R. J. *Acs Nano* **2010**, *4*, 2210-2216.

(5) Shi, H. Q.; Tsai, W. B.; Garrison, M. D.; Ferrari, S.; Ratner, B. D. *Nature* **1999**, *398*, 593-597.

(6) Schuck, P. *Ann. Rev. Biophys. Biomol. Struct.* **1997**, *26*, 541-566.

(7) Schuck, P.; Minton, A. P. *Anal. Biochem.* **1996**, *240*, 262-272.

(8) Myszka, D. G. *Curr. Opin. Biotechnol.* **1997**, *8*, 50-57.

(9) Rich, R. L.; Myszka, D. G. *Curr. Opin. Biotechnol.* **2000**, *11*, 54-61.

(10) Huang, C. J.; Dostalek, J.; Knoll, W. *Biosens. Bioelectron.* **2010**, *26*, 1425-1431.

(11) Lau, K. H. A.; Tan, L. S.; Tamada, K.; Sander, M. S.; Knoll, W. *J. Phys. Chem. B* **2004**, *108*, 10812-10818.

(12) Rabe, M.; Verdes, D.; Seeger, S. *Adv. Colloid Interface Sci.* **2011**, *162*, 87-106.

(13) Schuck, P. *Ann. Rev. . Biophys. Biomol. Struct.* **1997**, *26*, 541-566.

(14) Schuck, P. *Curr. Opin. Biotechnol.* **1997**, *8*, 498-502.

(15) Myszka, D. G.; He, X.; Dembo, M.; Morton, T. A.; Goldstein, B. *Biophys. J.* **1998**, *75*, 583-594.

(16) Myszka, D. G.; Morton, T. A.; Doyle, M. L.; Chaiken, I. M. *Biophys. J.* **1997**, *64*, 127-137.

(17) Bonanno, L. M.; Kwong, T. C.; DeLouise, L. A. *Anal. Chem.* **2010**, *82*, 9711-9718.

(18) Carrasquilla, C.; Li, Y.; Brennan, J. D. *Anal. Chem.* **2011**, *83*, 957-965.

(19) DeLouise, L. A.; Miller, B. L. *Anal. Chem.* **2004**, *76*, 6915-6920.

(20) Feng, L.; Musto, C. J.; Kemling, J. W.; Lim, S. H.; Zhong, W.; Suslick, K. S. *Anal. Chem.* **2010**, *82*, 9433-9440.

(21) Qiao, Y. H.; Wang, D.; Buriak, J. M. *Nano Lett.* **2007**, *7*, 464-469.

(22) Alvarez, S. D.; Li, C. P.; Chiang, C. E.; Schuller, I. K.; Sailor, M. J. *Acs Nano* **2009**, *3*, 3301-3307.

(23) Dancil, K. P. S.; Greiner, D. P.; Sailor, M. J. *J. Am. Chem. Soc.* **1999**, *121*, 7925-7930.

(24) Mun, K. S.; Alvarez, S. D.; Choi, W. Y.; Sailor, M. J. *Acs Nano* **2010**, *4*, 2070-2076.

(25) Schwartz, M. P.; Alvarez, S. D.; Sailor, M. J. *Anal. Chem.* **2007**, *79*, 327-334.

(26) Trivinho-Strixino, F.; Guerreiro, H. A.; Gomes, C. S.; Pereira, E. C.; Guimaraes, F. E. G. *Appl. Phys. Lett.* **2010**, *97*.

(27) Walt, D. R. *Acs Nano* **2009**, *3*, 2876-2880.

(28) Li, A. P.; Muller, F.; Birner, A.; Nielsch, K.; Gosele, U. *J. Appl. Phys.* **1998**, *84*, 6023-6026.

(29) Li, F. Y.; Zhang, L.; Metzger, R. M. *Chem. Mater.* **1998**, *10*, 2470-2480.

(30) Nielsch, K.; Choi, J.; Schwirn, K.; Wehrspohn, R. B.; Gosele, U. *Nano Lett.* **2002**, *2*, 677-680.

(31) O'Sullivan, J. P.; Wood, G. C. *Proc. R. Soc. Lond. A* **1970**, *317*, 511-543.

(32) Lee, S. B.; Mitchell, D. T.; Trofin, L.; Nevanen, T. K.; Soderlund, H.; Martin, C. R. *Science* **2002**, *296*, 2198-2200.

(33) Vlassiouk, I.; Krasnoslobodtsev, A.; Smirnov, S.; Germann, M. *Langmuir* **2004**, *20*, 9913-9915.

(34) Lazzara, T. D.; Lau, K. H. A.; Abou-Kandil, A. I.; Caminade, A. M.; Majoral, J. P.; Knoll, W. *Acs Nano* **2010**, *4*, 3909-3920.

(35) Bird, R. B.; Stewart, W. E.; Lightfoot, E. N. *Transport Phenomena*; 2nd ed.; John Wiley & Sons Canada, Ltd., 2001.

(36) Deen, W. M.; Bohrer, M. P.; Epstein, N. B. *AlChE J.* **1981**, *27*, 952-959.

(37) Probstein, R. F. *Physicochemical hydrodynamics: an introduction*; John Wiley and Sons, 1994.

(38) Deen, W. M. *AlChE J.* **1987**, *33*, 1409-1425.

(39) Rispens, T.; te Velthuis, H.; Hemker, P.; Speijer, H.; Hermens, W.; Aarden, L. *Journal of Immunological Methods* **2011**, *365*, 50-57.

(40) Stamm, C.; Lukosz, W. *Sens. Actuators, B* **1994**, *18*, 183-187.

(41) Wolny, P. M.; Spatz, J. P.; Richter, R. P. *Langmuir* **2009**, *26*, 1029-1034.

(42) Livnah, O.; Bayer, E. A.; Wilchek, M.; Sussman, J. L. *PNAS* **1993**, *90*, 5076-5080.

(43) Wu, S. C.; Wong, S. L. *J. Biol. Chem.* **2005**, *280*, 23225-23231.

(44) Lazzara, T. D.; Lau, K. H. A.; Knoll, W. *J. Nanosci. Nanotechnol.* **2010**, *10*, 4293-4299.

(45) Knoll, W. *Annu. Rev. Phys. Chem.* **1998**, *49*, 569-638.

(46) Gitsas, A.; Yameen, B.; Lazzara, T. D.; Steinhart, M.; H., D.; Knoll, W. *Nano Lett.* **2010**, *10*, 2173-2177.

Acknowledgements. A.J. and C.S. gratefully acknowledge financial support from the DFG (JA 963/8-1 and STE 884/9-1 as well as the SFB 803). T.D.L. acknowledges the award of a doctoral scholarship from *le Fonds Québécois de la Recherche sur la Nature et les Technologies* (FQRNT) and additional financial support from the Göttingen Graduate School for Neurosciences and molecular Biosciences (GGNB).

Supporting Information Available. .
S1: Stationary flow profiles and variation of the diffusion layer thickness δ as a function of u_{max} and D. **S2**: Simulation of c_b as a function of time for a single pore. **S3**: Schematic of the porous system used for FES. **S4**: Adsorption kinetics simulated for 1, 300 and 1200 pores. Variation of S_i with the number of simulated pores for low and high k_{ad}. **S5**: Flow profiles shown at different times for low and high k_{ad}. Flux as a function of time for a single pore. **S6**: Variation of S_i as a function of k_{ad}. **S7**: Experimental adsorption and desorption curves for avidin on AAO. **S8**: Experimental OWS spectra showing the angular shift obtained for avidin adsorption and the acquired kinetics. Materials and additional experimental details included. This material is available free of charge via the Internet at http://pubs.acs.org.

6.7. Supporting information

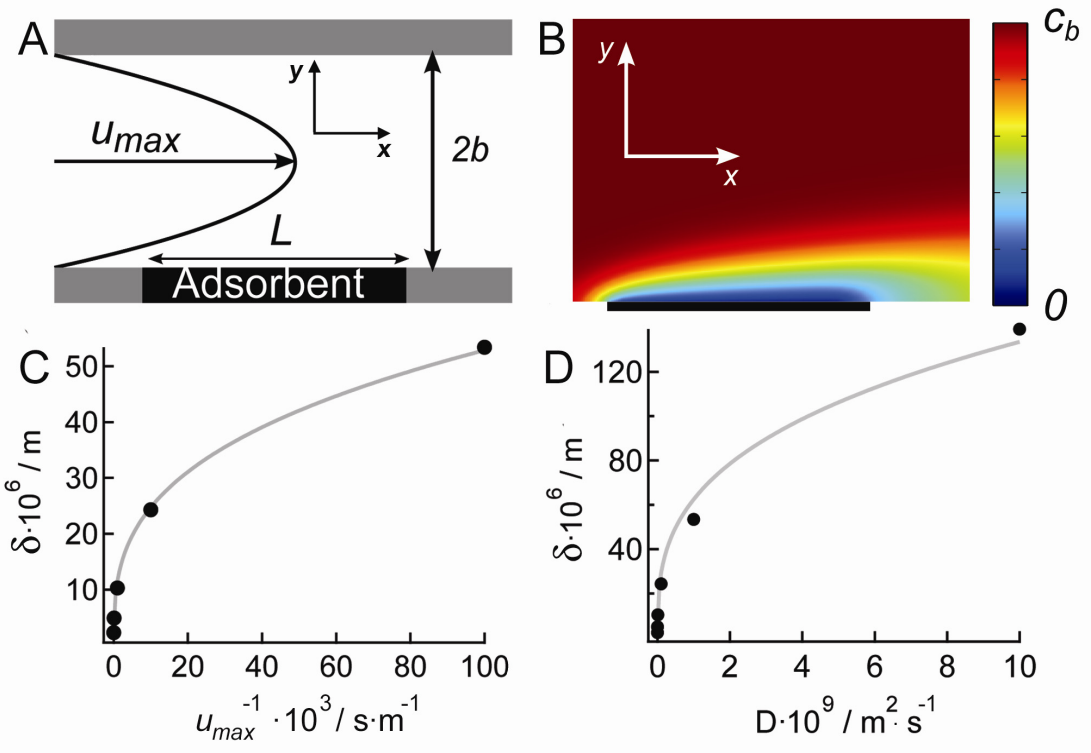

Figure 6.S1. (**A**) Geometry of the flow cell used for finite elements simulations according to the flow used for optical waveguide spectroscopy of protein adsorption. An adsorbent of length L=120 µm acts as a perfect sink with a boundary condition ($c(y = 0) = 0$) within a flow chamber of height $2b$=0.5 mm. The laminar flow shows the maximum speed u_{max} in the center at height h. (**B**) Stationary concentration profile, where the bulk concentration $c(x,y)$ is color coded ($c_b = 10^{-3}$ mol m^{-3}; $D = 10^{-11}$ m^2 s^{-1}). (**C, D**) Variation of the diffusion layer thickness $\delta(L/2)$ a function of u_{max} (C) and or D (D) assuming $D = 10^{-11}$ m^2 s^{-1} and u_{max}= 0.001 ms^{-1}, respectively. δ is arbitrarily taken as the value of y at which the concentration profile reaches 95% of the bulk concentration c_b, taken from a cross section at $x = L/2$. Black circles are from FEM simulations the solid line represents fits according to $\delta(L) \propto \left(\frac{D}{u_{max}}\right)^{\frac{1}{3}}$.

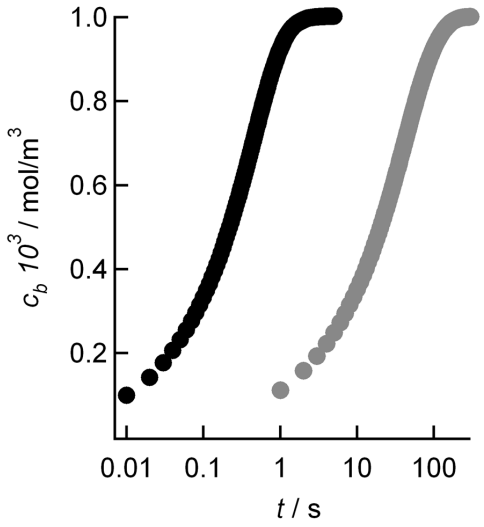

Figure 6.S2.
Kinetics of single pore-filling as a function of pore length h, black dots: h=3.2 µm, grey dots: h=32 µm. Initially, the protein concentration was assumed to be zero ($c(x,y,t) = 0$) and convection in y-direction excluded. Reflective boundary conditions were assumed to illustrate kinetics of pore diffusion until bulk concentration is reached in the pore.

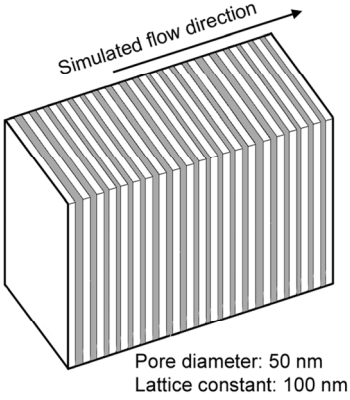

Figure 6.S3.
Schematic of the porous system used to simulate the adsorption kinetics using COMSOL.

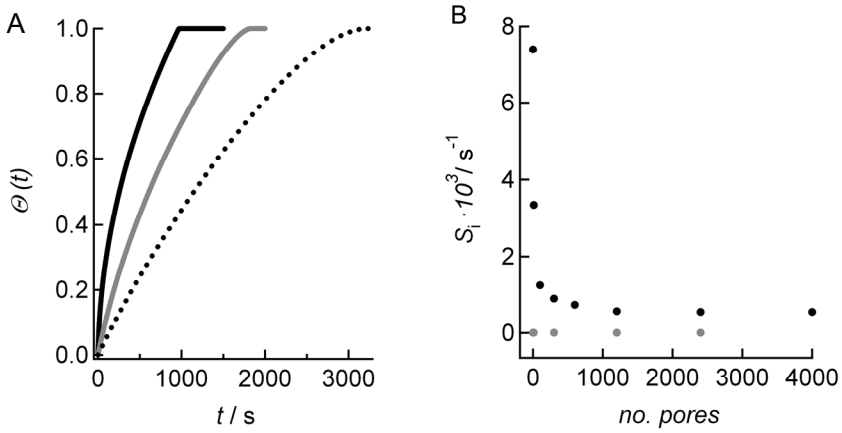

Figure 6.S4.
(**A**) Kinetics simulated for 1 (black), 100 (gray) and 1200 pores (dotted). (**B**) Standard parameters used to obtain the initial linear response (S_i) as a function of the number of pores for high k_{ad} (black, k_{ad} = 1000 m^3 mol^{-1} s^{-1}) and low k_{ad} (gray, , k_{ad} = 0.001 m^3 mol^{-1} s^{-1}).

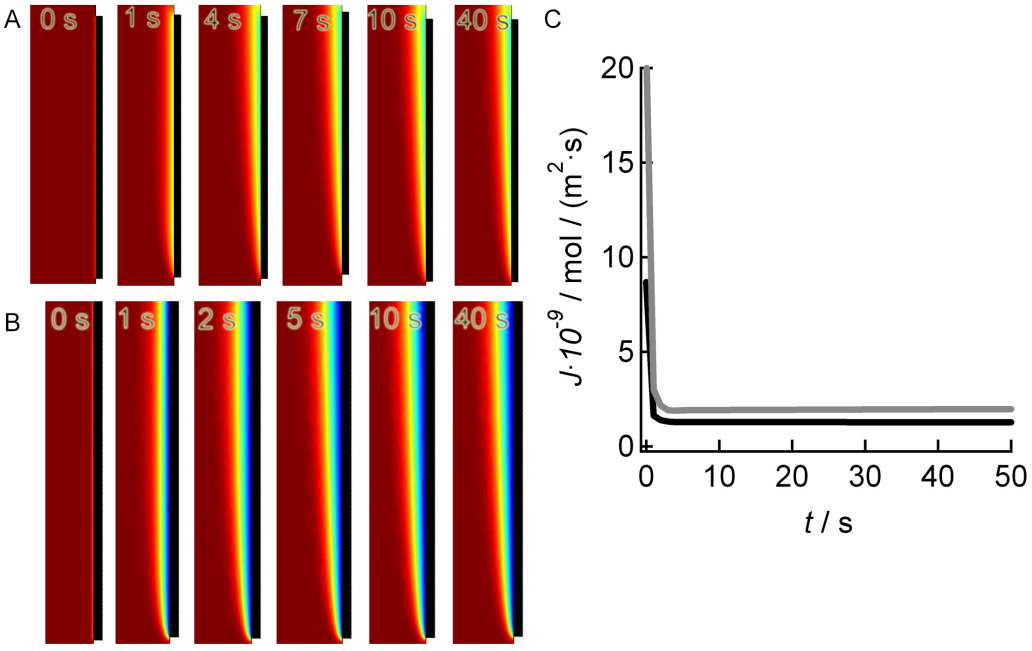

Figure 6.S5. Simulated concentration profiles on a nanoporous array with 1200 pores at different times (h = 3.2 μm) for low k_{ad} (1 m^3 mol^{-1} s^{-1}) (shown in (**A**)) and high k_{ad} (10^3 m^3 mol^{-1} s^{-1}) (shown in (**B**)). (**C**) Macromolecular flux (J) within a single pore as a function of time for low k_{ad} (gray) and high k_{ad} (black).

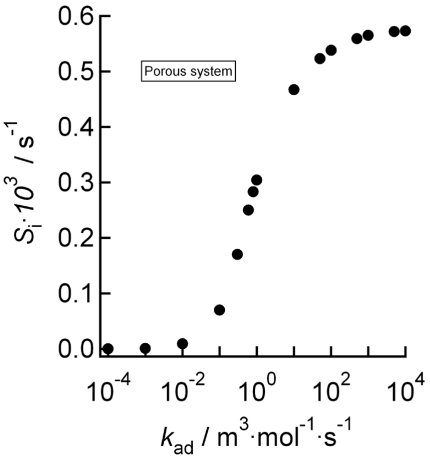

Figure 6.S6.
Initial linear response (S_i) from simulations with a 1200 pore array for various k_{ad} values.

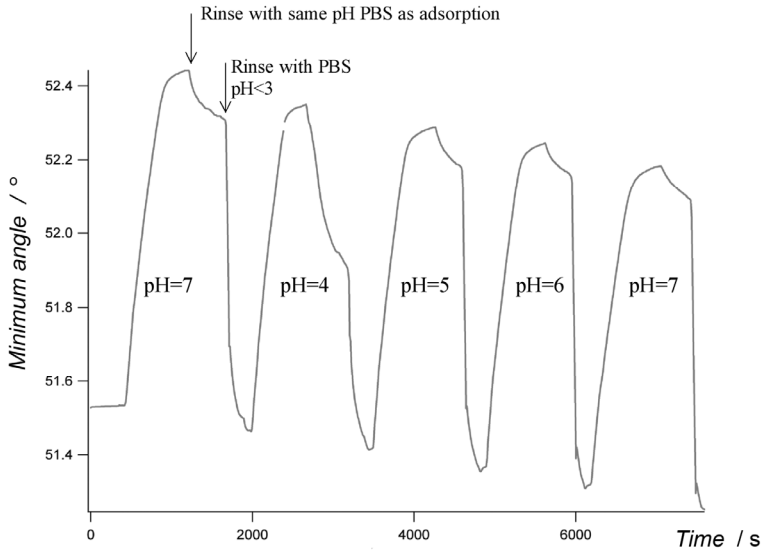

Figure 6.S7.
(A) Experimental avidin adsorption regeneration curves showing that strong protein adsorption occurs at pH > 5. The avidin was removed by using a pH < 3. The AAO isoelectric point therefore lies near pH 4.

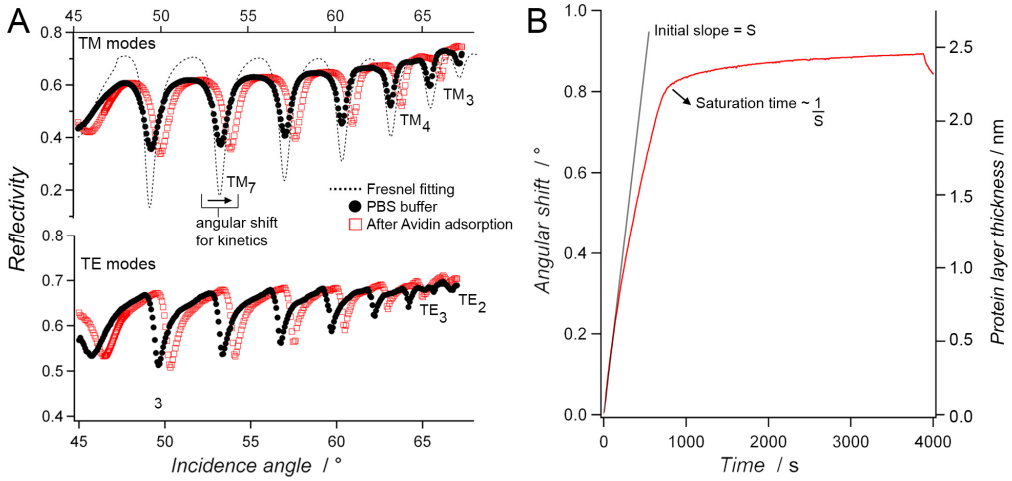

Figure 6.S8. (**A**) Experimental OWS spectra before and after avidin adsorption in PBS buffer on AAO with R_{pore} ~ 26 nm and h = 3.2 µm. Both TE and TM polarizations are shown together with the Fresnel fitting for the TM modes in buffer, which shows good agreement. The kinetic data was obtained by monitoring the increase in the angular position of the TM_7 waveguide modes with time. (**B**) The adsorption kinetics were obtained by following the angular shift with time in the TM_7 mode in (A), every 10 s. Also shown is the initial linear response, which corresponds to the slope of the initial adsorption.

Chapter 7

Orthogonal functionalization of nanoporous substrates: control of 3D surface functionality

by:

Thomas D. Lazzara, [†] *Torben-Tobias Kliesch,* [†] *Andreas Janshoff,* [§] *Claudia Steinem* [†]

Graphical abstract:

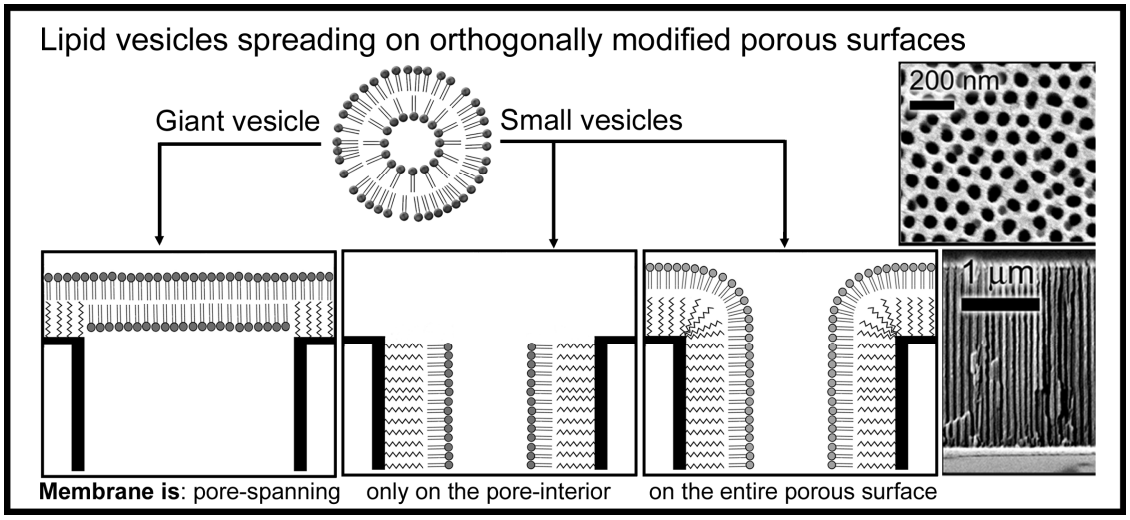

Published in: *ACS applied materials and interfaces*, in press

[†] Institute of Organic and Biomolecular Chemistry, Tamannstrasse 2, 37077 Göttingen, Germany.
[§] Institute of Physical Chemistry, Tamannstrasse 6, 37077 Göttingen, Germany.

Abstract

Anodic aluminum oxide (AAO) membranes with aligned, cylindrical, non-intersecting pores were selectively functionalized in order to create dual-functionality substrates with different pore-rim and pore-interior surface functionalities, using silane chemistry. We used a two-step process involving an evaporated thin gold film to protect the underlying surface functionality of the pore-rim surface. Subsequent treatment with oxygen plasma of the modified AAO membrane removed the unprotected organic functional groups, *i.e.* the pore-interior surface. After gold removal, the substrate became optically transparent, and displayed two distinct generated surface functionalities, one at the pore rims and another at the pore-interior surface. We achieved a selective hydrophobic functionalization with dodecyl-trichlorosilane of either the pore rims, or the pore-interior surface. The deposition of planar lipid membranes on the functionalized areas by addition of small unilamellar vesicles occurred in a predetermined fashion. Small unilamellar vesicles only ruptured upon contact with the hydrophobic substrate regions forming solid supported hybrid bilayers. In addition, pore-rim functionalization with dodecyl-trichlorosilane allowed the formation of pore-spanning hybrid lipid membranes as a result of giant unilamellar vesicle rupture. Confocal laser scanning microscopy was employed to identify the selective spatial localization of the adsorbed fluorescently labeled lipids. The corresponding increase in the AAO refractive index due to lipid adsorption on the hydrophobic regions was monitored by optical waveguide spectroscopy. This simple orthogonal functionalization route is a promising method to control the 3-dimensional surface functionality of nanoporous films by tailoring model systems for biomembranes.

Keywords: nanoporous substrates, optical light mode waveguide spectroscopy, orthogonal silanization, pore-spanning lipid membranes, reactive plasma, silane chemistry

7.1 Introduction

Anodic aluminum oxide (AAO) is one of the most promising ordered nanoporous materials. It has been widely used for its self-organized predictable structure that is composed of non-intersecting, hexagonally close-packed, cylindrical pores with conveniently adjustable monodisperse pore diameters, degree of lattice spacing, and membrane thickness.[1-4] AAO membranes have 1-3 orders of magnitude increased surface area due to their high porosity; for example, a 1 cm^2 AAO substrate with an inter-pore spacing of 100 nm, a thickness of 4 μm and pore diameters of 60 nm, has $1.2 \cdot 10^{10}$ pores$\cdot cm^{-1}$ and a total surface area of 90 cm^2.

A range of chemical strategies is available to chemically modify planar and porous substrates. Coinage metals,[5-7] polymers,[8-9] and inorganic or metal oxide[10-12] substrates can be functionalized by the formation of functional monolayers through surface reactions such as silanizations,[13] reactive plasma treatments,[14-15] thiol and phosphonate chemistry.[16] While a homogeneous deposition of molecules on these surface is rather straightforward, tailored micro-patterned chemistry is a more demanding task, but essential for designing locally addressable areas on substrates. In general, the areas to be addressed need to be selectively treated or protected, which requires an orthogonal functionalization procedure. At the micrometer scale, template-based methods are commonly used to selectively evaporate metals, cure photoresist films, or use soft-litography[17] to create micrometer-sized and spatially localized surfaces. At the sub-micrometer scale, more elaborate template procedures have been developed for orthogonal functionalization such as using nanoporous alumina films as a patterning mask to create ordered metal nano-dot arrays[18] or to localize arrays of seed catalytic sites.[19]

While selective functionalization methodologies have been developed for flat surfaces,[20-22] porous 3-dimensional substrates still remain a challenge for orthogonal functionalization, which can produce selective, spatially distinct surface chemistries. The orthogonal functionalization of porous materials would be an important advancement in technological fields such as separation and sieving applications, as well as high-sensitivity bi-functional detection platforms. AAO has already proven useful in non-destructive, high sensitivity assays such the selective separation of drug enantiomers[23-24] or DNA oligomers,[25] the development of on-chip biosensors,[26-28] for tailoring molecular transport properties,[29-30] and more recently for energy storage devices.[31]

We have shown in the past, that orthogonal functionalization of porous substrates can be achieved by directly depositing a gold metal layer on the substrate, which then allows pore-rim modification using functional thiols designed to direct the formation of lipid membranes.[32-33] However, for nanoporous materials with pore diameters below the scattering limit (< 100 nm), the attractive advantage of optical transparency is lost when a metal is deposited onto the porous film. Hence, this strategy prevents the study of processes occurring within the porous network using various optical methods. To circumvent this problem, silane based orthogonal functionalizations of AAO appear to be well suited,[34-36] but challenging to implement because spatial selectivity is difficult to achieve. Voelcker and coworkers[37] report on a silane-based strategy to selectively functionalize the aluminum

surface before the anodization process that generates AAO, which results in a selective functionalization of the pore rims. In this procedure, the deposited molecules must endure the anodization process, as well as pore widening in acidic solution. Thus, it is not suited for functional moieties that are moisture- or pH-sensitive. Other orthogonal functionalization strategies have been reported for nanoporous substrates, but are significantly more technically demanding and offer lower control on both, the degree of functionalization and spatial localization of the functionality.[38] Kilian *et al.*[39] used surface tension and capillary forces to facilitate or prevent pore-interior functionalization. Sailor and coworkers[40] produced porous silicon that was etched in a two-step process involving a hydrophobic functionalization after the first step to produce a membrane with dual-functionality. A porous membrane with hydrophilic pore rims and a hydrophobic pore-interior surface was achieved using plasma-polymerization of a fluorocarbon layer, followed by detachment from the solid-support generating hydrophilic rims at the bottom side.[41] Recently, the wetting properties of AAO were tuned by the selective deposition, by electrospray technique, of a thin polymer film at the pore rims.[42]

In this contribution, we present a simple technique, where AAO silanization is performed after the anodization and pore widening processes, *i.e.* on the desired final substrate, which ensures that the surface functionality is created just before use, therefore ensuring optimal chemical integrity, degree of functionalization and spatial localization of the surface chemistry. The presented method is based on a thin evaporated gold layer serving as a protective mask that prevents the removal of the functionalization from the underlying surface by the reactive oxygen plasma, which is used to remove the undesired surface functionality on the unprotected surface. We have used a hydrophobic silane, namely dodecyl-trichlorosilane, to differentially functionalize the AAO substrates and demonstrated that fluorescently labeled phospholipid vesicles interact only with the hydrophobic surface, *i.e.* pore-rim or pore-interior surface, or both. Depending on the size of the phospholipid vesicles, we were able to produce hybrid solid-supported lipid membranes on the pore-interior AAO surface using small unilamellar vesicles (SUVs), or hybrid pore-spanning membranes on functionalized AAO with hydrophobic pore-rim surfaces using giant unilamellar vesicles (GUVs).

7.2. Results and Discussion

The preparation of selectively functionalized nanoporous substrates using silane chemistry is challenging because the porous surface reacts homogeneously and typical planar surface patterning techniques are generally not applicable to porous structures. Therefore, the development of new functionalization strategies that can discriminate between the pore-rim and pore-interior surfaces are required. For our studies, we used anodic aluminum oxide (AAO), which was produced by anodizing aluminum in 0.3 M oxalic acid under a constant potential of 40 V. This procedure resulted in AAO substrates with an inter-pore distance of p = 100 nm, pore diameters that were enlarged to D_0 = 65-75 nm and with a chosen thickness of l = 3.5-4.0 μm (figure 7.1A).

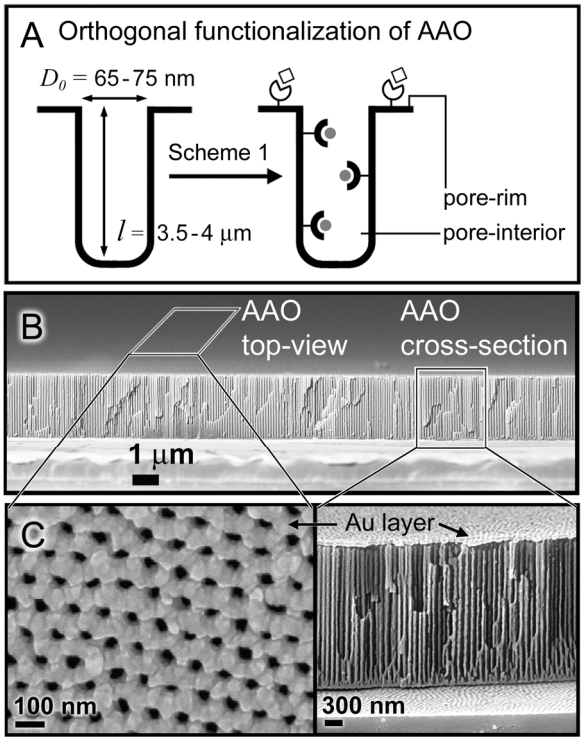

Figure 7.1. (**A**) AAO membranes with D_0 not larger than the scattering limit (~1/10 λ_{light}) can be used in applications requiring dual-functionality and optical transparency. (**B**) Scanning electron microscopy image of an AAO membrane, which was used as a thin-film mounted on a glass substrate using an optical adhesive. (**C**) Enlarged top and cross-section views of (B). Au was evaporated onto the AAO as a protective mask for the pore rims; a rather thick Au layer (about 50 nm) was evaporated to emphasize its location atop the AAO pores, as shown in the top view (left) and the cross-section view (right). A 10-20 nm Au layer is sufficient to create the protective layer for the orthogonal functionalization.

The AAO membranes were covered with a thin metal coupling layer of about 25 nm on the aluminum oxide barrier side (bottom) and then mounted on glass supports using an optical adhesive[43] (figure 7.1B) to allow the characterization of their refractive index using

optical waveguide spectroscopy (OWS). The AAO pores were hexagonally ordered (figure 1C, left image) with a cylindrical geometry (figure 7.1C, right image). On the AAO substrate shown in figure 7.1C, an excess of approx. 50 nm Au was evaporated to emphasize the location of the protective metal masking layer that is used to generate the orthogonal functionalization, *i.e.* the localized pore-rim surface functionalization.

7.2.1. Functionalization Strategies

Two different routes were developed to orthogonally functionalize the AAO substrates (Scheme 1, steps 1-5 and A-D). In both strategies, a 10-20 nm thick Au film serves as a protection layer preventing the underlying pore-rim surface to be chemically modified in further steps. We rely on the significantly larger pore-interior surface area, in comparison to the pore-rim surface area, to minimize the degree of pore-interior contamination with Au. Under high evaporation rate conditions (~1-2 nm/s) we did not observe significant Au deposition within the cavities of the substrate. Even for 50 nm of evaporated Au, we observed that the metal only forms small clusters within the AAO pores (SEM shown in supp. info.). The importance of the interior contamination is reduced by the large aspect-ratio of the AAO, and the degree of contamination can be estimated by the ratio of the pore area to pore-interior surface, which is <2% for a 4 μm thick AAO film.

Following route 1-5 (scheme 7.1), the hydroxyl terminated Al_2O_3 surface is first silanized to obtain the desired surface chemistry (–X) on the aluminum oxide (step 1). Second, a protective Au layer is evaporated (step 2) covering the pore rims, followed by an O_2 plasma treatment for about 60 s (step 3). During O_2 plasma treatment, organic groups are removed from the surface mainly via reaction with reactive radical species generated in the ionized gas.[44-46] The AAO surface functionalized with the organic silane present beneath the Au film remains intact, while the organic functionality within the pore-interior is oxidized and removed. The hydroxyl terminated surface generated on the pore-interiors is thereby ready for a second silanization (–Y) (step 4). Finally, (step 5) the Au film is removed using an iodine (KI/I_2) solution to obtain a metal-free orthogonally functionalized AAO substrate. The chemical integrity of the remaining functional groups was proven by fluorescence microscopy (see supporting information, figure 7.S1). The second strategy starts by evaporating a protective Au layer onto the AAO substrate (step A), followed by silanization (–X) of the remaining accessible Al_2O_3 pore-interior surface (step B). Removal of the gold layer by an iodine solution (KI/I_2) (step C) generates a hydroxyl terminated surface on the

pore rims, which can be functionalized with a second silanization reaction (–Y) (step D). We have proven and exploited both strategies to deposit lipid membranes by vesicle rupture on porous alumina surfaces, which were functionalized with dodecyl-trichlorosilane (C_{12}-TCS) on different areas.

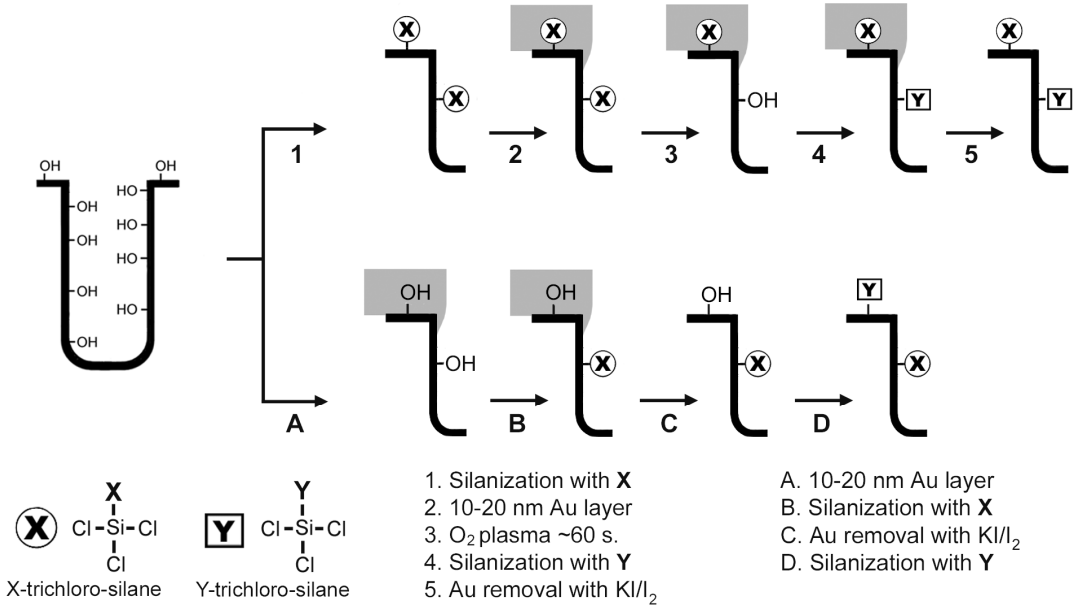

Scheme 7.1. Two experimental protocols (1-5 and A-D) to prepare AAO substrates with dual-functionality using a thin Au layer as a protective mask. Thermally evaporated gold is used to prevent the underlying AAO pore-rim functionalization from oxidation during O_2 plasma treatment and from any further chemical reactions. The final AAO substrates, after step 5 or step D, have different pore-rim *vs* pore-interior functionalities and most importantly, remain optically transparent.

7.2.2. Selective Deposition of Hybrid Solid-Supported Lipid Membranes.

According to the two procedures depicted in Scheme 1, we prepared AAO membranes with a hydrophobic C_{12}-TCS layer at different positions (figure 7.2A). Substrate **1** was functionalized entirely with C_{12}-TCS such that pore-rim and pore-interior surfaces were both hydrophobic. Substrate **2** was prepared according to steps A-D, without performing the last step (scheme 7.1), resulting in pore rims that are hydrophilic and pore-interiors that are hydrophobic after silanization with C_{12}-TCS. Substrate **3** is the inverse of **2**, with hydrophobic pore rims, prepared by following steps 1-5 (scheme 7.1). Substrate **4** was subjected to O_2 plasma treatment rendering it hydrophilic and non-functionalized and, as such, used as reference (figure 7.2A).

The substrates were incubated with fluorescently labeled small unilamellar vesicles (SUVs) composed of 1-Palmitoyl-2-oleoyl-sn-glycero-3-phosphocholine (POPC) phospholipids. The weighted-number SUV size distribution, measured by dynamic light

scattering, ranged mostly between 20-30 nm in diameter. SUVs are known to adhere strongly on different hydrophobic functionalities and can rupture to form hybrid solid-supported lipid monolayers[47] on alkyl-terminated hydrophobic surfaces. It has also been shown that SUVs do not adsorb on native hydrophilic Al_2O_3 surfaces.[47] Confocal laser scanning microscopy (CLSM) images in Y-Z plane obtained by Z-stacks of substrates **1**-**4** were taken to localize the lipids (figure 7.2B, left-side). Substrate **1** and **2** show a strong fluorescence throughout the Y-Z planes indicating that lipids are lining the pore-interiors throughout the AAO. For substrate **3**, fluorescence is not observed in the pore interior but only atop due to surface adsorbed vesicles. The bottom of the AAO substrate can be readily located by a reflection owing to the metal layer on the AAO barrier side. For CLSM scans performed in the Z-direction (63×), the resolution is ~0.9 μm for a numerical aperture of 1. For the Z-stacks, multiple thin slides about 100 nm thick were taken, over the 12-15 μm vertical range that was scanned, in order to improve the spatial localization of the fluorescence.

Substrate **4** does not show any significant fluorescence, only a weak auto-fluorescence, as the SUVs adsorb weakly on the non-functionalized AAO. Epifluorescence images of substrates **1** and **3** (figure 7.2B, right-side) taken under identical experimental and exposure conditions show that hybrid solid supported lipid membranes formed within the AAO pore-interiors (substrate **1**, top image), which increases significantly the overall fluorescence intensity compared to only surface adsorbed lipids (substrate **3**, bottom image). The epifluorescence images were taken at the AAO substrate edge, where the optical glue is also visible to emphasize the contrast. The left-hand side of figure 7.2B shows confocal scans in the Z-direction that were taken for all 4 substrates with similar exposure conditions. To analyze whether a hybrid solid supported continuous lipid monolayer has been formed on substrate **1**, which is not expected for substrate **2**, fluorescence recovery after photobleaching (FRAP) experiments were performed on both these substrates using POPC SUVs doped with 0.1 mol% Bodipy DHPE.

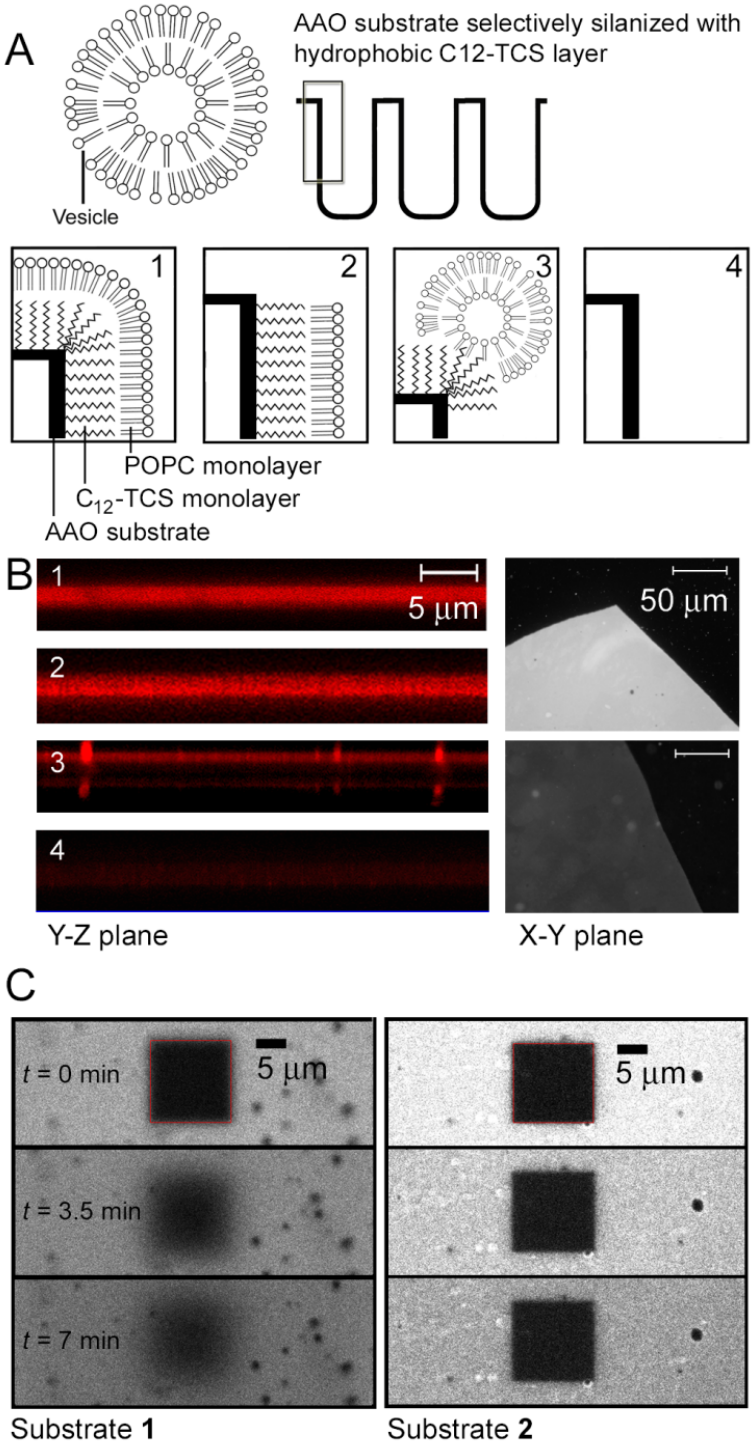

Figure 7.2. (**A**) Schematic representation of AAO substrates differing in their orthogonal surface functionalities. Small unilamellar POPC vesicles are expected to interact differently with these surfaces. (**B**) Fluorescence images of the substrates with D_0 = 75 nm and l = 3.8 µm after addition of SUVs are shown. The left side shows CLSM fluorescence cross-sectional Y-Z plane images for AAO substrates **1**-**4**. The images on the right are top *X-Y* plane epi-fluorescence images of substrates **1** (top image) and **3** (bottom image) under identical exposure conditions showing the increased fluorescence intensity of **1** due to lipids adsorbed on the entire AAO surface *vs* only atop for **3**. (**C**) FRAP experiments on substrate **1** and **2,** to which SUVs doped with Bodipy DHPE were added.

The fluorescence of a square region was photobleached (figure 7.2C) and its recovery monitored. Significant fluorescence recovery was found for substrate **1**. This observation is consistent with the scenario sketched in figure 7.2A for substrate **1**. A continuous lipid monolayer on top of the hydrophobic C_{12}-TCS monolayer is formed, which results in laterally mobile lipids. In contrast, no recovery was observed for substrate **2** within the time scale of the experiment. In this case (figure 7.2A, substrate **2**), the pore rims are not covered with lipids but are composed of Al_2O_3 serving as a barrier for the lipids to laterally move and therefore, fluorescence recovery is not expected.

In addition to the fluorescence image analysis, the kinetics of interaction of the POPC SUVs with the substrates **1**-**4** were analyzed by time resolved OWS measurements (figure 7.3). For constant thickness samples, OWS provides information on the overall change in the dielectric constant of the optically transparent films. A uniform increase in the AAO dielectric constant can be observed as significantly large and uniform positive angular shifts in all of the waveguide modes, if lipids adsorb within the pores (see supporting information, figure 7.S2). If vesicle adsorption only takes place atop the AAO film, only the higher order modes slightly shift while the lower order modes remain unchanged. OWS measurements of substrates **1** and **2** demonstrate that a dielectric layer with a thickness of about 2.0-2.5 nm has been adsorbed on the either fully functionalized (**1**) or inner-pore wall (**2**) functionalized AAO substrate. This change in thickness supports the notion of the formation of a hybrid solid supported lipid bilayer obtained by spreading of the SUVs on the hydrophobic C_{12}-TCS monolayer.

In the case of substrates **3** and **4**, no significant interior deposition was observed, indicated by the very small change in optical thickness. However, for substrate **3** a significant atop SUV deposition with a thickness change of about 25 nm was observed, which was considerably larger than that observed for substrate **4**, which was only about 2 nm. This result confirms that intact SUVs adhere only on the hydrophobic monolayer on the pore rims, while they did not bind to native Al_2O_3 surfaces. The vesicles do not spread due to the limited contact area with the substrate. The results clearly demonstrate that a selective functionalization of the AAO substrates is feasible. We next asked the question, whether the developed strategy allows us to pattern the substrates, *i.e.* to generate laterally distinct areas of the AAO substrates.

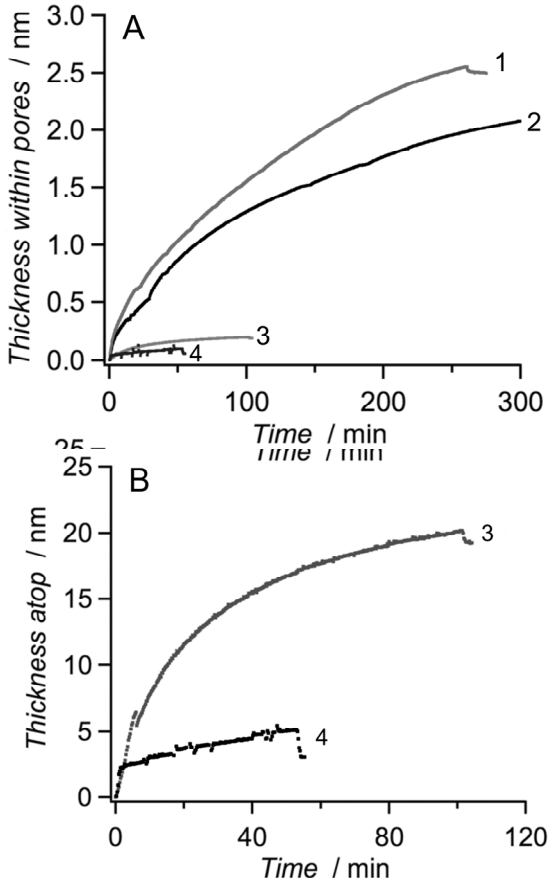

Figure 7.3. (**A**) Kinetics of POPC SUV interaction with the differently functionalized substrates (**1**-**4**) presented in figure 7.2A measured using OWS. The overall dielectric constant of the AAO membrane with D_0 = 75 nm and l = 3.8 μm increases due to the deposition of a 2.0-2.5 nm phospholipid monolayer within the pores for substrates **1** and **2**, which is not observed for substrates **3** and **4**. (**B**) The atop deposition of vesicles is much larger for substrate **3** than for **4** because only the hydrophobic pore rims of substrate **3** interact strongly with SUVs.

7.2.3. Patterned Substrates

As the deposition of gold is a key step in generating a selective functionalization of the AAO substrates, we used a TEM grid with rectangular openings as a patterning-mask for Au deposition to laterally define rectangular areas that were to remain functionalized after plasma treatment. AAO substrates with hydrophobic pore rims were again obtained by silanization with C_{12}-TCS. Gold was subsequently evaporated through the TEM grid (see inset of figure 7.4A) to form rectangular patterns on the surface and then O_2 plasma treated, followed by Au removal leading to substrate **3** (figure 7.2A). To confirm the presence of hydrophobic pore rims, sonicated POPC SUVs doped with Texas Red DHPE were added. In figure 7.4, fluorescence images of the functionalized AAO substrate displaying

hydrophobic pore rims and O_2 plasma treated pore-interiors, after the addition of fluorescently labeled SUVs, are shown. The areas that were Au protected, and thus were functionalized with C_{12}-TCS at the pore rims, show a bright TexasRed fluorescence, while the hydroxyl terminated remaining pore rims and pore-interiors appear black demonstrating the selective adsorption of lipids on the hydrophobic pore-rim regions.

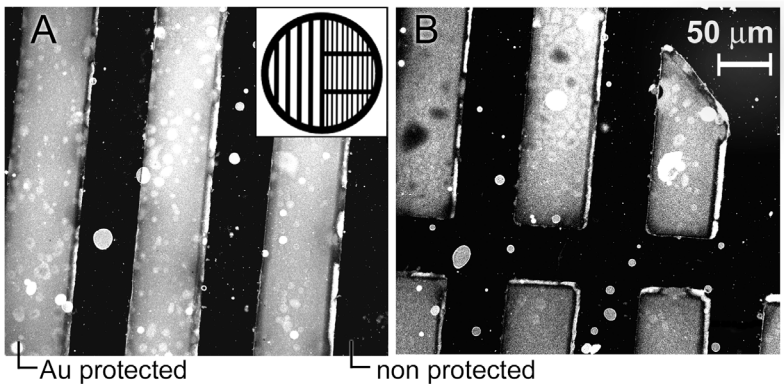

Figure 7.4. (**A**/**B**) Confocal fluorescence images of an AAO substrate with pore rims that were selectively silanized with dodecyl-trichlorosilane (C_{12}-TCS). Au was evaporated through a TEM grid used as a patterning-mask, shown in the inset of (A) to generate the micrometer-sized rectangles. Texas Red DHPE labeled POPC SUVs adhered to the hydrophobic pore rims functionalized with C_{12}-TCS, while they did not bind to the hydrophilic remainder of the unprotected AAO surface (scale bar for both images).

7.2.4. Pore-Spanning Lipid Membranes.

Silane-based surface modifications have the particular advantage that fluorescence near the functionalized surface is not quenched, in contrast to metals where quenching occurs up to 15 nm away from the surface.[48-49] On porous substrates with micrometer-sized pores (0.5-2 μm), hydrophobic functionalized Au pore rims have been used to induce rupture of giant unilamellar vesicles (GUVs) to form hybrid pore-spanning lipid membranes. However, the fluorescence of the pore rims is quenched by the metal and only the fluorescence in the pore area remains visible.[32] Using the silane-based functionalization presented in Scheme 1, we prepared a porous AAO substrate with a selective hydrophobic functionalization of the pore rims using C_{12}-TCS (substrate **3,** figure 7.2A).

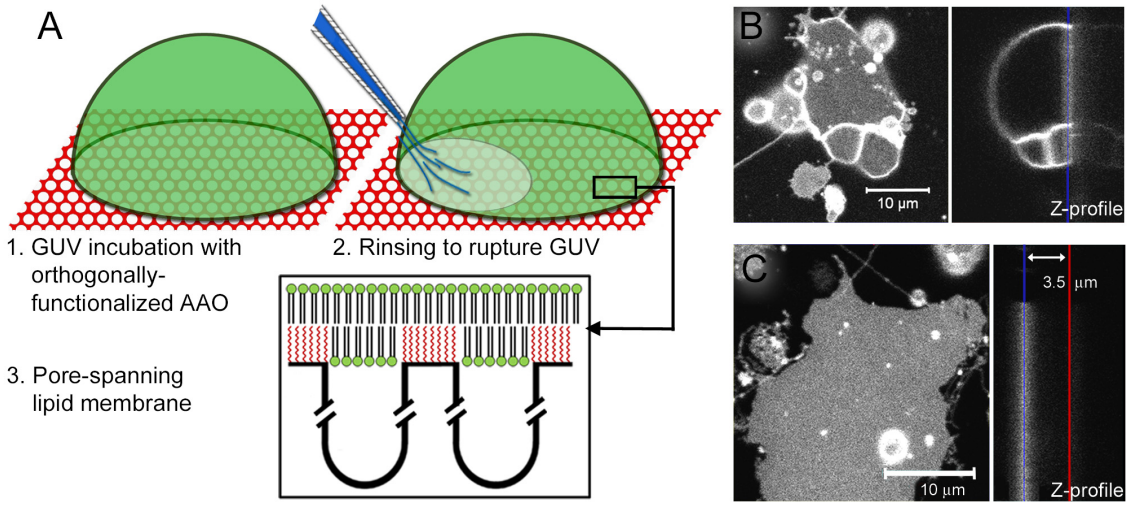

Figure 7.5. (**A**) Illustration of the steps leading to the formation of hybrid pore-spanning lipid membranes on orthogonally functionalized AAO with hydrophobic pore rims obtained from silanization with C_{12}-TCS following Scheme 1. (**B**) Confocal fluorescent image of a giant unilamellar POPC vesicle on an orthogonal functionalized AAO substrate (D_0 = 65 nm and l = 3.5 µm) with C_{12}-TCS on the pore rims: *X-Y* plane (left) and Z-profile (right). (**C**) Confocal fluorescent image of a hybrid lipid membrane patch formed by the rupture of flattened POPC GUVs: the membrane, which is visible in the *X-Y* focal plane (left) and the Z-profile (right) shows that the fluorescence is localized atop the AAO, not within the AAO. The blue line indicates the top of the 3.5 µm thick substrate, while the red line indicates the bottom.

The POPC GUVs, labeled with Texas Red DHPE, can rupture on this substrate forming a pore-spanning hybrid lipid membrane as illustrated in figure 7.5A. GUVs were firstly left to incubate with the hydrophobic pore rims, during which time they flatten on the substrate surface. In comparison to SUVs, the large surface area of GUVs allows them to deform and form large flat areas at the interface with the substrate. The flattened area is the pore-spanning membrane. A Z-profile of fluorescence images after the incubation period obtained by CLSM, is shown in figure 7.5B, and illustrates how the vesicles deform on the AAO surface; the fluorescence image in the *X-Y* focal plane was taken at the AAO top surface and is focused at the flattened GUV bottom. To obtain pore-spanning membrane patches, the adsorbed vesicles were then gently rinsed until they ruptured. The lipid membrane patches obtained were effectively the bottom of the GUVs, which interacted with the hydrophobic pore rims. The fluorescence of these pore-spanning membranes originates solely from the top of the functionalized 3.5 µm thick AAO substrate, which indicates that the lipids are localized in the atop focal plane (figure 7.5C).

When AAO was not orthogonally functionalized, as for substrate **1** (figure 7.2A), where the entire AAO surface was hydrophobic, the volume beneath the measured patch was fluorescent throughout the thickness of the AAO due to lateral lipid diffusion within the membranes lining the pore walls, as observed in the results obtained with SUVs incubated

with substrate **1**. Using Bodipy DHPE labeled POPC GUVs, we were able to perform fluorescence recovery after photobleaching (FRAP) experiments on membrane patches. In figure 7.6, a typical FRAP experiment is shown, where the reference was taken near the edge of the patch. Recovery was typically about 80 %. During bleaching, fluorescence originating from the lipids in the lower leaflet is lost and does not recover because these lipids are immobile due to the hydrophobic pore rims that confine them (figure 7.5A, step 3). The recovery observed is therefore predominantly from the top lipid leaflet, whose fluorescence can fully recover.

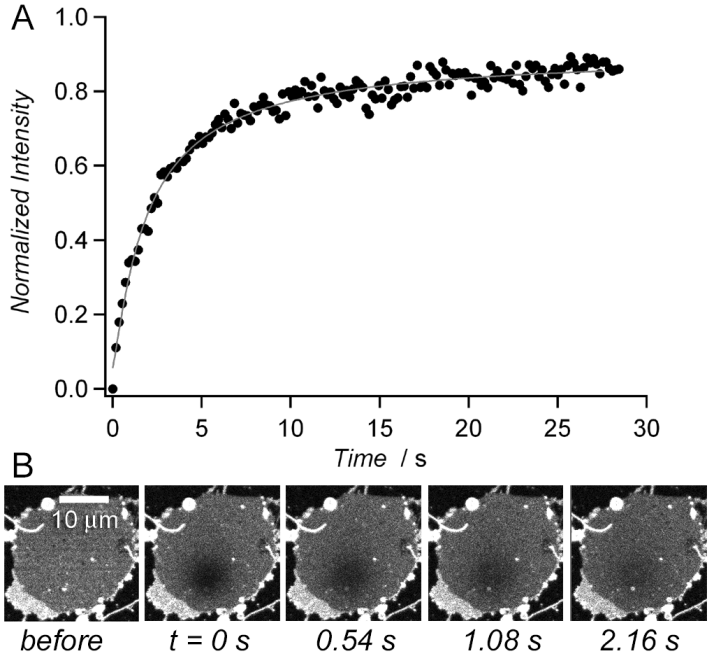

Figure 7.6. (**A**) FRAP recovery curve obtained on a pore-spanning hybrid POPC lipid membrane patch. The solid line is the result of the fitting procedure. (**B**) FRAP experiment carried out on an isolated pore-spanning lipid membrane patch obtained from GUV rupture. Frames from time series taken at different times during the fluorescence recovery shown in (A).

The diffusion coefficient obtained was $D_{\text{lipids}} = 7 \pm 3\ \mu m^2\ s^{-1}$. The rather large error is due to the limited size of the membrane patches that only permits bleaching areas with Gauss radii < 10 µm. Despite this error, we can conclude that a planar homogeneous bilayer was formed, which leads to a uniform fluorescence recovery with a diffusion coefficient characteristic for continuous planar lipid membranes.[50-53] These observations further support the formation of pore-spanning membranes.

7.3. Concluding Remarks

The challenge in the fabrication of differential porous substrates is to provide a selective pore-rim functionalization, without simultaneous functionalizing the pore-interior surface. Here, we have developed a strategy based on silane chemistry to generate orthogonally functionalized nanoporous anodic aluminum oxide (AAO) substrates, where the pore-rim surface chemistry is distinctly different from the pore-interior surface. The advantage of this strategy is the possibility to carry out a wide range of well-established anhydrous or aqueous solution-phase, as well as gas-phase silanization procedures. Furthermore, the deposition of the protective Au mask and the subsequent O_2 plasma removal of the undesired pore-interior functionality are all carried out under vacuum conditions that optimizes the stability of the functionalized surface in comparison to solution treatments. A vacuum environment proves useful for different air/moisture and pH sensitive surface chemistries. Plasma treatments can also be performed with other gases than O_2 and also with reactive monomer species to modify and impart the surfaces of materials with various functionalities.[54-55] By using silane-based chemistry on AAO substrates, the material remains optically transparent. Owing to this transparency of AAO, it can be used as an optical waveguide, which has allowed us to determine the spatial localization of the adsorption of fluorescently labeled lipids atop and within the pores by confocal laser scanning fluorescence microscopy. In addition, the deposition of non-labeled molecules was quantified by optical waveguide spectroscopy. We believe that this type of functionalization methodology can also be applied towards other types of porous networks and substrates, where the pore-rim surface is required to be chemically distinct from the surface within the porous channels. The silane-based strategy will pave the way to design multi-functional surfaces with pore-spanning membranes, including membranes built from polymer-multilayers, from polymer brushes, from *in-situ* pore-rim polymerizations, or from various layer-by-layer assemblies. We have already demonstrated that the formation of hybrid pore-spanning lipid membranes from GUV rupture is feasible. Such lipid membrane patches on orthogonally functionalized AAO substrates have the potential to be used to study membrane permeability properties by monitoring the transport kinetics across membranes through optical imaging techniques that allow the study of micrometer-sized areas of interest. Furthermore, pore-lining membranes may also be of potential interest for the tailored collection of membrane proteins from solution mixtures.

7.4. Experimental Section

Materials. 1-Palmitoyl-2-oleoyl-*sn*-glycero-3-phosphocholine (POPC) was purchased from Avanti Polar Lipids Inc. (Alabaster, AL, USA). 2-(4,4-difluoro-5-methyl-4-bora-3a,4a-diaza-s-indacene-3-dodecanoyl)-1-hexadecanoyl-*sn*-glycero-3-phosphocholine (Bodipy DHPE) was purchased from Invitrogen (Eugene, OR, USA). Texas Red DHPE was purchased from Biotinum Inc. (Hayward, CA, USA). Disodium hydrogen phosphate, and oxalic acid dihydrate were purchased from AppliChem (Darmstadt, Germany). Perchloric acid (70 %) and phosphoric acid (85 %) were purchased from Merck (Darmstadt, Germany). Sucrose was purchased from Acros Organics (Geel, Belgium). Ethanol was p.a. grade (VWR, France). The water used was ion exchanged and filtered using a Millipore system (MilliQ System from Millipore, Molsheim, France; specific resistance $R > 18$ MΩ cm^{-1}, pH ~ 5.5). High refractive index LaSFN9 glass substrates ($\varepsilon = 3.406$, $\lambda = 632.8$ nm) were obtained from Hellma Optik (Halle, Germany). Aluminum foils (0.25 mm thick, purity: 99.999 %) were purchased from Goodfellow (Huntington, UK). The UV-curable optical adhesive (NOA 83H) was purchased from Norland Products (Cranbury, NJ, USA). $CuCl_2$, dodecyl-trichlorosilane (C_{12}-TCS) and sodium chloride were purchased from Sigma Aldrich (St-Louis, MO, USA). Toluene was p.a. grade (VWR, France) and dried over 0.4 nm molecular sieves from Roth (Karlsruhe, Germany). Indium tin oxide (ITO) slides were from Präzisions Glas & Optik GmbH (Iserlohn, Germany).

Scanning electron microscopy (SEM). SEM measurements were performed with a LEO Supra-35 SEM from Zeiss with acceleration voltages between 6 and 10 kV. 50 nm of Au were evaporated onto the samples before measuring.

Au evaporation and removal. Au and Cr were evaporated on a Bal-Tec MCS610 evaporator. For the metal coupling layer in OWS measurements, 2 nm of Cr and 25 nm of Au were evaporated on the AAO barrier layer. When Au was used as a protective mask for orthogonal functionalization, only 10-20 nm of Au were evaporated directly onto the AAO pores at a high deposition rate of 1.0-1.5 nm s^{-1}. Au was removed with an iodine solution (50 g/l KI, 12.5 g/l I_2), filtered through a PTFE 200 nm filter.

O_2 plasma treatment. O_2 plasma treatments were carried out with a Harrick plasma cleaner (Ithaca, NY, USA). The vacuum chamber was flushed with O_2 and evacuated with an oil-pump for 2 min. The plasma was turned on and the O_2 pressure in the chamber increased to obtain a faint purple plasma. The samples with a protective Au mask were exposed for about 60 s, starting with the initiation of the purple plasma.

Fluorescence microscopy. CLSM measurements were performed on an upright confocal microscope from Carl Zeiss MicroImaging GmbH (Jena, Germany), model LSM 710 Axio Examiner. A 63× magnification water immersion objective from Zeiss was used, WPlan-APO-CHROMAT (N.A. = 1.0). The upright epi-fluorescence optical microscope, model Olympus BX-51, was equipped with a filter for Nile Red (UMNG2), both purchased from Olympus Germany GmbH (Hamburg, Germany). A water immersion objective was used, 40× magnification from Olympus: LUMPlanF1 40XW (N.A. = 0.8). The evaporated metal layer between the alumina and the optical glue is required as a coupling layer for OWS measurements. This thin metal layer has also been found to be very useful for the microscopy measurements as it can be used as a positioning tool to locate the AAO in both the *X*-*Y* plane and the Y-Z plane.

Optical waveguide spectroscopy (OWS). OWS measurements of the AAO membranes prepared on glass slides were performed on a purpose-built setup. The glass-side was attached to the base of a symmetric LaSFN9 glass prism by optical immersion oil ($\varepsilon = 2.89$). The laser (λ = 632.8 nm) was incident through the prism-substrate assembly and reflected off the thin metal coupling layer in between the AAO and the optical adhesive as the incidence angle (θ) was varied. At specific θ's determined by the thickness and the dielectric constant of AAO (ε_{AAO}), the laser was coupled into the AAO film and these waveguide modes were recorded as sharp minima in a reflectivity R vs. θ scan. Transverse electric (TE) and transverse electric (TM) modes were indexed according to the number of nodes in their electromagnetic field distributions.[56] ε_{AAO} and the thickness of the AAO film, were obtained by fitting[56-58] the angles of the waveguide mode reflectivity minima using Fresnel simulations carried out with Winspall program.[59] Tracking the coupling angle of a mode enables real time, *in situ* monitoring of changes in the dielectric constant of the film, *i.e.* adsorption kinetics.

Effective medium theory analysis. The ε_{AAO} measured by OWS includes contributions from the alumina, the pore-filling medium (e.g. water), and any organic thin layer coating the pore surfaces (*i.e.* silanes, phospholipids). ε_{AAO} has an anisotropic component that is described by the infinite, prolate ellipsoid approximation within the Maxwell-Garnett theory, and well-described elsewhere.[60-62]

$$\varepsilon_{AAO}^{\perp} = \varepsilon_{alumina} + f_{pore}(\varepsilon_{pore} - \varepsilon_{alumina}) \quad (1)$$

$$\varepsilon_{AAO}^{//} = \varepsilon_{alumina} \frac{\varepsilon_{alumina} + \tfrac{1}{2}(1 + f_{pore})(\varepsilon_{pore} - \varepsilon_{alumina})}{\varepsilon_{alumina} + \tfrac{1}{2}(1 - f_{pore})(\varepsilon_{pore} - \varepsilon_{alumina})} \quad (2)$$

where $\varepsilon_{AAO}^{\perp}$ and $\varepsilon_{AAO}^{//}$ are, respectively, the dielectric constant components normal and parallel to the AAO membrane surface, f_{pore} is the pore volume fraction within the AAO, $\varepsilon_{alumina} = 2.68$[61] is the dielectric constant of bulk anodic alumina at $\lambda = 632.8$ nm, and ε_{pore} is the (effective) dielectric constant within the pores. For a blank AAO film in water, $\varepsilon_{pore} = \varepsilon_{water} = 1.77$. With the addition of an organic film ($\varepsilon_{organic} = 2.2$) on the internal pore surfaces (e.g. silane, lipid monolayer), the volume within the pores is occupied by a combination of the organic material and the pore filling buffer. Recursively applying equations (1) and (2) for the organic-filled AAO pores, using a new effective ε'_{pore} for the pore interior, provides ε_{AAO} after molecular adsorption.

AAO membranes on glass supports. AAO anodized from bulk aluminum foils were mounted on LaSFN9 glass slides using an optical adhesive according to a previously reported technique.[43] Briefly, AAO membrane thin films were fabricated by electrochemical anodization of aluminum foils, which were annealed at 500 °C overnight. Aluminum foils were polished in a solution of perchloric acid/ethanol (1:4 *v*/*v*) for 15 min, 0 °C at 20 V. They were then anodized for 2 hr in 0.3 M oxalic acid, 1 °C at 40 V. The alumina was removed with a 5 % *vol.* phosphoric acid solution for 2-3 hours. As prepared aluminum foils were then anodized a second time for 1.5 hr to obtain the desired thickness of about 3.5 μm. Aluminum was removed from the anodized foil by immersing it in a 17 g/l $CuCl_2$ in 18.5 M HCl solution until the AAO became visible and no metal remained. Prior to Al removal, the AAO side was isolated from solution by immobilization onto a glass slide and sealed using epoxy adhesive. 2 nm of Cr and 25 nm of Au were evaporated onto the barrier layer of the AAO membranes. This underlying metal is required for OWS studies and also serves as a positioning tool to locate the transparent alumina using the microscope. Norland 83H adhesive was diluted in tetrahydrofurane (1:10) and spin-coated on LASFN9 glass slides at 20 rpm for 2-3 s. The Au-coated AAO was glued, barrier side down, onto the glass side and UV-cured for 2 hr with a UV hand lamp, with both lamps on (λ = 254 + 354 nm, 4 W) from Herolab (Wiesloch, Germany). The pore diameter D_0 for all AAO membranes was widened to the desired diameter by etching in 5 % *vol*. phosphoric acid (diameter increase: 0.75 nm min^{-1}).

C_{12}-TCS-silanization of AAO. The hydrophobic regions on the AAO substrates were obtained by O_2 plasma treatment for 2 min, followed by immersion in dry toluene in a desiccator under vacuum. Dodecyl-trichlorosilane (C_{12}-TCS), 2 % *vol.*, was added and left under vacuum for 15 min.[47,63] The substrates were finally immersed in excess dry toluene, dried under N_2, and left overnight under vacuum at 65 °C.

Small unilamellar vesicles (SUVs). POPC dissolved in chloroform with 2 mol% of Texas Red DHPE or 0.1 mol% of Bodipy DHPE was transferred to a test tube (0.2 mg), air dried and then dried under vacuum in an oven at 60 °C for 3 hr.[64] The phospholipid films were rehydrated by adding 1 ml of 20 mM phosphate buffer (100 mM NaCl, pH 7; PBS buffer), left to hydrate for 30 min, vortexed and sonicated on ice using a tip-sonifier for 3 × 6 min periods, at 80 % power (sonifier tip, Bandelin Sonoplus, Berlin, Germany). Vesicle solutions of 0.4 mg/ml were prepared for fluorescence experiments and 0.1 mg/ml for OWS experiments. Vesicle solutions were used immediately after sonication and sonicated every 15 min during the experiment. For CLSM experiments, Texas Red DHPE vesicles were left to interact for 2 hr with the functionalized AAO substrates and gently rinsed with excess PBS buffer. For FRAP experiments on square regions, Bodipy DHPE labeled SUVs were used. Z-stacks were taken using 50-100 nm thick slices over the 10-15 μm range that was scanned.

Giant unilamellar vesicles (GUVs). GUVs were prepared by electroformation.[65] Briefly, 50 μl of a 1 mg/ml POPC lipid solution (1 mol% Texas Red DHPE) was left to dry on ITO slides and then spread uniformly on the slide using the length of a sterile needle. The slides were left at 64 °C under vacuum for at least 3 hr. The chamber was assembled using conductive copper tape at the ITO slide edges and a 1 mm thick square Teflon spacer between them (volume ~1.7 ml) and was filled with 0.3 M sucrose solution. The cycle was carried out at 12 Hz with voltage increments every 60 s for 3 hr: starting at 0.05 V, followed by 0.01 V steps until 0.2 V, finally 0.1 V steps until a constant 1.6 V was applied for the remaining duration. Afterwards, a 5 Hz square wave was applied for 10 min. GUVs were stored at 4 °C and used for no longer than 2 weeks. Pore-spanning hybrid lipid membranes were formed on AAO with hydrophobic pore rims, obtained by the orthogonal functionalization of AAO using C_{12}-TCS. The AAO was rinsed with p.a. ethanol, and then the measuring chamber was rinsed and filled with 1 ml of PBS buffer. 50 μl of GUV solution was slowly added and incubated for 1 hr. The heavier sucrose-filled vesicles sink to the substrate. The chamber was then carefully rinsed with an equal volume of PBS buffer and the sample observed under the microscope. Some vesicles rupture by themselves, but the majority require gentle squirting with a 10 μl pipette to rupture. FRAP experiments were performed on circular regions of interest using POPC membranes doped with 0.1 mol% Bodipy DHPE.

7.5. References

(1) Li, A. P.; Muller, F.; Birner, A.; Nielsch, K.; Gosele, U. *J. Appl. Phys.* **1998**, *84*, 6023.

(2) Masuda, H.; Yamada, H.; Satoh, M.; Asoh, H.; Nakao, M.; Tamamura, T. *Appl. Phys. Lett.* **1997**, *71*, 2770.

(3) Nielsch, K.; Choi, J.; Schwirn, K.; Wehrspohn, R. B.; Gosele, U. *Nano Lett.* **2002**, *2*, 677.

(4) O'Sullivan, J. P.; Wood, G. C. *Proc. R. Soc. Lond. A* **1970**, *317*, 511.

(5) Bain, C. D.; Troughton, E. B.; Tao, Y. T.; Evall, J.; Whitesides, G. M.; Nuzzo, R. G. *J. Am. Chem. Soc.* **1989**, *111*, 321.

(6) Schreiber, F. *Prog. Surf. Sc.* **2000**, *65*, 151.

(7) Sellers, H.; Ulman, A.; Shnidman, Y.; Eilers, J. E. *J. Am. Chem. Soc.* **1993**, *115*, 9389.

(8) Gombotz, W. R.; Guanghui, W.; Horbett, T. A.; Hoffman, A. S. *J. Biomed. Mat. Res.* **1991**, *25*, 1547.

(9) Tran, Y.; Auroy, P. *J. Am. Chem. Soc.* **2001**, *123*, 3644.

(10) Brzoska, J. B.; Benazouz, I.; Rondelez, F. *Langmuir* **1994**, *10*, 4367.

(11) Fadeev, A. Y.; McCarthy, T. J. *Langmuir* **2000**, *16*, 7268.

(12) Nanci, A.; Wuest, J. D.; Peru, L.; Brunet, P.; Sharma, V.; Zalzal, S.; McKee, M. D. *J. Biomed. Mat. Res.* **1998**, *40*, 324.

(13) Fadeev, A. Y.; McCarthy, T. J. *Langmuir* **1999**, *15*, 3759.

(14) Liston, E. M.; Martinu, L.; Wertheimer, M. R. *J. Adhes. Sci. Technol.* **1993**, *7*, 1091.

(15) Medard, N.; Soutif, J. C.; Poncin-Epaillard, F. *Surf. Coat. Technol.* **2002**, *160*, 197.

(16) Templeton, M. K.; Weinberg, W. H. *J. Am. Chem. Soc.* **1985**, *107*, 97.

(17) Xia, Y. N.; Whitesides, G. M. *Ann. Rev. Mat. Sc.* **1998**, *28*, 153.

(18) Park, S. K.; Noh, J. S.; Chin, W. B.; Sung, D. D. *Curr. Appl. Phys.* **2007**, *7*, 180.

(19) Wang, Y. D.; Zang, K. Y.; Chua, S. J. *J. Appl. Phys.* **2006**, *100*.

(20) Gorton, L. *Biosensors and Modern Biospecific Analytical Techniques*; 1st ed.; Elsevier: Amsterdam, 2005.

(21) Soriaga, M. P.; Stickney, J.; A. Bottomley, L.; Kim, Y.-G. *Thin Films: Preparation, Characterization, Applications*; first ed.; Springer: New York, 2002.

(22) Wilbur, J. L.; Whitesides, G. M. In *Nanotechnol.*; Timp, G. L., Ed.; Springer-Verlag: New York, NY, 1999, p 331.

(23) Lee, S. B.; Mitchell, D. T.; Trofin, L.; Nevanen, T. K.; Soderlund, H.; Martin, C. R. *Science* **2002**, *296*, 2198.

(24) Mitchell, D. T.; Lee, S. B.; Trofin, L.; Li, N. C.; Nevanen, T. K.; Soderlund, H.; Martin, C. R. *J. Am. Chem. Soc.* **2002**, *124*, 11864.

(25) Vlassiouk, I.; Krasnoslobodtsev, A.; Smirnov, S.; Germann, M. *Langmuir* **2004**, *20*, 9913.

(26) Figeys, D.; Pinto, D. *Anal. Chem.* **2000**, *72*, 330A.

(27) Alvarez, S. D.; Li, C. P.; Chiang, C. E.; Schuller, I. K.; Sailor, M. J. *Acs Nano* **2009**, *3*, 3301.

(28) Walt, D. R. *Acs Nano* **2009**, *3*, 2876.

(29) Fu, J.; Mao, P.; Han, J. *Trends Biotechnol.* **2008**, *26*, 311.

(30) Steinle, E. D.; Mitchell, D. T.; Wirtz, M.; Lee, S. B.; Young, V. Y.; Martin, C. R. *Anal. Chem.* **2002**, *74*, 2416.

(31) Banerjee, P.; Perez, I.; Henn-Lecordier, L.; Lee, S. B.; Rubloff, G. W. *Nat. Nanotechnol.* **2009**, *4*, 292.

(32) Mey, I.; Stephan, M.; Schmitt, E. K.; Muller, M. M.; Ben Amar, M.; Steinem, C.; Janshoff, A. *J. Am. Chem. Soc.* **2009**, *131*, 7031.

(33) Schmitt, E. K.; Vrouenraets, M.; Steinem, C. *Biophys. J.* **2006**, *91*, 2163.

(34) Hobler, C.; Bakowsky, U.; Keusgen, M. *Phys. Status Solidi A* **2010**, *207*, 872.

(35) Popat, K. C.; Mor, G.; Grimes, C. A.; Desai, T. A. *Langmuir* **2004**, *20*, 8035.

(36) Velleman, L.; Triani, G.; Evans, P. J.; Shapter, J. G.; Losic, D. *Microporous Mesoporous Mater.* **2009**, *126*, 87.

(37) Mutalib Md Jani, A.; Anglin, E. J.; McInnes, S. J. P.; Losic, D.; Shapter, J. G.; Voelcker, N. H. *Chem. Commun.* **2009**, 3062.

(38) Busby, M.; Kerschbaumer, H.; Calzaferri, G.; De Cola, L. *Adv. Mat.* **2008**, *20*, 1614.

(39) Kilian, K. A.; Bocking, T.; Gaus, K.; Gooding, J. J. *Angew. Chem. Int. Ed.* **2008**, *47*, 2697.

(40) Sailor, M. J.; Link, J. R. *Chem. Commun.* **2005**, 1375.

(41) Brevnov, D. A.; Barela, M. J.; Brooks, M. J.; Lopez, G. P.; Atanassov, P. B. *J. Electrochem. Soc.* **2004**, *151*, B484.

(42) Jee, S. E.; Lee, P. S.; Yoon, B. J.; Jeong, S. H.; Lee, K. H. *Chemistry of Materials* **2005**, *17*, 4049.

(43) Lazzara, T. D.; Lau, K. H. A.; Knoll, W. *J. Nanosc. Nanotechnol.* **2010**, *10*, 4293.

(44) Aronsson, B. O.; Lausmaa, J.; Kasemo, B. *J. Biomed. Mater. Res.* **1997**, *35*, 49.

(45) Harrick-Plasma *Applications involving plasma treatments with Harrick plasma devices*; http://www.harrickplasma.com/applications_cleaning.php, 2010.

(46) PLASMAtech-literature *Ultra-pure Cleaning with Low Pressure Gas Plasma*; PLASMAtech, Inc., 2007.

(47) Fliniaux, O.; Elie-Caille, C.; Pantigny, J.; Bourdillon, C. *Electrochem. Commun.* **2005**, *7*, 697.

(48) Liebermann, T.; Knoll, W. *Colloids Surf. A-Physicochem. Eng. Asp.* **2000**, *171*, 115.

(49) Vasilev, K.; Knoll, W.; Kreiter, M. *J. Chem. Phys.* **2004**, *120*, 3439.

(50) Dietrich, C.; Bagatolli, L. A.; Volovyk, Z. N.; Thompson, N. L.; Levi, M.; Jacobson, K.; Gratton, E. *Biophys. J.* **2001**, *80*, 1417.

(51) Fortig, A.; Jordan, R.; Graf, K.; Schiavon, G.; Purrucker, O.; Tanaka, M. *Macromol. Symp.* **2004**, *210*, 329.

(52) Han, X. J.; Pradeep, S. N. D.; Critchley, K.; Sheikh, K.; Bushby, R. J.; Evans, S. D. *Chem. Eur. J.* **2007**, *13*, 7957.

(53) Stottrup, B. L.; Veatch, S. L.; Keller, S. L. *Biophys. J.* **2004**, *86*, 2942.

(54) Chu, P. K.; Chen, J. Y.; Wang, L. P.; Huang, N. *Mat. Sci. Eng. R* **2002**, *36*, 143.

(55) Ulbricht, M. *Polymer* **2006**, *47*, 2217.

(56) Knoll, W. *Annu. Rev. Phys. Chem.* **1998**, *49*, 569.

(57) Gitsas, A.; Yameen, B.; Lazzara, T. D.; Steinhart, M.; H., D.; Knoll, W. *Nano Lett.* **2010**, *10*, 2173.

(58) Lazzara, T. D.; Lau, K. H. A.; Abou-Kandil, A. I.; Caminade, A. M.; Majoral, J. P.; Knoll, W. *Acs Nano* **2010**, *4*, 3909.

(59) Scheller, A.; Winspall program, version 3.01; Max-Planck Institute for Polymer Research: Mainz. Gernany, Reflectivity simulation program solving Fresnel Equations.

(60) Aspnes, D. E. *Thin Solid Films* **1982**, *89*, 249.

(61) Lau, K. H. A.; Tan, L. S.; Tamada, K.; Sander, M. S.; Knoll, W. *J. Phys. Chem. B* **2004**, *108*, 10812.

(62) Lau, K. H. A.; Duran, H.; Knoll, W. *J. Phys. Chem. B* **2009**, *113*, 3179.

(63) Carson, G.; Granick, S. *J. Appl. Polym. Sc.* **1989**, *37*, 2767.

(64) Mayer, L. D.; Hope, M. J.; Cullis, P. R. *Biochim. Biophys. Acta* **1986**, *858*, 161.

(65) Bagatolli, L. A.; Parasassi, T.; Gratton, E. *Chem. Phys. Lipids* **2000**, *105*, 135.

Acknowledgements

T.D.L. acknowledges the award of a doctoral scholarship from *les Fonds Québécois sur la Nature et les Technologies* (FQRNT) and additional financial support from the Göttingen Graduate School for Neurosciences and Molecular Biosciences (GGNB). We thank the SFB-803 for financial support.

Supporting Information Available. Fluorescence microscopy of the fluorescence being preserved by the Au-mask is shown, as well as the fluorescence loss with plasma treatment duration. Fresnel simulations of the angular shifts of waveguide modes for two scenarios are presented: 1) only atop deposition and 2) deposition atop and within

the AAO nanopores. A sample measurement of the OWS spectra before and after deposition of a lipid monolayer onto the hydrophobic AAO, substrate 1, together with the raw data of angular shift and the total angular shift for every waveguide mode measured that indicate whether the deposition occurs only atop or uniformly along the entire AAO pore depth. Also available are SEM images showing that Au deposition within the AAO pore-interiors is minimal, and photos showing the optical transparency of AAO films. This material is available free of charge via the Internet at http://pubs.acs.org

7.6. Supporting information

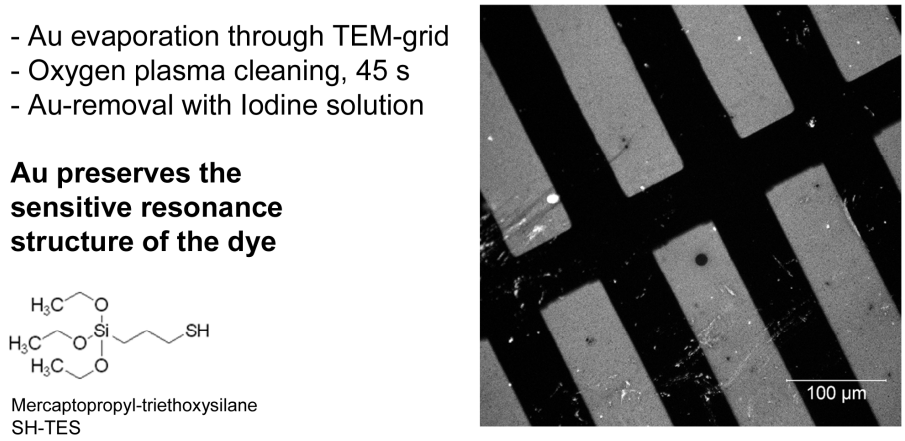

Figure 7.S1. A glass slide was silanized with mercaptopropyl-triethoxysilane (SH-TES), followed by reacting the thiol groups with cyanine-3-maleimide dye (maleimide-Cy3). The substrate was then patterned with a TEM-grid (see also Figure 4) during Au evaporation (15 nm). The Au layer protects the sensitive chemical structure of the Cy3 dye during the 45 s O_2 plasma treatment. Shown on the right is a confocal fluorescence image of the substrate after Au removal with iodine solution (I_2/KI).

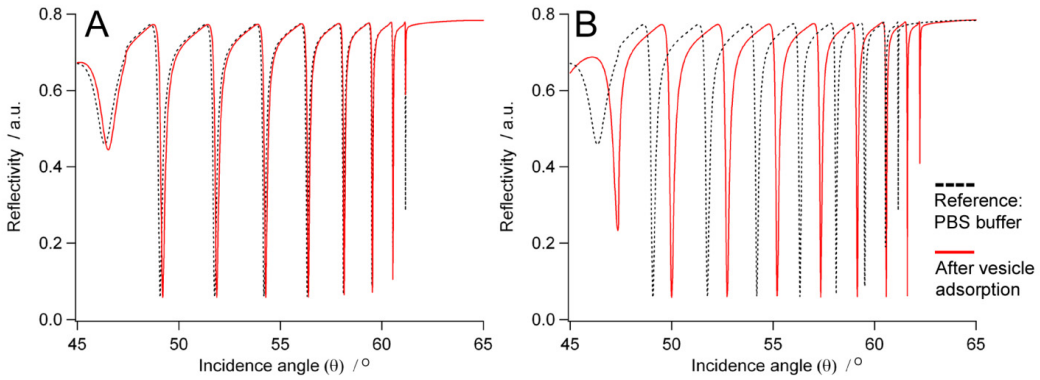

Figure 7.S2. Fresnel simulations of the optical waveguide spectra before and after the addition of vesicles on 4 µm thick AAO samples containing pores with diameters of 65 nm for two possible scenarios. The case for a 25 nm film forming only atop is shown in (**A**). In contrast, the deposition of a 2.5 nm film on the entire surface of the AAO film, atop and within, is shown in (**B**). When material deposition occurs only atop the film, such as in the case of vesicle adsorption, the waveguide mode angular shifts are smaller and only the higher order modes shift, while the lower order modes remain unchanged, as shown in (A). In contrast, if the entire AAO surface is modified with a thin layer, the optical density of the film increases significantly and a large angular shift is observed for all waveguide modes.

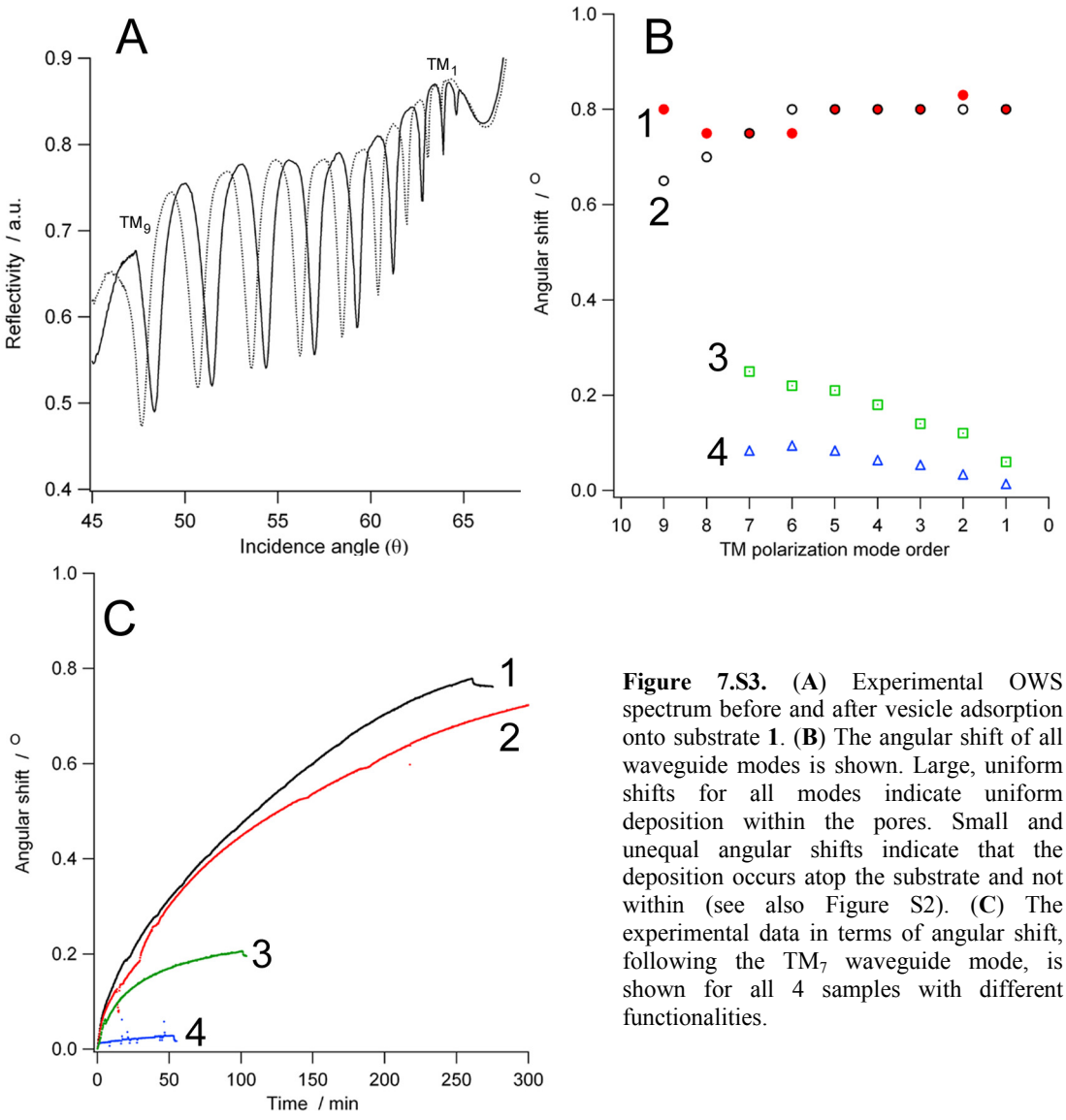

Figure 7.S3. (**A**) Experimental OWS spectrum before and after vesicle adsorption onto substrate **1**. (**B**) The angular shift of all waveguide modes is shown. Large, uniform shifts for all modes indicate uniform deposition within the pores. Small and unequal angular shifts indicate that the deposition occurs atop the substrate and not within (see also Figure S2). (**C**) The experimental data in terms of angular shift, following the TM_7 waveguide mode, is shown for all 4 samples with different functionalities.

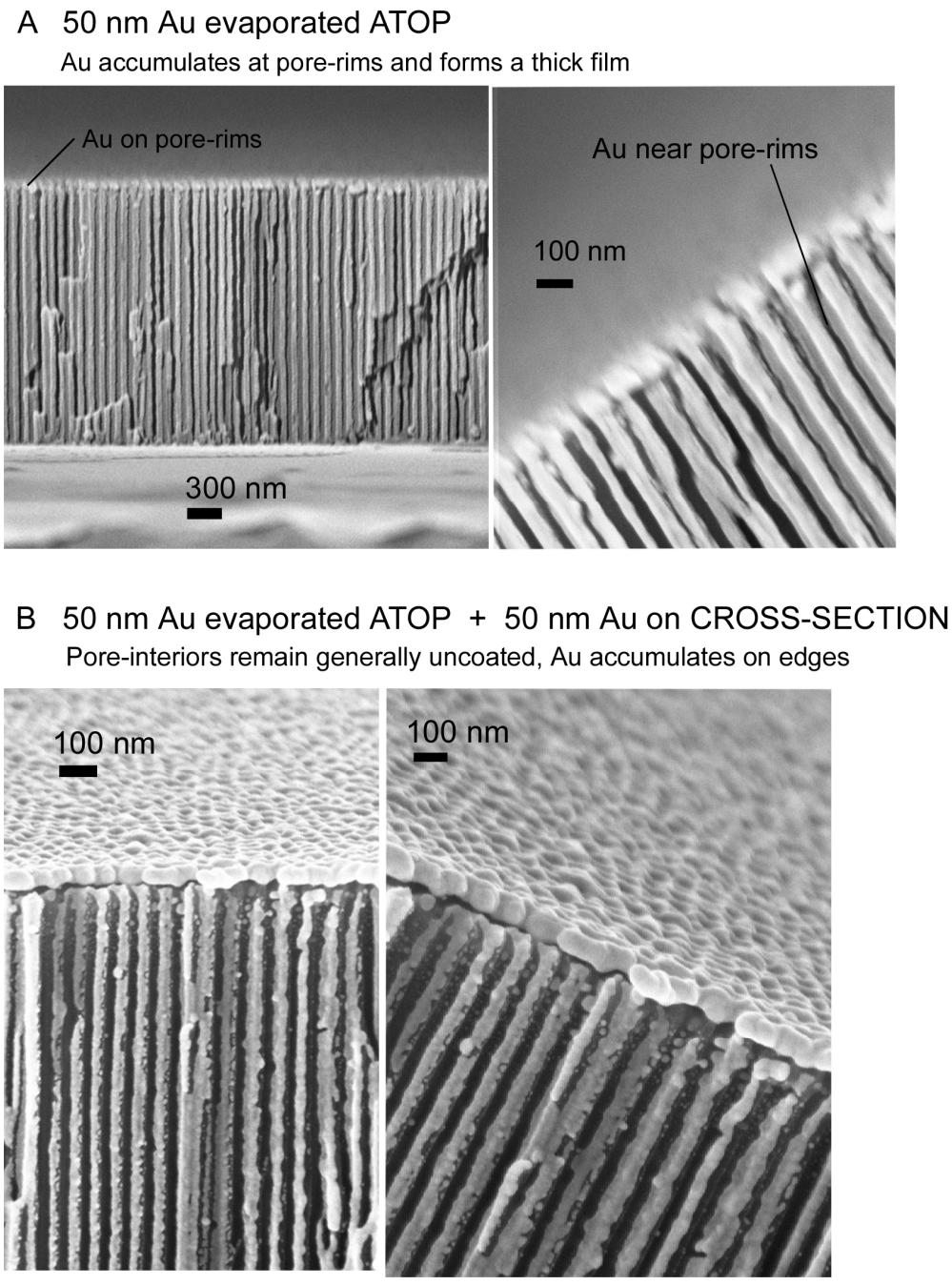

Figure 7.S4. (**A**) 50 nm of Au were evaporated only atop the film before imaging. (**B**) The AAO substrate was cracked to reveal the cross-section and another 50 nm of Au was evaporated directly on the cross-section: total of 100 nm, 50 nm atop + 50 nm in the cross-section. The resolution is better since the sample is more conductive. These results show that Au does not deposit significantly within the AAO pores (aggregates). Even in the cross-sectional evaporation, Au accumulates at the rims between the linear pore grooves. We do not expect more than about 1-5 % maximum pore interior contamination (for a 4 μm thick AAO), which is approximately the ratio of pore area (πr^2) to pore-interior area.

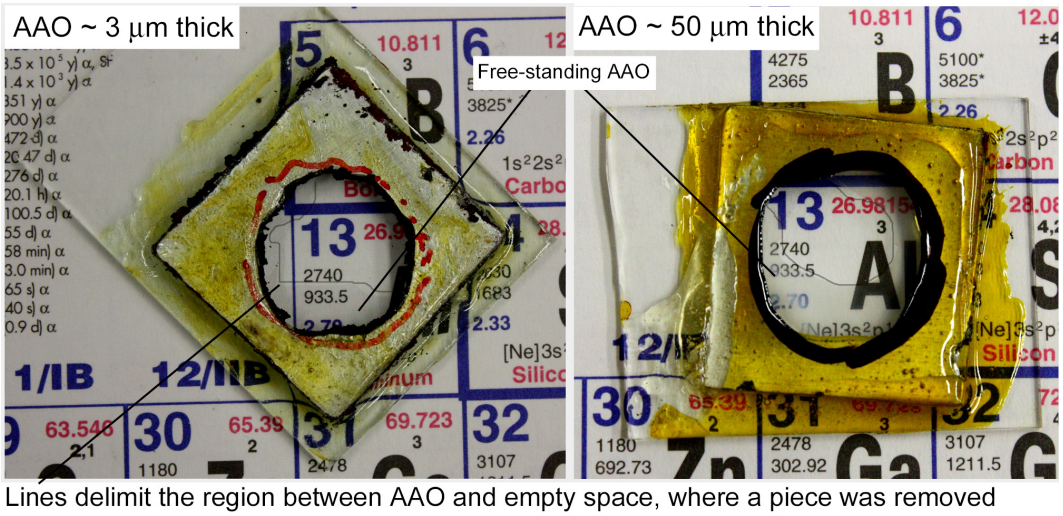

Figure 7.S5. Photographs showing the transparency of free-standing AAO films (preparation step before mounting the films on glass slides). About half of the AAO free-standing film was broken off in order to show the transparency difference with and without AAO. The AAO on the left-hand side picture is thinner (3 µm) and much more transparent than a thicker (50 µm) AAO, shown on the right-hand picture. The thicker AAO is slightly hazy and therefore less transparent.

Experimental Section

Mercaptopropyl-triethoxysilane was purchased from ABCR (Karlsruhe, Germany). Cyanine-3 maleimide was purchased from Toronto Research Chemicals (North York (ON), Canada).

Silanization of glass substrates (Figure S1). Regular SiO_2 microscope glass slides were cleaned in 2 % *vol.* Hellmanex, rinsed, and O_2 plasma cleaned for 2 min prior to silanization to increase the surface density of OH-groups. The glass slides were then inserted into a glass staining jar and 50 µl of mercaptopropyl-triethoxysilane (SHTES) were added in a glass test tube, inside the chamber. The container was covered with its glass cover and sealed using Scotch vacuum tape from 3M (St-Paul (MN), USA), left in the oven at 130 °C for 10 min to warm, followed by 3 hr under vacuum. The samples were cooled and 100 µl of cyanine-3-maleimide dye (0.02 mg) dissolved in PBS were added and left to incubate for 2 hr, followed by rinsing with PBS, deionized water and ethanol. They were dried and orthogonally functionalized (see manuscript) using a TEM grid as an evaporation mask to create protected and unprotected areas.

Chapter 8

Phospholipids as an Alternative to Direct Covalent Coupling: Surface Functionalization of Nanoporous Alumina for Protein Recognition

By
Thomas D. Lazzara,[†] *Daniela Behn*,[†] *Torben-Tobias Kliesch*,[†] *Andreas Janshoff*,[§] *Claudia Steinem*[†]

Graphical abstract:

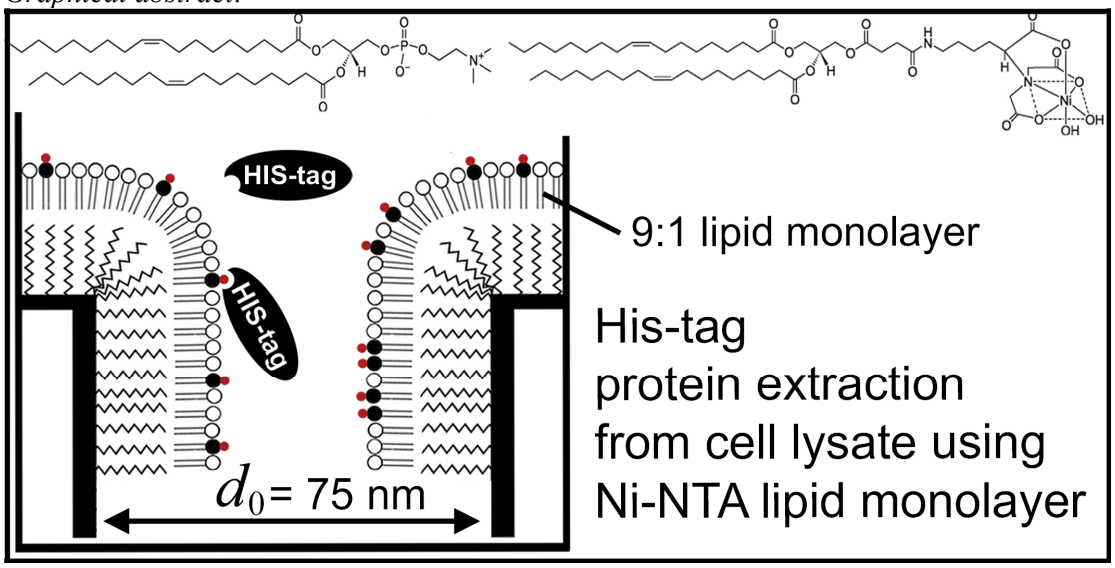

Manuscript prepared for submission.
2011

[†] Institute of Organic and Biomolecular Chemistry, Tamannstrasse 2, 37077 Göttingen, Germany.
[§] Institute of Physical Chemistry, Tamannstrasse 6, 37077 Göttingen, Germany.

Abstract

Anodic aluminum oxide (AAO) membranes with aligned, cylindrical, non-intersecting pores, were functionalized with dodecyl-trichlorosilane to obtain a hydrophobic surface. AAO had pore diameters (d_0 = 75 nm) and pore depths of 3.5 or 10 μm. Small unilamellar vesicles (SUVs) were used to form a lipid monolayer on the surface of the functionalized AAO. SUVs can be easily modified with different ratios of functional head-group lipids. Similarly to the formation of hybrid solid-supported membranes, vesicle spreading was used to transfer the lipid material from SUVs to the hydrophobic AAO surface. This method was used to control the density of functional sites on the AAO surface. SUVs spreading occurred at the hydrophobic AAO pore-rim surface/bulk interface, followed by lateral diffusion of lipids within the hydrophobic AAO until the surface was homogeneously covered. Owing to the optical transparency of the AAO substrates, we used time-resolved optical waveguide spectroscopy (OWS) to investigate the overall spreading process and subsequent protein binding experiments; both in terms of kinetics and absolute adsorbed thickness. Experiments with biotin-DOPE doped SUVs of various mol %, showed that the vesicles formed a lipid monolayer 2.3 ± 0.2 nm thick. The amount of streptavidin adsorption varied as a function of biotin-DOPE content, with a maximum at 10 mol %. Furthermore, being a lipid monolayer the surface molecules are laterally mobile in three-dimensions, which leads to dynamic surface functionalizations with surface mobile receptors. Starting with a biotin-DOPE doped lipid monolayer, 3 protein deposition (streptavidin, b-BSA, streptavidin) steps were carried out without steric hindrance, demonstrating that the pores remained free for potential sensing applications involving the formation of macromolecular complexes within the nanopores. Such membrane based surfaces modification can have practical application in biotechnology for selective protein extraction directly from cell lysate solutions We investigated the selective extraction of PIGEA14, a small 14 kDa protein, from a lysate by using a 10 mol % DOGS-NTA(Ni) lipid in a matrix of DOPC lipids. The protein binding, and recovery process by EDTA complexation, was monitored by time-resolved OWS and the efficiency of the protein extraction was confirmed by SDS-PAGE.

Keywords: nanoporous substrates, hybrid solid-supported membrane, multi-functional surface, lipid monolayers, optical light mode waveguide spectroscopy, affinity chromatography

8.1. Introduction

Many crucial biological functions involve the translocation of biological cargo across cellular compartments and often take place in geometrically confined environments such as microvilli or in the folded mitochondrial membrane. Planar surfaces are often inadequate to mimic the complex functions that are involved in these biological systems. However, porous materials specifically offer the possibility to study transport properties on a three-dimensional scale by investigating the kinetics of molecular adsorption/desorption occurring directly within the confined pores, < 100 nm, of nanoporous materials. In general, nanoporous materials have been of significant interest as high surface area sensing platforms. Using the structure of porous materials to mimic biological systems, together with high sensitivity thin-film detection methods, provides a platform to investigate biologically relevant processes.

Controlling the homogeneous distribution of multiple receptor molecules at the surface of porous materials is not always a straightforward task because the composition of reactive solution species rarely translates into equivalent surface functionalization ratios and homogeneous distributions of receptors. Alternatives to covalent coupling schemes involve using multifunctional macromolecules to control the surface properties of a material through electrostatic or molecular recognition interactions. For example, proteins such as avidin and streptavidin can be used to cover a surface with biotin active sites, which are subsequently modified with different ratios of biotinylated molecules. Alternatively, the deposition of polyelectrolyte polymers, that were *a priori* covalently functionalized with different functional groups, can be adsorbed on charged surfaces to impart a material with multifunctional components.[1] Another example that has been used to create multifunctional planar surfaces for sensor applications is the formation of multi-functional lipid monolayers. Modification of solid planar hydrophobic surfaces with lipid monolayers by Langmuir-Blodgett[2] or liposome spreading[3-4] has been extensively used to reproduce the complex lipid mixture composition of lipid films, lipid vesicles and even of ghost cells[5-6] onto flat surfaces.

The spreading of phospholipid vesicles on hydrophobic surface functionalizations generates hybrid lipid solid-supported membranes (SSMs), where only a lipid monolayer forms onto the covalently bound hydrophobic molecules. As long as the overall chemical structure of a phospholipid is preserved, the phosphate head groups can be modified with a variety of functional groups, often commercially available, and can be incorporated into a

matrix of phospholipids to generate multifunctional liposomes. Such hybrid bilayers are composed of laterally mobile lipids and therefore allow clustering around nucleation points or even reversible domain formation, which are properties that cannot be achieved using covalent coupling schemes. Such dynamic surface properties have been used to generate versatile planar biosensing platforms.

We propose here to use lipid liposomes with varying functional head-groups content to directly functionalize the nanoporous surface of anodic aluminum oxide (AAO), by transferring the surface chemistry of the liposome onto the AAO. AAO is a porous material with a self-organized predictable structure that is composed of non-intersecting, hexagonally close-packed, cylindrical pores with conveniently adjustable monodisperse pore diameters, degree of lattice spacing, and membrane thickness. Previous studies have shown that indeed hybrid solid-supported can be build in AAO.[7-8] However, this particular functionalization strategy has not been as such, exploited as a surface modification tool for potential analytical assays involving macromolecular adsorption detected by optical methods. Such a functionalization scheme is an invaluable tool to modify porous substrates that can be used as optical detection platforms. Furthermore, although the spreading of vesicles has been shown in AAO pores with pore diameters (d_0) larger than 100 nm,[7-9] liposome spreading has not been described for AAO with more narrow pores (d_0 = 70-80 nm), on the order of the vesicle diameter ($d_{vesicle}$ = 20-50 nm). We observed that vesicles are not required to enter the pores to form hybrid SSMs on the AAO surface. This therefore allows the use of substrates with pore diameters below the scattering limit, d_0 < 100 nm. Nanoporous materials have lattice constants and geometrical features that are below the scattering limit of visible light, making such thin-films optically transparent.[10-13] This allows investigation of processes occurring within the pore-interior by fluorescence microscopy[14-15] and thin-film characterization techniques that evaluate refractive index changes.[13, 16-19]

We show in this contribution that the hydrophobically functionalized three-dimensional nanoporous surface of AAO with d_0 = 75 nm can be modified with a functional lipid monolayer to bind macromolecular species, by spreading of small unilamellar vesicles (SUVs), analogously to hybrid SSMs. Owing to the AAO's optical transparency, we could use the AAO as an optical sensing device to investigate adsorption processes occurring within the thin-film AAO substrates by time resolved optical waveguide spectroscopy (OWS), as shown in other thin-film studies.[12-13, 20-23] OWS allowed the sub-nanometer detection of both the adsorption of lipids and the adsorption of proteins onto the lipid

monolayer. Furthermore, because the AAO was optically transparent, confocal fluorescence microscopy was used to corroborate the OWS measurements using fluorescently labeled lipids and proteins. As a model system, we studied streptavidin adsorption onto modified AAO using POPC phospholipid SUVs that were doped with different mol % of biotinylated phospholipids (biotin-DOPE). The protein adsorption was directly dependent on the biotin-DOPE mol %, showing maximum deposition at 10 mol %. The amount of deposited protein and the adsorption kinetics measured on the lipid monolayer modified AAO were comparable to a biotinylated AAO surface obtained by covalent coupling. Fluorescence recovery after photobleaching experiments showed that phospholipids diffused along the 3D AAO surface, in agreement with monolayer coverage. Furthermore, the formation of 3 protein layers, formed by the sequential adsorption of streptavidin and biotinylated-bovine serum albumen (b-BSA), showing that the nanopores were not obstructed and that the lipid monolayer surface can thus be used to build and detect bio-macromolecular assemblies. Finally, we show by OWS that a lipid monolayer containing DOGS-NTA(Ni) lipids can be used in a practical environment to selectively isolate the His-tag PIGEA14 protein from a cell lysate solution, a concept analogous to affinity chromatography. Essentially, we demonstrate that similarly to hybrid SSMs, the hydrophobic AAO can be used to transfer the complex lipid mixture composition of SUVs as a lipid monolayer on the three-dimensional hydrophobic AAO structure.

8.2. Results and Discussion

For our studies, we used anodic aluminum oxide (AAO), which was produced by anodizing aluminum in 0.3 M oxalic acid under a constant potential of 40 V. This procedure resulted in AAO substrates with an inter-pore distance of $p \sim 100$ nm, pore diameters that were enlarged to $d_0 = 75$ nm and with a chosen thickness of $l \sim 3.5$ or 10 μm (scheme 8.1A). The AAO membranes were covered with a thin metal coupling layer of about 25 nm on the aluminum oxide barrier side (bottom) and then mounted on glass supports using an optical adhesive (scheme 8.1) to allow the characterization of their refractive index using optical waveguide spectroscopy (OWS). The AAO pores were hexagonally ordered (scheme 8.1C, left image) with a cylindrical geometry (scheme 8.1C, right image).

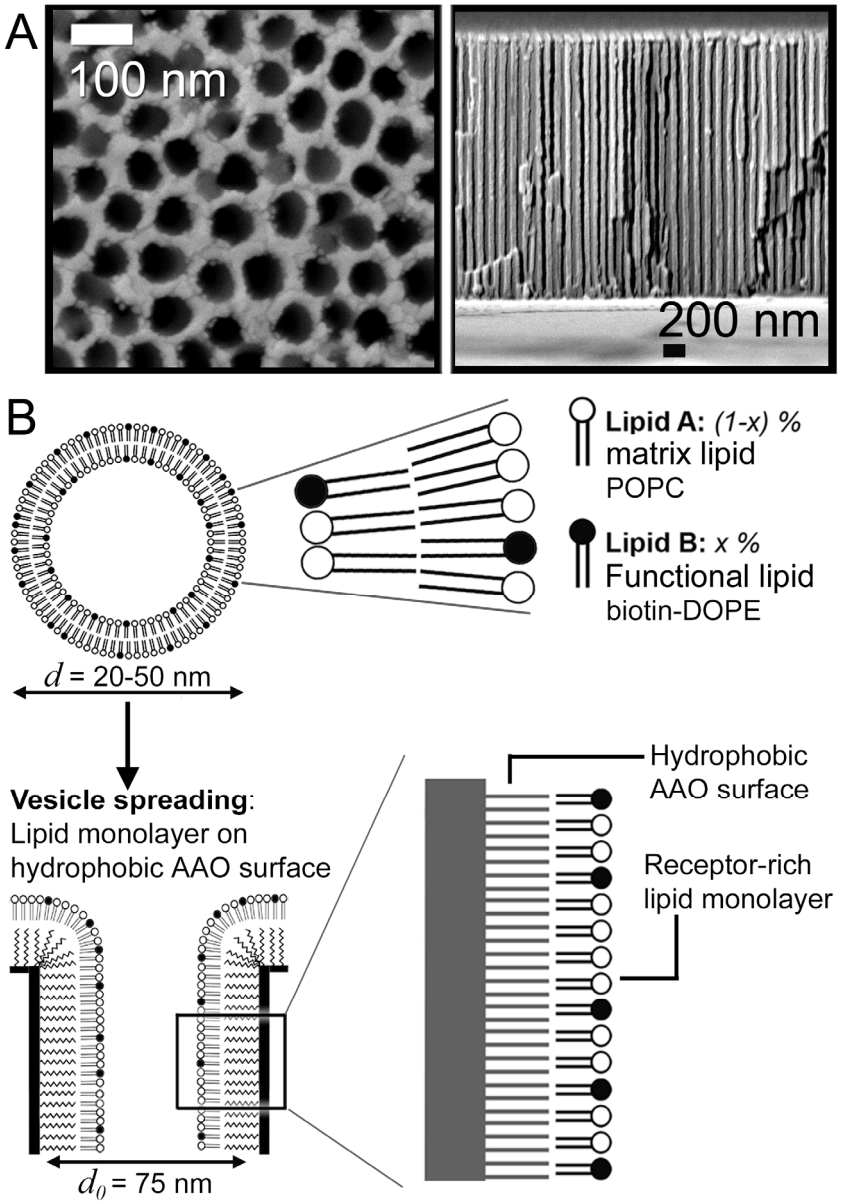

Scheme 8.1. (**A**) SEM of AAO (with 2 nm Cr and 5 nm Au for imaging purposes) showing the parallel nanopore structure from the top view (left) and cross-section view (right). (**B**) Schematic of the functionalization scheme used to cover hydrophobic AAO substrates (d_0 = 75 nm) with a lipid monolayer by the spreading of SUVs.

8.2.1. Lipid Monolayer Formation on AAO and Streptavidin Adsorption

To compare our functionalization procedure of the AAO with a lipid monolayer, we first modified an AAO with a biotin-terminated surface obtained by covalent coupling: the AAO was silanized with aminopropyl-triethoxysilane followed by coupling to a heterobifunctional biotin linker. Streptavidin binding to this biotinylated surface was performed for comparison with the lipid monolayer experiments. The amount of adsorbed

streptavidin was estimated to be approximately 2.3 ± 0.2 nm in thickness, which essentially corresponds to about 50% surface coverage of a tightly packed protein layer (figure 8.1B); considering that the protein measures 4.5×4.5×5.8 nm^3. According to the functionalization scheme presented in figure 8.1, we modified the AAO surface with a functional lipid monolayer. The AAO was first silanized with dodecyl-trichlorosilane to obtain a hydrophobic alkyl self-assembled monolayer and then small unilamellar vesicles (SUVs) doped with different mol % of biotin-DOPE lipids were spread on the AAO surface in order to transfer the lipid composition of the liposome directly onto the AAO surface. A typical measurement of the SUV spreading kinetics is shown in figure 8.1A for a 0.5 mg/ml lipid solution. Streptavidin adsorption kinetics on the AAO lipid monolayer modified surface were then be followed (figure 8.1B). Under identical conditions, the protein adsorption kinetics were similar for both a biotinylated AAO surface and a biotin-terminated lipid monolayer surface containing 5 mol % of biotin-DOPE, while a lipid POPC monolayer without biotin only shows low unspecific adsorption (figure 8.1B).

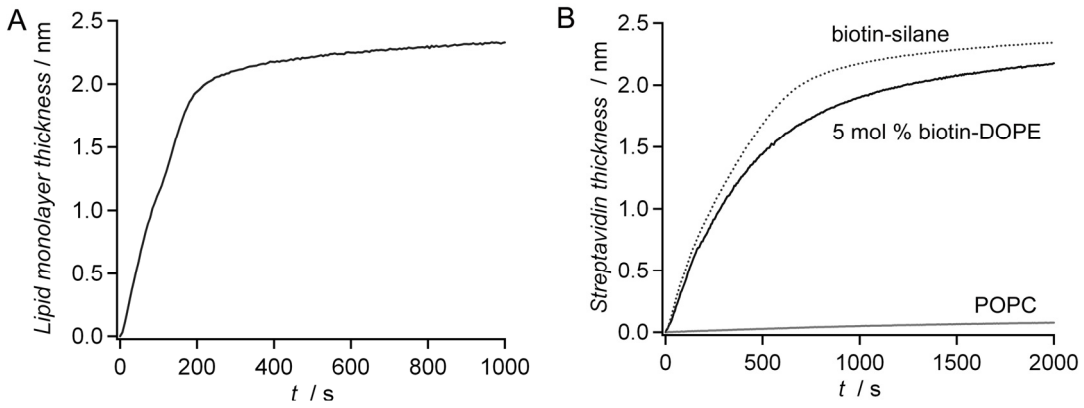

Figure 8.1. (**A**) OWS kinetics of SUV spreading to form a lipid monolayer on hydrophobic AAO (0.5 mg/ml POPC SUVs containing 5 mol % biotin-DOPE). (**B**) Kinetics of streptavidin adsorption on biotin-terminated surfaces: AAO was either biotinylated by covalent coupling or was modified with a POPC lipid monolayer containing 0 mol % and 5 mol % of biotin-DOPE.

The main advantages of working with AAO substrates having $p < 100$ nm is that the material's dielectric properties can be monitored by OWS and fluorescence microscopy, since they are optically transparent. For AAO with $p > 100$ nm, inelastic light scattering occurs, which leads to low optical transparency and high auto-fluorescence; these effects being more pronounced for greater values of p. As long as the geometrical features of nanoporous materials are < 100 nm, transparency is preserved. The AAO used in this study can therefore be used as an optical biosensor to investigate macromolecular adsorption. Although the vesicle diameter (d = 20-50 nm) was in the range of the AAO d_0 = 75 nm, we

observed that the surface was uniformly covered with phospholipids throughout the AAO thickness. Kinetic OWS measurements of the vesicle spreading process (Figure 8.1A) showed that POPC SUVs continued spreading until the AAO surface was completely saturated with a lipid monolayer, measuring about 2.3 ± 0.2 nm in thickness (*n=10*), in agreement with a lipid monolayer lining the pore-interior surface, as well as the pore-rim surface (ε_{lipids} = 2.1). The dielectric response increase due to adsorbed material is directly proportional to the occupied volume fraction of this material and thus, the surface coverage. An overall smaller lipid thickness (i.e. surface coverage) would have been expected if the entire AAO surface was not covered with a lipid monolayer. Conceivably, as the vesicles come into contact with the hydrophobic AAO pore-rim hydrophobic alkyl-modified interface, liposome bilayer delamination takes place, followed by lateral diffusion along the remainder of the AAO hydrophobic surface. Due to the large AAO surface area, lateral diffusion of phospholipids away from the pore-rim eventually depletes the surface sufficiently to induce additional SUV rupture events until the entire AAO becomes saturated with phospholipids. Furthermore, the relatively rapid spreading process indicates that the vesicle diffusion within the nanopores was not the major lipid transport mechanism, since this scenario would proceed over a much longer time scale because of the steric hindrance to vesicle transport within the AAO for $d_{vesicle} \sim d_0$. To prove this idea, performed the same experiment with large unilamellar vesicles (LUVs) prepared by extrusion through polycarbonate membranes with average pore diameters ($d_{vesicle}$) of 400 and 1000 nm (figure 8.S1), which cannot enter the pores ($d_{vesicle} > d_0$), but also formed a lipid monolayer on the AAO surface. The surface coverage was slightly lower for the larger vesicles, and the spreading kinetics were slower for the larger diameter liposomes indicating a partial hindering of lipid diffusion process. Therefore, under the conditions where vesicles are excluded from the pore interior, the spreading mechanism can only occur at the interface with the bulk solution and one can conclude that vesicles entrance within the nanopores is not required to functionalize the AAO surface with a lipid monolayer.

We studied POPC SUVs spreading on the hydrophobic AAO surface containing different mol % of the biotinylated phospholipids (biotin-DOPE): 0, 0.1, 1, 5, 10, and 20 mol % were tested. The lipid monolayer thickness obtained from each experiment was similar, 2.4 ± 0.2 nm (figure 8.2A), in agreement with a lipid monolayer lining the entire AAO pore depth. The amount of streptavidin adsorbed to the lipid modified AAO surfaces was directly proportional to the biotin-DOPE mol % content of the SUVs, as shown in figure 8.2B. In agreement with the work of Spinke et al.[24] and Lopez and co-workers[25], the highest

streptavidin surface coverage was obtained when using a biotin-DOPE to POPC ratio of 9:1. In our experiments, using 10 mol % biotin-DOPE gave a protein layer thickness about 15% greater than working with a 5 or 20 % biotin-DOPE lipid monolayer content.

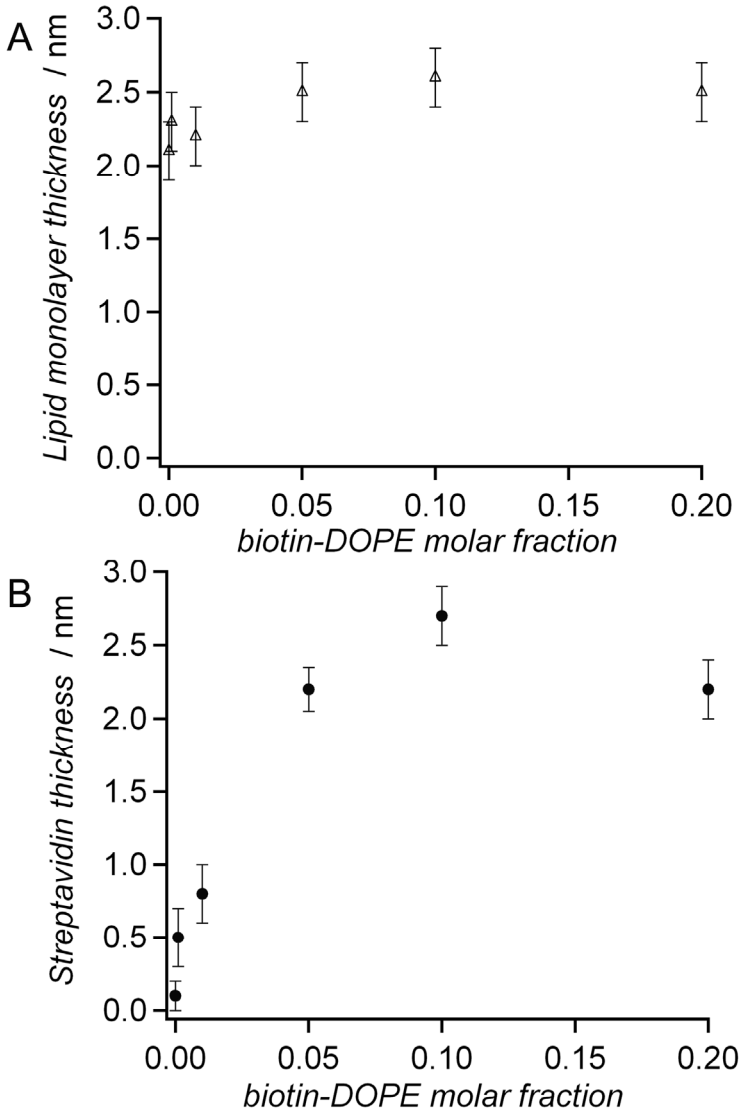

Figure 8.2. (**A**) Lipid monolayer thickness on AAO after spreading of different biotin-DOPE mol % SUVs. (**B**) Streptavidin thickness after binding to the biotinylated lipids. The amount of adsorbed protein can be tuned by varying the biotin-DOPE mol % content of SUVs, while this cannot be achieved by direct covalent surface modifications.

We then investigated if these lipids are mobile, i.e., if they could travel from pore-to-pore, by performing fluorescence recovery after photobleaching (FRAP) on the AAO covered with a lipid monolayer. The fluorescence recovery over several minutes of a bleached square region is shown in figure 8.3, where a 60% recovery was observed after 10 minutes. Since a diffusion coefficient was not calculated, a square bleach area, rather than a circle,

was chosen to emphasize the fluorescence recovery at the corners. Although the large surface area of AAO slows down the recovery, the fact that the fluorescence recovers demonstrates that the monolayer is laterally mobile in three-dimensions and fluorescently labeled lipids can diffuse from pore-to-pore, over tens of μm distances. Images of the fluorescence at different times during the recovery curve on the right of figure 8.3, illustrating the homogeneous fluorescence recovery with time.

The fluorescence recovery not only shows that a lipid monolayer is formed, but that surface lipids are mobile in three-dimensions along the AAO surface. This particular feature cannot be achieved with covalent coupling. In that respect, such a system could have interesting outcomes for studies involving dynamic surface functionalizations with mobile functional head-groups lipids that could laterally transport peripheral proteins within the pores or could aggregate around nucleation sites.

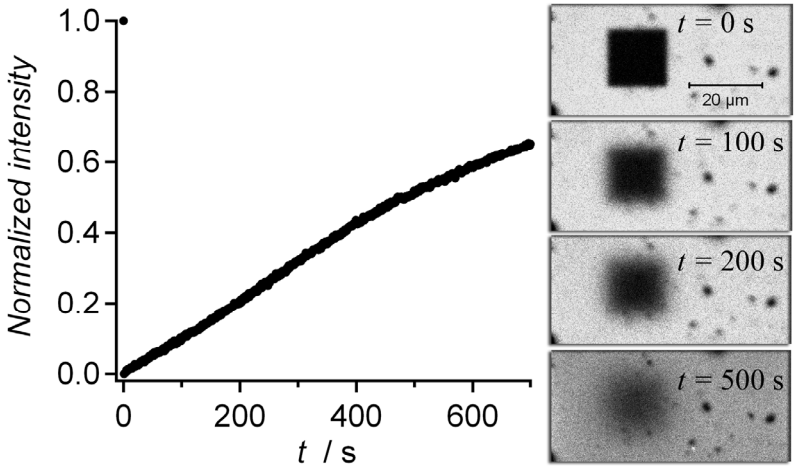

Figure 8.3. FRAP curve showing that the fluorescence inside the bleached area recovers after several minutes. Slow recovery is due to the large AAO surface area (d_0 = 75 nm, h = 3.5 μm), but demonstrates that the lipids are mobile over the AAO surface. Right-hand side shows the *x-y* focal plane scans of the fluorescence recovery at different times.

8.2.2. Investigation of Biomacromolecular Assemblies in Nanopores

As a further confirmation of our OWS measurements presented in the previous section, we performed a streptavidin adsorption experiment, as shown in figure 8.3, using SUVs that contained 10 mol % of biotin-DOPE. The vesicles were fluorescently labeled with 0.3 mol % Bodipy DHPE. The streptavidin was labeled with atto-633. A thicker AAO substrate having h = 10 μm (d_0 = 75 nm) was used to clearly distinguish the fluorescence evolution across the *z*-direction, with a resolution of 900 nm. The SUVs were left overnight to spread on the dodecyl-trichlorosilane functionalized AAO surface. The evolution of protein

adsorption of a 0.2 µM atto-633 labeled streptavidin solution was then studied using time-resolved confocal scanning microscopy by acquiring a *z*-profile scan of the AAO cross section, every 20 s over a 40 µm vertical range. The initial fluorescence at time t = 0 s, is shown in figure 8.4A for both the lipid and protein fluorescence. The Bodipy fluorescence was visible across the entire AAO depth, which indicates that lipids covered the AAO surface. The evolution of the atto-633 fluorescence within the 10 µm depth of AAO at different times is shown in figure 8.4A, where the pores were more than half-filled after 6000 s. Adsorption proceeded from near the pore entrance and continued until the entire pore depth was saturated with streptavidin. The adsorption was significantly slower than in figure 8.1B, due to the lower protein concentration and thicker AAO. Afterwards, a *z*-stack image (figure 8.4B), consisting of multiple *x*-*y* focal planes taken 300 nm apart over a 40 µm range, also shows that the entire AAO 10 µm depth was covered with a lipid monolayer and that streptavidin bound within the entire AAO depth. Both the Bodipy and atto-633 fluorescence in the vertical *z*-direction were correlated. In figure 8.4B, the *x*-*y* plane that was taken in the centre of AAO and shows the overlapping fluorescence (green-yellow) from both labeled species.

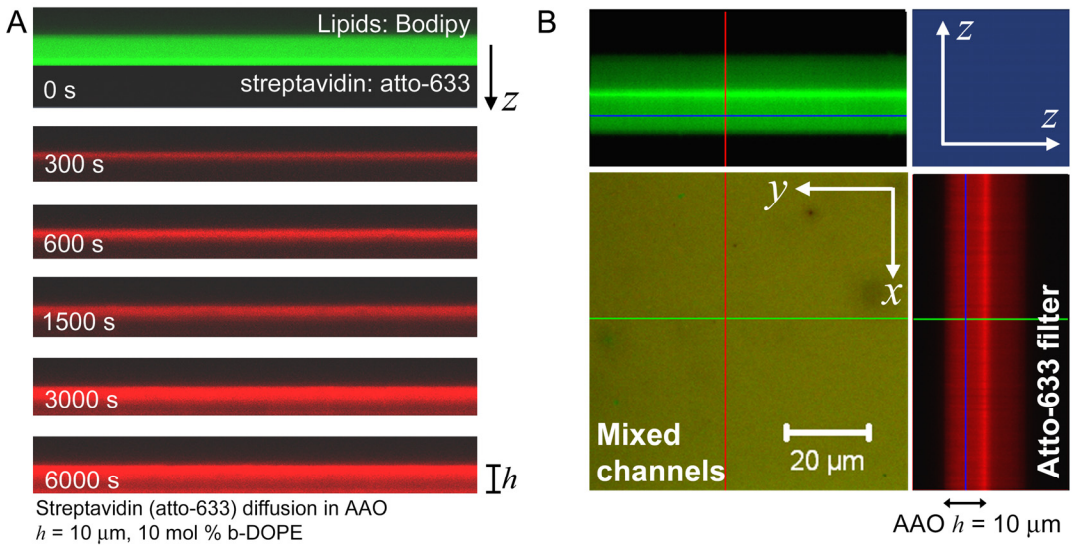

Figure 8.4. (**A**) *Z*-direction CLSM fluorescence profiles taken at progressive times showing the evolution of streptavidin adsorption (0.2 µM) on a 10 mol % biotin-DOPE containing POPC lipid monolayer on hydrophobic AAO (d_0 = 75 nm, h = 10 µm). (**B**) Confocal z-stack composite image after the experiment in (**B**) after 6 hours. The *x*-*y* focal plane consists in the overlayed mixed channels. The top *z*-profile shows the Bodipy fluorescence from the lipid monolayer, while the right-hand *z*-profile shows that atto-633 labeled streptavidin bound where the lipid monolayer was localized. The metal layer at the AAO bottom produces a reflection plane.

As shown in figure 8.1 and in figure 8.4, the AAO can serve as a detection platform for either the label free or the fluorescently labeled detection of protein adsorption to a lipid monolayer covering the porous surface. Although we showed that the lipids deposited on the AAO were mobile by FRAP experiments (figure 8.3), we wanted to further demonstrate that the SUVs did not pose any obstacle, under the form of possible non-spread vesicles that would block the pores, which is important for unhindered macromolecular complexation within the pores. To demonstrate this, we build two additional protein layers using biotinylated-BSA, followed by a second streptavidin deposition, onto an initial streptavidin layer bound to a biotin-DOPE lipid monolayer. As shown in figure 8.5, the amount of protein from a second streptavidin (2.1 nm) layer onto the biotinylation BSA layer was similar to the amount initially deposited from the first streptavidin layer on the lipid surface (2.2 nm). Both proteins are 5-6 nm in diameter, such that a total of three layers could not be build if vesicles hindered macromolecular transport within the pores. An non-rupture 30 nm vesicle would occupy from 65% of the available area fraction such that only 1 protein layer could be deposited. Therefore, the lipid monolayer surface functionalization can be used to study biomacromolecular assemblies within the AAO pores. Alternatively, this surface can also be used to initiate Layer-by-Layer assemblies, by taking advantage of the tunable head-group composition of the monolayer.

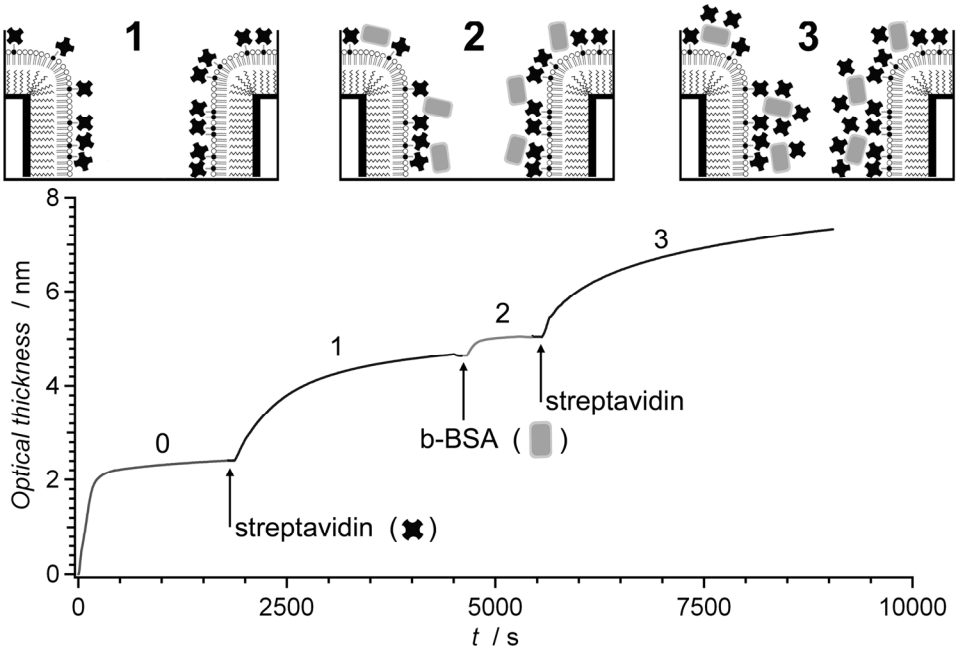

Figure 8.5. Kinetic measurements of lipid POPC monolayer formation containing 20 mol % biotin-DOPE (0), followed by streptavidin adsorption (1), then biotinylated-BSA (13 biotin per protein) (2) and finally a second layer of streptavidin (2). The pores remained accessible after AAO functionalization with a lipid monolayer (0) since step (2) shows as much deposition as step (1). Deposition is therefore not hindered by non-spread SUVs. Above are shown schematic representations of the different steps of the measurement.

8.2.3. Direct Protein Extraction from Cell Lysates

As a further demonstration of the versatile functions that can be carried out by modifying the AAO surface with a lipid monolayer, we performed a protein isolation experiment using Ni-NTA head-group lipids to capture histidine-tagged proteins directly from a raw cell lysate. As a test protein, we used PIGEA14, which was expressed with a hexa histidine-tag. This protein is composed of 126 amino acids and has a molecular weight of 14 kDa.[26] It has been shown by means of QCM and SPR experiments, that PIGEA14 can be immobilized onto a DOPC containing DOGS-NTA(Ni) SSMs.[27] This system was designed to reproduce the conditions used in affinity chromatography where complex biochemical mixtures can be separated with high specificity based on a specific receptor-ligand interaction.

DOPC SUVs containing 10 mol % of DOGS-NTA(Ni) lipids were spread on hydrophobic C_{12} AAO, silanized with C_{12}-TCS. The kinetics of the protein adsorption process on AAO (d_0 = 75 nm and h = 3.5 μm) were monitored by OWS, as shown in figure 8.5A, which shows the normalized angular shift recorded as a function of time. The angular shift of the PIGEA14 protein corresponded to a captured 1.8 nm protein layer. A schematic illustrating the experiment is shown in figure 8.5B. Assuming full surface coverage of the lipid monolayer with proteins about 2 nm in diameter, the AAO surface captured efficiency was approximately 3.5 $nM \cdot cm^{-2}$. The protein adsorption from the lysate took over 2 hrs. However, elution of the protein using 50 mM EDTA buffer took only about 10-15 min. A control experiment using only a DOPC lipid monolayer shows that some material from the cell lysate adsorbs unspecifically, about 0.2 nm thickness, which corresponds to the adsorbed material that was not removed after the EDTA buffer step in figure 8.5A. We should emphasize here that this particular methods allows us to monitor and control the adsorption and desorption at a sub-nanometer surface coverage. The same experiment was repeated on a larger scale using AAO with a surface area of 25 mm^2 (d_0 = 75 nm) measuring h = 10 μm in order to collect a larger amount of proteins to characterize the purity. A SDS-PAGE gel of the eluted EDTA fraction from this experiment shows the method's specificity for the capture of the 14 kDa protein directly from the lysate: aliquots 1 and 2 in figure 8.5C.

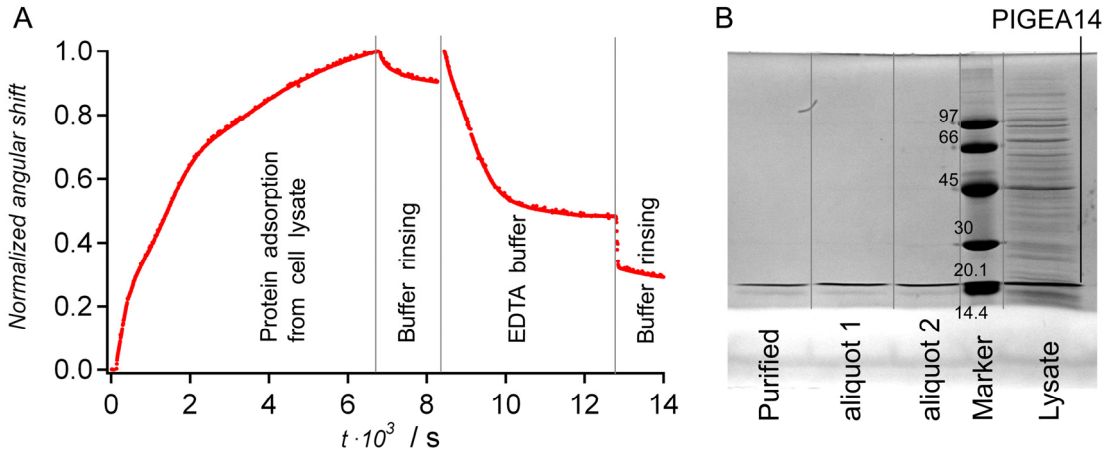

Figure 8.5. (**A**) Time-resolved OWS measurement of His-tag labeled PIGEA14 protein adsorption on a 10 mol % DGS-NTA(Ni) lipid monolayer directly from a cell lysate solution. The protein was collected using a TRIS elution buffer containing 50 mM EDTA. (**B**) SDS-PAGE gel showing that only the 14 kDa PIGEA14 protein was extracted from the cell lysate using the purification scheme. Columns from left-to-right are: purified protein using regular techniques, two replica measurements of the experimental extraction using DOGS-NTA(Ni) on a AAO (d_0 = 75 nm, h = 10 μm), marker bands (kDa units) and cell lysate. The cell lysate contained a range of different proteins, while the aliquots only contained PIGEA14.

8.3. Concluding Remarks

We have shown that solid-supported lipid membranes can be formed on the surface of nanoporous anodic aluminum oxide (AAO) with pore diameters of d_0 < 100 nm, on the order of the size of the small unilamellar vesicles (SUVs) used. Owing to the optical transparency of these substrates, they were used as optical bio-sensing platforms. Protein binding to functional lipid monolayers were studied by both time-resolved optical waveguide spectroscopy (OWS) and by confocal laser scanning fluorescence microscopy. The modification of AAO with a lipid monolayer containing biotin-DOPE was used to bind streptavidin, similarly to the behavior observed for a biotinylated AAO substrate obtained by direct covalent coupling. The optimal loading efficiency was observed for a 9:1 ratio of matrix lipids to functional lipids, in agreement with results found for self-assembled monolayers on flat gold surfaces. We showed that macromolecular assemblies between proteins can be carried out in AAO nanopores that are lined with a biotin-DOPE containing lipid monolayer using streptavidin and biotinylated BSA. We finally used the high surface area of AAO to demonstrate that the His-tag protein PIGEA14 could be selectively extracted from a cell lysate solution and released using an EDTA containing, Ni-complexing buffer; a concept analogous to affinity chromatography. The use of OWS allowed us to follow *in-situ* the binding process of both a moderately large protein, streptavidin, and a relatively small protein, PIGEA14. In summary, we have shown that

using SUV spreading on AAO that was silanized with dodecyl-trichlorosilane can be used as an alternative functionalization technique to modify the surface of a nanoporous material, such as AAO, with laterally mobile functional surface groups. By reproducing the complex surface chemistry of small unilamellar liposomes, biologically relevant applications involving the reproduction of cell membrane composition onto the AAO can be investigated. We have shown that the ability to tune the surface density of reactive groups can be used in three-dimensions, similarly to planar solid-supported membranes. This type of functionalization is particularly interesting in the field of material science, where it could be used to template the growth of tailored inorganic, metallic, and polymeric one-dimensional nanotube structures in aqueous solution phase by Layer-by-Layer deposition techniques,[28-29] or the in-situ precipitation of inorganic precursors,[30] or the in-situ reduction of metal salts.[31]

8.4. Experimental Section

Materials. 1-Palmitoyl-2-oleoyl-*sn*-glycero-3-phosphocholine (POPC), 1,2-dioleoyl-*sn*-glycero-3-{(N-(5-amino-1-carboxypentyl)iminodiacetic acid)succinyl} nickel salt (DOGS-NTA(Ni)) and 1,2-dioleoyl-*sn*-glycero-3-phosphocholine (DOPC) were purchased from Avanti Polar Lipids Inc. (Alabaster, AL, USA). 2-(4,4-difluoro-5-methyl-4-bora-3a,4a-diaza-s-indacene-3-dodecanoyl)-1-hexadecanoyl-*sn*-glycero-3-phosphocholine (Bodipy DHPE) was purchased from Invitrogen (Eugene, OR, USA). Texas Red DHPE was purchased from Biotinum Inc. (Hayward, CA, USA). Disodium hydrogen phosphate, and oxalic acid dihydrate were purchased from AppliChem (Darmstadt, Germany). Perchloric acid (70 vol. %) and phosphoric acid (85 %) were purchased from Merck (Darmstadt, Germany). Sucrose was purchased from Acros Organics (Geel, Belgium). Ethanol was p.a. grade (VWR, France). The water used was ion exchanged and filtered using a Millipore system (MilliQ System from Millipore, Molsheim, France; specific resistance $R > 18$ MΩ cm^{-1}, pH ~ 5.5). High refractive index LaSFN9 glass substrates ($\varepsilon = 3.406$, $\lambda = 632.8$ nm) were obtained from Hellma Optik (Halle, Germany). Aluminum foils (0.5 mm thick, purity: 99.999 %) were purchased from Goodfellow (Huntington, UK). The UV-curable optical adhesive (NOA 83H) was purchased from Norland Products (Cranbury, NJ, USA). $CuCl_2$, dodecyl-trichlorosilane (C_{12}-TCS) and sodium chloride were purchased from Sigma Aldrich (St-Louis, MO, USA). Toluene was p.a. grade (VWR, France) and dried over 0.4 nm molecular sieves from Roth (Karlsruhe, Germany).

Scanning electron microscopy (SEM). SEM measurements were performed with a LEO Supra-35 SEM from Zeiss with acceleration voltages between 6 and 10 kV. 2 nm of Cr and 5 nm of Au were evaporated onto the samples before imaging.

Au evaporation and removal. Au and Cr were evaporated on a Bal-Tec MCS610 evaporator. For the metal coupling layer in OWS measurements, 2 nm of Cr and 25 nm of Au were evaporated on the AAO barrier layer.

Fluorescence microscopy. CLSM measurements were performed on an upright confocal microscope from Carl Zeiss MicroImaging GmbH (Jena, Germany), model LSM 710 Axio Examiner. A 63× magnification water immersion objective from Zeiss was used, WPlan-APO-CHROMAT (N.A. = 1.0). The upright epi-fluorescence optical microscope, model Olympus BX-51, was equipped with a filter for Nile Red (UMNG2), both purchased from Olympus Germany GmbH (Hamburg, Germany). A water immersion objective was used, 40× magnification from Olympus: LUMPlanF1 40XW (N.A. = 0.8). The evaporated metal layer between the alumina and the optical glue is required as a coupling layer for OWS measurements. This thin metal layer has also been found to be very useful for the microscopy measurements as it can be used as a positioning tool to locate the AAO in both the *X*-*Y* plane and the *Y*-*Z* plane.

Optical waveguide spectroscopy (OWS). OWS measurements of the AAO membranes prepared on glass slides were performed on a purpose-built setup. The glass-side was attached to the base of a symmetric LaSFN9 glass prism by optical immersion oil ($\varepsilon = 2.89$). The laser (λ = 632.8 nm) was incident through the prism-substrate assembly and reflected off the thin metal coupling layer in between the AAO and the optical adhesive as the incidence angle (θ) was varied. At specific θ's, determined by the thickness and the dielectric constant of AAO (ε_{AAO}), the laser was coupled into the AAO film and these waveguide modes were recorded as sharp minima in a reflectivity R vs. θ scan. Transverse electric (TE) and transverse electric (TM) modes were indexed according to the number of nodes in their electromagnetic field distributions. ε_{AAO} and the thickness of the AAO film, were obtained by fitting the angles of the waveguide mode reflectivity minima using Fresnel simulations carried out with Winspall program.[32] Tracking the coupling angle of a mode enables real time, *in situ* monitoring of changes in the dielectric constant of the film, i.e. adsorption kinetics.

Effective medium theory analysis. The ε_{AAO} measured by OWS includes contributions from the alumina, the pore-filling medium (e.g. water), and any organic thin layer coating

the pore surfaces (i.e. silanes, phospholipids). ε_{AAO} has an anisotropic component that is described by the infinite, prolate ellipsoid approximation within the Maxwell-Garnett theory, and well-described elsewhere.

$$\varepsilon_{AAO}^{\perp} = \varepsilon_{alumina} + f_{pore}(\varepsilon_{pore} - \varepsilon_{alumina}) \quad (1)$$

$$\varepsilon_{AAO}^{//} = \varepsilon_{alumina} \frac{\varepsilon_{alumina} + \tfrac{1}{2}(1 + f_{pore})(\varepsilon_{pore} - \varepsilon_{alumina})}{\varepsilon_{alumina} + \tfrac{1}{2}(1 - f_{pore})(\varepsilon_{pore} - \varepsilon_{alumina})} \quad (2)$$

where $\varepsilon_{AAO}^{\perp}$ and $\varepsilon_{AAO}^{//}$ are, respectively, the dielectric constant components normal and parallel to the AAO membrane surface, f_{pore} is the pore volume fraction within the AAO, $\varepsilon_{alumina} = 2.68$[12] is the dielectric constant of bulk anodic alumina at $\lambda = 632.8$ nm, and ε_{pore} is the (effective) dielectric constant within the pores. For a blank AAO film in water, $\varepsilon_{pore} = \varepsilon_{water} = 1.77$. With the addition of an organic film ($\varepsilon_{organic} = 2.1$) on the internal pore surfaces (e.g. lipid monolayer, protein), the volume within the pores is occupied by a combination of the organic material and the pore filling buffer. Recursively applying equations (1) and (2) for the organic-filled AAO pores, using a new effective ε'_{pore} for the pore interior, provides ε_{AAO} after molecular adsorption.

AAO membranes on glass supports. AAO anodized from bulk aluminum foils were mounted on LaSFN9 glass slides using an optical adhesive according to a previously reported technique. Briefly, AAO membrane thin films were fabricated by electrochemical anodization of aluminum foils, which were annealed at 450 °C overnight. Al foils were polished in a solution of perchloric acid/ethanol (1:4 *v*/*v*) for 15 min, 0 °C at 20 V. They were then anodized for 2 hours in 0.3 M oxalic acid, 1 °C at 40 V. The alumina was removed with a 5% *vol.* phosphoric acid solution for 2-3 h. As prepared Al foils were then anodized a second time for 1h30 to obtain the desired thickness of ~ 3.5 μm. Al was removed from the anodized foil by immersion of the anodized Al foil in a 17 g/L $CuCl_2$ in HCl/H_2O (1:1, 37 M stock HCl solution : H_2O) solution until the AAO became visible and no metal remained. Prior to Al removal, the AAO side was isolated from solution by immobilization onto a glass slide and sealed using epoxy adhesive. 2 nm of Cr and 25 nm of Au were evaporated onto the barrier layer of the AAO membranes. This underlying metal is required for OWS studies and also serves as a positioning tool to locate the transparent alumina using the microscope. Norland 83H adhesive was diluted in THF (1:10) and spin-coated on LASFN9 glass slides at 20 rpm for 2-3 seconds. The Au-coated AAO was glued, barrier side down, onto the glass side and UV-cured for 2 hours with a UV hand lamp, with

both lamps on (λ = 254 + 354 nm, 4 W) from Herolab (Wiesloch, Germany). d_0 for all AAO membranes was widened to the desired diameter by etching in (5 % *v/v*) phosphoric acid (85 % solution) diluted in water.

Small unilamellar vesicles (SUVs). The lipid mixture dissolved in chloroform together with the fluorescently labeled lipid marker. The solution, inside a glass test tube, was air dried and then left under vacuum in an oven at 60 °C for at least 3 hours. The phospholipids films were rehydrated by adding 1 mL of phosphate buffer (20 mM NaH_2PO_4/Na_2HPO_4, 100 mM NaCl, pH 7), left to hydrate for 30 min, vortexed and sonicated on ice using a tip-sonifier for 3 × 6 min periods, at 50-70 % power (sonifier tip, Bandelin Sonoplus, Berlin, Germany). POPC SUV solutions of 0.5 mg/ml were prepared for confocal fluorescence experiments and OWS experiments. Vesicle solutions were used immediately after sonication and sonicated every 15 min during the experiment. For time-resolved *z*-profile CLSM experiments with AAO (h = 10 μm), 10 mol % biotin-DOPE SUVs were left with the substrate overnight. The substrates were rinsed with buffer and atto-633 labeled avidin was added to for a concentration of about 0.2 μM. *Z*-stacks were taken using 50-100 nm thick slices over the 10-15 μm range that was scanned. For FRAP experiments, 0.1 mol % Bodipy DHPE labeled POPC SUVs were used.

C_{12}-TCS-silanization of AAO. The hydrophobic regions on the AAO substrates were obtained by O_2 plasma treatment for 2 min, followed by immersion in dry toluene in a desiccator under vacuum. O_2 plasma treatments were carried out with a Harrick plasma cleaner (Ithaca, NY, USA). Dodecyl-trichlorosilane (C_{12}-TCS), 2 vol. %, was added and left under vacuum for 15 min. The substrates were finally immersed in excess dry toluene, dried under N_2, and left overnight under vacuum at 65 °C.

Atto-633 streptavidin labeling. Streptavidin was labeled at a 1:1 ratio with Atto-633 NHS ester reagent. To a 0.5 mg/ml solution of protein in 20 mM phosphate buffer (pH 7, 100 mM NaCl), 5 μl of a 2 mg/ml solution of the NHS atto-633 dye in DMSO, dissolved in 100 μL of buffer, was added dropwise and stirred at room temperature for 4 hours. 2 fold excess Tris was added to quench the unreacted NHS reagent. The solution was separated with a sephadex G-25 from GE-healthcare (Buckinghamshire, UK) and the first blue color fraction was collected, corresponding to the protein.

Covalent biotin coupling. AAO substrates were O_2 plasma cleaned for 2 min immediately prior to silanization to increase the surface density of OH groups. The glass

slide substrates to be silanized were inserted into a glass staining jar and 50 µl of amino-propyl-triethoxysilane (APTES) were added in a glass test tube, inside the chamber. The container was covered with its glass cover and sealed using Scotch vacuum tape from 3M (St-Paul (MN), USA), left in the oven at 130°C for 10 min to warm, followed by 3 hours under vacuum. The amine-functionalized samples were cooled and a drop of dry ethanol, followed by 25 µl of EZ-Link NHS-LC-LC-biotin (Thermo Fisher) solution in dried DMF (2 mg/ml) were added and left under vacuum for 30 min, covering the AAO with a drop DMF. Substrates were then rinsed with dry DMF and ethanol.

PIGEA14 protein expression, purification and SDS-PAGE gel. The hexahistidine tagged protein PIGEA14 (polycystin-2-interactor, Golgi- and endoplasmatic reticulum-associated protein with a molecular mass of 14 kDa) was expressed in *E. coli* (BL21 (DE3) strain) containing the expression vector pET21b/CIP1 (116/493). Cells were grown to $OD_{595} = 0.5$ at 37 °C. Gene expression was induced by adding isopropyl-*β*-D-thiogalactopyranoside to a final concentration of 1 mM. After 4 h at 30 °C, the cells were harvested, centrifuged for 20 min and 4000 x g at 4 °C and re-suspended in lysis buffer (5 mM imidazole, 500 mM NaCl, 20 mM TRIS/HCl, pH 8). Subsequently, the cells were lysed by sonication and the lysates were centrifuged for 60 min and $10^5 \times$ g at 4 °C. The supernatant was applied to a Ni-iminodiacetic acid (Ni-IDA) column (Novagen, Darmstadt, Germany) that was firstly charged with 10 column volumes of 50 mM $NiSO_4$ and then equilibrated with 15 column volumes lysis buffer. PIGEA14 was eluted with 50 mM EDTA, 500 mM NaCl, 20 mM TRIS/HCl, pH 8. The concentration of PIGEA14 was determined by Bradford assay.

8.5. References

1. Ali, M.; Yameen, B.; Neumann, R.; Ensinger, W.; Knoll, W.; Azzaroni, O.; Biosensing and Supramolecular Bioconjugation in Single Conical Polymer Nanochannels. Facile Incorporation of Biorecognition Elements into Nanoconfined Geometries. *J. Am. Chem. Soc.* **2008,** *130*, 16351-16357.

2. Tamm, L. K.; McConnell, H. M.; Supported Phospholipid-Bilayers. *Biophys. J.* **1985,** *47*, 105-113.

3. Plant, A. L.; Supported Hybrid Bilayer Membranes as Rugged Cell Membrane Mimics. *Langmuir* **1999,** *15*, 5128-5135.

4. Brian, A. A.; McConnell, H. M.; Allogeneic Stimulation of Cyto-Toxic T-Cells by Supported Planar Membranes. *PNAS* **1984,** *81*, 6159-6163.

5. Rao, N. M.; Plant, A. L.; Silin, V.; Wight, S.; Hui, S. W.; Characterization of Biomimetic Surfaces Formed from Cell Membranes. *Biophys. J.* **1997,** *73*, 3066-3077.

6. Rao, N. M.; Silin, V.; Ridge, K. D.; Woodward, J. T.; Plant, A. L.; Cell Membrane Hybrid Bilayers Containing the G-Protein-Coupled Receptor Ccr5. *Anal. Biochem.* **2002,** *307*, 117-130.

7. Largueze, J. B.; El Kirat, K.; Morandat, S.; Preparation of an Electrochemical Biosensor Based on Lipid Membranes in Nanoporous Alumina. *Colloid. Surf. B* **2010,** *79*, 33-40.

8. Torchut, E.; Laval, J. M.; Bourdillon, C.; Majda, M.; Electrochemical Measurements of the Lateral Diffusion of Electroactive Amphiphiles in Supported Phospholipid Monolayers. *Biophys. J.* **1994,** *66*, 753-762.

9. Fliniaux, O.; Elie-Caille, C.; Pantigny, J.; Bourdillon, C.; Production of Microporous Aluminum Oxide Electrodes as Supports for Tethered Lipid Bilayers of Large Surface Area. *Electrochem. Commun.* **2005,** *7*, 697-702.

10. Kim, D. H.; Lau, K. H. A.; Robertson, J. W. F.; Lee, O. J.; Jeong, U.; Lee, J. I.; Hawker, C. J.; Russell, T. P.; Kim, J. K.; Knoll, W.; Thin Films of Block Copolymers as Planar Optical Waveguides. *Adv. Mater.* **2005,** *17*, 2442.

11. Knoll, W.; Interfaces and Thin Films as Seen by Bound Electromagnetic Waves. *Annu. Rev. Phys. Chem.* **1998,** *49*, 569-638.

12. Lau, K. H. A.; Tan, L. S.; Tamada, K.; Sander, M. S.; Knoll, W.; Highly Sensitive Detection of Processes Occurring inside Nanoporous Anodic Alumina Templates: A Waveguide Optical Study. *J. Phys. Chem. B* **2004,** *108*, 10812-10818.

13. Lazzara, T. D.; Lau, K. H. A.; Abou-Kandil, A. I.; Caminade, A. M.; Majoral, J. P.; Knoll, W.; Polyelectrolyte Layer-by-Layer Deposition in Cylindrical Nanopores. *Acs Nano* **2010,** *4*, 3909-3920.

14. Dai, J. H.; Baker, G. L.; Bruening, M. L.; Use of Porous Membranes Modified with Polyelectrolyte Multilayers as Substrates for Protein Arrays with Low Nonspecific Adsorption. *Anal. Chem.* **2006,** *78*, 135-140.

15. Takmakov, P.; Vlassiouk, I.; Smirnov, S.; Application of Anodized Aluminum in Fluorescence Detection of Biological Species. *Anal. Bioanal.Chem.* **2006,** *385*, 954-958.

16. Casanova, F.; Chiang, C. E.; Li, C. P.; Roshchin, I. V.; Ruminski, A. M.; Sailor, M. J.; Schuller, I. K.; Gas Adsorption and Capillary Condensation in Nanoporous Alumina Films. *Nanotechnology* **2008,** *19*.

17. Janshoff, A.; Dancil, K. P. S.; Steinem, C.; Greiner, D. P.; Lin, V. S. Y.; Gurtner, C.; Motesharei, K.; Sailor, M. J.; Ghadiri, M. R.; Macroporous P-Type Silicon Fabry-Perot Layers. Fabrication, Characterization, and Applications in Biosensing. *J. Am. Chem. Soc.* **1998,** *120*, 12108-12116.

18. Schwartz, M. P.; Alvarez, S. D.; Sailor, M. J.; Porous Sio2 Interferometric Biosensor for Quantitative Determination of Protein Interactions: Binding of Protein a to Immunoglobulins Derived from Different Species. *Anal. Chem.* **2007,** *79*, 327-334.

19. Schwartz, M. P.; Yu, C.; Alvarez, S. D.; Migliori, B.; Godin, D.; Chao, L.; Sailor, M. J.; Using an Oxidized Porous Silicon Interferometer for Determination of Relative Protein Binding Affinity through Non-Covalent Capture Probe Immobilization. *Phys. Status Solidi A* **2007,** *204*, 1444-1448.

20. Lau, K. H. A.; Duran, H.; Knoll, W.; In Situ Characterization of N-Carboxy Anhydride Polymerization in Nanoporous Anodic Alumina. *J. Phys. Chem. B* **2009,** *113*, 3179-3189.

21. Awazu, K.; Rockstuhl, C.; Fujimaki, M.; Fukuda, N.; Tominaga, J.; Komatsubara, T.; Ikeda, T.; Ohki, Y.; High Sensitivity Sensors Made of Perforated Waveguides. *Opt. Express* **2007,** *15*, 2592-2597.

22. Hotta, K.; Yamaguchi, A.; Teramae, N.; Properties of a Metal Clad Waveguide Sensor

Based on a Nanoporous-Metal-Oxide/Metal Multilayer Film. *Anal. Chem.* **2010,** *82*, 6066-6073.

23. Yamaguchi, A.; Hotta, K.; Teramae, N.; Optical Waveguide Sensor Based on a Porous Anodic Alumina/Aluminum Multilayer Film. *Anal. Chem.* **2009,** *81*, 105-111.

24. Spinke, J.; Liley, M.; Schmitt, F. J.; Guder, H. J.; Angermaier, L.; Knoll, W.; Molecular Recognition at Self-Assembled Monolayer - Optimization of Surface Functionalization. *J. Chem. Phys.* **1993,** *99*, 7012-7019.

25. Perez-Luna, V. H.; O'Brien, M. J.; Opperman, K. A.; Hampton, P. D.; Lopez, G. P.; Klumb, L. A.; Stayton, P. S.; Molecular Recognition between Genetically Engineered Streptavidin and Surface-Bound Biotin. *J. Am. Chem. Soc.* **1999,** *121*, 6469-6478.

26. Hidaka, S.; Konecke, V.; Osten, L.; Witzgall, R.; Pigea-14, a Novel Coiled-Coil Protein Affecting the Intracellular Distribution of Polycystin-2. *J. Biol. Chem.* **2004,** *279*, 35009-35016.

27. Behn, D.; Bosk, S.; Hoffmeister, H.; Janshoff, A.; Witzgall, R.; Steinem, C.; Quantifying the Interaction of the C-Terminal Regions of Polycystin-2 and Polycystin-1 Attached to a Lipid Bilayer by Means of Qcm. *Biophys. Chem.* **2010,** *150*, 47-53.

28. Cho, Y.; Lee, W.; Jhon, Y. K.; Genzer, J.; Char, K.; Polymer Nanotubules Obtained by Layer-by-Layer Deposition within Aao-Membrane Templates with Sub-100-Nm Pore Diameters. *Small* **2010,** *6*, 2683-2689.

29. Kim, D. H.; Karan, P.; Goring, P.; Leclaire, J.; Caminade, A. M.; Majoral, J. P.; Gosele, U.; Steinhart, M.; Knoll, W.; Formation of Dendrimer Nanotubes by Layer-by-Layer Deposition. *Small* **2005,** *1*, 99-102.

30. Bernecker, A.; Ziomkowska, J.; Heitmuller, S.; Wieneke, R.; Geyer, A.; Steinem, C.; Formation of Silica Precipitates on Membrane Surfaces in Two and Three Dimensions. *Langmuir* **2010,** *26*, 13422-13428.

31. Orendorff, C. J.; Alam, T. M.; Sasaki, D. Y.; Bunker, B. C.; Voigt, J. A.; Phospholipid-Gold Nanorod Composites. *Acs Nano* **2009,** *3*, 971-983.

32. Scheller, A. *Winspall*, 3.01; Max-Planck Institute for Polymer Research: Mainz, Gernany.

Acknowledgements. A.J. and C.S. gratefully acknowledge financial support from the DFG (JA 963/8-1 and STE 884/9-1 as well as the SFB 803). T.D.L. acknowledges the award of a doctoral scholarship from *le Fonds Québécois de la Recherche sur la Nature et les Technologies* (FQRNT) and additional financial support from the Göttingen Graduate School for Neurosciences and molecular Biosciences (GGNB).

8.6. Supporting information

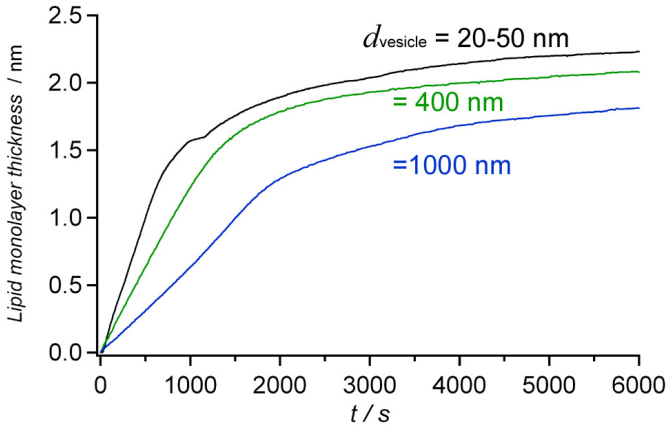

Figure 8.S1. POPC vesicle spreading kinetics on hydrophobically functionalized AAO for different vesicle sizes liposomes obtained by tip-sonication for, $d_{vesicle}$ = 20-50 nm, or by extrusion through a polycarbonate membranes for $d_{vesicle}$ = 400 nm and 1000 nm. Lipid concentrations were all 0.1 mg/ml, thus the kinetics are slower than in figure 1. The kinetics for larger vesicles are slower. However, all vesicles spread, even those larger than the pore diameter (d_0) to form a lipid monolayer on the AAO. Although the thickness using 1000 nm vesicles was lower, the thickness was comparable for the other sizes to the values shown in figure 8.2.

Chapter 9

Separating Attoliter-Sized Compartments using Fluid Pore-Spanning Lipid Bilayers

By:

Thomas D. Lazzara,[†] *Christian Carnarius*,[†] *Marta Kocun*,[§] *Andreas Janshoff*,[§] *Claudia Steinem*[†]

Graphical abstract:

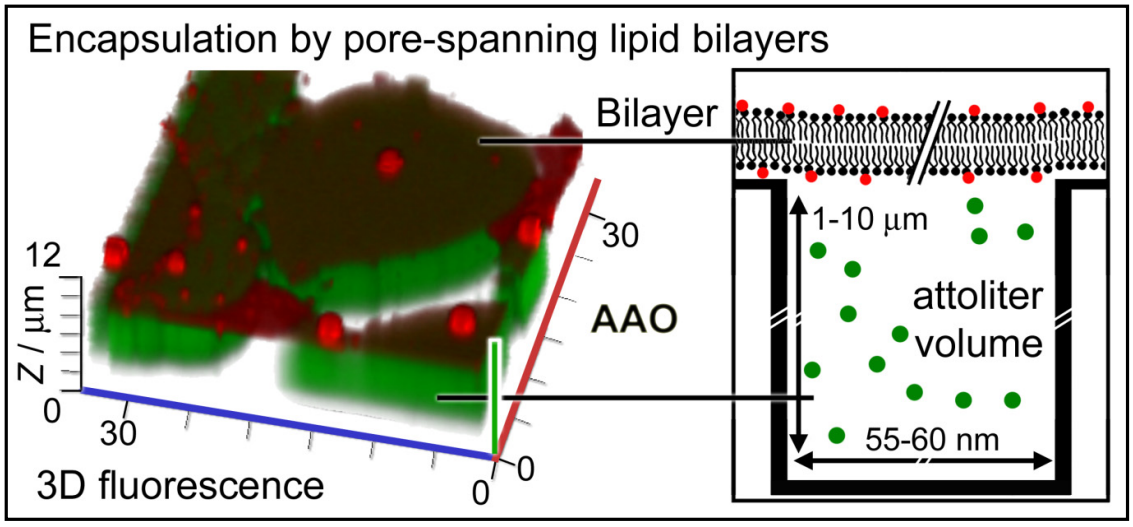

Manuscript submitted to:

ACS nano (ACS)

2011

[†] Institute of Organic and Biomolecular Chemistry, Tammannstrasse 2, 37077 Göttingen, Germany.

[§] Institute of Physical Chemistry, Tammannstrasse 6, 37077 Göttingen, Germany.

Abstract

Anodic aluminum oxide (AAO) is a porous material with aligned cylindrical compartments that was prepared with 55-60 nm diameter pores, several μm deep, resulting in an attoliter-sized volume for each pore. A protocol was developed to generate pore-spanning fluid lipid bilayers separating the attoliter compartments of the nanoporous material from the bulk solution, while preserving the optical transparency of the AAO. The AAO was selectively functionalized by silane chemistry to spread giant unilamellar vesicles (GUVs) resulting in large continuous membranes patches covering the pores. Formation of fluid single lipid bilayers through vesicle rupture could be readily observed by fluorescence videomicroscopy and further supported by conservation of membrane surface area, before and after GUV rupture. Fluorescence recovery after photobleaching showed that continuous bilayer patches were formed with a lipid lateral diffusion constant similar to those of solid supported membranes. The entrapment of molecules within the porous underlying cylindrical compartments as well as the exclusion of macromolecules from the nanopores demonstrate the barrier function of the pore-spanning membranes and was investigated in three-dimensions using confocal laser scanning fluorescence imaging.

Keywords: fluorescence microsocopy, fluorescence recovery after photobleaching, molecular encapsulation, nanoporous substrates, silane chemistry.

9.1. Introduction

The modification of solid surfaces with lipid monolayers and bilayers, obtained from the spreading of vesicles, requires careful attention to surface geometry and to surface chemistry.[1-2] Functionalization strategies are designed to specifically interact with either the hydrophilic phospholipid head-groups or with the hydrophobic lipid tails in order to form different solid supported membrane architectures.[1, 3] Prominent examples are hybrid lipid membranes,[4-5] where the lower mobile lipid leaflet is replaced with an immobile hydrophobic self-assembled monolayer. To decouple the membrane from the solid-support and increase the mobility of the lipids, polymer-cushioned bilayers[6-8] or tethered lipid bilayers[9-10] have been developed. Fluid bilayer membranes,[2, 11-15] where a thin water cushion separates the bilayer from the support,[14, 16-17] are typically formed on hydrophilic substrates such as SiO_2[18-20] and other hydroxyl-terminated surfaces.[21-22]

In recent years, as an improvement over solid supported membranes (SSMs), pore-spanning lipid membranes formed on porous substrates, have been introduced to probe the physical properties of lipid membranes and the functionality of different trans-membrane proteins.[23-25] Pore-spanning fluid membranes[26-28] are particularly attractive since they combine the mechanical stability of SSMs and the advantage of free-standing lipid membranes. However, until recently, many preparations relied mainly on gold-thiol chemistry to functionalize the porous surface interface with alkanethiols, fluorinated alkanethiols, phospholipid or cholesterol derivatives in order to form so called hybrid pore-spanning membranes.[25, 29-31] These membranes are hybrid on the pore-rim surface, i.e. composed of a covalently anchored self-assembled monolayer and a fluid lipid leaflet atop, while remaining homogeneous bilayers in the porous areas. Hybrid pore-spanning membranes have the advantage of being easily prepared on porous substrates, but are considerably pre-stressed because of the hydrophobic nature of the pore-rim tethering.[32] By using hydrophilic surfaces obtained through the deposition of SiO_2 directly onto a gold surface,[26] or directly using porous SiO_2 obtained by lithographical means,[33-35] fluid bilayer membranes have been generated. For generating pore-spanning membranes following preparation protocols based on vesicle spreading, the surface must be sufficiently reactive so that it induces liposome rupture, while simultaneously avoiding the rupture of the pore-spanning part.[33, 36] Furthermore, the surface chemistry inside the pores and on the pore rims needs to be distinct to avoid lining of the pore walls with lipids.[33, 37-39]

For generating pore-spanning membranes, pore arrays are prepared preferentially in silicon by photolithography.[31, 33-35, 40] Anodic aluminum oxide (AAO) is of particular interested as cylindrical non-intersecting pores with defined pore diameters are easily prepared without the use of photolithography. Another advantage is the fact that they are optically transparent,[41-43] when prepared with pore diameters below 100 nm, which allows for fluorescence microscopy detection of fluorescent molecules within the pores.[44-45] Optical transparency also implies that refractive index-based techniques can be used to study changes occurring within the nanopores.[43, 46-48] However, for such studies, metals such as gold cannot be used as they quench fluorescence,[49] and significantly decrease light propagation in thin nanoporous dielectric films even when trace amounts are incorporated within these.[50] Surface functionalizations that modify the material with reactive monolayers must be based on silanes or phosphonates, or alternatively inorganic oxides deposited by chemical vapor deposition or sputtering techniques.

In this study, we developed a method that allows nanoporous AAO substrates to be coated with a thin hydroxyl-terminated film at the interface between the nanoporous material and the bulk solution. We show that these functionalized AAO substrates allow rupturing of POPC GUVs forming pore-spanning bilayer patches with laterally mobile lipids. The optical transparency of the alumina substrate enabled us to visualize the entrapment of fluorescent molecules within the attoliter-sized compartments by confocal laser scanning microscopy.

9.2. Results and Discussion

9.2.1. Pore-Spanning Lipid Membranes on Functionalized AAO

We used AAO substrates with an inter-pore distance of p = 100 nm, and pore diameters that were enlarged to d_0 = 55-60 nm (figure 9.1A, top). The AAO thickness was adjusted to h = 3.5 or 7 µm (figure 9.1A, bottom). To produce pore-spanning membranes by phosphocholine lipid vesicle spreading on AAO substrates (figure 9.1B), vesicles have to adhere strongly onto the surface and then rupture to form a lipid bilayer that is located at the AAO/bulk interface. However, lipid vesicles adhere only weakly and do not rupture on untreated or plasma treated (oxygen or argon plasma) AAO surfaces (supplementary information, figure 9.S1A). This is likely attributable to the porosity of the AAO substrate (25-30%) that decreases the interfacial interaction area and also to the mixed chemical nature of the AAO surface, which has contributions from both, Al_2O_3 as well as surface incorporated oxalic acid anions.[51]

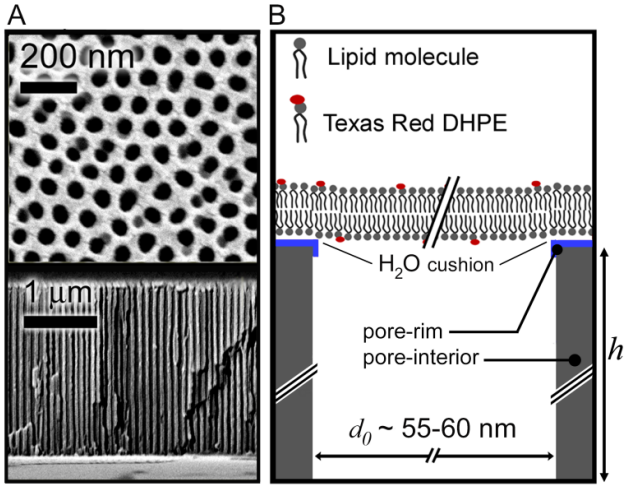

Figure 9.1. (**A**) Scanning electron microscopy images of an AAO substrate viewed from the top (top image) and the cross-section (bottom image). The AAO was mounted as a thin-film on a glass substrate using an optical adhesive. The layered structure, from top to bottom, in the cross section is: AAO/Cr-Au/adhesive on a glass substrate (glass not visible). (**B**) Schematic view of a solvent-free fluid pore-spanning membrane covering an AAO nanopore.

Chemical surface functionalization of AAO is therefore required to generate a hydrophilic surface that induces liposome rupture, while simultaneously ensuring that the substrate remains optically transparent. To generate the required functionality on the AAO substrates, they were first silanized with mercaptopropyltriethoxysilane by gas phase reaction, followed by a temporary thin gold layer (10-20 nm), thermally evaporated under vacuum. The gold layer served as a protective mask that prevented the removal of the pore-rim surface functionalization as reported previously.[52] The sample was then treated with O_2 plasma for 60 s, followed by argon plasma for 60 s, which removed the organosilane functionalization from the non-protected pore-interior surface by both, reactive oxygen radicals and physical ablation,[53-54] while the gold-coated pore-rim surface functionalization remained intact. Afterwards, the gold layer was removed by I_2/KI. The substrate was then rinsed, dried and treated with O_2 plasma for about 30 s to oxidize the ethoxy- and mercaptopropyl groups on the pore-rim surface without ablation. The substrates were incubated with fluorescently labeled (1 mol % Texas Red DHPE) giant unilamellar vesicles (GUVs) composed of POPC to investigate whether vesicles spread on such surfaces and whether they form pore-spanning membranes. GUVs have the advantage that they are relatively easy to image by optical microscopy and upon rupturing, form large membrane patches of several tens of μm^2. POPC GUVs, with 0.3 M sucrose in their interior, sedimented onto the functionalized AAO because of the outer solution being composed of lower density PBS buffer.

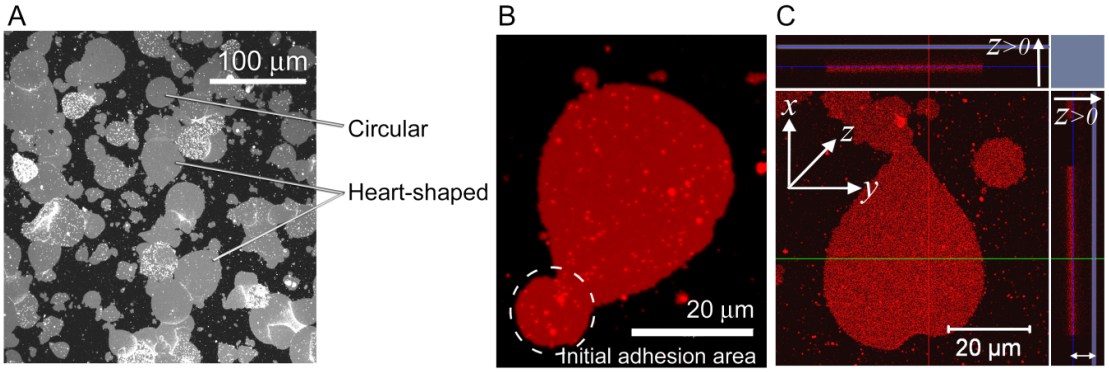

Figure 9.2. (**A**) Pore-spanning lipid bilayer patches obtained by the rupture of giant unilamellar POPC vesicles doped with 1 mol % Texas Red DHPE on functionalized AAO substrates. (**B**) Enlarged view of a heart-shaped lipid membrane patch, formed by vesicle rupture. (**C**) Confocal *z*-stack image illustrating the formation of a pore-spanning membrane atop functionalized AAO (d_0 = 60 nm, h = 3.5 µm). Scale bar also applies to the *z*-direction profiles with highlighted blue line delimiting the AAO bottom.

The process of vesicle attachment and spreading was followed by videomicroscopy. Typically, a GUV approached the AAO surface, then firmly attached and ruptured. The rupture step occurred within one video frame (30 frames/s) and thus could not be resolved in more detail with our camera (supplementary information, movie S1). Figure 9.2A shows the result of the spreading of fluorescently labeled GUVs on the functionalized porous AAO substrate. We observed two principle shapes of the planar pore-spanning membrane patches. While round and symmetric patches are seen, predominantly asymmetric heart-shaped patches were observed. The shape is a result of the rupture initiation site that is either at the top (round patch) of the adsorbed vesicle or closer to its side (heart-shape patch), as reported by Hamai et al.[13] In figure 9.2B, a typical non-circular patch is shown from rupture near the liposome's side, varying slightly from a heart-shape. The initial circular AAO adhesion area with the POPC GUV is also shown, and the deformation-induced rupture at the liposome side leads to vesicle spreading away from the adhesion area. Owing to the AAO transparency, *z*-stacks taken with confocal laser scanning fluorescence microscopy (CLSM) allowed us to show that pore-spanning membranes were formed, in contrast to membranes lining the pore-interior. The confocal *z*-stack image shown in figure 9.2C demonstrates that the fluorescence is only localized atop the AAO substrate (h = 3.5 μm), indicating that the membranes are localized only atop the AAO, as expected for pore-spanning membranes; the double arrow shows the AAO thickness and the blue line marks the pore bottoms.

We next asked the question, whether the planar membranes are continuous single bilayers and whether they experience an area expansion, i.e., whether they are pre-stressed, a phenomenon that was observed on hybrid pore-spanning membranes attached to hydrophobically functionalized pore rims.[32] Area expansion for hybrid systems occurs due the excess lipids being displaced by the immobile hydrophobic functionalization of the pore rims. For fluid non-tethering hydrophilic pore rims, area conservation is expected since the bilayer structure of the GUV is directly reproduced on the porous surface. The area of a pore-spanning membrane patch, as observed in fluorescence imaging, was compared to the value expected from the calculated area of a GUV before its rupture. Figure 9.3A shows a fluorescence image of a POPC GUV before and after rupture. An outline delimiting the size of the final membrane patch is drawn. For this particular GUV, we found that the surface area after rupture, calculated by pixel analysis was 93 μm^2 and agreed with the predicted GUV surface area, estimated from the diameter of the GUV, which was 103 μm^2. Lipid membrane surface area was conserved in agreement with the formation of a fluid bilayer.

The error associated with the lipid membrane area, for recorded rupture events by confocal fluorescence, was about 10 % between estimated and calculated areas (n = 5). The error mainly arises from the uncertainty in the estimation of the vesicle diameter.

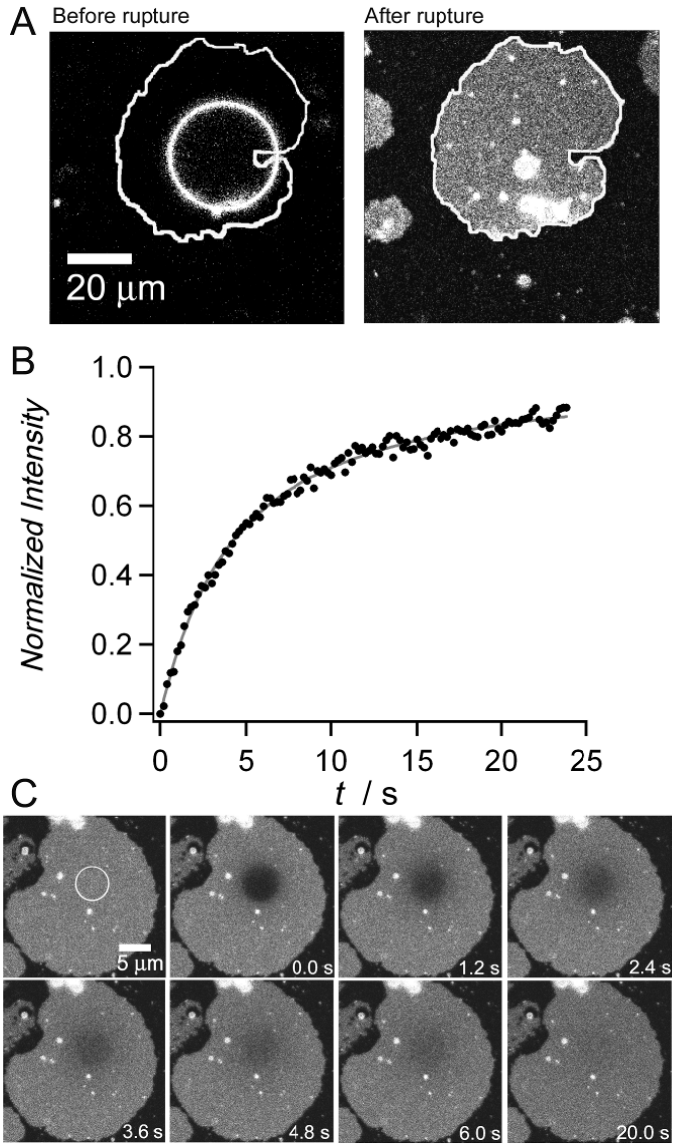

Figure 9.3. (**A**) CLSM image taken at approximately the center focal plane of a POPC GUV right before its adsorption and rupture on hydrophilic AAO. Lipid membrane area after rupture (93 µm^2) is preserved in comparison to the area of the vesicle (103 µm^2) before rupture, which agrees with the vesicle rupture mechanism leading to fluid lipid bilayers with continuous double-leaflet structure. (**B**) Recovery curve of a FRAP experiment performed on a membrane patch obtained from Bodipy DHPE (0.1 mol %) labeled POPC GUVs. A diffusion coefficient of 3.9 ± 0.4 µm^2/s was obtained for the labeled lipids, with an immobile fraction of 5 %. (**C**) Images for the FRAP experiment in (B) showing uniform fluorescence recovery after photobleaching.

To further confirm that continuous planar and fluid pore-spanning lipid bilayers are formed by this method, we performed fluorescence recovery after photobleaching (FRAP) experiments. POPC GUVs labeled with 0.1 mol % of Bodipy DHPE were used to form lipid bilayer patches on the functionalized AAO. Figure 9.3B shows a typical fluorescence recovery curve with a fit to the data, following the theory of Axelrod et al.[55] An average mobile fraction of 90 ± 5 %, and a diffusion coefficient of 3.8 ± 0.8 $\mu m^2/s$ (n = 6) were obtained for POPC bilayers. The small immobile fraction indicates that both, the top and bottom leaflet of the bilayer are mobile, while the diffusion coefficient is characteristic for a continuous solvent-free fluid lipid bilayer on a hydrophilic surface.[1, 56]

9.2. Macromolecular Exclusion and Molecular Encapsulation by Pore-Spanning Membranes

GUVs of 5-25 μm in diameter rupture to form pore-spanning membranes that cover an area of 25-600 μm^2 in area. These patches effectively separate thousands of individual attoliter compartments (AAO nanopores) from the outer medium. Furthermore, the individually covered pores are isolated from each other because of the cylindrical geometry and because of the fact that the AAO pores are closed at the substrate bottom (figure 9.1A).

To prove the integrity of the lipid bilayer patches, we investigated whether the pore-spanning membranes exclude macromolecules from entering and adsorbing into the nanopores. We used fluorescently labeled avidin (Alexa-488 avidin), which adsorbs electrostatically onto the AAO porous surface (supplementary information, figure 9.S2). Pore-spanning membranes composed of POPC and doped with Texas Red DHPE were first formed and then, Alexa-488 avidin was added. Fluorescence images revealed that in the regions, where pore-spanning membranes were formed, Alexa-488 fluorescence was not observed and thus remained dark. In contrast, the areas that were not covered by a membrane showed a bright green fluorescence because of protein adsorption onto the inner pore walls (figure 9.4A). Figure 9.4B schematically depicts the two possible protein adsorption scenarios: with and without a pore-spanning membrane. In figure 9.4C, two different focal plane views are shown: at the top AAO interface with the bulk solution where the lipid membrane is formed (top image) and within the AAO were no fluorescence was observed since neither lipids nor proteins were present within the PBS buffer filled AAO nanopores (bottom image). The z-projections clearly show that 1) the lipid fluorescence from the pore-spanning membrane is located at the top AAO surface only, 2) avidin can diffuse throughout the depth of the AAO substrate, and 3) fluorescently labeled

proteins are excluded from entering the pores that are covered by a pore-spanning lipid bilayer.

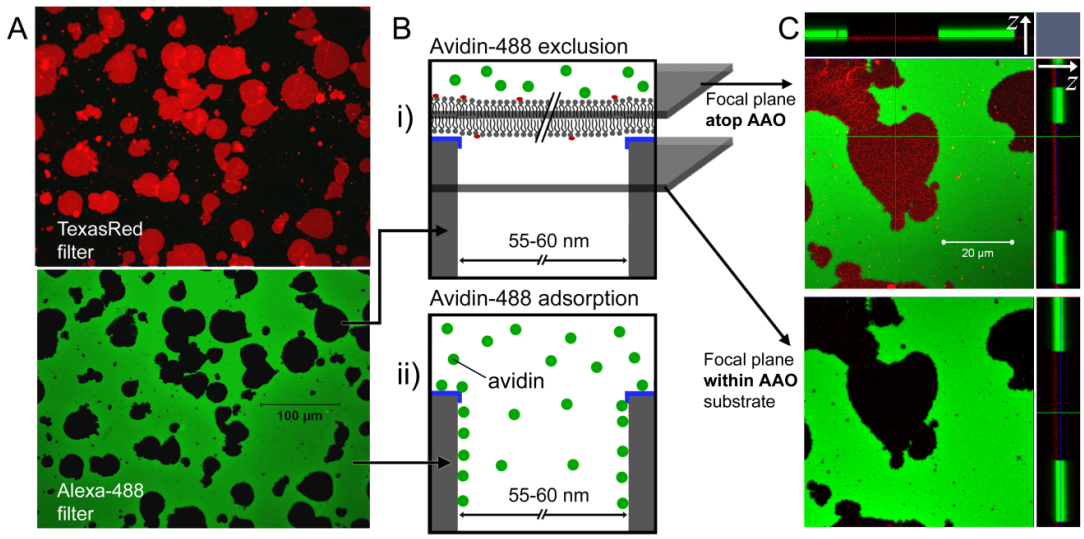

Figure 9.4. (**A**) CLSM images of AAO with POPC pore-spanning membranes (top image: red filter) that exclude Alexa-488 avidin from entering the pores (bottom image: green filter), fluorescence in same area, but recorded using two filters. The protein is either excluded (dark) or adsorbed within unblocked nanopores (green). Pore-spanning membrane fluorescence correlates with the absence of protein fluorescence. (**B**) Two scenarios: i) pore-spanning membrane blocks avidin entrance within pores and ii) adsorption in uncovered pores. (**C**) Composite *z*-stack images (total *z*-distance: 15 µm) of a pore-spanning POPC bilayer preventing avidin entrance into the underlying pores (black areas). Top image: lipid membrane is located at the interface between the AAO and the bulk solution, showing both Texas Red DHPE and Alexa-488 avidin fluorescence in the overlay. Bottom image: taken within the center focal plane of the AAO film, where Texas Red DHPE fluorescence is no longer observed. Top and right side images are line profiles (shown in top frame) in the *z*-direction and clearly show that the membrane prevents the fluorescently labeled proteins from entering the pores.

Since the pore-spanning membranes served as a permeability barrier, we exploited their insulating nature to entrap small water-soluble molecules inside the pores, which do not adsorb onto the pore walls. Pore-spanning membranes were produced by spreading Texas Red DHPE doped POPC GUVs on the functionalized AAO surface in the presence of pyranine dye (10 mM) in PBS buffer. The sample was then rinsed with buffer to remove the pyranine from the solution. Fluorescence images (figure 9.5A) demonstrate that in the regions, where pore-spanning membranes were formed, pyranine molecules remained entrapped within the pores. These areas show persistence fluorescence after rinsing for more than 48 hours. In areas where the membrane was not pore-spanning but still remained on the pore-rims, the Texas Red DHPE fluorescence was still visible, but the pyranine fluorescence was absent because the fluorophore were removed from the pores during rinsing. We also collected *z*-stacks, showing the fluorescence distribution in the vertical direction across these patches (figure 9.5B).

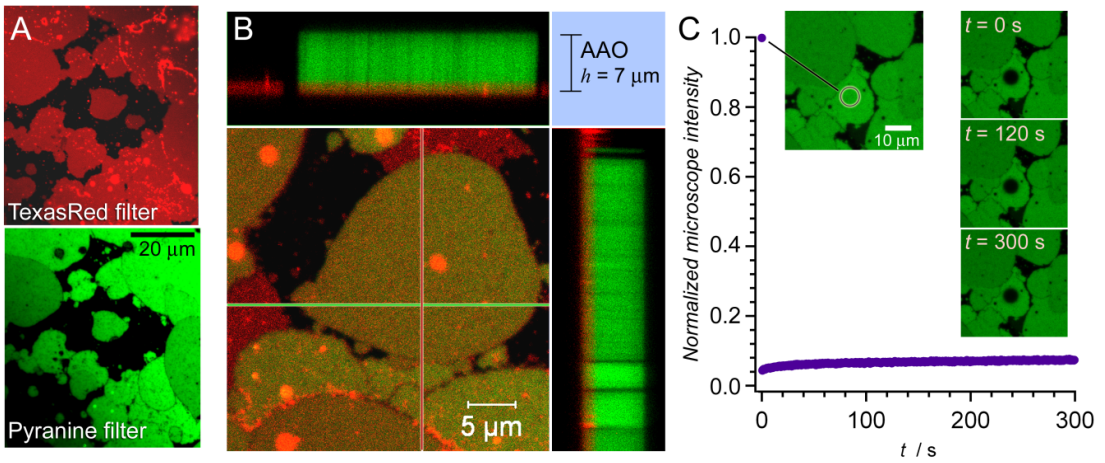

Figure 9.5. (**A**) 2D confocal fluorescence images of pore-spanning POPC lipid membranes with pyranine entrapped in the AAO pores. The pyranine fluorescence (bottom, green) correlates with the position of the POPC membranes (top, red). (**B**) 3D *z*-stack image of the membrane encapsulating dye molecules within the cylindrical nanopores of AAO (h = 7 µm). Only membrane-covered pores can entrap the pyranine dye. (**C**) Fluorescence recovery of the interior of the bleached nanoporous area filled with pyranine dyes. Each nanopore is isolated from its neighbors and therefore, the fluorescence cannot recover. Inset shows the lack of fluorescence recovery at t = 0, 120 and 300 s (right).

The localized fluorescence from the lipid membrane covering the top of AAO interface can be observed, independently of the fluorescence from the encapsulated pyranine dyes that fluoresces throughout the 7 µm thick AAO. Since the cylindrical pores of AAO are not inter-connected, each cylindrical pore is physically isolated from its neighbor. Therefore, the pyranine fluorescence in photobleached area with encapsulated pyranine dyes does not recover with time (figure 9.5C). In fact, fluorescence recovery was not observed within the bleached pores, even after 300 s, consistent with the assumption that the pyranine is localized in individually isolated pores. The small initial fluorescence recovery observed was due to unbleached dyes along the pore axis that diffused back into the focal plane. Interestingly, the pyranine fluorescence images also show that neighboring lipid membrane patches are discontinuous, showing interfacial faults between them. Each formed membrane patch corresponds to a single ruptured GUV and the dye does not remain entrapped in the pores lying at the interface between those patches. This observation implies that the membranes in those regions are not pore-spanning. Membrane self-healing over those uncovered pores, at the interface between patches, is prevented by the underlying porosity of the substrate. If a solvent-free pore-spanning membrane ruptures, its reformation is improbable since lipids tend to go around surface defects, rather over these (pores in this case).[57] This is in contrast to what has been observed for fluid SSMs where defects are easily healed by lateral merger of membrane edges,[58] leading to uniform surface bilayer coverage.

9.2.3. Impact of Surface Functionalization on Pore-Spanning Membrane Formation

We found that the intermediate gold-protective step, followed by O_2 and Ar plasma treatments, was essential for the vesicles to rupture and form pore-spanning membranes. If we applied only the O_2 plasma to silanized AAO samples, vesicles ruptured forming irregular patches. Confocal fluorescent *z*-stacks showed that these irregular domains had lipids that lined the inside of the nanopores, as well as having some areas where the lipid membranes remained pore-spanning (supplementary information, figure 9.S1B). Fluorescently labeled Texas Red DHPE lipids were also located within the interior of the AAO porous film, rather than being localized only at the AAO top interface, which was in clear contrast to the pore-spanning lipid membrane patches shown in the fluorescence images of figures 9.4 and 5. Argon plasma has been shown to modify surface films by physical ablation, while the reactive species present in O_2 plasma oxidize organic functional groups. By using both Ar and O_2 plasma, while protecting the pore-rim surface with the temporary gold layer, we believe that the pore-interior silanization was sufficiently removed, such that the hydrophilic SiOH functionalization was predominantly on the pore rims.

After removal of the protective gold layer, a short O_2 plasma treatment of 30 s was required to ensure that the organic functional groups on the pore-rim surface, i.e., ethoxy and mercaptopropyl, were oxidized to silanol groups. This step, prior to addition of GUVs, ensured that the pore-rim surface was hydrophilic. Estimation of the contact angles formed by a PBS buffer drop on silanized glass slides modified with three different ethoxysilanes (mercaptopropyl-triethoxysilane (SHTES), aminopropyl-triethoxysilane (APTES) or tetraethoxysilane (TEOS)) showed that the surface was hydrophobic directly after silanization, with a contact angle of about 80° for all three substrates. After 10 s of O_2 plasma treatment, all three surfaces regained their hydrophilic character and the water drop wet the surface with a contact angle < 5° (supplementary information, figure 9.S2). As we hypothesized that all organic groups are oxidized by the plasma treatment resulting in a hydrophilic surface, we repeated the selective functionalization procedure of AAO with both TEOS and APTES and found indeed no difference in the spreading behavior of GUVs on the nanoporous substrate. This implies that only the inorganic SiOH groups remain on the surface and are pivotal for vesicle spreading. In general, we believe that SHTES was a better choice of silane because it produces a lower degree of vertical polymerization.

To further support the idea that a high density of OH-groups on the pore rims is required for the vesicles to spread, we produced an analogous surface functionalization by directly modifying the pore-rim surface of AAO with a mercaptoethanol self-assembled monolayer on gold (figure 9.6). We evaporated 2 nm of Cr and 15 nm of Au onto AAO with d_0 = 60 nm. Under the same experimental conditions as presented in figure 9.4, POPC pore-spanning membranes patches, obtained from GUVs, were capable of excluding Alexa-466 avidin proteins, as shown in the confocal *z*-stack image in figure 9.6. As gold quenches the fluorescence of material within a range of about 15 nm, only material that is further than about 20 nm from the gold becomes visible. Thus, the fluorescently labeled pore-spanning membranes cannot be detected by fluorescence imaging. Contrasting figure 9.4 and figure 9.6 illustrates the advantage of using silane-chemistry vs. thiol-chemistry on gold to functionalize the AAO pore rims. An evaporated thin gold layer decreases the optical transparency, which decreases the visibility of processes occurring within the AAO, but more importantly, gold does not allow imaging of pore-spanning membrane formation and potential membrane-bound components.

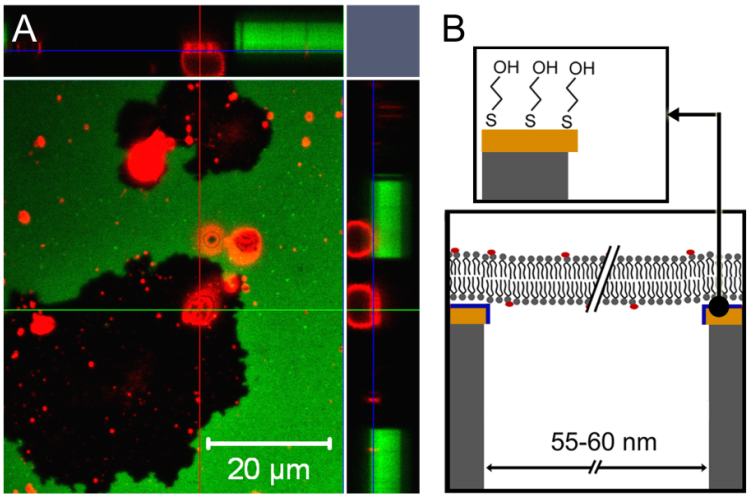

Figure 9.6. (**A**) Pore spanning membranes prepared from POPC GUV spreading on AAO functionalized with mercaptoethanol on gold. The membrane excludes Alexa-488 labeled avidin from adsorbing within the AAO nanopores visible as black patches (experimental conditions as in figure 9.4). (**B**) Illustration of the pore-rim surface functionalization obtained by evaporation of 2 nm of Cr and 15 nm of Au onto the AAO, followed by a mercaptoethanol self-assembled monolayer. Alexa-488 avidin exclusion was observed but gold quenched the fluorescence of the pore-spanning membrane.

This experiment also shows that differentiating pore-rim and pore-interior surface chemistries can contribute to the formation of stable pore-spanning membranes. We envision that the AAO surface after the silane-based functionalization scheme (figure 9.7A) has a surface functionalization as depicted in figure 9.7B. The pore-rim surface exhibits a

higher density of silanol groups that facilitates the rupture of phospholipid liposomes. Given that the pore-interior surface was exposed to longer periods of plasma treatments, with both O_2 and Ar, the silane functionality was possibly sufficiently ablated that the surface was less active towards lipids. The final substrates therefore behaved similarly to the gold-functionalized substrates, but with the invaluable advantage of optical transparency.

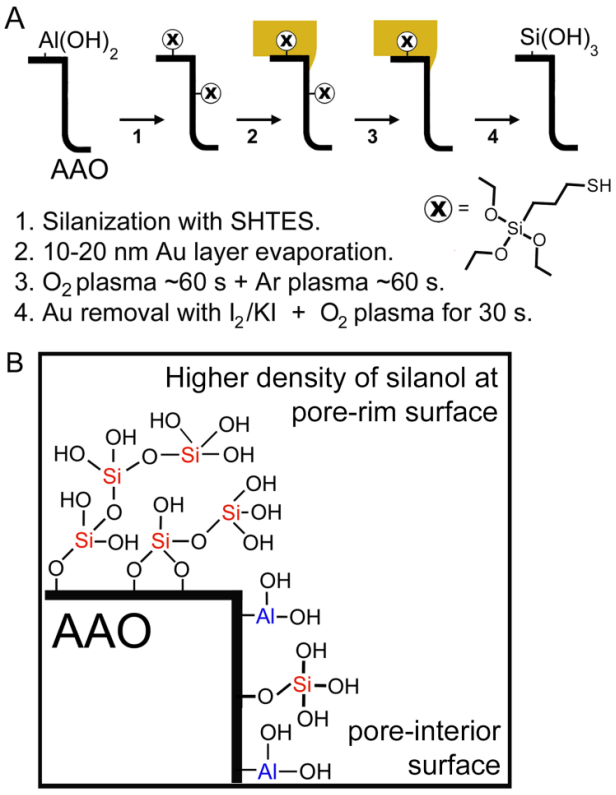

Figure 9.7. (**A**) AAO functionalization protocol: 1) AAO is silanized with SHTES, 2) a thin Au layer (protective mask) is evaporated, 3) the pore-interior surface is ablated using both O_2 and Ar plasma and 4) the Au is removed and the pore-rim surface are rendered hydrophilic with a short O_2 plasma treatment. (**B**) The final AAO substrates have hydrophilic pore rims and most importantly, remain optically transparent.

9.3. Conclusions

We presented a method that allowed the preparation of fluid laterally mobile pore-spanning membranes on optically transparent nanoporous anodic aluminum oxide (AAO) substrates, with pore diameters of 55-60 nm, by vesicle spreading. A hydrophilic hydroxyl-terminated pore-rim surface functionalization was developed that was used to induce giant vesicle rupture in the same manner as observed for native planar SiO_2 substrates. The method produced stable and solvent-free pore-spanning lipid bilayers separating attoliter-sized compartments. Owing to the optical transparency of the functionalized AAO

substrates, the deposition and encapsulation of material within the porous matrix could be readily followed by confocal laser scanning microscopy. These pore-spanning lipid membranes on AAO provide a membrane architecture that is particularly interesting because it isolates the pore-interior chemical environment of several thousand AAO nanopores from the bulk solution while remaining optically transparent and as such offers a way to study both membrane permeability properties and transport properties across functional membrane components such as channel proteins.

9.4. Materials and Methods

Materials: 1-Palmitoyl-2-oleoyl-*sn*-glycero-3-phosphocholine (POPC) was purchased from Avanti Polar Lipids Inc. (Alabaster, AL, USA). Lyophilized Alexa-488 labeled avidin (1 mg) and 2-(4,4-difluoro-5-methyl-4-bora-3a,4a-diaza-s-indacene-3-dodecanoyl)-1-hexadecanoyl-*sn*-glycero-3-phosphocholine (Bodipy DHPE) was obtained from Invitrogen (Eugene, OR, USA). Texas Red DHPE was from Biotinum Inc. (Hayward, CA, USA). Disodium hydrogen phosphate, and oxalic acid dihydrate were purchased from AppliChem (Darmstadt, Germany). Perchloric acid (70 %) and phosphoric acid (85 %) were from Merck (Darmstadt, Germany). Sucrose was purchased from Acros Organics (Geel, Belgium). Ethanol was p.a. grade (VWR, Germany). The water used was ion exchanged and filtered using a Millipore system (MilliQ System from Millipore, Molsheim, France; specific resistance $R > 18$ MΩ cm^{-1}, pH ~ 5.5). Aluminum foils (0.25 mm thick, purity: 99.999 %) were purchased from Goodfellow (Huntington, UK). The UV-curable optical adhesive (NOA 83H) was obtained from Norland Products (Cranbury, NJ, USA). $CuCl_2$, and sodium chloride were purchased from Sigma Aldrich (St-Louis, MO, USA). Mercaptopropyl-triethoxysilane (SHTES) was purchased from ABCR (Karlsruhe, Germany). Indium tin oxide (ITO) slides were from Präzisions Glas & Optik GmbH (Iserlohn, Germany). Pyranine was purchased from Acros organics (Geel, Belgium), aminopropyltriethoxysilane (APTES) from Fluka (Steinheim, Germany) and tetraethoxysilane (TEOS) from Alfa Aeser (Karlsruhe, Germany).

Au evaporation and removal: Au and Cr were evaporated on a Bal-Tec MCS610 evaporator equipped with a Bal-Tec QSG100 quartz film thickness monitor. For the metal layer at the AAO bottom, 2 nm of Cr and 25 nm of Au were evaporated on the AAO barrier layer. When Au was used as a temporary protective mask for functionalization, only 10-20 nm of Au were evaporated directly onto the AAO pores at a high deposition rate, 1.0 nm s^{-1}.

Plasma treatments: Argon and oxygen plasma treatments were carried out with a Harrick plasma cleaner (Ithaca, NY, USA), under high power. The vacuum chamber was flushed with the desired gas and evacuated with an oil-pump for 2 minutes. The plasma was turned on and the gas pressure in the chamber was increased to obtain a faint color plasma. Ar (purple) plasma treatments were carried out for 60 s and O_2 plasma (faint blue) treatments for 60 and 30 s; the duration was calculated using the initiation of the colored plasma as $t = 0$.

Deposition of AAO membranes on planar glass supports: AAO anodized from bulk aluminum foils were mounted on microscope glass slides using an optical adhesive according to a previously reported technique.[59] Briefly, AAO membrane thin films were fabricated by electrochemical anodization of aluminum foils, which were annealed at 500 °C overnight. Al foils were electrochemically polished first in a solution of concentrated H_2SO_4, 85% H_3PO_4 and H_2O (1:1:1) at 25 V. Secondly, the Al foils were polished in a solution of perchloric acid/ethanol (1:4, *v*/*v*) for 15 min, 0 °C at 20 V. They were then anodized for 2 h in 0.3 M oxalic acid, 1 °C at 40 V. The alumina was removed with a 5 vol. % phosphoric acid solution for 2-3 h. Al foils were then anodized a second time for 1 h 35 min to obtain the desired thickness of 3.5 μm or for 3.0 h to obtain 7 μm thick AAO. Al was removed from the anodized foil by immersion of the anodized Al foil in a 17 g/L $CuCl_2$ in HCl/H_2O (37 M HCl and H_2O, 1:1) solution until the AAO became visible and no metal remained. Prior to Al removal, the AAO side was isolated from solution by immobilization onto a glass slide and sealed using epoxy adhesive. 2 nm of Cr and 25 nm of Au were evaporated onto the barrier layer of the AAO membranes. The metal does not enter the pores and lies under the AAO barrier layer. The metal serves as a useful positioning tool to locate the transparent alumina using the microscope. Norland 83H adhesive was diluted in THF (1:10) and spin-coated on LASFN9 glass slides at 20 rpm for 2-3 seconds. The Au-coated AAO was glued, barrier side down, onto the glue covered glass side and UV-cured for 2 h with a UV hand lamp, with both lamps on (λ = 254 + 354 nm, 4 W) from Herolab (Wiesloch, Germany). The pore diameter (d_0) for all AAO membranes was widened to the desired diameter by etching in 5 vol. % phosphoric acid ($\Delta d_0 \sim 0.75$ nm·min^{-1}).

AAO silanization, selective functionalization: AAO substrates were O_2 plasma cleaned for 60 s immediately prior to gas-phase silanization to increase the surface density of OH-groups. The glass slide substrates to be silanized were inserted into a glass staining jar and 50 μL of mercaptopropyl-triethoxysilane (SHTES) were added in a glass test tube, inside the chamber. When performing the tests with APTES and TEOS, the same volume was

added. The container was covered with its glass cover and sealed using Scotch vacuum tape from 3M (St-Paul, MN, USA), left in the oven at 130 °C for 5 min to warm, followed by 3 h under continuous vacuum. The functionalized samples were cooled. Directly after silanization (step 1), 10-20 nm of Au were evaporated onto the substrates (step 2). They were then treated with O_2 plasma for 60 s, followed by 60 s of Ar plasma (step 3). The substrates could be stored for several weeks in this condition. Before use, the Au layer was removed with I_2/KI solution (50 g/L KI, 12.5 g/L I_2), for 20-30 seconds. The substrate was then rinsed, dried, and O_2 plasma treated for 30 s (step 4). These substrates were then used directly

Fluorescence microscopy: CLSM measurements were performed on an upright confocal microscope LSM 710 from Carl Zeiss MicroImaging GmbH (Jena, Germany). A 63× water immersion objective (WPlan-APO-CHROMAT (N.A. = 1.0)) from Zeiss was used. The upright epi-fluorescence optical microscope BX-51, was equipped with a filter for Nile Red (UMNG2), (Olympus Germany GmbH, Hamburg, Germany) was used for videomicroscopy. A water immersion objective was used, 40× magnification from Olympus: LUMPlanF1 40XW (N.A. = 0.8). The *z*-stack images were obtained by acquiring multiple confocal *x*-*y* focal plane images along the vertical *z*-direction, which allow for a three-dimensional image reconstruction. Slices of about 100 nm thick over a 12-20 μm range were acquired with an axial resolution of 0.9 μm.

Giant unilamellar vesicles (GUVs): GUVs were prepared by electroformation.[60] Briefly, 50 μL of a 1 mg/mL POPC lipid solution (1 mol % Texas Red DHPE) was left to dry on ITO slides and then spread uniformly on the slide using the length of a sterile needle. The slides were left at 64 °C under vacuum for at least 3 h. The chamber was assembled using conductive copper tape at the ITO slide edges and a 1 mm thick square Teflon spacer between them (volume: 1.7 mL) and was filled with 0.3 M sucrose solution through an opening. The cycle was carried out at 12 Hz with voltage increments every 60 s for 3 h: starting at 0.05 V, followed by 0.01 V steps until 0.2 V, finally 0.1 V steps until a constant 1.6 V was applied for the remaining duration. Afterwards, a 5 Hz square wave was applied for 10 min. The osmolarity of the sucrose solution was 0.25-0.30 Osm/L and was measured with a cryoscopic osmometer, model Osmomat 030 from Gonotec (Berlin, Germany). GUVs were stored at 4 °C and used for no longer than 2 weeks. The AAO was rinsed with p.a. ethanol, and then the measuring chamber was rinsed and filled with 1.5 mL of a PBS buffer (20 mM NaH_2PO_4/Na_2HPO_4, 100 mM NaCl, pH 7.2) before adding the GUVs (measured osmolarity: 0.26 Osm/L). The heavier sucrose-filled vesicles sink to the

substrate. For FRAP experiments, 50 µL of GUV solution was slowly added and incubated for 1 h. The chamber was then carefully rinsed with an equal volume of PBS buffer and the sample observed under the microscope. FRAP experiments were performed by CLSM on circular regions of interest using POPC membranes doped with 0.1 mol % Bodipy DHPE. For the Alexa488 avidin exclusion experiments, Texas Red DHPE labeled GUVs (25 µL) were added to the PBS buffer-filled measuring chamber and left to incubate for 30 min. The chamber was rinsed until about 200 µl remained and 0.05 mg of the fluorescently labeled Alexa-488 avidin was added and left to incubate for 1 h. The substrate was gently rinsed with buffer and observed using CLSM. *Z*-stacks were acquired with 1.0 a.u. setting (1.4 µm pinholes), which reduced the fluorescence signal, but increases spatial resolution. For the molecular encapsulation experiments, 200 µL of 100 mM pyranine solution in PBS buffer was diluted in 1.8 mL of PBS buffer in the measuring chamber and mixed. 50 µL of GUV solution was added and incubated for 1 h. After spreading, the solution was rinsed extensively to remove the pyranine dye, until the background fluorescence disappeared. The encapsulated dye was observed as bright fluorescence areas, as deep as the AAO thickness. Furthermore, pyranine fluorescence was superimposed the membrane fluorescence only if the pore-spanning membrane was non-ruptured.

9.5 References

1. Castellana, E. T.; Cremer, P. S. Solid Supported Lipid Bilayers: From Biophysical Studies to Sensor Design. *Surf. Sci. Rep.* **2006,** *61*, 429-444.

2. Richter, R. P.; Berat, R.; Brisson, A. R. Formation of Solid-Supported Lipid Bilayers: An Integrated View. *Langmuir* **2006,** *22*, 3497-3505.

3. Sackmann, E. Supported Membranes: Scientific and Practical Applications. *Science* **1996,** *271*, 43-48.

4. Hubbard, J. B.; Silin, V.; Plant, A. L. Self-Assembly Driven by Hydrophobic Interactions at Alkanethiol Monolayers: Mechanism of Formation of Hybrid Bilayer Membranes. *Biophys. Chem.* **1998,** *75*, 163-176.

5. Plant, A. L. Supported Hybrid Bilayer Membranes as Rugged Cell Membrane Mimics. *Langmuir* **1999,** *15*, 5128-5135.

6. Sackmann, E.; Tanaka, M. Supported Membranes on Soft Polymer Cushions: Fabrication, Characterization and Applications. *Trends in Biotechnol.* **2000,** *18*, 58-64.

7. Tanaka, M.; Sackmann, E. Polymer-Supported Membranes as Models of the Cell Surface. *Nature* **2005,** *437*, 656-663.

8. McBee, T. W.; Wang, L. Y.; Ge, C. H.; Beam, B. M.; Moore, A. L.; Gust, D.; Moore, T. A.; Armstrong, N. R.; Saavedra, S. S. Characterization of Proton Transport Across a Waveguide-Supported Lipid Bilayer. *J. Am. Chem. Soc.* **2006,** *128*, 2184-2185.

9. Naumann, R.; Schiller, S. M.; Giess, F.; Grohe, B.; Hartman, K. B.; Karcher, I.; Koper, I.; Lubben, J.; Vasilev, K.; Knoll, W. Tethered Lipid Bilayers on Ultraflat Gold Surfaces. *Langmuir* **2003,** *19*, 5435-5443.

10. Erbe, A.; Bushby, R. J.; Evans, S. D.; Jeuken, L. J. C. Tethered Bilayer Lipid Membranes Studied by Simultaneous Attenuated Total Reflectance Infrared Spectroscopy and Electrochemical Impedance Spectroscopy. *J. Phys. Chem. B* **2007,** *111*, 3515-3524.

11. Anderson, T. H.; Min, Y. J.; Weirich, K. L.; Zeng, H. B.; Fygenson, D.; Israelachvili, J. N. Formation of Supported Bilayers on Silica Substrates. *Langmuir* **2009,** *25*, 6997-7005.

12. Cremer, P. S.; Boxer, S. G. Formation and Spreading of Lipid Bilayers on Planar Glass Supports. *J. Phys. Chem. B* **1999,** *103*, 2554-2559.

13. Hamai, C.; Cremer, P. S.; Musser, S. M. Single Giant Vesicle Rupture Events Reveal Multiple Mechanisms of Glass-Supported Bilayer Formation. *Biophys. J.* **2007,** *92*, 1988-1999.

14. Radler, J.; Strey, H.; Sackmann, E. Phenomenology and Kinetics of Lipid Bilayer Spreading on Hydrophilic Surfaces. *Langmuir* **1995,** *11*, 4539-4548.

15. Khan, T. R.; Grandin, H. M.; Mashaghi, A.; Textor, M.; Reimhult, E.; Reviakine, I. Lipid Redistribution in Phosphatidylserine-Containing Vesicles Adsorbing on Titania. *Biointerphases* **2008,** *3*, FA90-FA95.

16. Lagerholm, B. C.; Starr, T. E.; Volovyk, Z. N.; Thompson, N. L. Rebinding of IgE Fabs at Haptenated Planar Membranes: Measurement by Total Internal Reflection with Fluorescence Photobleaching Recovery. *Biochem.* **2000,** *39*, 2042-2051.

17. Tamm, L. K.; McConnell, H. M. Supported Phospholipid-Bilayers. *Biophys. J.* **1985,** *47*, 105-113.

18. Reimhult, E.; Hook, F.; Kasemo, B. Vesicle Adsorption on SiO2 and TiO2: Dependence on Vesicle Size. *J. Chem. Phys.* **2002,** *117*, 7401-7404.

19. Savarala, S.; Ahmed, S.; Ilies, M. A.; Wunder, S. L. Formation and Colloidal Stability of DMPC Supported Lipid Bilayers on SiO2 Nanobeads. *Langmuir* **2010,** *26*, 12081-12088.

20. Claesson, M.; Cho, N. J.; Frank, C. W.; Andersson, M. Vesicle Adsorption on Mesoporous Silica and Titania. *Langmuir* **2010,** *26*, 16630-16633.

21. Williams, L. M.; Evans, S. D.; Flynn, T. M.; Marsh, A.; Knowles, P. F.; Bushby, R. J.; Boden, N. Kinetics of the Unrolling of Small Unilamellar Phospholipid Vesicles onto Self-Assembled Monolayers. *Langmuir* **1997,** *13*, 751-757.

22. Pera, I.; Stark, R.; Kappl, M.; Butt, H. J.; Benfenati, F. Using the Atomic Force Microscope to Study the Interaction Between two Solid Supported Lipid Bilayers and the Influence of Synapsin I. *Biophys. J.* **2004,** *87*, 2446-2455.

23. Gassmann, O.; Kreir, M.; Ambrosi, C.; Pranskevich, J.; Oshima, A.; Roling, C.; Sosinsky, G.; Fertig, N.; Steinem, C. The M34A Nutant of Connexin26 Reveals Active Conductance States in Pore-Suspending Membranes. *J. Struct. Biol.* **2009,** *168*, 168-176.

24. Kleefen, A.; Pedone, D.; Grunwald, C.; Wei, R.; Firnkes, M.; Abstreiter, G.; Rant, U.;

Tampe, R. Multiplexed Parallel Single Transport Recordings on Nanopore Arrays. *Nano Lett.* **2010,** *10*, 5080-5087.

25. Schmitt, E. K.; Nurnabi, M.; Bushby, R. J.; Steinem, C. Electrically Insulating Pore-Suspending Membranes on Highly Ordered Porous Alumina Obtained from Vesicle Spreading. *Soft Matter* **2008,** *4*, 250-253.

26. Im, H.; Wittenberg, N. J.; Lesuffleur, A.; Lindquist, N. C.; Oh, S. H. Membrane Protein Biosensing with Plasmonic Nanopore Arrays and Pore-Spanning Lipid Membranes. *Chem. Sci.* **2010,** *1*, 688-696.

27. Kresak, S.; Hianik, T.; Naumann, R. L. C. Giga-Seal Solvent-Free Bilayer Lipid Membranes: From Single Nanopores to Nanopore Arrays. *Soft Matter* **2009,** *5*, 4021-4032.

28. Sugihara, K.; Voros, J.; Zambelli, T. A Gigaseal Obtained with a Self-Assembled Long-Lifetime Lipid Bilayer on a Single Polyelectrolyte Multilayer-Filled Nanopore. *Acs Nano* **2010,** *4*, 5047-5054.

29. Schmitt, E. K.; Vrouenraets, M.; Steinem, C.; Channel Activity of OmpF Monitored in Nano-BLMs. *Biophys. J.* **2006,** *91*, 2163-2171.

30. Weiskopf, D.; Schmitt, E. K.; Kluhr, M. H.; Dertinger, S. K.; Steinem, C. Micro-BLMs on Highly Ordered Porous Silicon Substrates: Rupture Process and Lateral Mobility. *Langmuir* **2007,** *23*, 9134-9139.

31. Han, X. J.; Studer, A.; Sehr, H.; Geissbuhler, I.; Di Berardino, M.; Winkler, F. K.; Tiefenauer, L. X. Nanopore Arrays for Stable and Functional Free-Standing Lipid Bilayers. *Adv. Mater.* **2007,** *19*, 4466-4470.

32. Mey, I.; Stephan, M.; Schmitt, E. K.; Muller, M. M.; Ben Amar, M.; Steinem, C.; Janshoff, A. Local Membrane Mechanics of Pore-Spanning Bilayers. *J. Am. Chem. Soc.* **2009,** *131*, 7031-7039.

33. Jonsson, P.; Jonsson, M. P.; Hook, F. Sealing of Submicrometer Wells by a Shear-Driven Lipid Bilayer. *Nano Lett.* **2010,** *10*, 1900-1906.

34. Worsfold, O.; Voelcker, N. H.; Nishiya, T. Biosensing Using Lipid Bilayers Suspended on Porous Silicon. *Langmuir* **2006,** *22*, 7078-7083.

35. Cunin, F.; Milhiet, P. E.; Anglin, E.; Sailor, M. J.; Espenel, C.; Le Grimellec, C.; Brunel, D.; Devoisselle, J. M. Continuous Planar Phospholipid Bilayer Supported on Porous Silicon Thin Film Reflector. *Ultramicroscopy* **2007,** *107*, 1048-1052.

36. Bhattacharya, J.; Kisner, A.; Offenhäusser, A.; Wolfrum, B. Microfluidic Anodization of Aluminum Films for the Fabrication of Nanoporous Lipid Bilayer Support Structures. *Beilstein J. Nanotechnol.* **2011,** *2*, 104-109.

37. Suzuki, K.; Masuhara, H. Groove-Spanning Behavior of Lipid Membranes on Microfabricated Silicon Substrates. *Langmuir* **2005,** *21*, 6487-6494.

38. Pfeiffer, I.; Seantier, B.; Petronis, S.; Sutherland, D.; Kasemo, B.; Zach, M. Influence of Nanotopography on Phospholipid Bilayer Formation on Silicon Dioxide. *J. Phys. Chem. B* **2008,** *112*, 5175-5181.

39. Pfeiffer, I.; Petronis, S.; Koper, I.; Kasemo, B.; Zach, M. Vesicle Adsorption and Phospholipid Bilayer Formation on Topographically and Chemically Nanostructured Surfaces. *J. Phys. Chem. B* **2010,** *114*, 4623-4631.

40. Simon, A.; Girard-Egrot, A.; Sauter, F.; Pudda, C.; D'Hahan, N. P.; Blum, L.; Chatelain, F.; Fuchs, A. Formation and Stability of a Suspended Biomimetic Lipid Bilayer on Silicon Submicrometer-Sized Pores. *J. Colloid Interface Sci.* **2007,** *308*, 337-343.

41. Knoll, W. Interfaces and Thin Films as Seen by Bound Electromagnetic Waves. *Annu. Rev. Phys. Chem.* **1998,** *49*, 569-638.

42. Lau, K. H. A.; Tan, L. S.; Tamada, K.; Sander, M. S.; Knoll, W. Highly Sensitive Detection of Processes Occurring Inside Nanoporous Anodic Alumina Templates: A Waveguide Optical Study. *J. Phys. Chem. B* **2004,** *108*, 10812-10818.

43. Lazzara, T. D.; Lau, K. H. A.; Abou-Kandil, A. I.; Caminade, A. M.; Majoral, J. P.; Knoll, W. Polyelectrolyte Layer-by-Layer Deposition in Cylindrical Nanopores. *Acs Nano* **2010,** *4*, 3909-3920.

44. Dai, J. H.; Baker, G. L.; Bruening, M. L. Use of Porous Membranes Modified with Polyelectrolyte Multilayers as Substrates for Protein Arrays with low Nonspecific Adsorption. *Anal. Chem.* **2006,** *78*, 135-140.

45. Takmakov, P.; Vlassiouk, I.; Smirnov, S. Application of Anodized Aluminum in Fluorescence Detection of Biological Species. *Anal. Bioanal.Chem.* **2006,** *385*, 954-958.

46. Casanova, F.; Chiang, C. E.; Li, C. P.; Roshchin, I. V.; Ruminski, A. M.; Sailor, M. J.; Schuller, I. K. Gas Adsorption and Capillary Condensation in Nanoporous Alumina Films. *Nanotechnology* **2008,** *19*.

47. Janshoff, A.; Dancil, K. P. S.; Steinem, C.; Greiner, D. P.; Lin, V. S. Y.; Gurtner, C.; Motesharei, K.; Sailor, M. J.; Ghadiri, M. R. Macroporous p-Type Silicon Fabry-Perot Layers. Fabrication, Characterization, and Applications in Biosensing. *J. Am. Chem. Soc.* **1998,** *120*, 12108-12116.

48. Schwartz, M. P.; Alvarez, S. D.; Sailor, M. J. Porous SiO2 Interferometric Biosensor for Quantitative Determination of Protein Interactions: Binding of Protein a to Immunoglobulins Derived from Different Species. *Anal. Chem.* **2007,** *79*, 327-334.

49. Vasilev, K.; Knoll, W.; Kreiter, M. Fluorescence Intensities of Chromophores in Front of a Thin Metal Film. *J. Chem. Phys.* **2004,** *120*, 3439-3445.

50. Lau, K. H. A.; Knoll, W.; Kim, D. H. Theoretical Optical Waveguide Investigation of Self-Organized Polymer Thin Film Nanostructures with Nanoparticle Incorporation. *Macromol. Res.* **2007,** *15*, 211-215.

51. Ono, S.; Masuko, N. The Duplex Structure of Cell-Walls of Porous Anodic Films Formed on Aluminum. *Corrosion Science* **1992,** *33*, 503-505.

52. Lazzara, T. D.; Kliesch, T. T.; Janshoff, A.; Steinem, C. Orthogonal Functionalization of Nanoporous Substrates: Control of 3D Surface Functionality. *ACS Appl. Mater. Interfaces* **2011,** *in press*.

53. Aronsson, B. O.; Lausmaa, J.; Kasemo, B. Glow Discharge Plasma Treatment for Surface Cleaning and Modification of Metallic Biomaterials. *J. Biomed. Mater. Res.* **1997,** *35*, 49-73.

54. Raiber, K.; Terfort, A.; Benndorf, C.; Krings, N.; Strehblow, H. H. Removal of Self-Assembled Monolayers of Alkanethiolates on Gold by Plasma Cleaning. *Surf. Sci.* **2005,** *595*, 56-63.

55. Axelrod, D.; Koppel, D. E.; Schlessinger, J.; Elson, E.; Webb, W. W. Mobility Measurement by Analysis of Fluorescence Photobleaching Recovery Kinetics. *Biophys. J.* **1976,** *16*, 1055-1069.

56. Stelzle, M.; Miehlich, R.; Sackmann, E. 2-Dimensional Microelectrophoresis in Supported Lipid Bilayers. *Biophys. J.* **1992,** *63*, 1346-1354.

57. Boxer, S. G. Molecular Transport and Organization in Supported Lipid Membranes. *Curr. Opin. Chem. Biol.* **2000,** *4*, 704-709.

58. Nissen, J.; Gritsch, S.; Wiegand, G.; Radler, J. O. Wetting of Phospholipid Membranes on Hydrophilic Surfaces - Concepts Towards Self-Healing Membranes. *Eur. Phys. J. B* **1999,** *10*, 335-344.

59. Lazzara, T. D.; Lau, K. H. A.; Knoll, W. Mounted Nanoporous Anodic Alumina Thin Films as Planar Optical Waveguides. *J. Nanosci. Nanotechnol.* **2010,** *10*, 4293-4299.

60. Bagatolli, L. A.; Parasassi, T.; Gratton, E. Giant Phospholipid Vesicles: Comparison Among the Whole Lipid Sample Characteristics using Different Preparation Methods - A Two Photon Fluorescence Microscopy Study. *Chem. Phys. Lipids* **2000,** *105*, 135-147.

Acknowledgement. A.J. and C.S. gratefully acknowledge financial support from the DFG (JA 963/8-1, SFB 803). T.D.L. acknowledges the award of a doctoral scholarship from *le Fonds Québécois de la Recherche sur la Nature et les Technologies* (FQRNT) and additional financial support from the Göttingen Graduate School for Neurosciences and Molecular Biosciences (GGNB). M.K. acknowledges financial support from MPIP-IMPRS Mainz and IMPRS-PBCS Göttingen doctoral scholarships. C.S. thanks the SFB 803 for financial support.

Supporting Information Available. Figure S1: Behavior of GUVs with different functionalized substrates. Figure S2: Measurement of contact angle, before and after O_2 treatment of gas-phase silanized glass slides with SHTES, APTES and TEOS. Figure S3: Alexa-488 labeled avidin adsorbed on a non-functionalized AAO was bleached. Figure S4: Example of high surface area membrane coverage of AAO, shown with pyranine experiment. Figure S5: High resolution Z-line profile after bleaching of entrapped pyranine in AAO pores. Figure S6: FRAP curve of a membrane formed on the planar adhesive surface, also hydrophilic. Movie S1: Vesicle approach and rupture. This material is available free of charge *via* the Internet at http://pubs.acs.org

9.7. Supporting Information

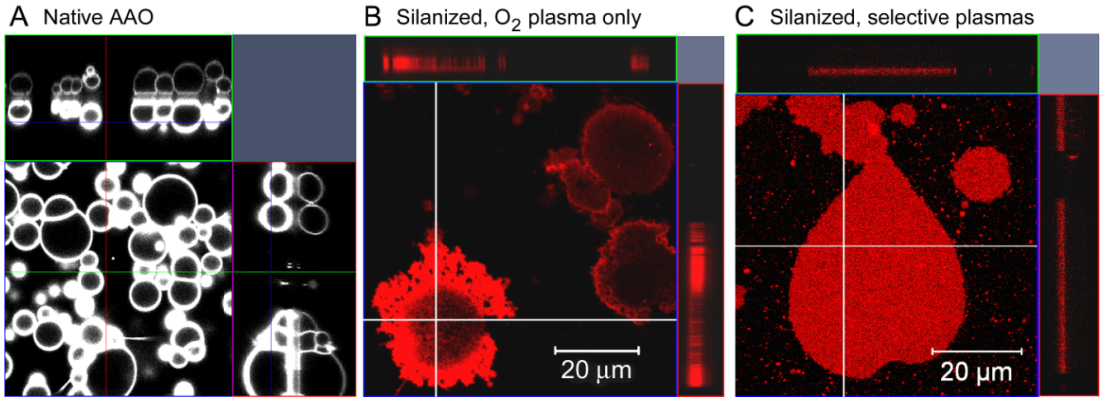

Figure 9.S1. Confocal fluorescence image composites showing the *X*-*Y* plane in the larger center images and *Z*-direction profiles in the top and right side images (distances in *X, Y* and *Z* directions are proportional to the scale. POPC GUVs interact differently with AAO (about 5 µm thick), depending on the AAO functionalization. (**A**) On native AAO substrates, GUVs left to incubate for several hours simply adsorb weakly on the nanoporous AAO and do not rupture (reflection of vesicles is observed due to a metal layer). AAO lies in between the reflection planes (full image width: 130 µm) (**B**) On an AAO silanized with SHTES and oxygen plasma treated to ensure a hydrophilic SiOH-terminated surface, GUVs rupture to form partial SSMs on the AAO surface: fluorescent lipids are both atop and within the AAO thickness. (**C**) When the AAO substrate is treated with the selective functionalization procedure, GUVs rupture to form pore-spanning membranes that are localized at the AAO surface (horizontal and vertical white lines correspond to the orthogonal projections shown atop and to the right, respectively) (Scales are valid for all projections).

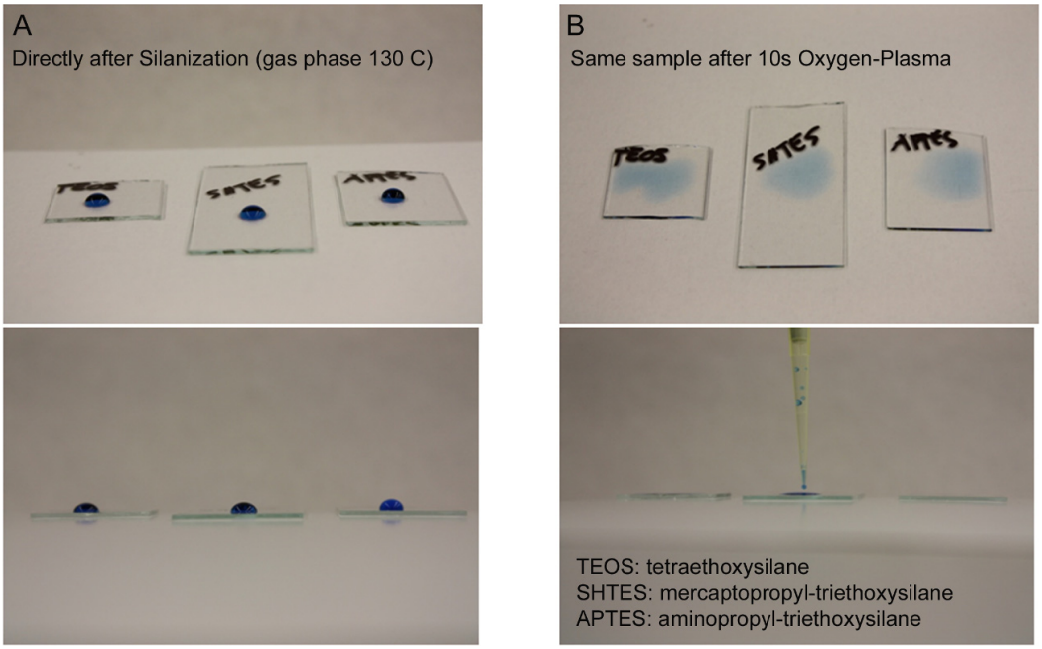

Figure 9.S2. (**A**) Wetting behavior of phosphate buffer drop on freshly silanized glass slides with tetraethoxysilane (TEOS), mercaptopropyl-triethoxysilane (SHTES) and aminopropyl-triethoxysilane (APTES), respectively. The surface is hydrophobic with contact angles ~80°. (**B**) After 10 s of O_2 plasma treatment, phosphate buffer wets the surface, the contact angle is < 5°, due to oxidation of hydrophobic ethoxy and mercaptopropyl surface groups.

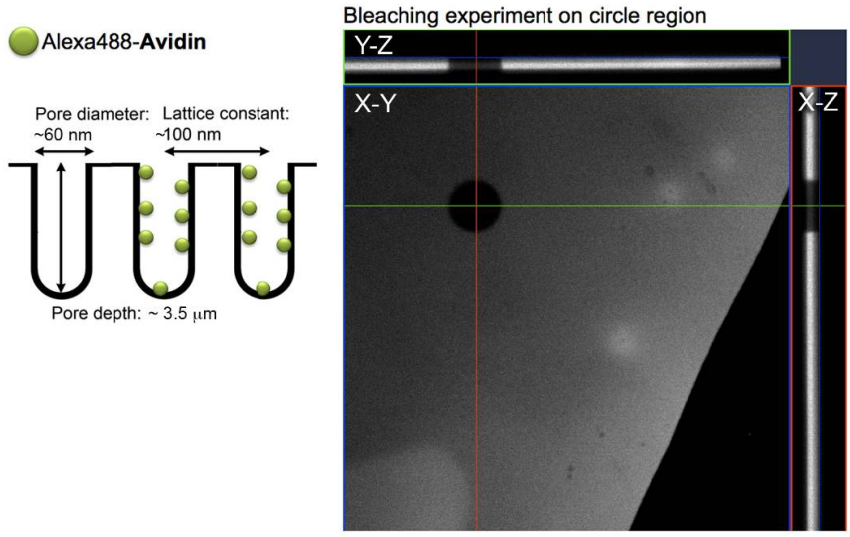

Figure 9.S3. Confocal laser scanning fluorescence microscopy image of labeled Alexa488-avidin adsorbed on alumina. *X-Y* plane shows that the alumina is fluorescent due to protein adsorption. The *Z*-stack in the *X-Z* and *Y-Z* shows that the AAO is fluorescent throughout the AAO substrate. Avidin adsorption throughout the AAO nanopores is further confirmed when a circular area on the AAO is photobleached: *Z*-stack composite image of that area shows a lack of fluorescence. With fluorescence microscopy, protein adsorption was observed as an increase in the overall green fluorescence of the AAO substrate, and was also confirmed by observing the permanent loss of fluorescence from photobleached areas on the AAO.

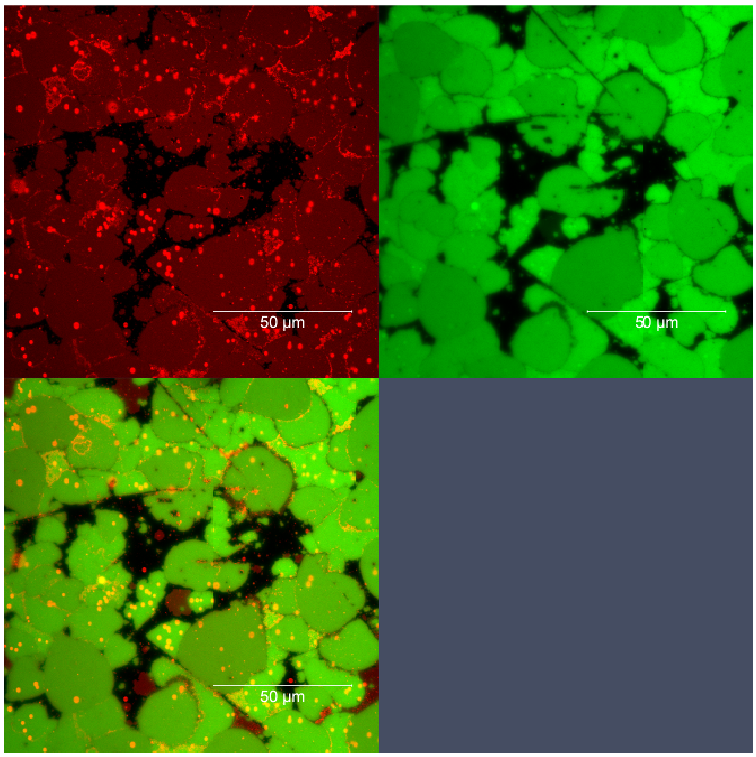

Figure 9.S4. Pyranine encapsulation experiments showing: high POPC membrane coverage (top left, red) and effective pyranine encapsulation (top right, green) of the dye within the AAO nanopores. The composite image (bottom left) shows that the encapsulation of pyranine coincides with the membrane patches. (scale bar: 50 μm).

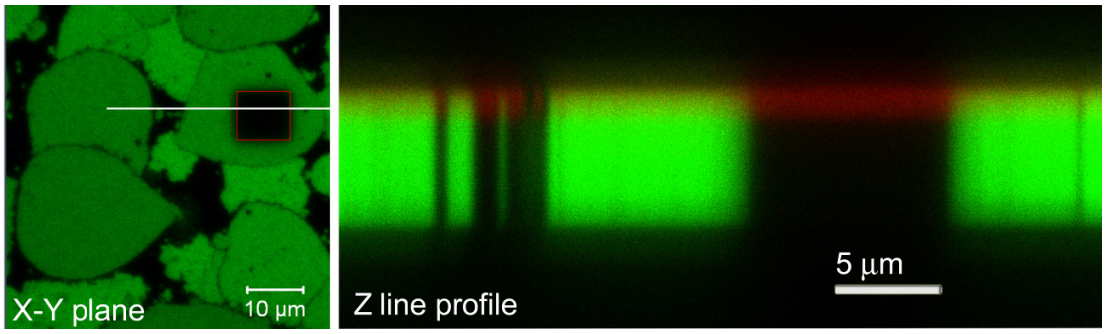

Figure 9.S5. *X-Y* image (left) of pyranine entrapped in AAO nanopores by POPC membrane patches (only green filter corresponding to pyranine fluorescence is shown). A square region was photobleached and did not recover, even after several minutes (image shown after 2 min), note that the edges remain sharp. A *Z*-line profile (right) corresponds to the white line across the squared photobleached region from figure on the left, image was taken 5 min after photobleaching. The profile shows that the pyranine trapped in the cylindrical pores was photobleached and did not recover, here both green (pyranine) and red (membrane) filters are shown. The membrane (red) is clearly visible and the fluorescence is only localized atop the AAO.

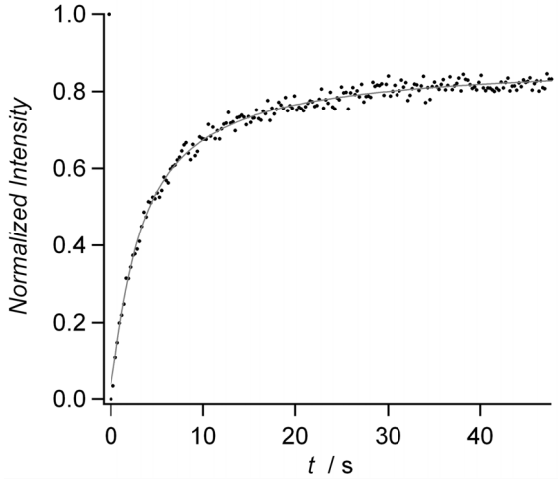

Figure 9.S6. Fluorescent recovery after photobleaching was performed on a lipid membrane patch lying on the flat non-porous adhesive surface (next to the AAO), which was used to bind the AAO onto the glass slide. The diffusion coefficient found on the planar surface, 4.5 ± 1.5 $\mu m^2/s$, was similar to that observed for the pore-spanning lipid membrane patches. The planar adhesive surface was also silanized with mercaptopropyl-triethoxysilane and subjected to the same selective plasma treatments as the pore-rims since it was also covered by Au. Therefore this surface also had a hydrophilic surface functionalization.

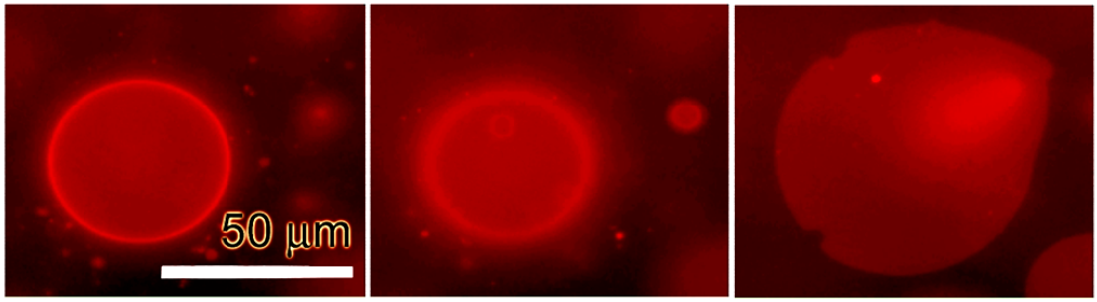

Movie 9.S1. Videomicroscopy frames of GUVs rupturing on hydrophilic AAO. Background fluorescence is due to the high number of vesicles in solution. The video frame rate shown was slowed to 1 frame per second (fps): 1 frame = 77 ms real-time. The original movie was recorded at 13 fps.

Chapter 10 Discussion

10.1. AAO studied by optical waveguide spectroscopy

Porous materials have been considered as improved biosensing platforms because of their increased surface area in comparison to an equivalent planar surface. When prepared as thin-films, these porous materials can be probed by optical surface analysis techniques such as ellipsometry, thin-film reflectometry, optical waveguide spectroscopy and fluorescence as long as the nanostructured pores are below the scattering limit of light (~ 1/10λ). Macroporous materials generally possess geometrical features that are above the scattering limit and therefore give rise to inelastic light scattering and therefore cannot be used for optical studies. Microporous materials are optically transparent, but their pore diameters are too narrow to allow macromolecular inclusion. However, materials such as anodic aluminum oxide (AAO), which have a highly ordered cylindrical pore structure, can be prepared with pore diameters ranging from 10-100 nm that allow the inclusion of macromolecules. Such AAO is sufficiently optically transparent, with minimal background fluorescence, such that it can efficiently be used in optical studies. Previous studies have demonstrated that the AAO refractive index can be monitored by thin-film techniques[1-6] or optical fluorescence[7-8] that probe the sample from atop.

Furthermore, time-resolved confocal fluorescence microscopy studies, as those we have performed, do not appear to have been performed. In fact, fluorescence studies of AAO have not been frequently reported.[9-11] One possible reason is that thick films, > 10-20 μm, start to exhibit background fluorescence, which is not observed when AAO is prepared as thin-film. Thick film are typically preferred due to ease of handling, but inelastic light scattering increases with the AAO membrane thickness due to the greater number of scattering defects that are present.

Optical waveguide spectroscopy (OWS) studies[12-15] offer a sub-nanometer resolution, but require light coupling through a prism from beneath the AAO thin-film, rather than from the top. To satisfy this particular requirement, the technique presented in chapter 3 was developed. The AAO produced in this thesis for waveguiding studies was highly ordered, optically transparent and had tunable pore diameters and pore depths. In fact, the success of this method relied on the initial preparation of a high quality AAO film from bulk Al metal, which was subsequently transferred onto a measurement slide. Other methods rely on the direct anodization of Al-films deposited by electrochemical reduction, sputtering or thermal vacuum deposition.[5-6, 14, 16-17] These techniques are inherently more expensive and offers lower control over the AAO thickness, lattice constant and pore ordering. Furthermore, the large scale production of reproducible samples is difficult to achieve.

In contrast to previous studies involving AAO, the experiments carried-out in this thesis were detailed studies that elucidated the contribution of different parameters towards the deposition of macromolecules in the confined cylindrical geometry of AAO. We therefore did not simply demonstrate that the detection of molecular deposition was possible, as in previous reports, going beyond the simple proof-of-principle. On the one hand we have directly investigated how the AAO geometry and solution parameters influence adsorption kinetics within the AAO and supported our experimental observation with finite element simulations. This established a reference framework that can be used to predict and understand the instrumental response expected for nanoporous detection platforms. On the other hand, we have experimentally demonstrated that steric hindrance at low pore diameters (25-30 nm) and electrostatic repulsion at low salt concentrations inhibit deposition within the cylindrical nanopores. These results establish a reference framework that can be used to optimize Layer-by-Layer (LbL) structure formation in nanoporous materials.

10.2. What limits macromolecular deposition in nanopores

An important conclusion derived from our studies of adsorption kinetics in AAO is that macromolecular transport within the nanopores is limited by mass-transport, such that even at μM concentrations, only a few macromolecules per pore are present at any time. This

hides any information about adsorption constants, since pore-entrance is the limiting step in a porous geometry. However, because the response is slow and linear with concentration, a porous material such as AAO can be used as an accurate molecular concentration sensor, with a linear range over several orders of magnitude, at least 10^4 for avidin, from 1 nM to 10 mM.

LbL assemblies are generally carried out on flat surfaces and therefore can be studied by various planar surface characterization techniques. However, the characterization of LbL processes within porous substrates is not a straightforward task. Even current characterization of LbL self-assembled nanotubes is typically carried out by post-synthesis investigation of the structures. A recent example by Cho *et al.* in 2010 involved the characterization of polyelectrolyte nanotubes by scanning electron microscopy and energy dispersive x-ray spectroscopy.[18] An alternative characterization strategy involves the fluorescent labeling of macromolecules to study the deposition *in-situ*, which is also a time consuming task and the chemistry is not always straightforward. Optimization of pore-loading parameters therefore requires a significant amount of time and experimental material. OWS allows a label-free investigation of molecular deposition with sub-nanometer resolution. The technique can be used to detect the amount of deposited material and to partly estimate the deposition uniformity along the pore length. The OWS advantage of *in-situ* detection also implies that the effects of changing various solution parameters can be directly investigated, without the need for *ex-situ* methods. OWS can therefore be used as both a characterization tool and as an optical label-free sensor, similarly to surface plasmon resonance. Conceivably, one may test the stability of different systems to external stimuli, such as the immobilization retention efficiency of nanoparticle catalysts embedded in nanoporous solid-supported media.

10.3. The Importance of Controlling Surface Chemistry in 3D

The preparation of biosensing porous platforms, or any reactive surface for that matter, typically entails an initial surface functionalization step that is usually carried out by covalent coupling of functional groups onto a surface, as we have shown using positively charged silanes. However, the introduction of multiple functional groups by covalent coupling is not a simple straightforward task. We have demonstrated that by using a solid-supported lipid monolayer, formed from SUVs, we can take advantage of the rich liposome

surface chemistry and reproduce it onto the AAO surface. This method is straightforward and provides laterally mobile lipids in three-dimensions, which is something that cannot be achieved using covalent coupling. This can open possibilities to design tailored porous sensing platforms by accurately varying the multi-component surface composition, similarly as it has been done for solid-supported membranes.[19-23]

In many applications, a homogeneous surface functionalization is not desired since functional components adsorb without any selectivity. To direct the self-assembly of heterogeneous components, surfaces require an orthogonal functionalization that creates spatially distinct domains.[24-25] We presented a method for the orthogonal functionalization of porous substrates that involved the differentiation of the AAO surface chemistry on a 3D scale: the pore-rim and pore-interior surfaces were functionalized with a different surface chemistry, using silanes. The simple route of using gold-thiol chemistry could not be used because metal inclusion within the nanopores significantly dampens waveguide modes,[26] while gold on the pore rims quenches the fluorescence atop.[27] If Au was used as a pore-rim surface modification tool, neither OWS nor fluorescence could be used at their full potential. Therefore, the use of silanes was required to preserve the optical transparency of AAO.

The advantage of orthogonally functionalized AAO is that it can be used to direct the assembly of complex functional 3D architectures by relying on the spatially distinct surface functionalizations to selectively interact with solution components, as illustrated in figure 10.1. Here, the selective functionalization effectively directs the self-assembly of functional components.

As we have shown in chapters 7 and 9, the deposition of a pore-spanning membrane can be obtained from GUVs by tailoring the surface chemistry of the pore rims. Hydrophobic pore rims produced hybrid pore-spanning membranes, while hydrophilic pore rims produced fluid pore-spanning *bilayers*. These results show the importance of tuning the properties of a material to direct the organization of complex systems, such a lipid vesicles. Membranes formed from polymers are particularly relevant in molecular sieving and filtering applications. These surface species can be deposited by either LbL or by surface initiated polymerization of covalently attached molecular species.

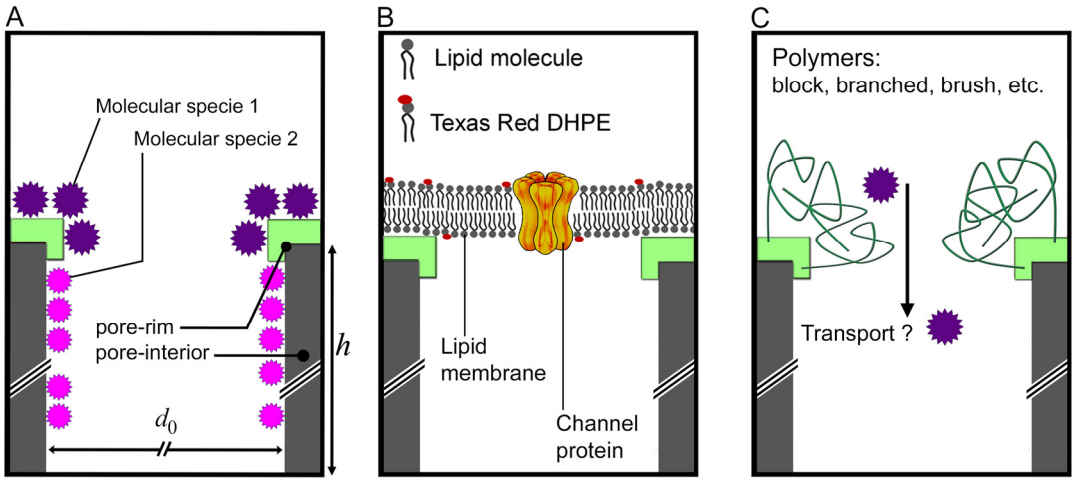

Figure 10.1. Orthogonal functionalization of nanoporous AAO membranes can be used to direct the formation of spatially selective architectures. Transport properties across the bulk/AAO interface can be investigated. (**A**) Adsorption of different macromolecular species on the pore rims and the pore-interior. (**B**) Biologically relevant systems to study membrane transport processes. (**C**) Relevant molecular and macromolecular sieving systems based on pore-entry modulation at the nanoporous/bulk interface by different polymer-based pore-rim coatings.

In contrast to previous reports, we have used OWS as a characterization tool to investigate the parameters that affect macromolecular transport within the cylindrical nanopores geometry in terms of solution parameters and porous geometry. These results are of general applicability in various nanoporous systems, and as such, of fundamental importance to understand and optimize sensing platforms and self-assembled LbL structures. Finally, we demonstrated that by tuning the spatial localization of the silanization on AAO, the formation of different lipid membrane structures could be directed. By rendering the AAO hydrophobic, a lipid monolayer was formed on the entire surface. By localizing the functionalization on the pore rims, we directed the formation of pore-spanning membranes. In general, orthogonal functionalized substrates allow the compartmentalization of the nanopore environment and, therefore, these materials open new possibilities for controlling molecular transport properties across synthetic membranes.

10.4. Original Contribution to Knowledge

- A mounting technique was developed to deposit highly ordered anodic aluminum oxide (AAO) membranes, applicable to any lattice constant. This technique is particular to the deposition of very thin membranes (1-10 μm thick) on heterogeneous substrates.

- The Layer-by-Layer (LbL) deposition of macromolecules was studied for linear-polyelectrolytes, dendrimer-polyelectrolytes and proteins. We proposed a method that allowed the estimation of the LbL film geometry, which is not possible on flat surfaces. The method consisted in comparing the optical thickness and number of LbL steps of the multilayer formation process in different initial diameter pores and extrapolating an average layer thickness.

- Ideal pore-loading conditions, for macromolecules of about 5 nm diameter, were determined. These consist in using higher concentrations, higher ionic strengths than required for planar surfaces, and pore diameters that are larger than 40 nm. Macromolecular transport was not hindered, within the tested pore depths (1-8 μm).

- The potential benefits and limitation of using AAO as a biosensing platform were investigated, by both experiments and finite element simulations. The instrumental response of the porous structure is limited by mass-transport within the nanopores. Alternatively, desorption kinetics hold potentially greater benefits for sensing applications.

- An orthogonal AAO functionalization method was presented, to modify AAO with different pore-interior and pore-rim surface chemistries. Silane-chemistry was used and the AAO substrates therefore remained optically transparent for fluorescent microscopy studies. This method was used to form hybrid solvent-free pore-spanning lipid membranes that could be visualized by optical microscopy.

- By modifying the AAO with a hydrophobic surface functionalization, hybrid solid-supported membranes were formed on the entire AAO surface. This surface modification tool was used to finely tune the density of receptor groups on the AAO surface and provided laterally mobile lipids on a three-dimensional scale.

- AAO substrates were orthogonally modified to obtain a hydrophilic pore-rim functionalization. These substrates were then used to form fluid pore-spanning bilayers atop the AAO, which are not tethered at the pore-rims. The AAO remained transparent and fluorescence studies were possible.

- The concept of molecular exclusion and molecular encapsulation with a fluid pore-spanning bilayer was demonstrated and visualized in three-dimensions using confocal fluorescence microscopy.

10.2. References

1. Alvarez, S. D.; Li, C. P.; Chiang, C. E.; Schuller, I. K.; Sailor, M. J.; A Label-Free Porous Alumina Interferometric Immunosensor. *Acs Nano* **2009,** *3*, 3301-3307.

2. Casanova, F.; Chiang, C. E.; Li, C. P.; Roshchin, I. V.; Ruminski, A. M.; Sailor, M. J.; Schuller, I. K.; Gas Adsorption and Capillary Condensation in Nanoporous Alumina Films. *Nanotechnology* **2008,** *19*.

3. Dancil, K. P. S.; Greiner, D. P.; Sailor, M. J.; A Porous Silicon Optical Biosensor: Detection of Reversible Binding of Igg to a Protein a-Modified Surface. *J. Am. Chem. Soc.* **1999,** *121*, 7925-7930.

4. Lin, V. S. Y.; Motesharei, K.; Dancil, K. P. S.; Sailor, M. J.; Ghadiri, M. R.; A Porous Silicon-Based Optical Interferometric Biosensor. *Science* **1997,** *278*, 840-843.

5. Lau, K. H. A.; Duran, H.; Knoll, W.; In Situ Characterization of N-Carboxy Anhydride Polymerization in Nanoporous Anodic Alumina. *J. Phys. Chem. B* **2009,** *113*, 3179-3189.

6. Lau, K. H. A.; Tan, L. S.; Tamada, K.; Sander, M. S.; Knoll, W.; Highly Sensitive Detection of Processes Occurring inside Nanoporous Anodic Alumina Templates: A Waveguide Optical Study. *J. Phys. Chem. B* **2004,** *108*, 10812-10818.

7. Takmakov, P.; Vlassiouk, I.; Smirnov, S.; Application of Anodized Aluminum in Fluorescence Detection of Biological Species. *Anal. Bioanal.Chem.* **2006,** *385*, 954-958.

8. Kim, S. Y.; Yu, J.; Son, S. J.; Min, J.; Signal Enhancement in a Protein Chip Array Using a 3-D Nanosurface. *Ultramicroscopy* **2010,** *110*, 659-665.

9. Matsumoto, F.; Nishio, K.; Masuda, H.; Flow-through-Type DNA Array Based on Ideally Ordered Anodic Porous Alumina Substrate. *Adv. Mater.* **2004,** *16*, 2105-+.

10. Kennard, R.; DeSisto, W. J.; Mason, M. D.; Molecular Diffusivity Measurement through an Alumina Membrane Using Time-Resolved Fluorescence Imaging. *Appl. Phys. Lett.* **2010,** *97*.

11. Penumetcha, S. S.; Kona, R.; Hardin, J. L.; Molder, A. L.; Steinle, E. D.; Monitoring Transport across Modified Nanoporous Alumina Membranes. *Sensors* **2007,** *7*, 2942-2952.

12. Aust, E. F.; Knoll, W.; Electrooptical Wave-Guide Microscopy. *J. Appl. Phys.* **1993,** *73*, 2705-2708.

13. Hickel, W.; Knoll, W.; Optical Wave-Guide Microscopy. *Appl. Phys. Lett.* **1990,** *57*, 1286-1288.

14. Kim, D. H.; Lau, K. H. A.; Robertson, J. W. F.; Lee, O. J.; Jeong, U.; Lee, J. I.; Hawker, C. J.; Russell, T. P.; Kim, J. K.; Knoll, W.; Thin Films of Block Copolymers as Planar Optical Waveguides. *Adv. Mater.* **2005,** *17*, 2442.

15. Knoll, W.; Interfaces and Thin Films as Seen by Bound Electromagnetic Waves. *Annu. Rev. Phys. Chem.* **1998,** *49*, 569-638.

16. Hotta, K.; Yamaguchi, A.; Teramae, N.; Properties of a Metal Clad Waveguide Sensor Based on a Nanoporous-Metal-Oxide/Metal Multilayer Film. *Anal. Chem.* **2010,** *82*, 6066-6073.

17. Trivinho-Strixino, F.; Guerreiro, H. A.; Gomes, C. S.; Pereira, E. C.; Guimaraes, F. E. G.; Active Waveguide Effects from Porous Anodic Alumina: An Optical Sensor Proposition. *Appl. Phys. Lett.* **2010,** *97*.

18. Cho, Y.; Lee, W.; Jhon, Y. K.; Genzer, J.; Char, K.; Polymer Nanotubules Obtained by Layer-by-Layer Deposition within Aao-Membrane Templates with Sub-100-Nm Pore Diameters. *Small* **2010,** *6*, 2683-2689.

19. Steinem, C.; Janshoff, A.; Multicomponent Membranes on Solid Substrates Interfaces for Protein Binding. *Curr. Opin. Colloid Interface Sci.* **2010,** *15*, 479-488.

20. Han, X. J.; Pradeep, S. N. D.; Critchley, K.; Sheikh, K.; Bushby, R. J.; Evans, S. D.; Supported Bilayer Lipid Membrane Arrays on Photopatterned Self-Assembled Monolavers. *Chem.Eur. J.* **2007,** *13*, 7957-7964.

21. Plant, A. L.; Self-Assembled Phospholipid Alkanethiol Biometic Bilayers on Gold. *Langmuir* **1993,** *9*, 2764-2767.

22. Plant, A. L.; Supported Hybrid Bilayer Membranes as Rugged Cell Membrane Mimics. *Langmuir* **1999,** *15*, 5128-5135.

23. Vontscharner, V.; McConnell, H. M.; Physical-Properties of Lipid Monolayers on Alkylated Planar Glass Surfaces. *Biophys. J.* **1981,** *36*, 421-427.

24. Busby, M.; Kerschbaumer, H.; Calzaferri, G.; De Cola, L.; Orthogonally Bifunctional

Fluorescent Zeolite-L Microcrystals. *Adv. Mater.* **2008,** *20*, 1614-1618.

25. Smith, R. K.; Lewis, P. A.; Weiss, P. S.; Patterning Self-Assembled Monolayers. *Prog. Surf. Sc.* **2004,** *75*, 1-68.

26. Lau, K. H. A.; Knoll, W.; Kim, D. H.; Theoretical Optical Waveguide Investigation of Self-Organized Polymer Thin Film Nanostructures with Nanoparticle Incorporation. *Macromol. Res.* **2007,** *15*, 211-215.

27. Vasilev, K.; Knoll, W.; Kreiter, M.; Fluorescence Intensities of Chromophores in Front of a Thin Metal Film. *J. Chem. Phys.* **2004,** *120*, 3439-3445.